

Scrape-Off Layer physics in limited plasmas in TCV

THÈSE N° 7475 (2017)

PRÉSENTÉE LE 17 FÉVRIER 2017

À LA FACULTÉ DES SCIENCES DE BASE
CRPP - PHYSIQUE DES PLASMAS DE BASE
PROGRAMME DOCTORAL EN PHYSIQUE

ÉCOLE POLYTECHNIQUE FÉDÉRALE DE LAUSANNE

POUR L'OBTENTION DU GRADE DE DOCTEUR ÈS SCIENCES

PAR

Federico NESPOLI

acceptée sur proposition du jury:

Prof. H. M. Rønnow, président du jury
Dr I. Furno, Dr B. Labit, directeurs de thèse
Prof. B. Lipschultz, rapporteur
Dr N. Vianello, rapporteur
Prof. P. Ricci, rapporteur



ÉCOLE POLYTECHNIQUE
FÉDÉRALE DE LAUSANNE

Suisse
2017

Abstract

Controlled nuclear fusion is the most promising candidate for being an inexhaustible, clean and intrinsically safe energy source. Research in the last 60 years has focused on the fusion reactor concept called tokamak, in which a high temperature plasma is confined using magnetic fields, producing fusion reactions. Because of turbulence, the confined plasma diffuses to the outermost region of the tokamak, featuring open field lines, called the Scrape-Off Layer (SOL). In the SOL, the plasma is convected along the field lines and is deposited on the solid surfaces of the tokamak wall. The plasma-wall interaction through the SOL is believed to strongly affect the reactor performances, and the elevated heat loads on the solid surfaces are one of the most limiting factors for fusion. Even though a variety of magnetic configurations has been developed through the years to decouple the main plasma from the reactor wall and improve the reactor performances, the SOL physics is not completely understood, not even in the simpler, “limited” configuration. In this configuration, the main plasma touches the reactor wall, or a “limiter”, and the contact point defines the so called Last Closed Flux Surface (LCFS), separating the SOL region, featuring open field lines, from the core region, where the plasma is confined with closed field lines.

In this thesis, we advance the understanding of SOL physics in limited plasmas, combining experiments and numerical simulations. In particular, two topics are addressed. First, the separation of the SOL into two different regions, the “near” and “far” SOL, is investigated. The near SOL extends typically a few mm from the LCFS, features steep radial profiles of parallel heat flux and is responsible for the peak of heat deposition on the tokamak first wall. The far SOL, typically a few cm wide, features flatter heat flux profiles, and accounts for the majority of the heat deposited on the first wall. In a second instance, blob dynamics is investigated. Blobs are high density plasma filaments generated by turbulence, and are an ubiquitous feature of plasmas in open magnetic field line configurations. The blobs are self-propelled and travel outwards to the reactor walls, substantially increasing the cross field transport.

A series of dedicated experiments has been performed on the TCV tokamak in Lausanne, Switzerland. Several inboard-limited Deuterium (D) and Helium (He) plasma discharges are performed, varying the main plasma parameters (current, density and shaping). The heat fluxes deposited onto the wall are determined by means of infrared thermography. The cross field heat flux at the contact point is evaluated and discussed with respect to its dependence upon the plasma parameters. The radial profiles of the parallel heat flux are analyzed. The

evidence for the presence of a near SOL in TCV limited plasmas is reported for the first time, both for D and He discharges. The dependence of the near SOL upon the plasma parameters is discussed. In particular, for the first time the disappearance of the near SOL is reported, for low plasma current and high plasma density. The dependence of the strength of the near SOL heat fluxes upon resistivity and collisionality is discussed.

Non-ambipolar currents are measured to flow to the limiter in the near SOL using Langmuir probes embedded in the limiter. The presence of the non-ambipolar currents is found to correlate with the strength of the near SOL heat fluxes. An interpretation involving velocity shear is given.

The comparison of the heat fluxes and electric potentials measured on the limiter are compared with the measurements taken on the Low Field Side (LFS) using a reciprocating Langmuir probe. A near SOL is present at the two locations simultaneously, but wider at the LFS, and it is observed to also vanish at the LFS when vanishing at the limiter.

A method for the mitigation and suppression of the near SOL heat fluxes through impurity seeding is proposed, and first experimental evidences are presented and discussed.

The experimental results are compared with the results of non-linear, full-turbulence 3D simulations of the SOL of a TCV discharge, performed with the GBS code. The simulated parallel heat flux profiles qualitatively agree with the experimental ones, showing the presence of a near and far SOL. Also, non-ambipolar currents are observed to flow to the limiter, as seen in the experiments. The main discrepancies between simulations and experiments are discussed. The effect of resistivity on the simulated turbulence is investigated through a second simulation, identical to the first one but with a 40 times higher resistivity.

The blob dynamics in TCV is investigated using a conditional average sampling technique on the reciprocating Langmuir probe data. The results for two discharges, for low and high resistivity respectively, are discussed. In particular, the blob sizes and velocity are determined and compared with an existing scaling law.

A blob detection and tracking algorithm is applied to the numerical simulation outputs to study blob dynamics, and the results are discussed. The spatial distribution of blob birth is discussed. The 3D shape of the blobs is analyzed, characterizing the typical blob size and their connection to the limiter plates. The results of a cross-correlation analysis are exposed and compared with those from the blob detection algorithm. The velocities resulting from the tracking are presented and compared with an existing scaling law. The blob contribution to cross field particle and heat flux is evaluated.

Finally, the results of the blob analysis on the experiments are compared with those obtained from the simulations.

Key words: plasma physics, nuclear fusion, tokamak, scrape-off layer, limiter, infrared, langmuir probes, simulations, blobs

Sinossi

La fusione termonucleare è il candidato più promettente per fornire una nuova sorgente di energia pulita, intrinsecamente sicura e praticamente inesauribile. Negli ultimi 60 anni, la ricerca si è concentrata sul concetto di reattore a fusione chiamato tokamak, nel quale un plasma ad alta temperatura viene confinato usando dei campi magnetici, producendo reazioni di fusione nucleare. A causa della turbolenza, il plasma confinato diffonde nella regione più esterna del tokamak, chiamata “Scrape-Off Layer” (SOL), in cui le linee del campo magnetico sono aperte. Nello SOL, il plasma fluisce lungo le linee di campo ed è depositato sulla superficie della parete del reattore. Gli studi condotti fino ad oggi suggeriscono che le prestazioni di un reattore a fusione siano condizionate dall’interazione plasma-parete attraverso lo SOL. In particolare, gli elevati carichi termici risultanti dalla deposizione del plasma sulle superfici solide sono uno dei principali fattori che limitano il successo della fusione nucleare. Nonostante diverse configurazioni magnetiche siano state sviluppate con l’obiettivo di disaccoppiare il plasma principale dalla parete, la fisica dello SOL non è stata ancora completamente compresa, nemmeno nella configurazione magnetica più semplice, quella “limitata”. In questa configurazione, il plasma tocca direttamente la parete del reattore, e il punto di contatto definisce l’ultima superficie di flusso chiusa (“Last Closed Flux Surface”, LCFS), che separa lo SOL, in cui le linee di campo sono aperte, dalla regione dove il plasma è confinato da linee di campo chiuse.

In questa tesi, approfondiamo la nostra comprensione della fisica dello SOL, con un approccio che combina esperimenti e simulazioni numeriche. In particolare, due argomenti vengono affrontati. Il primo, è la separazione dello SOL in due regioni, lo SOL “vicino” e “lontano”. Il vicino SOL, che tipicamente si estende qualche mm dalla LCFS, presenta profili radiali di flusso di calore molto ripidi, ed è la causa del picco del carico termico sulla parete. Il lontano SOL, con una larghezza tipica di qualche cm, presenta profili più piatti ed è la causa della maggior parte del carico termico sulla parete. In secondo luogo, studiamo la dinamica dei “blob”. I blob sono dei filamenti di plasma ad alta densità, generati dalla turbolenza, e sono un tratto distintivo dei plasmi in linee di campo aperte. I blob sono spinti verso la parete esterna del reattore da un meccanismo di propulsione interna, aumentando il trasporto trasversale alle linee di campo.

Una serie di esperimenti è stata appositamente condotta sul tokamak TCV, a Losanna, Svizzera. Diverse scariche di plasma limitate sulla parete interna sono state eseguite sia in Deuterio

(D) che in Elio (He), variando i principali parametri del plasma : corrente, densità, forma. I flussi di calore depositati sulla parete sono stati determinati tramite termografia a infrarossi. Eseguiamo l'analisi del flusso di calore trasversale al campo magnetico, valutato al punto di contatto, per poi studiarne la variazione coi parametri di plasma. In seguito, analizziamo i profili radiali del flusso di calore parallelo, mettendo in evidenza, per la prima volta, l'esistenza di un vicino SOL in plasmi limitati in TCV, sia per scariche di D che di He. Discutiamo quindi l'influenza dei parametri di plasma sul vicino SOL. In particolare, riportiamo per la prima volta la scomparsa del vicino SOL per bassa corrente di plasma o alta densità. Mostriamo dunque come l'intensità del flusso di calore nel vicino SOL dipenda dalla resistività e collisionalità del plasma. Utilizzando sonde di Langmuir installate sul limiter, sono state misurate delle correnti non-ambipolari nello SOL. Viene qui mostrato come l'intensità di queste correnti sia strettamente correlata all'intensità del flusso di calore nel vicino SOL. Ne diamo una semplice interpretazione, utilizzando la variazione radiale del flusso poloidale del plasma.

Le misure effettuate con una sonda di Langmuir retraibile ci permettono di paragonare i flussi di calore e potenziali elettrici misurati sul limiter, discussi in precedenza, con quelli sul lato a basso campo ("Low Field Side", LFS). Ogni volta che il vicino SOL è stato misurato sul limiter, la sua presenza viene riscontrata anche al LFS. Tipicamente, il vicino SOL risulta essere più largo al LFS rispetto che al limiter. Inoltre, la scomparsa del vicino SOL avviene contemporaneamente al LFS e al limiter.

Proponiamo nel seguito un metodo per mitigare e sopprimere il flusso di calore nel vicino SOL tramite l'iniezione di impurità, e ne riportiamo i primi incoraggianti risultati sperimentali.

Compariamo quindi i risultati sperimentali con una simulazione nonlineare 3D della turbolenza del plasma, realizzata col codice GBS. I profili di flusso di calore simulati, che mostrano la presenza di un vicino e lontano SOL, sono in accordo qualitativo con quelli sperimentali. Inoltre, osserviamo il fluire di correnti non-ambipolari verso il limiter, similmente a quanto visto negli esperimenti. Discutiamo quindi le maggiori discrepanze tra simulazione ed esperimenti. Investighiamo poi l'effetto della resistività sulla turbolenza simulata tramite una seconda simulazione, identica alla prima ma con una resistività 40 volte maggiore.

Nel seguito, investighiamo la dinamica dei blob applicando un metodo di "conditional average sampling" ai dati della sonda di Langmuir retraibile. Esponiamo il risultato di questa analisi per due scariche, per alta e bassa resistività. In particolare, determiniamo la dimensione e la velocità dei blob, e li compariamo con una legge di scala presente in letteratura.

Un'analisi simile viene quindi eseguita sulle simulazioni della turbolenza del plasma, applicandovi un algoritmo di detezione e tracciamento dei blob, con l'obiettivo di studiarne la dinamica. Nel seguito, vengono esposti i risultati di tale analisi, cominciando con la discussione della distribuzione spaziale delle nascite dei blob ; segue l'analisi della struttura 3D dei blob, caratterizzandone la dimensione tipica e la connessione al limiter. Esponiamo dunque i risultati di un'analisi di correlazione, confrontandoli con quelli ottenuti dall'algoritmo di detezione dei blob. Le velocità risultanti dal tracciamento dei blob vengono discusse e confrontate con una legge di scala presente in letteratura. Il tracciamento dei blob ci permette inoltre di

stimare il loro contributo ai flussi trasversali di particelle e calore.

Infine, confrontiamo il risultato dell'analisi dei blob negli esperimenti con quella condotta sulle simulazioni.

Parole chiave : fisica del plasma, fusione nucleare, tokamak, scrape-off layer, limiter, infrarosso, sonde di Langmuir, simulazioni, blob

Contents

Abstract (English/Italiano)	iii
1 Introduction	1
1.1 Thermonuclear Fusion	1
1.2 The tokamak concept	2
1.3 The Scrape-Off Layer (SOL)	5
1.4 Context of this thesis	8
2 Experimental and numerical tools	13
2.1 The TCV tokamak	13
2.2 Metal foil bolometers (BOLO)	17
2.2.1 Determination of the plasma radiated power through tomography . . .	21
2.3 Infrared thermography	23
2.3.1 Thermosensorik Horizontal InfraRed system (HIR)	23
2.3.2 IRCam HIR	24
2.3.3 In situ calibration of the IR cameras	25
2.3.4 IR data analysis: estimation of the deposited heat flux	26
2.4 Langmuir probes (LP)	34
2.5 Reciprocating Langmuir probe (RP)	37
2.6 The THEODOR code	40
2.7 Numerical tools for TCV SOL turbulence simulations	42
2.7.1 The GBS code	42
2.7.2 The plasma model in GBS	44
2.7.3 The boundary conditions	45
2.7.4 The blob detection and tracking technique	48
3 SOL physics in inboard limited L-mode plasmas in TCV	49
3.1 Near SOL experiments in TCV: motivation and overview	49
3.1.1 First observations of the near SOL in TCV limited plasmas (2013)	51
3.1.2 Improved near SOL experiments in Deuterium and Helium plasmas (2015-2016)	52
3.2 Heat loads on the limiter	54
3.2.1 IR data analysis method	54
3.2.2 Perpendicular heat flux at the contact point	60

Contents

3.2.3	Parallel heat fluxes in Deuterium plasmas	61
3.2.4	Parallel heat fluxes in Helium plasmas	67
3.2.5	Comparison of the near and far SOL widths with existing theoretical scalings	70
3.2.6	Power in the near SOL and correlation with resistivity and collisionality .	73
3.3	Non-ambipolar currents flowing to the limiter	79
3.3.1	Role of the velocity shear layer	82
3.4	Steady state profiles at the outer midplane	84
3.5	Mitigation and suppression of the near SOL by impurity seeding	87
3.6	Comparison with nonlinear simulations	90
3.6.1	Numerical modeling of TCV discharge #49170	91
3.6.2	Comparison with the experimental data	92
3.6.3	Effect of resistivity on simulation results	95
3.7	Summary	98
4	Blob Physics in inboard limited L-mode plasmas in TCV	101
4.1	Blob detection with the reciprocating Langmuir probe (RP) in TCV	101
4.1.1	Conditional Average Sampling (CAS) of blobs	102
4.1.2	Determination of blob velocity and size	105
4.1.3	Blob detection results	107
4.1.4	Scaling of blob radial velocity	109
4.2	Blob tracking in the GBS simulations	110
4.2.1	Blob detection	111
4.2.2	Blob generation	113
4.2.3	Characterization of the blob size and shape	113
4.2.4	Cross correlation analysis	116
4.2.5	Blob velocity	119
4.2.6	Blob contribution to particle and heat radial fluxes	121
4.2.7	Experiments/simulations comparison	122
4.3	Summary	123
5	Conclusions and outlook	125
	Bibliography	136
	Acknowledgements	137
	Curriculum Vitae	139

1 Introduction

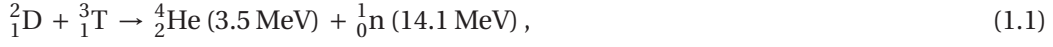
As the world population and the standard of the quality of life increase, the energy demand and consumption grow. Energy production is currently mostly based on fossil fuels (coal, oil, gas). Crude oil known reserves are estimated to last up to 60 years at the current rate of consumption [1], while carbon reserves are estimated to last in between one and two centuries. Also, the combustion of fossil fuels pollutes the air with CO_2 and other composites (CO_x , NO_x), nocive for the environment and people's health. Furthermore, CO_2 and the other byproducts of fossil fuel combustion are often referred to as green-house gases, being believed to be one of the causes of global climate change. Renewable energy production with photovoltaic panels and wind turbines rely on resources whose short and long term variability is of difficult prediction. Nuclear fission produces long-lived radioactive waste, and the risk of potential radioactive fallout is considered a no longer acceptable price to pay for energy production by the public opinion. A new carbon-free, reliable, globally distributed unlimited source of energy, not producing long-lived radioactive waste and intrinsically safe, is needed to face the increasing power demand and take over the role of fossil fuels. One of the most promising candidates for this is thermonuclear fusion.

1.1 Thermonuclear Fusion

Thermonuclear fusion is the source of energy that powers the stars. A nuclear fusion reaction happens when two positively charged nuclei overcome the Coulomb barrier, and the attractive nuclear force (or strong force) causes them to fuse into a single nucleus. The mass of the products of the fusion reaction is smaller than the sum of the masses of the reactants. The difference in mass Δm is transformed into energy via the famous Einstein's formula for mass-energy equivalence $E = \Delta mc^2$ [2]. Inside a star, the matter is in the state of plasma, the temperature being so high that the otherwise neutral atoms are dissociated into positive ions and electrons. The plasma is confined by the intense gravitational field generated by the star mass itself. The resulting high temperature and pressure allow fusion reactions to take place. In the last 60 years, many efforts have been made to exploit thermonuclear fusion on Earth to produce energy, by creating and confining a plasma of hydrogen isotopes. Indeed, the most

Chapter 1. Introduction

efficient fusion reaction is



where the hydrogen isotopes deuterium (D) and tritium (T) fuse into an Helium (He) ion and a neutron, the latter carrying most of the produced energy (17.6 MeV). This reaction has the highest cross section at the lowest energy threshold, and the fuel is a mixture of isotopes of the most abundant element in the universe, hydrogen, practically unlimited. Deuterium can be extracted from sea water, while tritium is radioactive with a very short half-life time (12.32 years) and it has therefore to be produced, e.g. by neutron activation of lithium (${}^6\text{Li}$) or D.

The rate of fusion reactions in a plasma depends on a combination of the plasma density n , temperature T , and confinement time $\tau = W/P_{\text{loss}}$. This is defined as the time necessary for the energy density confined in the plasma W to be lost by the power loss density P_{loss} . In particular, the fusion power produced by a plasma is larger than the lost power if the Lawson criterion [3] is satisfied:

$$n \times T \times \tau \geq C_{\text{crit}}, \quad (1.2)$$

where the critical value $C_{\text{crit}} \sim 3 \times 10^{21} \text{ sm}^{-3}\text{keV}$ for the D-T fusion reaction. In the stars, the criterion is satisfied by high density and confinement time, due to the huge gravitational field. Such a strong gravitational field can not be reproduced on Earth. There are then two main approaches for satisfying Eq. (1.2) in laboratory plasmas:

- Inertial confinement: a dense ($n \sim 10^{31} \text{ m}^{-3}$) and hot ($T \sim 30 \text{ keV}$) plasma is created for a very short time ($\tau \sim 10^{-11} \text{ s}$) compressing a solid pellet of D-T fuel via laser radiation pressure [4];
- Magnetic confinement: a rare ($n \sim 10^{20} \text{ m}^{-3}$) and hot plasma ($T \sim 30 \text{ keV}$) is confined with magnetic fields for a long time ($\tau \sim 1 \text{ s}$) [5].

Magnetic confinement is, nowadays, the most advanced and promising approach to exploit nuclear fusion for energy production. Here, the electrons and ions constituting the plasma are confined using intense magnetic fields ($\sim 1 \text{ T}$). The Lorentz force makes the charged particles gyrate around the magnetic field lines, confining them in the direction perpendicular to the magnetic field lines. Different possibilities have been considered to confine the particles also in the parallel direction. Among the different concepts proposed and developed for a magnetic confinement fusion reactor, the one on which the research has most focused, i.e. the most advanced, is the tokamak.

1.2 The tokamak concept

In the tokamak concept, the magnetic field lines are closed onto themselves by disposing several magnetic coils, called toroidal field (TF) coils, in a toroidal configuration. A schematics

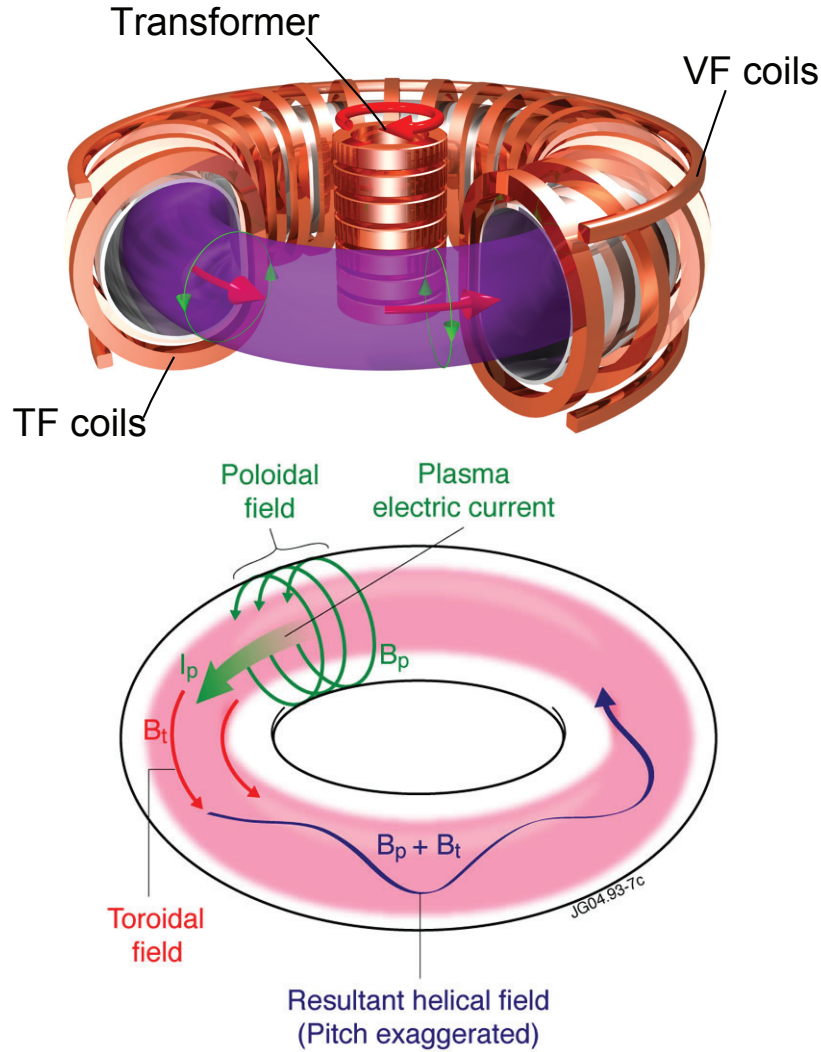


Figure 1.1: Schematics of the tokamak concept. Top: the central transformer, the toroidal field (TF) coils and the vertical field (VF) coils are shown, together with the vacuum vessel. Bottom: the toroidal magnetic field B_t (red), the plasma current I_p and the resulting poloidal magnetic field B_p (green) are shown together with the total magnetic field (blue).

of the tokamak is shown in the top of Fig. 1.1. The resulting purely circular (toroidal) magnetic field lines (red arrows), are not sufficient to confine the plasma. Indeed, the toroidal magnetic field B_t is stronger closer to the geometrical axis of the torus, since $B_t \sim 1/R$, where R is the distance from the axis. The non uniformity of the magnetic field results in vertical drifts in the charged particle motion that are opposite for ions and electrons. The charge separation results in a vertical electric field \mathbf{E} , leading to an outward $\mathbf{E} \times \mathbf{B}$ drift causing the plasma to be lost on the reactor walls. A second component of the magnetic field in the plane perpendicular to the toroidal direction (poloidal plane) is needed to balance the effect of the drifts and confine the plasma. The poloidal field B_p is created by a toroidal plasma current I_p , induced by a

Chapter 1. Introduction

variation of the magnetic field produced by the central solenoid, acting as a transformer. The plasma current I_p and the resulting poloidal field B_p are both shown with green arrows at the bottom of Fig. 1.1. An additional vertical magnetic field, created by the vertical field (VF) coils, improves plasma stability. The total magnetic field field lines, shown in blue in Fig. 1.1, are wound on concentric surfaces with toroidal symmetry, called flux surfaces. For a given field line, the number of toroidal turns to perform one poloidal turn is equal to the safety factor q , defined as [6]

$$q = \frac{1}{2\pi} \int_0^{2\pi} \frac{r}{R} \frac{B_t}{B_p} d\theta, \quad (1.3)$$

where θ is the poloidal angle, r is the plasma minor radius, and the integral is performed over one poloidal turn. In the large aspect ratio limit ($R \gg r$), the safety factor can be approximated by q_{cyl} defined as

$$q_{cyl} = \frac{r B_t}{R B_p}. \quad (1.4)$$

The plasma current is also used to heat the plasma through the Joule effect. Though, the resistivity of the plasma decreases with temperature $\propto T^{-3/2}$ [7], and ohmic heating alone is not sufficient to achieve temperatures of the order of 10 keV. Additional heating sources are hence used to heat the confined plasma up to fusion relevant temperatures. Some additional heating sources are, e.g., Electron Cyclotron Resonance Heating (ECRH), Ion Cyclotron Resonance Heating (ICRH), and Neutral Beam Heating (NBH).

A relevant figure of merit for a fusion reactor is the gain factor Q

$$Q = \frac{P_{out}}{P_{in}} = \frac{P_f}{P_{in}} \quad (1.5)$$

where P_{out} is the net output power, P_f is the power resulting from fusion reactions, P_{in} is the input power needed to confine and heat the plasma, and at steady state $P_{out} = P_f$. So far, the “break even” condition $Q = 1$ has never been achieved, the best recorded performance being the one of the Joint European Torus (JET) in 1997 featuring $Q = 0.62$ [8]. Since the fusion power P_f is proportional to the volume of the confined plasma, while the power losses are proportional to its surface, a way to increase Q is increasing the tokamak size. The construction of the ITER tokamak ([9] and references within) is currently ongoing in Cadarache, France. ITER will be the largest tokamak in the world with a major radius of 6 m and it is foreseen to achieve a gain factor of $Q = 10$ for long pulses (400-600 s). ITER will demonstrate the feasibility of the exploitation of nuclear fusion for energy production. Still, it will not convert the produced energy into electricity. A further step is needed, building the prototype of a fusion power plant, called DEMO [5], that will actually produce electric energy from fusion reactions.

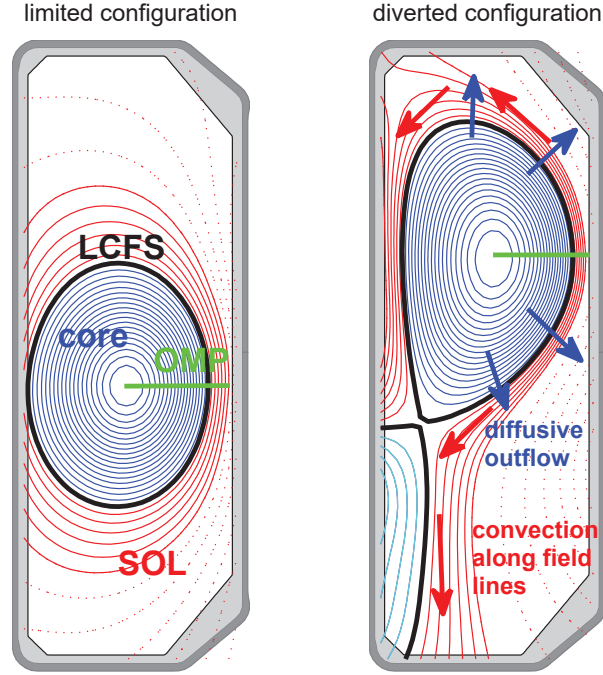


Figure 1.2: Flux surfaces in limited (left) and diverted (right) configurations. The closed magnetic surfaces in the core (blue) and the open ones in the SOL (red) are shown together with the LCFS (thick black). The private flux region in the diverted configuration is shown in cyan. The SOL open field lines in the shadow of the reactor wall are shown with red dotted lines. The outer midplane (OMP) is shown with a green line.

1.3 The Scrape-Off Layer (SOL)

In a tokamak, the plasma is confined on nested closed flux surfaces. Of these closed surfaces, the outermost one is called the Last Closed Flux Surface (LCFS), or separatrix. The LCFS can be defined by the contact of a closed flux surface with a solid surface, called the “limiter”, (limited plasma), or by the magnetic field itself (diverted configuration). An example of the two configurations is shown in Fig. 1.2 for the TCV tokamak, where the flux surfaces are displayed in the poloidal cross section for a limited (left) and diverted (right) configuration. The LCFS is shown with a thick black line. All the flux surfaces contained inside the LCFS are formed by closed magnetic field lines. The plasma flows mainly along the field lines, closed on themselves, and is therefore confined. We will refer to this region as “core region”. All flux surfaces outside the LCFS intersect the tokamak wall and the field lines lying on them are open. The region outside the LCFS is called the Scrape-Off Layer (SOL). In Fig. 1.2, the closed flux surfaces in the core are shown in blue, and the open ones in the SOL are shown in red. Unavoidable collisional and turbulent processes lead the plasma, confined in the core, to diffuse and outflow into the SOL. The competition between perpendicular (diffusive) and

parallel (convective) transport in the SOL results in the exponential decay of plasma density and temperature moving away from the LCFS in the radial direction. The plasma is convected along the field lines at velocities $v_{||}$ of the order of the sound speed $c_s \sim 10^4$ m/s, while the effective cross field velocity v_{\perp} , estimated from a diffusive model, is of the order of 100 m/s and can be as low as 1 m/s. The resulting SOL is very thin, with an average width of 1 cm [10], varying between a few mm for diverted configurations [11] and several cm for limited plasmas [12].

In a diffusive model of the SOL, its width is determined by the diffusion coefficient D . Diffusion coefficients computed from first principle arguments are usually too small to describe SOL widths of ~ 1 cm. An “anomalous” perpendicular transport [10], $D \sim 1 \text{ m}^2 \text{ s}^{-1}$, has to be invoked to explain the experimentally observed SOL widths. Such anomalous transport is believed to be caused by plasma turbulence. Indeed, the SOL is characterized by large fluctuations driven by turbulence. Such turbulence results in the formation of coherent filamentary structures, called blobs.

Blobs are an ubiquitous feature of plasmas in open magnetic field lines. The blobs are elongated along the field lines and can therefore have length of the order of the connection length (typically 10-100 m), while in the poloidal cross section their linear dimensions are typically of the order of 1 cm. Inside blobs, charge dependent drifts driven by curvature and magnetic field non-uniformity (∇B drift) result in a vertical charge separation, i.e. in the formation of an electric dipole. The dipole electric field \mathbf{E} leads in turn to a radially directed $\mathbf{E} \times \mathbf{B}$ drift that propels the blobs outwards [13]. This model is sketched in Fig. 1.3.

Due to their radially outwards motion, blobs enhance the cross field transport in the SOL. Blobs can extend from one end to the other of the SOL open magnetic field line, being connected to the plasma sheaths on the first wall solid surfaces. But blob can also detach from the sheaths; in this case their radial velocity is observed to increase [14, 15], and the $\mathbf{E} \times \mathbf{B}$ propelled coherent structures can travel distances up to several SOL widths before being dissipated. The blobs can be deposited on the outer first wall, enhancing the heat deposition onto it, and affecting the material durability [16].

Nevertheless, the plasma motion is essentially directed along the open field lines, since

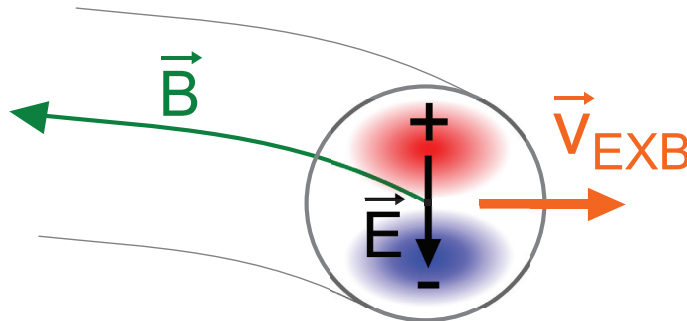


Figure 1.3: Schematics of a blob. The blob contour and cross section are shown in grey. The tokamak magnetic field \mathbf{B} (green) and the electric field \mathbf{E} (black) resulting from charge separation (red, blue) internal to the blob, lead to an outwards $\mathbf{E} \times \mathbf{B}$ velocity (orange).

$v_{||}/v_{\perp} \sim 10^2$. The open field lines intersect the wall, where the plasma is deposited. The plasma-surface interaction leads to phenomena such as sputtering and erosion. This, in a limited plasma, leads to the penetration of impurities in the core region, degrading the plasma performances. To move the impurity sources away from the confined plasma, the diverted configuration has been developed. In this configuration, external coils are used to create a null in the poloidal field (X-point). The resulting separatrix is indeed formed by a closed surface from which two “legs” depart and intersect the wall in the so called divertor. Moving the impurities sources away from the confined plasma results in better confinement, facilitating the access to the high confinement regime (H-mode). In this regime, higher densities and temperatures are achieved in the core region, with steeper gradients in the edge region with respect to the (usual) low-confinement regime (L-mode). Even though H-mode has been achieved in limited plasmas, the diverted configurations result in a lower power threshold for the L-H transition in between the two regimes, and in generally higher energy confinement times τ . For this reason, the more performing diverted configuration is preferred to the limited configuration and is routinely used in most tokamaks.

The SOL is believed to affect the reactor performance [17], being coupled to the core plasma through the LCFS. Furthermore, in a DEMO-sized fusion reactor, the power outflowing from the core in the SOL will be in the order of $P_{SOL} = 150$ MW [5]. In the DEMO design, detailed in Ref. [5], the major radius is $R_0 = 9$ m. If we assume a SOL width $\lambda_q \sim 1$ cm, the resulting heat flux impinging on the divertor plates is $q = P_{SOL}/(2\pi R_0 \lambda_q) \sim 250$ MW/m². This value exceeds the thermal capabilities of materials (~ 20 MW/m²) by an order of magnitude, and would result in melting the divertor or the first wall.

The power handling in the SOL is therefore one of the crucial points that has to be addressed for the design of a performing fusion reactor. Different solutions have been proposed and implemented to handle the heat loads on the plasma facing components (PFC) by:

- increasing the wetted area on which the plasma exhaust is deposited by tilting of the divertor plates
- splitting the SOL by increasing the number of divertor legs (Snow Flake divertor) [18]
- increase the wetted area by flux expansion and flaring of the field lines (X-divertor [19], super-X divertor [20], X-point divertor [21])
- increasing the radiated fraction by impurity seeding (N₂, Ne) [22]
- a combination of the previous ones

Even though the diverted configurations are more efficient, the physics of the SOL is not fully understood, not even in the simplest magnetic configuration, the limited one. The use of a limited configuration is indeed still needed in the start-up phase of a plasma discharge, where the plasma current has to be ramped up to a threshold value, allowing for the detachment

of the main plasma from the inner wall and the creation of a diverted configuration. A limited configuration is also used in the ramp-down phase of a plasma discharge, where the plasma current is progressively ramped down to zero. A successful start-up phase is therefore fundamental for a fusion reactor, and the plasma-wall interaction through the SOL is one of the key points that needs to be addressed.

Furthermore, the simple magnetic geometry of the limited configuration makes it the easiest to be modeled with nonlinear numerical simulations. A comparison between experiments and simulations is therefore directly possible. The advantage of such a comparison is twofold: the validation of the code against the experimental data, and the better insight in the physics of the SOL.

For these reasons, in this thesis we investigate the physics of the SOL, focusing on the limited configuration.

1.4 Context of this thesis

The heat flux along the field lines in the SOL is usually assumed to decay exponentially with the distance from the LCFS at the Outer Midplane (OMP, in green in Fig. 1.2), r_u , as $q_{||}(r_u) = q_{||0} \exp(-r_u/\lambda_q)$ where $q_{||0}$ is the flux at the separatrix and λ_q is the heat flux decay length in the SOL. In a limited plasma, the heat flux deposited on the inboard limiter is $q_{dep} = q_{||} \sin \alpha$, where α is the angle between the magnetic field and the direction tangent to the solid surface. The deposition of the heat flux onto a solid surface is sketched in Fig. 1.4. Recently, inboard-limited discharges in JET have shown an enhanced flux at the limiter up to a factor 3 with respect to what is foreseen from the heat flux measured at the OMP [23]. In these discharges, the SOL exhibits two different regions:

- a “near” SOL, extending a few mm from the LCFS, which is characterized by a steep profile of $q_{||}$ and is responsible for the peak heat load on the limiter
- a “far” SOL, typically some cm wide, which features a flatter profile of $q_{||}$ and accounts for most of the heat deposited onto the first wall.

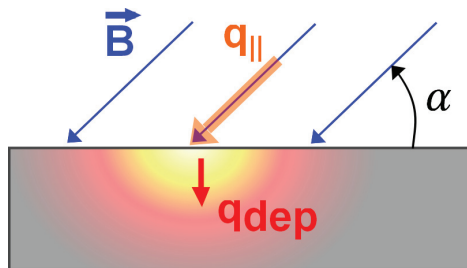


Figure 1.4: Schematics of heat deposition from the plasma onto a solid surface: the magnetic field \mathbf{B} (blue), the incidence angle α (black), the parallel heat flux $q_{||}$ (orange) and the deposited heat flux q_{dep} (red) are shown.

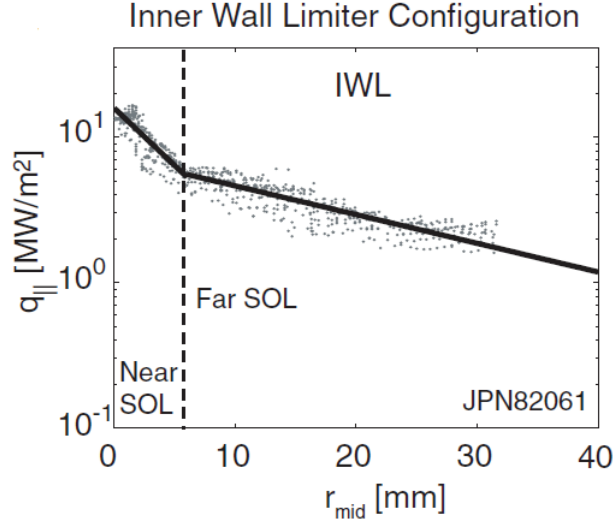


Figure 1.5: Parallel heat flux radial profile in JET measured by means of infrared thermography. Figure taken from [23].

The near and far SOL are clearly distinguishable in Fig. 1.5, where a typical profile of the parallel heat flux, obtained by means of infrared thermography, is shown. The parallel heat flux radial profile $q_{||}(r_u)$ is then better described by a sum of two exponentials, associated with the two different regions

$$q_{||}(r_u) = q_n \exp(-r_u/\lambda_n) + q_f \exp(-r_u/\lambda_f), \quad (1.6)$$

where λ_n and λ_f are the near and far SOL decay lengths, respectively, and q_n and q_f are the associated heat flux magnitudes.

For example in ITER, inboard limited L-mode plasmas are foreseen for the startup and ramp down phases [24]. If such an enhanced heat flux is present, the heat load on the limiter could result in the melting of the beryllium first wall panels, according to their original design [25]. The aim of this thesis is to advance the understanding of the physics of the SOL. In particular we aim at investigating the physics of the near and far SOL, starting from the simplest magnetic configuration, i.e. limited plasmas. Indeed, even though ITER first wall panel have been redesigned to handle the heat flux associated with the near SOL [26], the physical mechanism behind its formation is still not well understood.

Furthermore, we aim at investigating the dynamics of blobs in the SOL, improving our understanding of the mechanisms governing perpendicular transport and heat deposition in the far SOL. The investigation of the near and far SOL will be carried out combining dedicated experiments on the TCV tokamak and nonlinear numerical simulations.

The thesis is structured as follows:

- In Chapter 2, the experimental setup used in this work is detailed. The TCV tokamak facility is introduced and the main diagnostics employed in the experiments are described. The numerical tools used for data analysis and the code used to simulate the TCV SOL are introduced.
- In Chapter 3, the experimental results are detailed: in particular the first observations of the near SOL in TCV limited D and He plasmas are reported. The disappearance of the near SOL is observed for low plasma current or high plasma density. The dependence of the power in the near SOL on plasma normalized resistivity is suggested. The near SOL formation is shown to be bound to the presence of non-ambipolar currents. The measurements at the OMP are compared with those performed at the limiter. A method for mitigating and suppressing the near SOL heat flux via impurity injection is proposed and first encouraging experimental results are reported. Numerical simulations of the TCV SOL are presented, and their results are compared with the experiments. Part of the experiments presented in this chapter are part of the EUROFUSION MST1 2015 campaign, with the author of this thesis being the Scientific Coordinator of two experiments, namely TCV15-2.2-4 and TCV15-He-13. Part of his work already features in journal publications and has been presented as an invited talk to an international conference:

F. Nespoli, et al., “*Heat loads in inboard limited L-mode plasmas in TCV*”, Journal of Nuclear Materials **463** (2015) 393–396

F. Nespoli, et al., “*Non-linear simulations of the TCV Scrape-Off Layer*”, Nuclear Materials and Energy, (2016) <http://dx.doi.org/10.1016/j.nme.2016.10.019>

F. Nespoli, et al., “*Near and far SOL physics in inboard-limited plasmas in TCV*”, 21st Joint EU-US Transport Task Force Meeting, Leysin, Switzerland (2016).

- In Chapter 4, we investigate blobs dynamics in the SOL at the OMP using experimental data. A pattern recognition technique is applied to the simulation results of the TCV SOL turbulence to detect the blobs and study their dynamics, giving a better insight on the mechanisms leading to heat deposition on the first wall. The results of the analysis performed on the numerical simulations is compared with the experimental ones. Part of this work has been submitted to a journal for publication:

F. Nespoli, et al., “*Blob properties in full-turbulence simulations of the TCV Scrape-Off Layer*”, Plasma Physics and Controlled Fusion, (2016) submitted for publication.

- Finally, in Chapter 5, the main results presented in this thesis are summarized. The picture of the SOL in limited configuration resulting from the work exposed in this thesis

is exposed, highlighting the progresses made towards a consistent physical description of the SOL, connecting the separation in between near and far SOL to a change of regimes in blob dynamics, which is currently still missing. Finally, an outlook on a possible continuation of this work is given.

2 Experimental and numerical tools

In this chapter, the experimental setup for the experiments detailed in this thesis is described. First, the Tokamak à Configuration Variable (TCV) is introduced in section 2.1. In the following, the main diagnostics employed in the experiments presented in chapters 3 and 4 are described. TCV is equipped with an extensive set of diagnostics, and many of them are routinely used during experimental campaigns. We describe in detail only the diagnostics that have been object of development, maintenance, improvement and direct operation during this thesis:

- the gold foil bolometers (BOLO, section 2.2)
- the horizontal infrared camera (HIR, section 2.3)
- the flush mounted Langmuir probes (LP, section 2.4)
- the fast reciprocating Langmuir probe (RP, section 2.5).

In section 2.6, we introduce the THEODOR code, used to compute the heat flux deposited on the tiles from the temperature measurements.

Finally, in section 2.7, the numerical tools used to simulate the SOL of TCV are detailed: the GBS code is introduced, and a pattern recognition technique for blob detection and tracking is described.

2.1 The TCV tokamak

The Tokamak à Configuration Variable (TCV) is a medium sized tokamak (major radius $R_0 = 0.89$ m) located at the SPC/EPFL in Lausanne, Switzerland. TCV has been operational since 1992 and it was designed to study the effect of plasma shape (elongation κ and triangularity δ) on the plasma behavior, i.e. confinement and stability [27]. For this reason, TCV features a vacuum vessel with a rectangular, highly elongated cross section, as shown in Fig. 2.1. Such a vacuum vessel is able to accommodate elongated plasmas, and allows TCV to hold the world record for the most elongated plasma ($\kappa = 2.8$) [28].

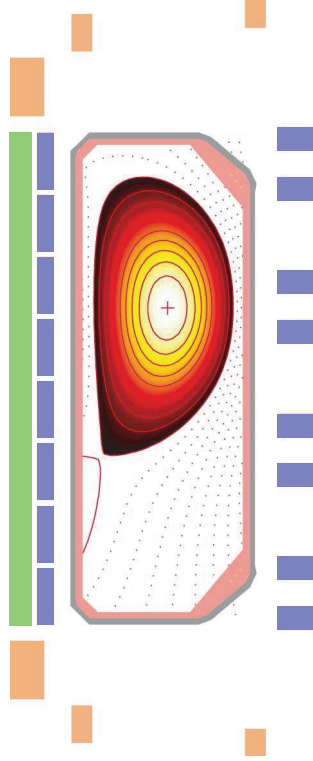


Figure 2.1: Poloidal cross section of TCV. The vacuum vessel (grey), the OH-coil (green), the PF coils (blue) , and the vertical field coils (orange) are shown, together with an example of diverted plasma.

Sixteen toroidal field coils connected in series generate the toroidal field that can be as strong as 1.54 T on axis. The central “OH-coil” (in green in Fig. 2.1) is used to inductively drive current in the plasma up to 1 MA. 16 independently powered poloidal field (PF) coils (in blue in Fig. 2.1) allow shaping the plasma with a unique flexibility. All TCV coils are in copper and are air cooled. A typical discharge lasts 2 s and consumes approximately 100 MJ of energy. The large power required for the plasma discharges can not directly be provided by the electrical grid and is therefore stored in a flywheel connected to a motor-generator. The latter provides the power for the magnetic fields coils, the ohmic transformer and the additional heating system. TCV features a unique power and current drive capability provided by a flexible Electron Cyclotron Resonance Heating (ECRH) system. The ECRH system is composed by 9 gyrotrons for a total power up to 4.5 MW. The gyrotrons can inject both ordinary (O) or extraordinary (X) electron cyclotron (EC) waves. Six of the gyrotrons operate at the second harmonic of the EC frequency ($2\omega_{ce} = 82.7$ GHz) and three operate at the third harmonic ($3\omega_{ce} = 118$ GHz). Since late 2015, TCV is also equipped with a Neutral Beam Heating (NBH) system, able to deliver up to 1 MW power. The NBH can inject hydrogen (H) or deuterium (D) neutral atoms at the energy of 25 keV, with typical pulse length up to 2 s.

Owing to TCV unique shaping capabilities, a number of different magnetic configurations are accessible: limited plasmas, upper and lower Single Null (SN) diverted plasmas, Double

Parameter	Symbol	Values
Major radius	R_0	0.89 m
Plasma minor radius	a	≤ 0.25 m
Vacuum vessel height	b	1.45 m
Aspect ratio	$\epsilon = R_0/a$	~ 3.5
Plasma current	I_p	≤ 1 MA
Toroidal magnetic field on axis	B_0	≤ 1.54 T
Central plasma density	n	$\leq 20 \times 10^{19} \text{ m}^{-3}$
Electron temperature	T_e	≤ 15 keV
Ion temperature	T_i	≤ 1 keV (2.5 keV with NBH)
Plasma elongation	κ	$0.9 \leq \kappa \leq 2.8$
Plasma triangularity	δ	$-0.8 \leq \delta \leq 1$
Typical/maximum discharge duration		2s / 4s (EC)
Main ion component		H, D, He

Table 2.1: Main parameters of the TCV tokamak.

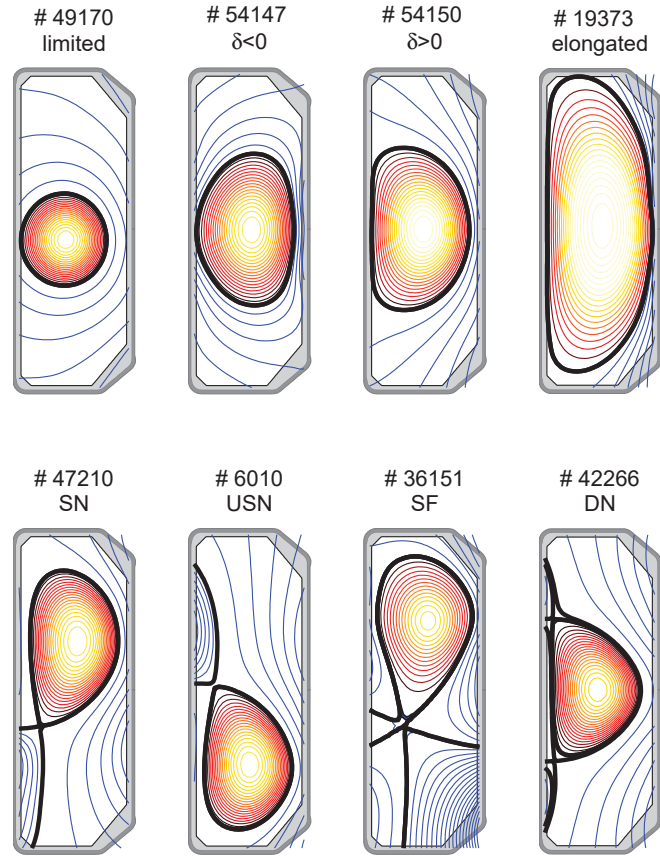


Figure 2.2: Some of the possible plasma shapes accessible on TCV thanks to the 16 independently powered PF coils.

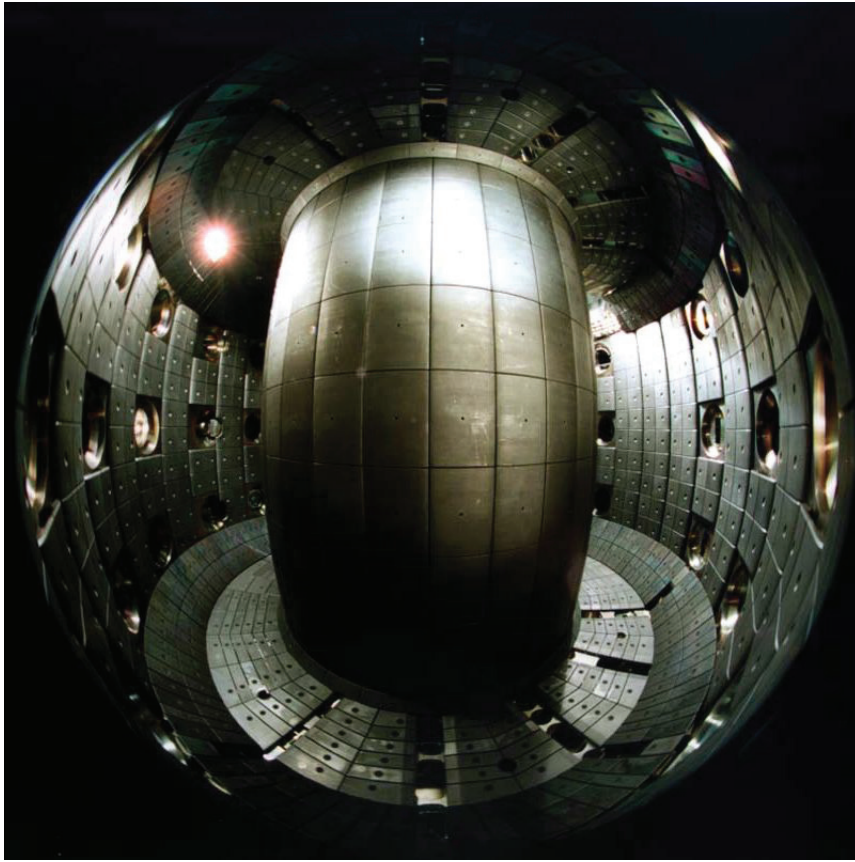


Figure 2.3: View of the inside of TCV. The graphite tiles cover most of the stainless steel vacuum vessel.

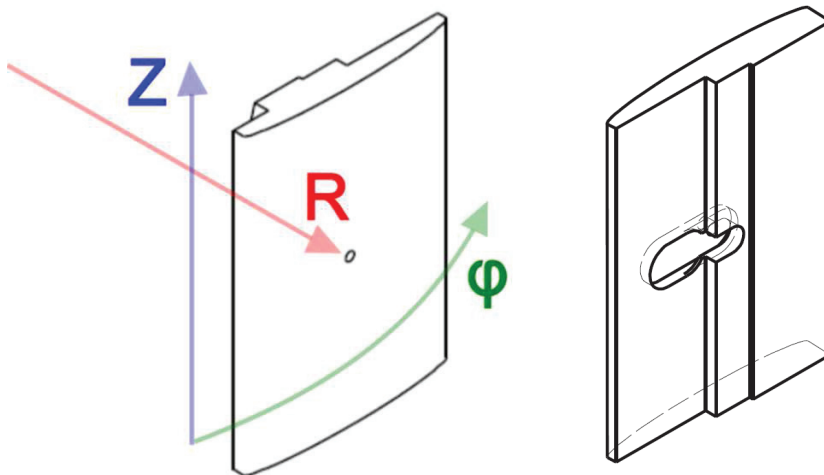


Figure 2.4: Drawing of a graphite tile from TCV CC, front (left) and rear (right). The set of real space coordinates (R, Z, ϕ) is shown. On the right, the hole in the rear side that allows the mounting of the tile on the CC is visible.

Null (DN) diverted plasmas, snowflake (SF) divertor, X-divertor, Super-X divertor. For each configuration, the triangularity can also be changed from positive to negative and a large range of elongation is available. Some possible configurations are shown in Fig. 2.2.

The main parameters of the TCV tokamak are summarized in Table 2.1.

The TCV vacuum vessel is almost entirely covered with graphite protection tiles. 1692 individual graphite tiles were installed in 1998, covering almost 90% of the internal surface area [29]. For this reason, carbon is the main impurity in TCV plasmas. A picture of the inside of TCV is shown in Fig. 2.3. The choice of graphite is driven mainly by two reasons: 1) carbon is a relatively low-atomic number material. This avoids excessive radiative losses with respect to impurities from the stainless steel vacuum vessel. 2) Graphite does not melt, instead it sublimates at high temperatures (~ 3900 K).

In order to avoid leading edges and minimize the deposited heat loads, the tiles covering the Central Column (CC) are shaped in the toroidal direction (ϕ) [30]. The shaping of the tile in the toroidal direction is visible in Fig. 2.4, where the drawing of one of the CC graphite tiles is shown.

2.2 Metal foil bolometers (BOLO)

Bolometers are dedicated devices providing the measurement of the power flux associated with electromagnetic radiation. They usually combine an absorber and a thermometer (a temperature-sensitive resistor or an infrared detector). Various types of bolometers are widely used in different technological applications, such as infrared imaging and laser light measurements. In magnetic fusion experiments, the most used bolometers are the metal foil resistors bolometers, since they are less sensitive to neutron damage with respect to other technologies (e.g. photodiode-based bolometers). The main purpose of bolometers in tokamaks is to measure the total power radiated by the plasma P_{rad} .

Metal foil bolometers measure the radiation emitted from the plasma in the range between the VUV and the soft X-rays, as well as part of the power of the neutral particles impinging on them. They are composed by an absorber and a resistor. The absorber (usually a micrometric gold layer) determines the spectral response of the device.

A bolometer usually consists of two identical absorber-resistor units. A first one measures the radiation from the plasma, while a second one is shielded from the plasma radiation to provide a reference, as it is visible in Fig. 2.5a. They are arranged in a Wheatstone bridge configuration (two resistors for each absorber), allowing for differential measurements. The arrangement of the four gold meander resistors of a metal foil bolometer in a Wheatstone bridge configuration is shown in Fig. 2.6.

The incident power on the bolometer is given by

$$P_{rad} = C \left(\frac{d\Delta T}{dt} + \frac{\Delta T}{\tau} \right), \quad (2.1)$$

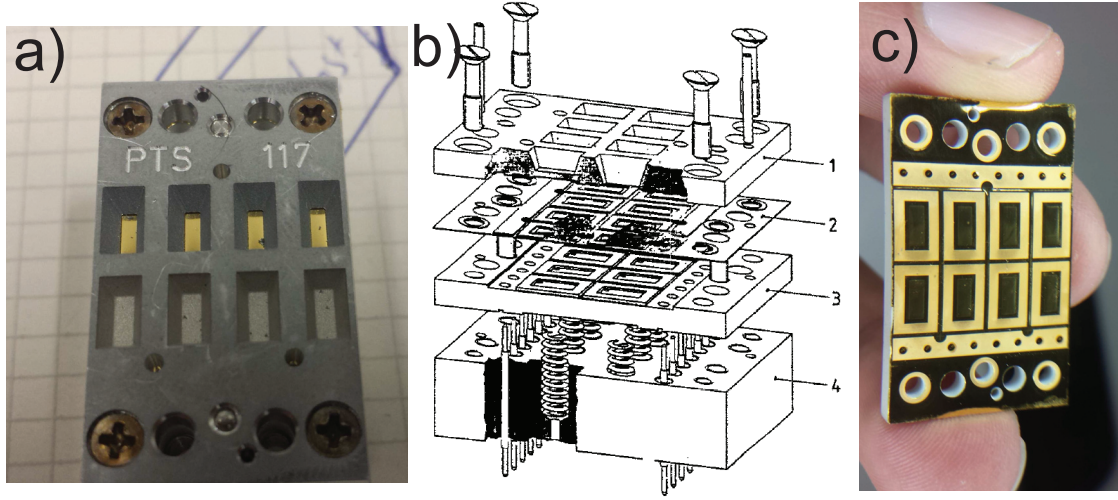


Figure 2.5: a) Photography of a module of the TCV bolometers featuring 4 bolometers. b) Exploded section of the bolometers from Ref. [31], showing the front cooling plate (1), the bolometer foil (2), the back cooling plate (3), and the support plate with spring contacts (4). c) The bolometer foil with the gold resistors.

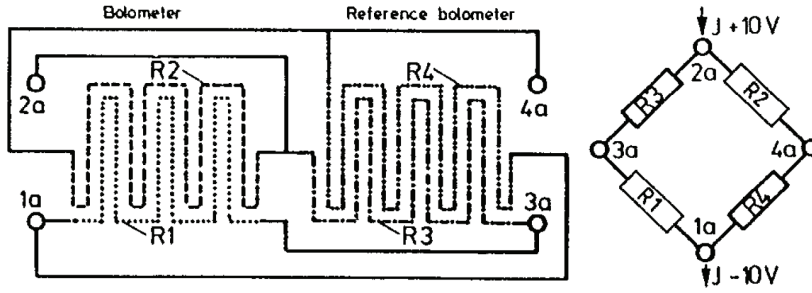


Figure 2.6: Arrangement of the gold meander resistors in a Wheatstone bridge configuration, taken from Ref. [31].

where C is the heat capacity, ΔT is the temperature change, which is proportional to the measured output voltage of the Wheatstone bridge ΔU_{br} , and τ is the cooling time constant. Equation (2.1) can be derived as follows: the time dynamics of the detector can be described by the dimensionless function $K(t)$, which is proportional to the response function of the detector to a δ -pulse of absorbed power. The change in the temperature of the absorber (connected to the heat sink) can be related to the absorbed power P_{abs} by assuming a linear response:

$$\Delta T(t) = \int_{-\infty}^t \frac{P_{abs}(t')}{C} K(t - t') dt'. \quad (2.2)$$

Since the temperature change is determined by the convolution of an instrumental function and the absorbed power, a deconvolution is required to obtain $P_{abs}(t)$. The cooling of a hot

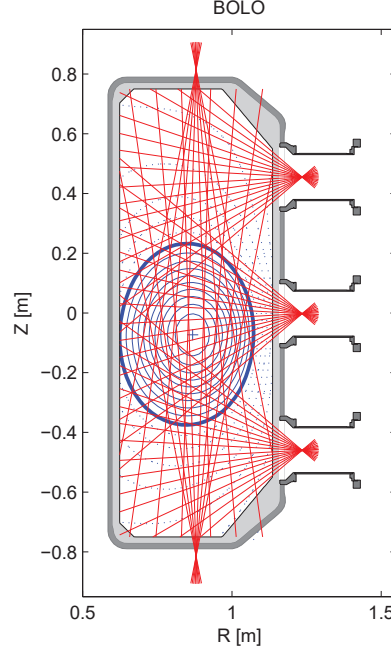


Figure 2.7: Lines of sight of the 8 foil bolometer cameras in the TCV cross section.

medium connected to a heat sink can be described by an exponential response function

$$K(t) = e^{-t/\tau}. \quad (2.3)$$

Differentiating Eq. (2.2) leads to

$$\frac{d\Delta T(t)}{dt} = \frac{P_{abs}(t)}{C} K(0) \int_{-\infty}^t \frac{P_{abs}(t')}{C} \frac{dK(t-t')}{dt} dt'. \quad (2.4)$$

Substituting Eq. (2.3) gives

$$\frac{d\Delta T(t)}{dt} = \frac{P_{abs}(t)}{C} + \frac{\Delta T(t)}{\tau}, \quad (2.5)$$

which is equivalent to Equation (2.1) for the radiated power measured by the bolometer with $P_{abs} = P_{rad}$.

The TCV bolometric system is shown in Fig. 2.7. It consists of 8 pinhole cameras installed at the same toroidal location: one at the top of the vacuum vessel, one at the bottom, and three double cameras on the low field side. Each camera is composed by 8 Wheatstone bridge foil bolometers, for a total of 64 lines of sight (shown in red in Fig. 2.7). The bolometers were designed at IPP-Garching [31] and each detector is composed of a $7.5 \mu\text{m}$ insulating

(Kapton) foil, covered on by a 4 μm structured gold layer acting as an absorber, surrounded by a massive aluminum (Al) cooling plate acting as a heat sink (Fig. 2.5a,b). On the rear side of each absorber, two meander-like gold resistors are deposited (Fig. 2.5c).

The reference bolometers are shielded from neutrals and radiation in the range from visible light to soft x-rays by a residual thickness of 0.6 mm of the Al front cooling plate (Fig. 2.5a). In front of each camera, a remotely controlled hydraulic engine can open or close a shutter to shield the camera. For the low field side cameras, it is also possible to select two different filters. The absorbance A of a 4 μm gold foil has to be considered ~ 1 for $E_{ph} < 5$ keV, where E_{ph} is the energy of the photons impinging on the metal foil. A decreases for $E_{ph} < 100$ eV reaching ~ 0.6 at $\lambda=480$ nm. For lower energy, the absorbance fastly drops to 0. The Wheatstone bridge is excited by a sinusoidal voltage with $U_{peak} = 9.4$ V and $f_0 = 50$ kHz, in order to obtain adequate detection (sampling rates up to 10 kHz) and noise rejection. A dedicated electronic board provides the proper balancing of the bridge. The output voltage of the Wheatstone bridge is amplified and demodulated. In this latter stage, a portion of the exciting voltage is inverted and added to the bridge output signal in order to compensate for possible offsets in the signal due to imperfect balancing of the bridge or to thermal drift. The resulting signal is then filtered by a low pass filter (8 poles Bessel filter) and finally acquired. The resistors in the bridge change their resistance according to $R = R_0(1 + \alpha\Delta T)$, where α is the material temperature coefficient. The output voltage of the bridge ΔU_{br} is directly proportional to the input (exciting) voltage U_{peak} , so that the relation between ΔU_{br} and ΔT is $\Delta U_{br} = U_{peak}\alpha\Delta T$.

The chord brightness measured by the detector is related to the incident power through the etendue Et of the optical system. The equation for the measured line integrated radiation flux can thus be written as

$$P_{lin} = \frac{1}{Et g S U_{peak}} \left(\tau \frac{d\Delta V_{br}}{dt} + \Delta V_{br} \right), \quad (2.6)$$

where $\Delta V_{br} = g\Delta U_{br}$ is the acquired signal, amplified by the gain factor g , and S is the calibration factor, combining α and τ . The characteristic time τ for the TCV bolometers is on average 0.08 s, and can be determined, e.g., by fitting the measured voltage with an exponential decay just after a plasma disruption. The acquired voltage raw data ΔV_{br} , before being used to compute the line integrated radiated power that will be used for the tomographic inversion, has to be treated further. The eventual residual offset (mean of data with $t < 0$) is subtracted, and the signal is filtered to reduce the noise after the deconvolution. In fact the differentiation highlights the high frequency part of a signal, since $\text{FT}[df(t)/dt](\omega) = i\omega\text{FT}[f](\omega)$, where FT denotes Fourier transform. The deconvoluted signal has to be filtered with a low-pass filter (usually a Bessel filter) or to be smoothed (usually with the Savitsky-Golay or the Gottardi method).

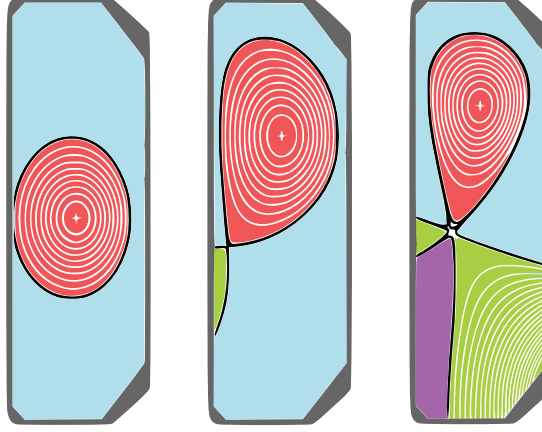


Figure 2.8: Different plasma zones based on the magnetic equilibrium for a limited plasma (left), a SN (middle) and SF (right) diverted configurations. The core (red), the external zone (light blue), the private flux region (green), and the very private flux region (purple) are shown.

2.2.1 Determination of the plasma radiated power through tomography

The resulting line integrated power for the 64 lines of sight is tomographically inverted using the General Tomographic Inversion (GTI) package [32]. Without making any assumption on the magnetic equilibrium, a rectangular pixels grid is used, providing the 2D map in the TCV poloidal cross section of the emissivity radiated by the plasma $\epsilon_{rad}(R, Z)$.

Using the magnetic equilibrium reconstruction provided by the LIUQE code [33], the poloidal cross section can be divided into zones, namely the core, the external zone (main SOL), the private flux region (for diverted configurations), and the very private flux region (for snowflake configuration). The subdivision of the cross section in such regions is depicted in Fig. 2.8. Being able to discriminate the amount of power radiated from the different zones can be useful for different purposes. First, the power radiated in the core region P_{core} is necessary for the estimate of the energy confinement time τ_E . Secondly, P_{core} is used to compute the power entering the SOL, as $P_{SOL} = P_{in} - P_{core}$ (at steady state), where P_{in} is the input power. This is in turn useful to perform a power balance of the discharge, where P_{SOL} is evaluated using the power deposited at the targets given by, e.g., IR thermography. The fraction of power radiated in the SOL is also important for the power balance in the SOL, mainly in diverted detached plasmas, where atomic physics plays a major role and most of the power is dissipated before reaching the divertor plates.

During this thesis, an algorithm to differentiate between the different zones and to compute the radiated power from each of them has been developed. The core zone is defined by the grid pixels contained inside the contour of the LCFS, provided by the LIUQE magnetic reconstruction. The remaining part of the poloidal cross section has to be divided in between the external zone, the private flux region and the very private flux region. If no X-points are present, all the region outside the core is regarded as external zone. If one X-point is present,

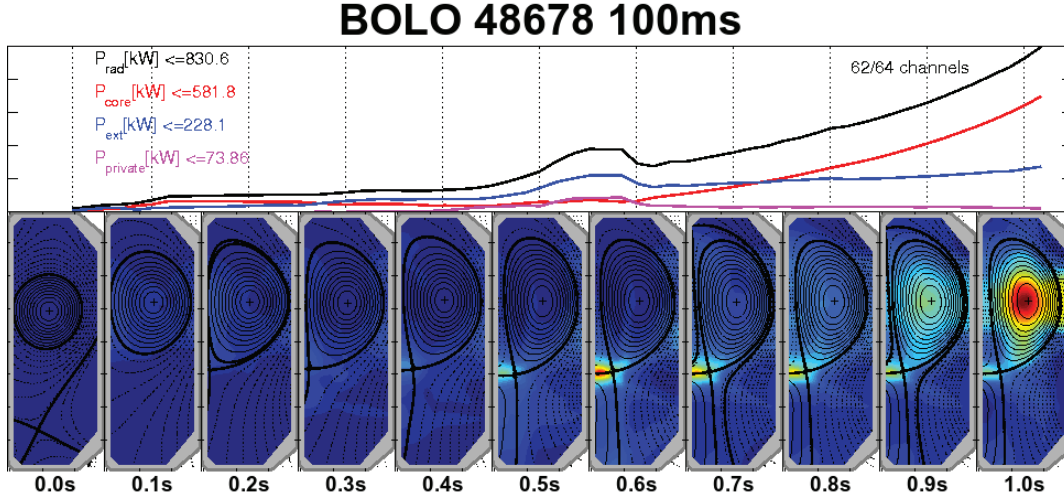


Figure 2.9: Snapshots of the inverted emissivity for different times, together with the corresponding magnetic equilibrium reconstruction. The time traces of the total power radiated from the different plasma zones (core, external, private flux region) are also shown.

the value of the poloidal magnetic flux Ψ allows to differentiate between the external zone ($\Psi \cdot \Psi_{ax} < 0$) and the private flux region ($\Psi \cdot \Psi_{ax} > 0$), where Ψ_{ax} is the poloidal magnetic flux on the magnetic axis. If two X-points are present, Ψ in the very private flux region and in the external region have the same sign ($\Psi \cdot \Psi_{ax} < 0$). Geometric considerations on the relative positions of the X-points, the magnetic axis and the position of the LCFS are necessary to identify correctly the two zones in this case.

Once the plasma zones have been correctly identified, the power radiated in the zone X, P_X , is computed by integrating ϵ_{rad} in the desired region:

$$P_X = \iint_X \epsilon_{rad}(R, Z) 2\pi R dR dZ, \quad (2.7)$$

where toroidal symmetry is assumed. An example of the result of such a procedure is shown in Fig. 2.9, where the snapshots of the inverted emissivity ϵ_{rad} at different times are shown, together with the magnetic equilibrium reconstructions and the time traces of the power radiated in each zone. The total radiated power P_{rad} is the sum of the power radiated in all the different zones, given by Eq. (2.7) where the integration is performed over the entire TCV poloidal cross-section.

During this thesis, the snapshot framework developed in Ref. [32], was implemented for bolometric inversion. As a result, a picture similar to the one in Fig. 2.9 is generated automatically after each TCV discharge and it is used for monitoring purposes.

2.3 Infrared thermography

The final aim of infrared (IR) thermography in tokamaks is to estimate the heat fluxes deposited from the plasma onto the first wall and divertor plasma facing components.

IR thermography has been used for many years for a number of purposes, including military, industrial and scientific applications. Its goal is to determine the temperature of an object by measuring radiation in the IR range. Indeed, every object with a finite temperature T emits electromagnetic waves in a range of wavelengths λ centered around λ_{max} , the wavelength for which the radiated power is maximum. According to the Wien's displacement law [34], such a wavelength is inversely proportional to the object's temperature:

$$\lambda_{max}[\mu\text{m}] = 2.8978 \times 10^3 / T[\text{K}] . \quad (2.8)$$

Objects with a temperature ranging from a few Kelvins up to few thousands Kelvins emit therefore in the IR range, $700 \text{ nm} < \lambda_{max} < 1 \text{ mm}$. IR cameras are generally based on semiconductor detectors. The IR photons are detected when their energy is sufficient to excite an electron from the valence band to the conduction band. These electrons are then collected by an external readout integrated circuit. The resulting signal is subsequently digitized and is acquired by a frame grabber inside the acquisition system.

TCV is equipped with two infrared thermography systems, namely the Vertical IR camera (VIR) and the Horizontal IR camera (HIR), used to measure the temperature of the graphite tiles covering the floor of the vessel and the central column, respectively. In the experiments exposed in this thesis, only the HIR has been used. Since this system has been upgraded during this thesis (middle of 2015), we describe in the following the two different setups. We will refer to the former system as Thermosensorik HIR and to the most recent one as IRCam HIR, from the name of the cameras, the central component of the diagnostic.

2.3.1 Thermosensorik Horizontal InfraRed system (HIR)

This system, illustrated schematically in Fig. 2.10, is based on a Thermosensorik CMT 256 M HS fast framing IR camera, also used for the vertical system (VIR). Its detector is composed by 256×256 Cadmium Mercury Telluride (CdHgTe or CMT) pixels. Using subframes, it can acquire up to 25 kfps. The CMT detector is sensitive to the broad-wave infrared spectrum, nominally to photons with wavelength $1.5 \mu\text{m} < \lambda < 5.1 \mu\text{m}$. A long wavelength filter, limiting the detector sensitivity to the wavelength range $4.5 \mu\text{m} < \lambda < 5.1 \mu\text{m}$, has been used in some experiments to avoid saturation. Since the detector is sensitive to magnetic fields, the camera is placed on a stand at approximately 1 m distance from the midplane port of TCV sector 4. An optical system connects the camera to the infrared window mounted on the port, allowing to image the inner wall of the tokamak. The Field Of View (FOV) includes approximately 3×3 tiles on the central column, in the vertical and toroidal direction respectively, with a spatial resolution of approximately 2.0 mm/pixel.

During a plasma discharge, the tokamak vibrates independently from the camera stand and

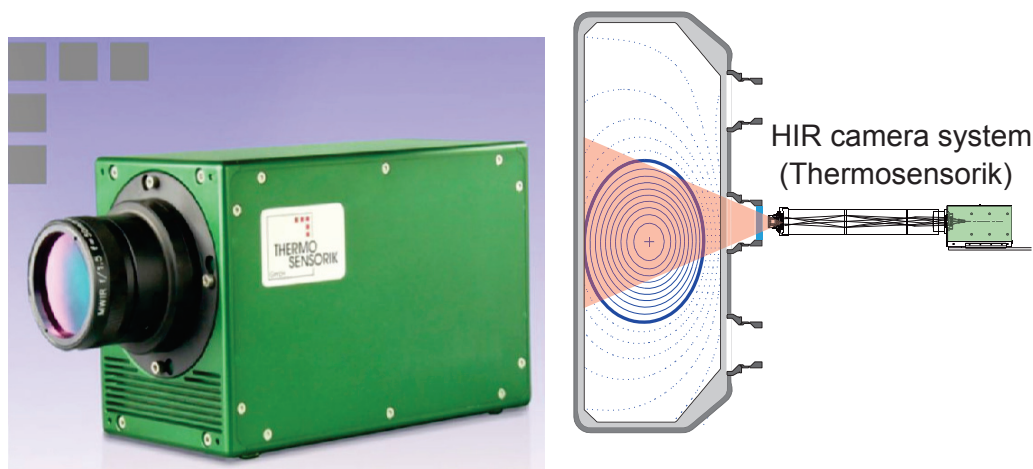


Figure 2.10: The Thermosensorik CMT 256 M HS camera (left) and a schematics of the associated IR optic on TCV (right)

the optical system, resulting in displacements of the frames which are particularly difficult to correct. This, together with the need of using the VIR and HIR systems simultaneously, drove the decision to buy a second camera and upgrade the HIR system.

2.3.2 IRCam HIR

This system, illustrated schematically in Fig. 2.11, is based on a IRCam EQUUS 81k M fast framing camera. Its detector is composed by 320×256 CdHgTe pixels, sensitive to mid-wave IR spectrum, nominally to photons with wavelength $3.7 \pm 0.2 \mu\text{m} < \lambda < 4.8 \pm 0.2 \mu\text{m}$. The camera is equipped with a rotating wheel that can house up to six different filters. In the experiments

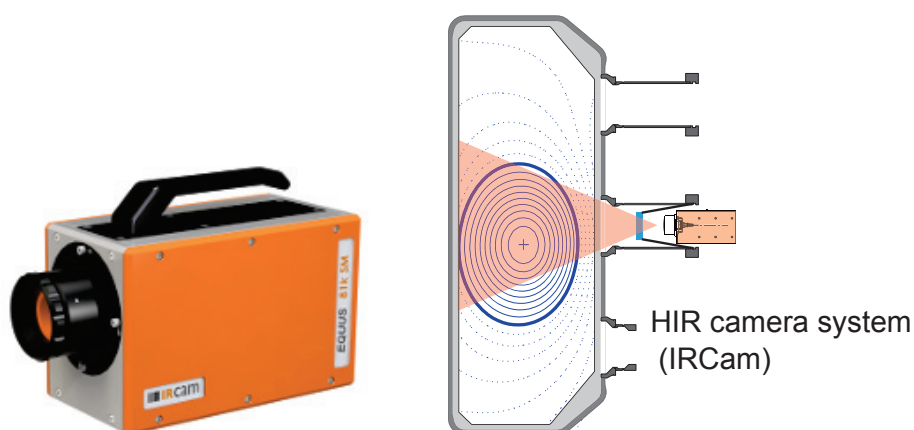


Figure 2.11: The IRCam EQUUS 81k M camera (left) and a schematics of the associated HIR system on TCV (right)

presented in this thesis, a long wavelength pass filter with cutoff at 4034 nm has been used, limiting the detector sensitivity to the range $4\ \mu\text{m} < \lambda < 4.8\ \mu\text{m}$.

The maximum acquisition frequency for the full frame image is 487 fps. The detector is designed to operate in the presence of large magnetic fields ($\sim 1\ \text{T}$). This allows the camera to be mounted directly on the vessel port, without the need of relay optics. With this solution, during the plasma discharge, the camera vibrates together with the tokamak, resulting in steady images with no need for a-posteriori correction. In particular, for our experiments, the camera is mounted on the equatorial port in sector 7. A reentrant port featuring an IR window has been machined to install the camera close to the vessel, as shown in Fig. 2.11, to avoid the TCV port to excessively limit the FOV. A 12.5 mm lens has been used instead of the standard 25 mm lens to double the FOV, resulting in the imaging of 3×3 tiles on the central column. The spatial resolution is approximately 1 mm/pixel with the 25 mm lens, and 2 mm/pixel with the 12.5 mm lens.

2.3.3 In situ calibration of the IR cameras

The TCV IR cameras measure the number of photons impinging on the detector, which are emitted from the graphite surfaces. A calibration curve relating the number of photons and the temperature of the emitting surface is needed to estimate the surface temperature. The number of detected photons depends, apart from the emitting surface temperature, from a number of factors, such as the distance between the camera and the surface, the transmittance

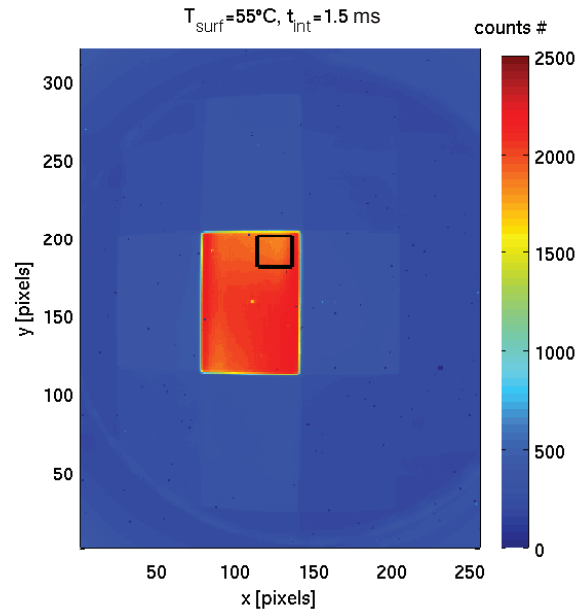


Figure 2.12: IR image of the CC in which the heated tile, used for the in situ calibration of the IR camera, is visible. The measurements for the calibration are averaged over the region defined by the black rectangle.

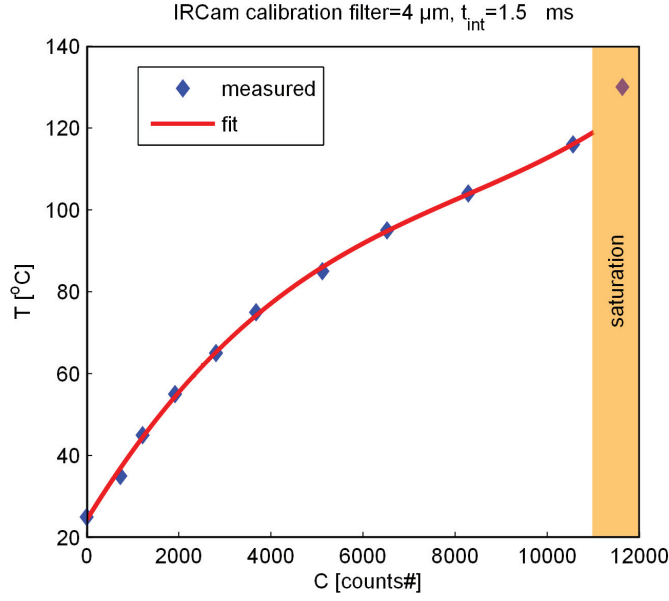


Figure 2.13: Calibration of the IRCam HIR system using the 4 μm filter and integration time $t_{\text{int}} = 1.5$ ms. The measured photon counts number C at different surface temperatures T_{surf} are shown by blue diamonds. The $C(T_{\text{surf}})$ interpolated by a 4th degree polynomial is plotted in red.

of the IR window, the surface material, the relay optics and filters used (if any), the detector integration time...

To directly account for all these factors, the calibration of the IR cameras is performed in situ. A heated tile is mounted on the TCV central column in the FOV of the camera. The tile features a conducting filament, which can be ohmically heated by driving a current through it, and a set of thermo couples (TC) to monitor its temperature. An IR image of the heated tile at the temperature of 55°C is shown in Fig. 2.12. A set of images of the heated tile for different temperatures, ranging from room temperature (25 °C) up to the saturation level of the camera, is acquired. The image acquired at 25 °C is used as a reference and subtracted as a background from all the other (calibration and experiment) images. The number of detected photons C at the surface temperature T_{surf} is computed as the average of the image over the region close to the heating element, monitored by a TC, shown as a black rectangle in Fig. 2.12.

The calibration curve is obtained by fitting $C(T_{\text{surf}})$ with a 4th degree polynomial. The resulting calibration curve for the IRCam HIR system, for 1.5 ms integration time using the 4 μm filter, is shown in Fig. 2.13. The calibration procedure is repeated for every combination of filters and integration times.

2.3.4 IR data analysis: estimation of the deposited heat flux

The final goal of IR thermography on TCV is to estimate the heat fluxes deposited by the plasma onto the graphite tiles. A number of steps are required to correctly treat the images

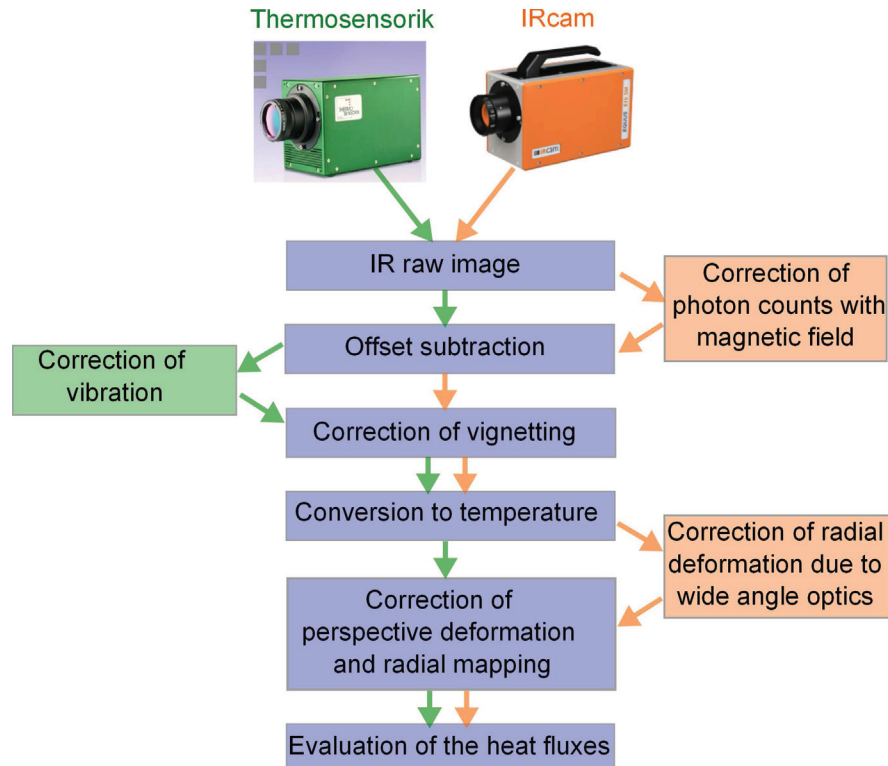


Figure 2.14: Flow chart leading to the estimate of the deposited heat fluxes starting from the IR raw images.

and account for distortions/deformations. The following operations are performed on the raw data, as illustrated in the diagram in Fig. 2.14:

1. correction of the influence of the magnetic field on the number of detected photons
2. offset subtraction
3. correction of vibration
4. correction of vignetting
5. conversion to temperature
6. correction of radial deformation for wide angle optics
7. correction of perspective deformation and spatial mapping
8. evaluation of the heat fluxes.

The points 1 and 6 are necessary only for the IRCam HIR and not for the Thermosensorik one, since the Thermosensorik camera is not affected by the TCV magnetic field, being placed 1 m away from the tokamak coils, and it does not have a wide angle optic. The point 3 is needed only for the Thermosensorik HIR system. We briefly describe each step in the following.

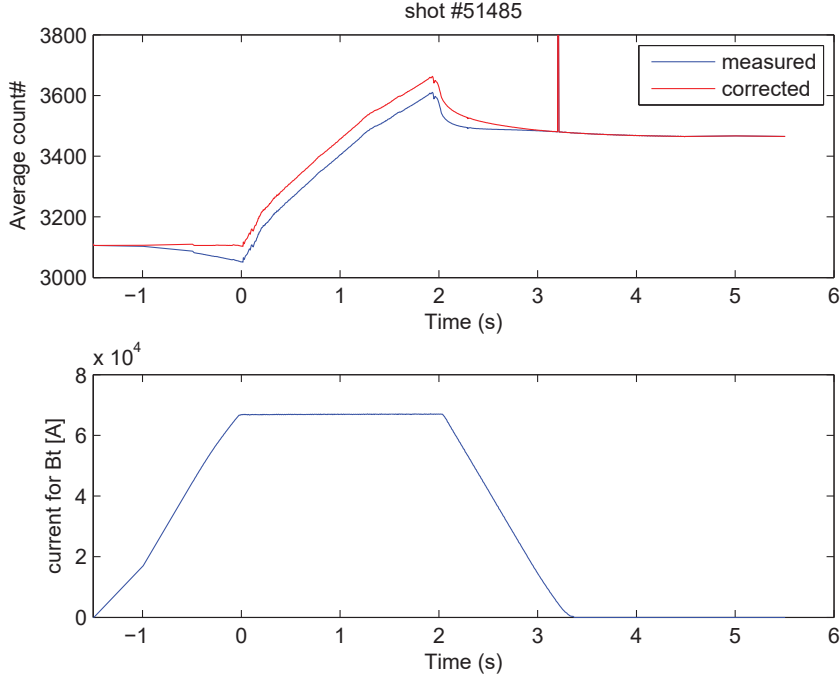


Figure 2.15: Correction of the number of counts with the toroidal magnetic field. Top plot: the measured average count number (blue) and the corrected one (red). Bottom plot: the time trace of the current I_t generating the toroidal magnetic field.

Correction of photon counts due to toroidal magnetic field

Although the IRCam EQUUS 81k M camera is designed to operate in the presence of magnetic fields, it has been observed that a strong magnetic field (~ 1 T) reduces the number of detected photons. Since the calibration of the camera is performed in the absence of a magnetic field, the variation in the counts has to be taken into account in order to correctly evaluate the temperature during the plasma discharge. Furthermore, approximately 1.5 s before the beginning of the plasma discharge, the magnetic field is ramped up to $B_t = 1.45$ T on axis, which results in $B_t \sim 0.85$ T at the camera location. The magnetic field is then ramped down back to zero after the plasma discharge. The time variation of the transformer current during the start up phase, which generates the toroidal field, is displayed in the bottom panel of Fig. 2.15. $t = 0$ corresponds to the beginning of the plasma discharge.

If the variation in detected intensity given by the change in the magnetic field is not corrected for, it results in a decrease (rise) of the temperature, i.e. an artificial negative (positive) heat flux in the start up (ramp down) phase of the discharge.

Comparing a wide number of discharges in the presence/absence of plasma (disruptions, blips), the average relative variation of the detected counts $\Delta C/C_0$ has been computed. This correlates well with the transformer current I_t generating the toroidal magnetic field. In particular $\Delta C/C_0(I_t) = f_B(I_t) = a + bI_t + cI_t^2$, where a, b, c are fitting parameters. The raw image counts at a given time $C(t)$ are then corrected accordingly to $C_{corr}(t) = C(t)\{1 - f_B[I_t(t)]\}$. An

example of such a correction is shown in Fig. 2.15.

Offset subtraction

The offset subtraction procedure is illustrated in Fig. 2.16. A uniform image of the central column at room temperature (25 °C) is taken as a reference and subtracted to all the raw images. This removes the fixed pattern noise given by the difference in offset in between the different detector pixels. Such fixed pattern is visible Fig. 2.16a, where the raw photon count recorded by the IRCam camera is shown. In Fig. 2.16c, the same image after offset subtraction is shown. The fixed pattern (Fig. 2.16b) is removed, resulting in a smoother image.

Correction of vibration

As mentioned in section 2.3.1, the Thermosensorik HIR system is affected by mechanical vibrations that result in frame displacements. A vibration correction technique based on cross-correlation between frames should be applied after the offset subtraction. This technique relies on the identification of particular features in the image that remain unaltered in the different frames (typically tile corners). Unfortunately, for limited plasmas, the heat deposition occurs on all the FOV. The change in temperature of the tiles edges causes the vibration correction algorithm to fail. No vibration correction could be applied for the experiments presented in this thesis. On the other hand, the IRCam HIR system is not affected by vibrations since the camera is mounted directly on the tokamak vessel. The camera and the tokamak vibrate together and no image correction is needed.

Correction of vignetting

Vignetting results in a reduction of the image brightness or saturation at the periphery of the image compared to its center. This can be caused by several factors such as camera aperture and angular dependence of the detector pixels. An example of vignetting is visible in Fig. 2.16c, where an image of the CC at uniform temperature is shown. In order to properly estimate the temperature in the whole image, a vignetting correction matrix $M(i, j)$, where i and j are the pixel indexes, is applied to the images used for calibration and the ones from the experiments. The vignetting correction procedure is depicted in Fig. 2.17. The matrix $M(i, j)$ is computed as follows. An image of the central column at uniform (room) temperature is acquired. The offset is subtracted (Fig. 2.17a). The average number of counts C_0 within a square region in the center of the image is computed (white rectangle in Fig. 2.17a). The matrix $A(i, j) = C_0/C(i, j)$, where $C(i, j)$ is the count number of the pixel of indexes i, j is evaluated on the region defined by the black rectangle in Fig. 2.17a, to avoid the parts of the image picturing the TCV port. $M(i, j)$ is the fit of the matrix $A(i, j)$ with a gaussian shape $M(x, y) = 1 + a\{1 - \exp[-(x^2 + y^2)/s^2]\}$, where $x = i - i_0$, $y = j - j_0$ are the distance of the pixel from the image center (i_0, j_0) , and a, s are fitting parameters. The result of such a procedure

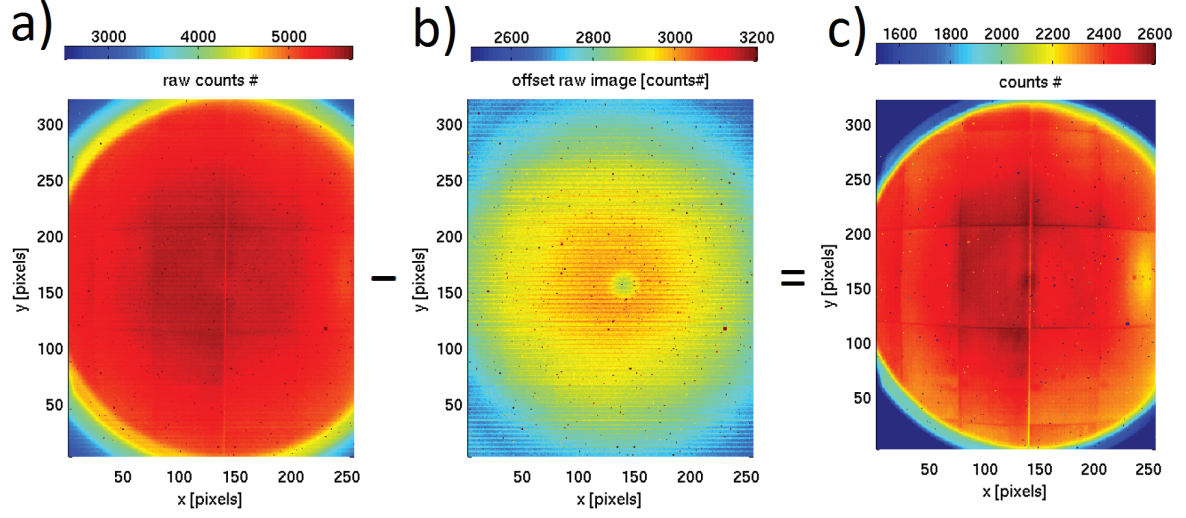


Figure 2.16: a) Raw photon counts, b) offset image, c) net photon counts, for an image of TCV CC at uniform temperature ($T \sim 65^\circ\text{C}$), from the IRCam HIR system for $t_{int} = 1.5\text{ ms}$, $4\text{ }\mu\text{m}$ filter.

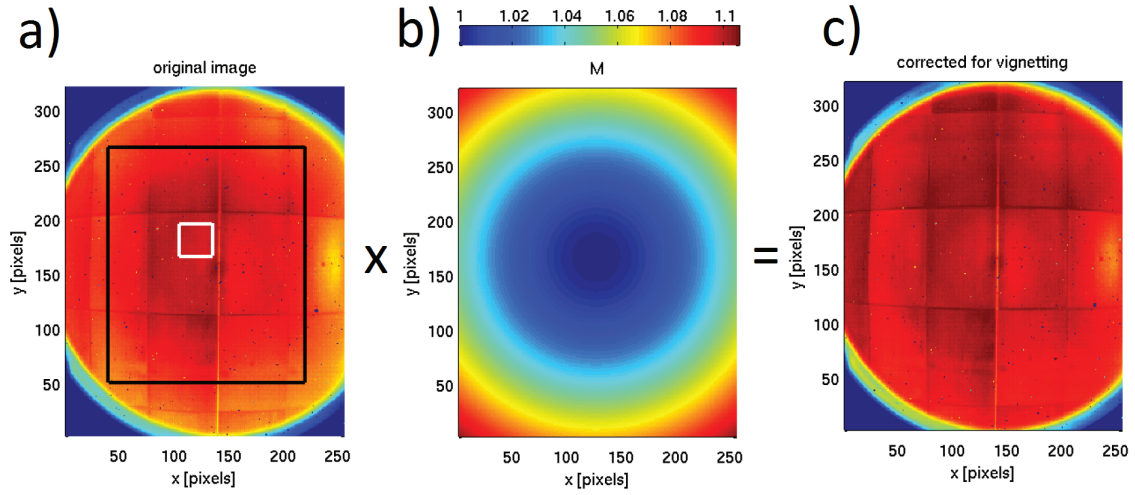


Figure 2.17: a) Net photon count C , same as in Fig. 2.16c. C_0 is the average of C inside the region defined by the white rectangle. $A = C_0/C$ is fitted with a gaussian shape in the region defined the black rectangle to obtain the correction matrix M . b) The correction matrix M . c) The corrected image $C_{corr} = C \times M$.

is shown in Fig. 2.17b. The corrected image is then given by $C_{corr} = C \times M$. An example of vignetting correction is shown in Fig. 2.17c. Since $M = 1$ by definition at the center of the image, and its maximum value is $M_{max} = 1.106$ at the border of the image, the variation of intensity induced by the vignetting correction is at most 10%.

Conversion to temperature

The image resulting from the previous steps is converted into a temperature two-dimensional distribution using the appropriate calibration curve, computed as explained in subsection 2.3.3. As an example, the image in Fig. 2.17c is converted to temperature in Fig. 2.18a.

Correction of radial deformation for wide angle optics

For wide angle optics, radially symmetric barrel distortion usually appears, arising from the symmetry of a photographic lens. In barrel distortion, image magnification decreases with distance from the optical axis. The apparent effect is that of an image which has been mapped around a sphere (or barrel). In our case, it results in the vertical borders of the tiles converging towards the top and the bottom of the image. The radial distortion is corrected using the Matlab built-in "undistortImage" routine, where the camera input parameters have been optimized so that, in the resulting corrected images, the vertical tile edges are parallel. As an example such a correction is applied to the image in Fig. 2.18a. The resulting corrected image is shown in Fig. 2.18b.

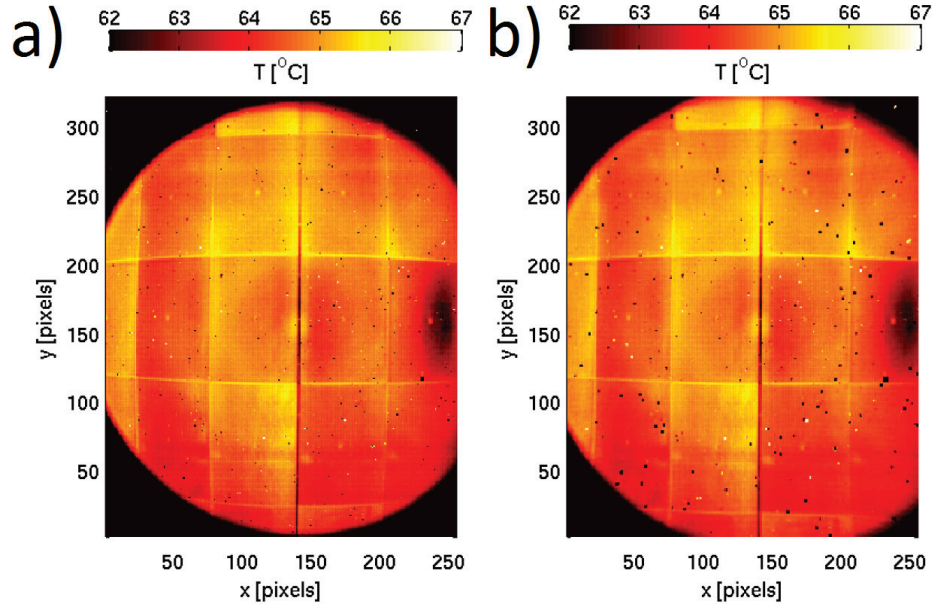


Figure 2.18: a) Conversion to temperature of the image in Fig. 2.17c. b) Correction of the radial deformation introduced by the wide angle optics applied to the image in a).

Correction of perspective deformation and spatial mapping

The TCV central column is cylindrical. In order to properly map tiles that do not lie on the image plane, the perspective deformation has to be taken into account. A drawing of the tile, together with a sketch of the physical coordinates (R, Z, ϕ) , is shown in Fig. 2.4. At the center of the tile, the screw used to install the tile on the CC is visible.

The image is first mapped on an arbitrary grid (X, Y) . The coordinates of the corners of the tile and of the screw at the center of the tile $V = (X_v, Y_v)$ are selected. The coordinates of the vanishing point $P = (X_p, Y_p)$, defined as the crossing-point of the deformed upper and lower edges of the tile, are computed. The vanishing point P is sketched in Fig. 2.19a, together with screw V at the center of the tile and the vertical extension of the right border of the tile ΔY_r . A temperature image of the tiles to be remapped is shown in Fig. 2.19b, together with the screw V and the horizontal coordinates of the left and right corners of the tile, X_l and X_r .

The new set of coordinate $(R\phi, Z)$ is given by

$$R\phi = \begin{cases} (X - X_v) \frac{\Delta R\phi_{0,r}}{X_r - X_v} & X > X_v \\ (X - X_v) \frac{\Delta R\phi_{0,l}}{X_v - X_l} & X < X_v \end{cases}, \quad Z = \left[Y - Y_v + \frac{X_r - X}{X_p - X} (Y - Y_p) \right] \frac{\Delta Z_0}{\Delta Y_r}, \quad (2.9)$$

where $\Delta Z_0 = 172$ mm is the physical height of the tile, $\Delta R\phi_{0,l} = 56.4$ mm and $\Delta R\phi_{0,r} = 63.4$ mm are the horizontal distance from the screw V to the left and right borders of the tile, respectively. The temperature image of the tile after the perspective correction and mapping is shown in Fig. 2.19c.

Evaluation of the heat fluxes

The heat flux deposited onto the tiles is finally computed using the THEODOR [35] code. A brief review of the code is given in section 2.6. The temporal evolution of the tile surface temperature is given as an input, and the heat flux deposited by the plasma on the tile surface is determined by solving the inverse problem of the heat diffusion inside the tile.

For the experiments presented in this thesis, the analysis is usually restricted to two tiles, one being located at the machine midplane ($Z = 0$) and the one above it, as shown in Fig. 2.20a. The pair of tiles that give no sign of misalignment is chosen. Since THEODOR solves the heat diffusion equation in two dimensions, namely into the depth of the tile and in one direction perpendicular to it, the tile is divided into 50 horizontal slices. For each slice q_{dep} is computed, and the 2D map of q_{dep} on the tile surface is obtained reassembling the slices back together. An example of the resulting q_{dep} 2D map is shown in Fig. 2.20b.

The choice of using horizontal slices (instead of vertical) is driven by the fact that for limited plasmas the gradients of the tile temperature in the vertical direction Z result to be smaller than those in the horizontal direction $R\phi$, $\partial_Z T < \partial_{R\phi} T$, so that neglecting the heat diffusion in the Z direction minimizes the error. Furthermore, we assume that for the timescale of a plasma discharge (2 s) the heat diffusion is mainly in the direction perpendicular to the tile surface $\partial_Z T, \partial_{R\phi} T \ll \partial_x T$, where x is the coordinate along the tile depth. This assumption is

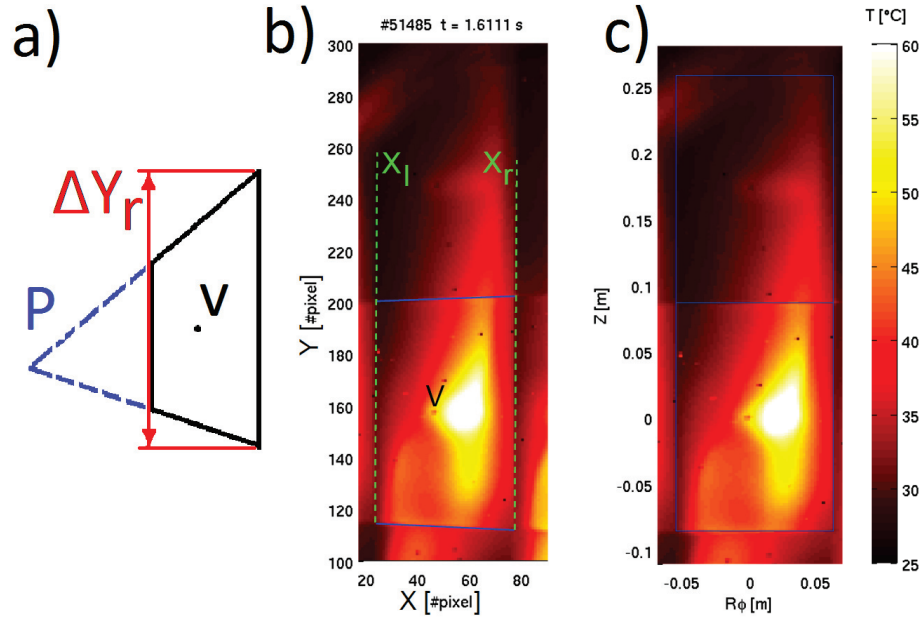


Figure 2.19: a) Sketch of the vanishing point P, defined as the crossing point of the deformed upper and lower borders of the tile (exaggerated), screw V at the center of the tile and vertical extension of the right border of the tile ΔY_r . b) Original temperature image, with the horizontal coordinates of the left and right borders of the tile X_l and X_r and the screw at the center of the tile V. c) Tile remapped to the toroidal and vertical coordinates ($R\phi$, Z).

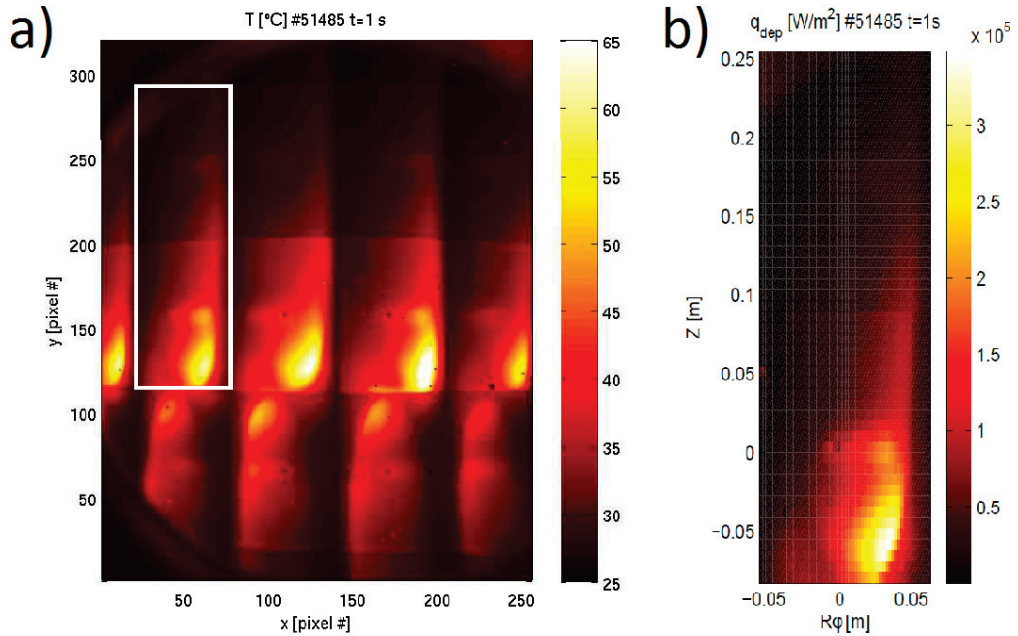


Figure 2.20: a) FOV of the IRCam HIR system (perspective not corrected). The IR analysis is performed on the two tiles marked by the white rectangle. b) Deposited heat flux on the two tiles marked by a white rectangle in a).

confirmed a posteriori comparing the q_{dep} obtained from THEODOR analysis with different values of the anisotropy parameter $a = 1, 0$, which reveals no appreciable changes, except at the border of the tile. This region is anyway excluded from the subsequent analysis since it is shadowed by the neighboring tiles and no plasma deposition occurs in this region (see section 3.2.1).

THEODOR allows only for a uniform tile thickness. For this reason, the zones of the tile whose thickness is too different from the average tile thickness are excluded from the analysis. This is the case, e.g., of the zone corresponding to the hole in the back of the tile that allows its mounting on the CC (Fig. 2.4). Details will be given in section 3.2.1.

2.4 Langmuir probes (LP)

Langmuir probes (LP) [36] are one of the simplest and most common diagnostics used to monitor plasma temperature, density, and electric potential of relatively low temperature and density plasmas. They are widely used in basic plasma experiments, on satellites for space plasma measurements, and in the tokamak SOL. A Langmuir probe consists of a conductor that is inserted into the plasma. An electric potential V is applied to the conductor and the current I flowing through it, resulting from both ions and electron currents from the plasma, is measured. If the probe is at floating potential V_{fl} , the electron and the ion currents flowing to the probe are equal and their sum is zero. If the probe is biased with a sufficiently negative voltage (with respect to V_{fl}), only ions are collected by the probe: this is referred to as “ion saturation mode”. On the contrary, if the applied voltage is larger than the plasma potential V_p , the ions are repelled and only electrons are collected. This regime of operation is called “electron saturation mode”. As the applied voltage V is swept from negative to positive values, the I-V characteristic of the probe is described by

$$I(V) = I_{sat} \left\{ 1 + \alpha_{sh}(V - V_{fl}) - \exp \left[\frac{e(V - V_{fl})}{k_B T_e} \right] \right\}, \quad (2.10)$$

where I_{sat} is the ion saturation current, T_e is the electron temperature and k_B is the Boltzmann constant. The sheath expansion factor α_{sh} comes from the linearization of Child's Law [37], and describes the dependence of the sheath thickness on the probe voltage. According to the Bohm criterion [10], in a magnetized plasma the ion saturation current can be expressed as

$$I_{sat} = A_p n_e c_s / 2, \quad (2.11)$$

where A_p is the projection of the collecting surface perpendicularly to the magnetic field lines, n_e is the bulk plasma electron density and $c_s = \sqrt{k_B(T_e + T_i)/m_i}$ is the ion sound speed, T_i and m_i being the ion temperature and mass, respectively. The plasma potential V_p and the floating potential are related through the equation

$$V_p = V_{fl} + \Lambda T_e, \quad (2.12)$$

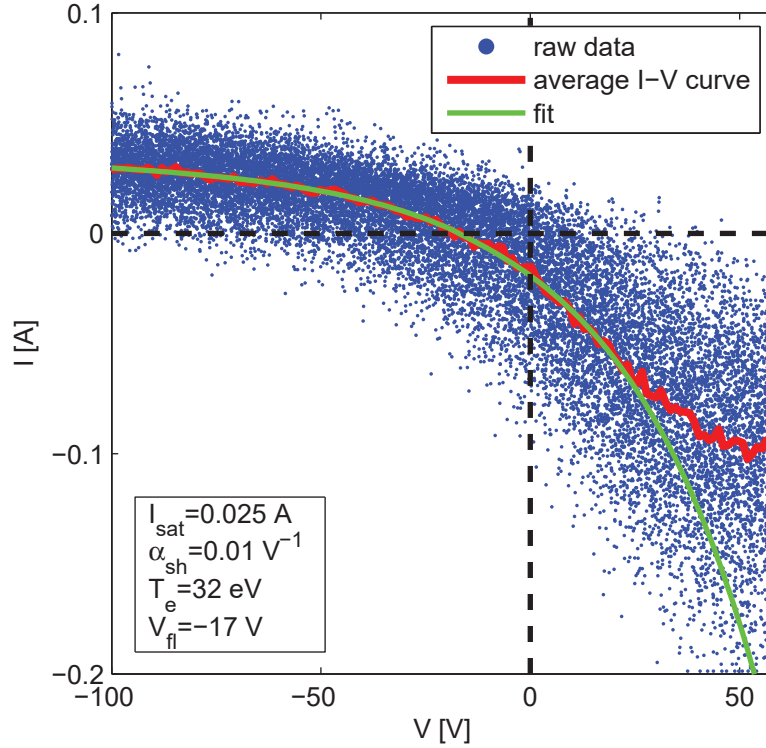


Figure 2.21: Example of I-V curve (red line) from a LP from TCV CC fitted with eq. (2.10) (green line). The I-V curve is obtained by binning the raw data (blue dots). The resulting fit parameters are displayed.

where $\Lambda = -1/2 \ln[2\pi m_e(1 + T_i/T_e)/m_i] \sim 3$ for hydrogen or deuterium plasmas. When LPs are biased with a swept potential, the resulting I-V curve can be fitted with Eq. (2.10), giving the fitting parameters I_{sat} , V_{fl} , T_e , and α_{sh} . An example of a I-V curve from TCV is shown in Fig. 2.21, together with the result of the fitting procedure. Using Equations (2.11) and (2.12), the plasma density and potential can then be computed.

We point out that a non-zero floating potential is the result of non-ambipolar currents flowing to the limiter, and the sign of the floating potential is given by the sign of the non-ambipolar currents. Indeed, as shown in Fig. 2.21, a negative floating potential, given by the intersection of the I-V curve (red) with the $I = 0$ line (horizontal dashed black), corresponds to a negative current flowing to the (unbiased) solid surface hosting the probe, given by the intersection of the I-V curve with the line $V = 0$ (vertical dashed black). Similar considerations hold in the case $V_{fl} > 0$. We also point out that the magnitude of the non-ambipolar currents is not proportional to V_{fl} , since the intersection with the vertical line in Fig. 2.21 does also depend on the electron temperature T_e (an higher temperature gives a steeper curve). Still, in this thesis, we will consider a non-zero V_{fl} as an evidence of non-ambipolar currents flowing to the limiter.

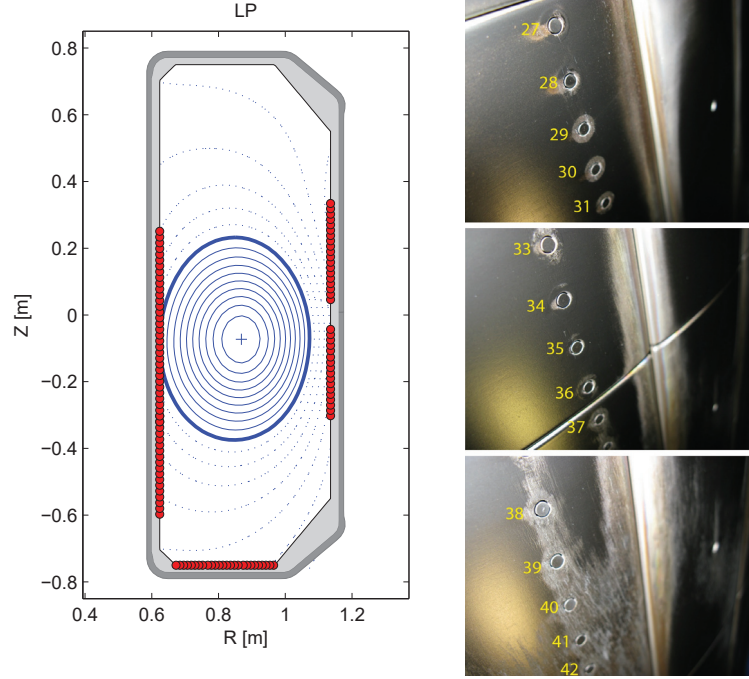


Figure 2.22: Left: location of the Langmuir probes (LP) in the TCV cross section. Right: some of the flush-mounted LP on the CC.

The parallel heat flux at the probe location can be computed as

$$q_{||} = (\gamma T_e + \epsilon_{pot}) J_{sat} , \quad (2.13)$$

where $J_{sat} = I_{sat} / A_p$ is the ion saturation current density, $\epsilon_{pot} = 15.8$ eV is the potential energy per incident ion, which includes the ionization potential (13.6 eV) and half of the molecular binding energy (2.2 eV), and γ is the sheath transmission factor [10]. The sheath transmission factor depends on the floating potential and includes the contributions of electrons and ions convective heat flows, which are due to the acceleration of electrons in the electric field of the sheath, and secondary electron emission from the collecting surface. In a first approximation, $\gamma \sim 6$. For TCV, it has been shown that $\gamma \sim 5$ is more appropriate [38].

For grazing angle of incidence, i.e. when the angle of incidence of the magnetic field onto the probe collecting surface is small ($\alpha \lesssim 1^\circ$), the fitting of the I-V curve is known to produce unreliable results, overestimating T_e and I_{sat} (i.e. n_e) [39]. In particular, small incidence angles are found close to the contact point of a limited plasma on the limiter.

In addition to the swept mode, the probes can also be operated in ion saturation mode, in floating mode, or in grounded mode.

In the ion saturation mode operation, a constant large negative voltage is applied to the probes. The measured current provides directly I_{sat} . This operational mode is used to study fluctuations of the ion saturation current, which in first approximation are proportional to the fluctuations of n_e (assuming the T_e fluctuations to be small).

In the floating mode, no voltage is applied to the probes. The total current flowing to the probes self adjusts to zero and the measured voltage provides directly V_{fl} . This option is used to measure the fluctuations of the floating potential, that in first approximation provide the fluctuations of the plasma potential (assuming the T_e fluctuations to be small).

In the grounded mode, the probes are kept at the limiter potential: $V = 0$. The measured current I_0 is the current that flows to the wall.

TCV is equipped with 114 LP embedded in the first wall tiles on the central column (CC), the floor, and the outer wall (OW). The location of the probes on the poloidal cross section is shown in Fig. 2.22. The probe spacing is 1.72 cm. The probes on the CC and OW are mainly flush-mounted, while a few of them have a roof-top shape. The probes on the floor are domed (hemispherical shape). The probe cross section is circular with radius $r_p = 2$ mm. This ensures that the plasma can be considered magnetized for typical TCV SOL parameters, i.e. that the condition $r_p \gg \lambda_D, \rho_s$ is satisfied, where r_p is the probe radius, λ_D is the Debye length and ρ_s is the ion sound gyroradius. Indeed, for typical TCV SOL plasmas ($B \sim 1.5$ T, $T_e = 50$ eV, $n_e = 10^{19} \text{ m}^{-3}$) we have $\lambda_D \sim 0.5 \mu\text{m}$, $\rho_s = 0.5$ mm, which satisfies the condition.

The number of probes that can be operated simultaneously is limited by the number of available amplifiers, 48. The applied voltage and measured current are acquired at a frequency of 250 kHz, and the sweeping frequency is usually 300 Hz.

2.5 Reciprocating Langmuir probe (RP)

The use of fixed Langmuir probes in tokamaks is limited to the SOL region, since exposing the probe tips to the high density and temperature confined plasma would result in excessive thermal loads, which could damage them. Reciprocating Probes (RPs) are a compromise solution that allows probe measurements even inside the LCFS. In this diagnostic, a set of LP is mounted on a fast manipulator that can insert and extract rapidly the probes from the plasma. The dwelling time inside the plasma is a trade-off between the minimization of the heat load onto the probe and the quality of the acquired data.

From 2015, TCV is equipped with a RP, on loan from the UCSD [40]. The technical drawing of the final RP assembly connected to TCV is shown in Fig. 2.23, and a picture is shown in Fig. 2.24. The probe is located in TCV sector 3. It can be mounted on all three lateral ports ($Z = -45, 0, +45$ cm). In our experiments, the probe is always located at the middle port ($Z = 0$). An example of the probe trajectory is given in the left panel of Fig. 2.25, where its radial coordinate (blue) and the radial position of the LCFS (red) are plotted as a function of time.

The RP head assembly is propelled by a fast pneumatic cylinder and can span 20 cm distance in 100 ms, undergoing accelerations up to 20g.

The RP features a set of interchangeable boron nitride heads that are specifically designed for different magnetic configurations, so that all the pins lie on the same flux surface and they do not magnetically shadow each other. Indeed it is important for two pins to lie on the same flux surface if one wants to compute the poloidal electric field, or to cross-correlate the

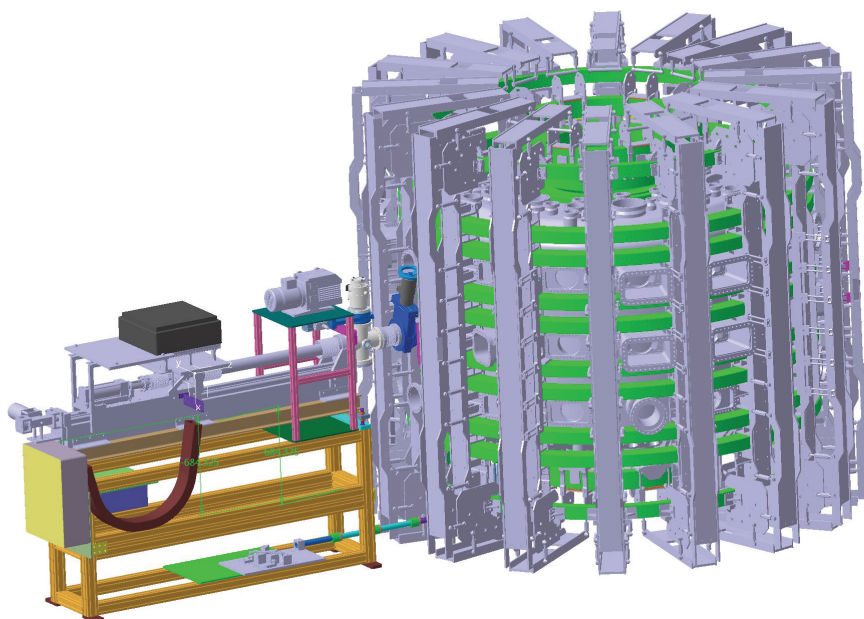


Figure 2.23: Technical drawing of the RP assembly connected to TCV sector 3 middle port.

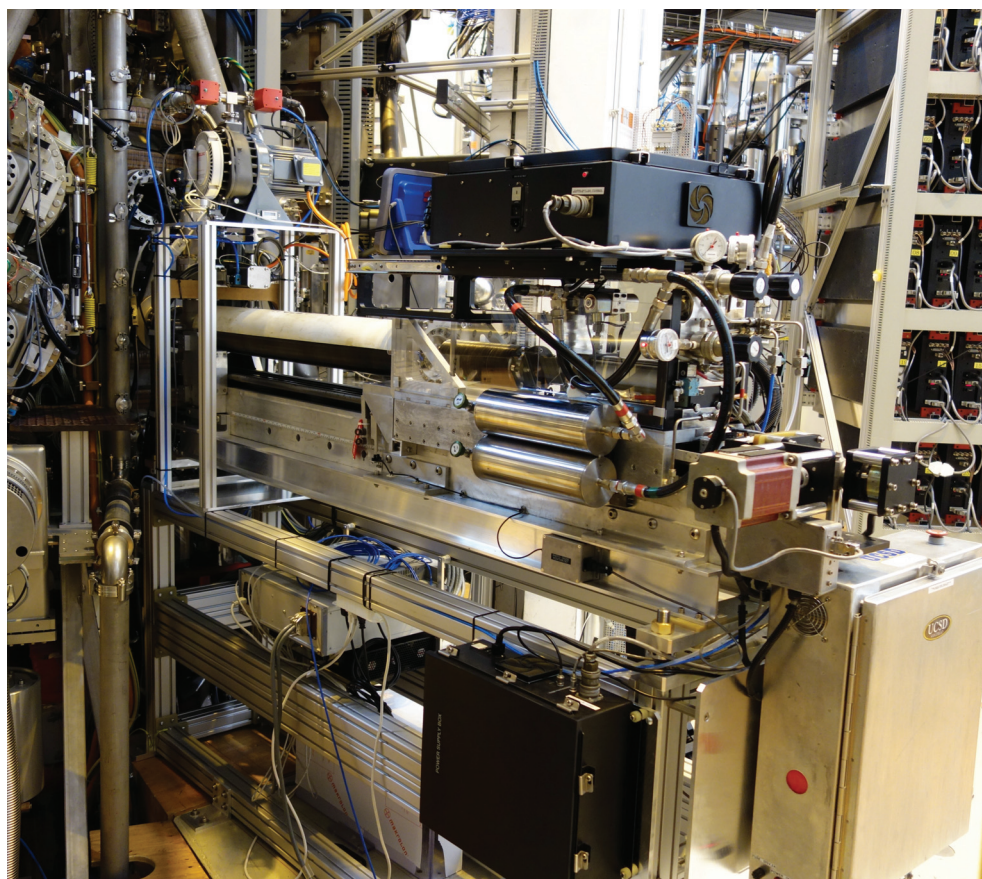


Figure 2.24: Photography of the RP connected to TCV sector 3 middle port.

2.5. Reciprocating Langmuir probe (RP)

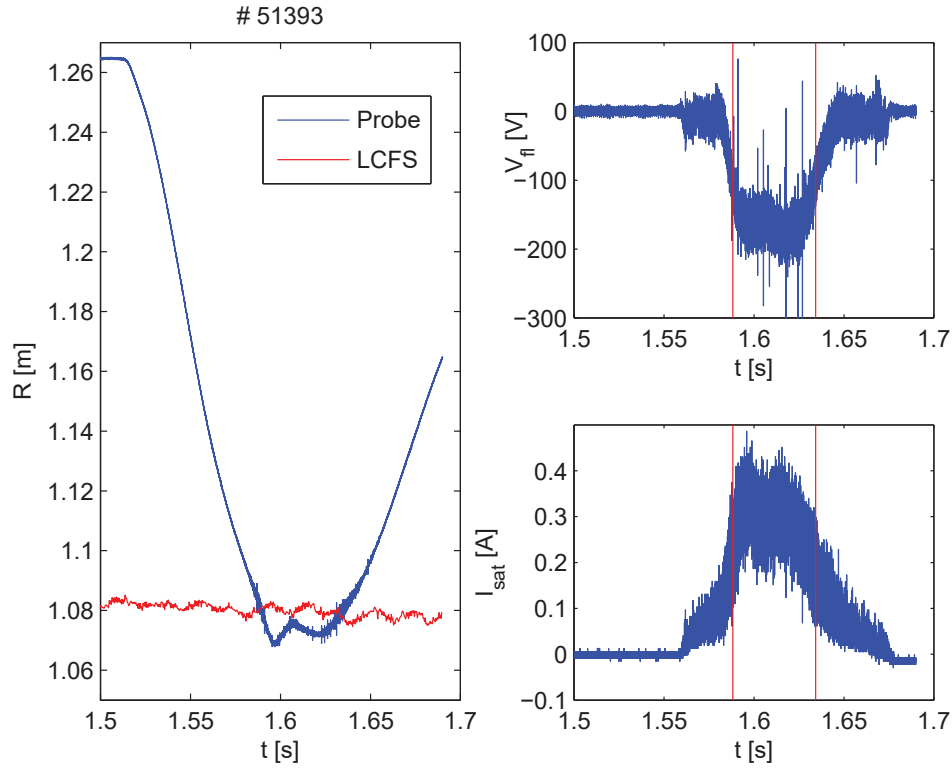


Figure 2.25: Left: time traces of the RP head radial coordinate (blue) and of the radial position of the LCFS (red). Right: time traces of V_{fl} (top) and I_{sat} (bottom). The times corresponding to the crossing of the LCFS are shown by vertical red lines.

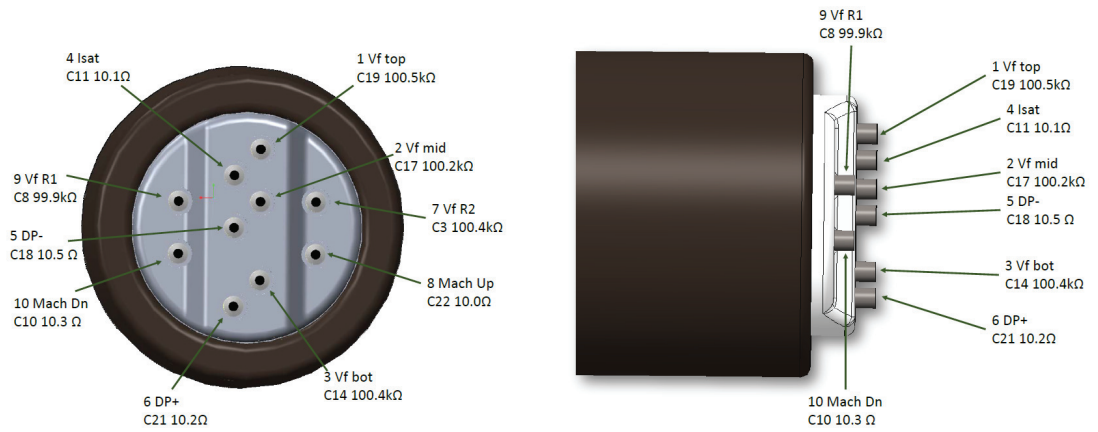


Figure 2.26: Technical drawing of the flat probe head, front view (left) and side view (right). The measured quantity associated with each pin indicated. The external diameter of the (black) graphite shroud is 2.5 cm.

fluctuations measured by both pins.

During this thesis, we have developed the tools to design the correct probe head shape and geometry to better fit the different magnetic configurations. However, in the experiments exposed in this thesis, only one probe head with a “flat” profile has been used, designed for reciprocation at the plasma outer midplane. The probe head is shown in Fig. 2.26. The boron nitride RP head is equipped with 10 pins that allow measuring plasma density, temperature, electric potential, and the plasma toroidal flow across the SOL. In particular, a double probe (pins #5,6 in Fig. 2.26) is used to measure plasma density and temperature. The determination of the plasma temperature T_e and ion saturation current density J_{sat} relies on the fit of the double probe I-V characteristics with the function

$$I = J_{sat}(A_0 + l_p l_{sh}) \tanh\left(\frac{V - V_{off}}{2k_b T_e / e}\right) + I_{off}, \quad (2.14)$$

where A_0 is the geometric projection of the pin surface area perpendicularly to the field line (both sides), $l_p = 3\sqrt{A_0}$ is the exposed perimeter of the electrode, and l_{sh} is the sheath width given by the Child law [37]. V_{off} and I_{off} are offset values that need to be subtracted for the I-V curve to be symmetric. The plasma density is then computed as $n_e = 2J_{sat}c_s$, as it is done for the LP.

In addition to the double probe, a Mach probe (pins #8,10 in Fig. 2.26) is used to measure plasma flows, and one pin (#4) is used in ion saturation mode to measure I_{sat} and its fluctuations. The floating potential and its fluctuations can be measured simultaneously by different pins separated both radially (#2,7,9) and poloidally (#1,2,3), allowing for the determination of the radial and poloidal components of the electric field. All the data are collected at 2.5 MHz sampling rate, and the voltage sweep frequency for the double probe is 1 kHz. Examples of time traces of V_{fl} and I_{sat} are shown in the right panels of Fig. 2.25.

2.6 The THEODOR code

The THERmal Energy Onto DivertOR (THEODOR) code [35] is a 2D code that solves the heat diffusion equation into the depth of the tile, and in one direction perpendicular to it (parallel to the tile surface). THEODOR has been developed to determine the heat flux density profile onto the surface of a target tile from the measured surface temperature evolution. A schematics of the problem solved by the code is given in Fig. 2.27. The equation to be solved is

$$\rho c_p \frac{\partial T}{\partial t} = \nabla \cdot (\kappa \nabla T) = \nabla \cdot \left[\kappa \left(\frac{\partial T}{\partial x} + a \frac{\partial T}{\partial y} \right) \right], \quad (2.15)$$

where $T = T(x, y, t)$ is the temperature distribution, x is the coordinate in the direction perpendicular to the tile surface, y is the coordinate parallel to the tile surface, ρ , c_p and κ are the material density, the specific heat capacity and heat conductivity respectively. a is a parameter that can be varied between 0 and 1 to neglect or take into account the heat diffusion

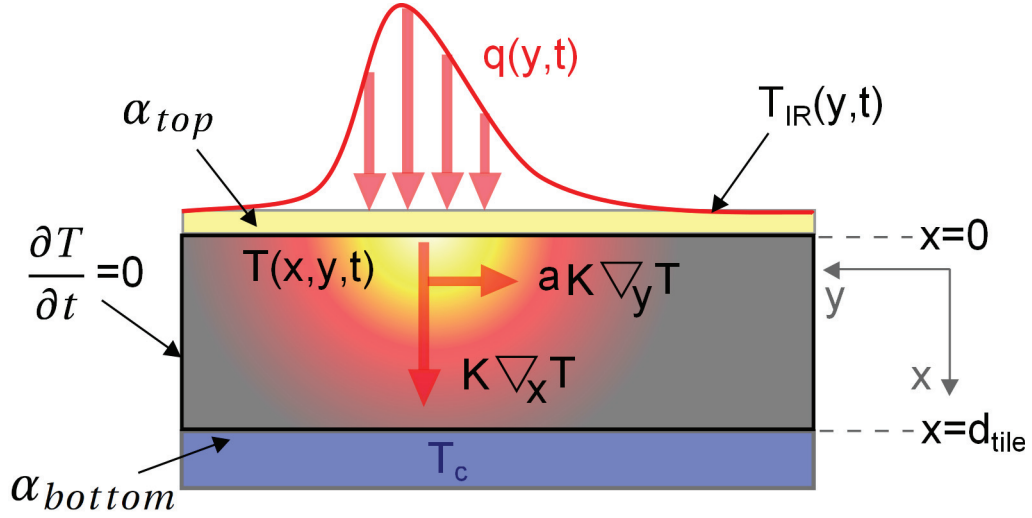


Figure 2.27: Schematics of THEODOR: the deposited heat flux profile $q(y, t)$ (red), the high conductivity redeposited layer (yellow), the cooling temperature at the back of the tile (blue) are shown together with the temperature distribution inside the tile and the coordinate system. The heat conduction inside the tile is illustrated and the boundary condition at the lateral boundary of the tile is shown.

in the direction parallel to the tile surface. The variation of c_p and κ with the temperature is implemented in the code.

The unknown heat flux deposited on the tile $q(y, t)$ enters in the problem through the boundary condition imposed on the tile surface (defined by $x = 0$)

$$T(x = 0, y, t) = T_{IR}(y, t) + q(y, t)/\alpha_{top}, \quad (2.16)$$

where T_{IR} is the input temperature measured by the IR camera, and α_{top} is the heat transfer coefficient of a highly-conductive thin layer on top of the tile. Indeed, in carbon machines, impurities can redeposit on the tile surface creating a thin layer of composited material. The coefficient α_{top} is unknown and is determined as follows: the analysis is performed for a set of different values of α_{top} (typically 20). The value of α_{top} that minimizes the heat fluxes after the end of the discharge is chosen.

The boundary conditions at the lateral borders ($y = y_b$) and the rear ($x = d_{tile}$) of the tiles are:

$$\frac{\partial T}{\partial t}(x, y = y_b, t) = 0, \quad (2.17)$$

$$q_b = \alpha_{bottom}[T_c - T(x = d_{tile}, y, t)], \quad (2.18)$$

where q_b and α_{bottom} are the heat flux and the heat transmission at the back of the tile, respectively, and d_{tile} is the tile thickness. The code is currently implemented with a uniform tile thickness $d_{tile}(y) = const$. In the case of non uniform tile thickness, as e.g. for TCV CC tiles, the analysis has to be restricted to a zone where the tile thickness can be approximated

as constant. Usually, $\alpha_{bottom} = 0$ so that eq. (2.18) can be rewritten as:

$$\frac{\partial T}{\partial t}(x = d_{tile}, y, t) = 0. \quad (2.19)$$

The numerical method used to solve the inverse problem to extract the deposited heat flux q from equations (2.15-2.18), is exposed in details in Ref. [41].

2.7 Numerical tools for TCV SOL turbulence simulations

To improve our understanding of the physics of the SOL, we perform non linear numerical simulations of the TCV SOL plasma using the GBS code [42, 43]. The motivations to perform such simulations are multiple:

1. Validating the GBS code through comparisons between the simulation results and the experimental data. In particular, we aim at comparing the heat fluxes deposited on the simulation limiter with the ones measured by means of IR thermography. Such validation, attempted for the first time for TCV, is exposed in section 3.6.
2. While only a limited amount of measurements at predefined locations are available in the experiments, the simulations provide access to all physical quantities of interest in all points of the three-dimensional domain at the desired time. Taking advantage of this, a simulation of an existing discharge can provide a deeper insight on the physical processes behind the experimental observations.
3. In the GBS code, the plasma turbulence sets self-consistently both the time-averaged quantities and their fluctuations. In particular, the turbulence generates coherent structures, called blobs, that travel in the SOL and are believed to enhance the cross-field transport. In section 4.2, a pattern recognition technique is applied to the simulation results to detect the blobs and track them. Using such a method, we aim at investigating the blobs dynamics in the SOL and to evaluate their contribution to the heat deposition onto the first wall.

2.7.1 The GBS code

The Global Braginskii Solver (GBS) code [42, 43] is a 3D global, flux driven code that simulates the dynamics of the plasma turbulence in the SOL, which sets self-consistently both the equilibrium quantities and their fluctuations. As an output of the numerical simulations, the temporal evolution in 3D of several physical quantities is given. Among these quantities, the more relevant are the plasma density n , the electron and ion temperature T_e and T_i , the electron and ion parallel velocity $v_{||e}$ and $v_{||i}$, and the plasma potential V_{pl} . An example of a snapshot of these quantities resulting from a GBS simulation is given in Fig. 2.28.

The philosophy behind the development of GBS is to approach a complex problem, such

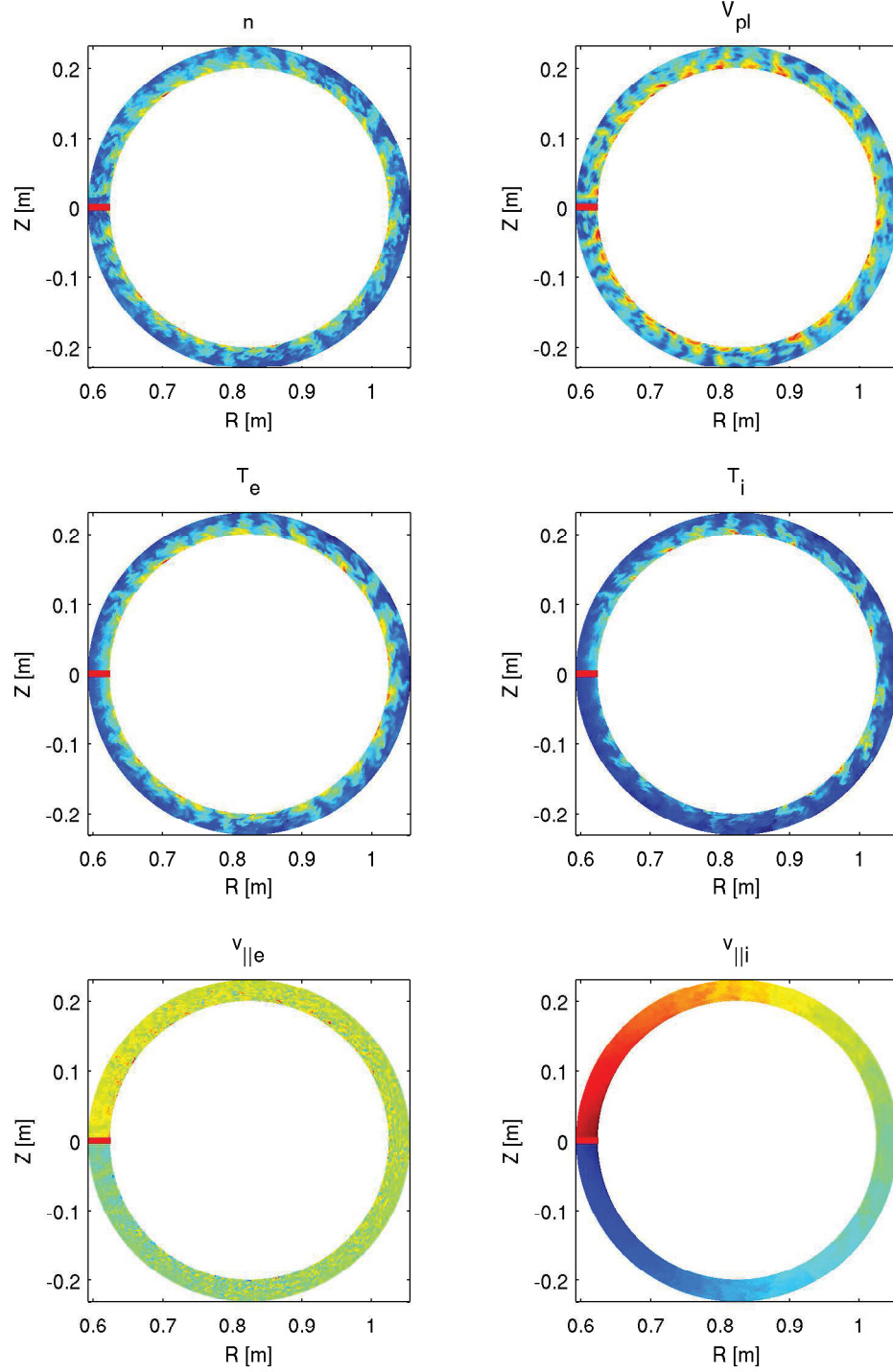


Figure 2.28: Example of the output of a GBS simulation: snapshots of the plasma density n , the plasma potential V_{pl} , the electron and ion temperature T_e and T_i , the electron and ion parallel velocity $v_{||e}$ and $v_{||i}$. The limiter is shown in red.

as tokamak edge turbulent dynamics, in steps of increasing complexity. GBS was initially designed to simulate the cross-field (2D) plasma dynamics of basic plasma experiments with open, straight field lines such as LAPD [44]. In basic plasma experiments, the cold ion approximation holds since typically $T_i \ll T_e$. The modeling of the Simple Magnetized Torus (SMT) configuration, in which the open field lines result from the superposition of the strong toroidal field with a smaller vertical component, required a correct description of the parallel dynamics. This motivation led to the implementation of the 3D version of GBS, able to model plasmas in the TORPEX experiment [45]. The introduction of a toroidal limiter allowed the study of turbulence in the SOL of a limited plasma. The modeling of a tokamak SOL required the development of a set of realistic boundary conditions to be applied at the limiter, to better describe the interaction between the plasma and the solid surface [46]. Also the ion temperature dynamics, which can no longer be neglected as in basic plasma experiments, has been implemented, together with the effect of magnetic shear and finite aspect ratio [47]. GBS was then able to reproduce limited plasma discharges of the size of Alcator C-Mod [48].

Still, the model of the tokamak SOL is not complete. At the time of the writing of this thesis, great efforts are ongoing to include the plasma-neutrals interactions [49], the effect of the plasma shaping, the coupling between the open field line SOL and a region with closed field lines [43]. Also, the possibility to simulate diverted plasmas is presently being implemented [50].

2.7.2 The plasma model in GBS

In GBS, the plasma is described by a two-fluid model (ions and electrons). The derivation of the fluid equations starts from the Boltzmann equations for the ion and electron species distribution functions $f_{i,e}$, and is exposed in details in [51], and is summarized in the following. The fluid equations can be obtained by computing the first three moments of the kinetic equations in the Braginskii limit, describing the evolution of ion and electron density n (quasi-neutrality $n_e = n_i = n$ is assumed), velocity $\mathbf{v}_{i,e}$, and temperature $T_{i,e}$, respectively. The Braginskii closure [52] is used for both species.

The resulting fluid equations still feature time scales that are not of interest for the simulation of turbulence dynamics ($\tau_c \sim \omega_c^{-1}$, with ω_c being the Larmor frequency). Furthermore, the turbulence develops on spatial scales of the order of the ion sound Larmor radius $\rho_s \sim 1$ mm in the direction perpendicular to the magnetic field, while along the field lines, the turbulence varies on lengths of the order of the plasma major radius $R \sim 1$ m. For this reason, the equations can be averaged over the gyration time scale, leading to the so-called drift-reduced equations. The fast temporal scales are eliminated and the perpendicular and parallel dynamics can be separated, i.e. the ion and electron velocities can be rewritten as $\mathbf{v}_{i,e} = v_{\parallel i,e} \hat{\mathbf{b}} + \mathbf{v}_{\perp i,e}$, being $\hat{\mathbf{b}} = \mathbf{B}/B$ the unit vector of the magnetic field.

The resulting fluid equations are:

$$\frac{\partial n}{\partial t} = -\frac{1}{B}[\phi, n] - \nabla_{\parallel}(nv_{\parallel e}) + \frac{2}{eB}[C(p_e) - enC(\phi)] + \mathcal{D}_n + S_n \quad (2.20)$$

$$\frac{\partial \tilde{\omega}}{\partial t} = -\frac{1}{B}[\phi, \tilde{\omega}] - v_{\parallel i} \nabla_{\parallel} \tilde{\omega} + \frac{B^2}{m_i n} \nabla_{\parallel} j_{\parallel} + \frac{2B}{m_i n} C(p) + \mathcal{D}_{\tilde{\omega}}(\tilde{\omega}) \quad (2.21)$$

$$\begin{aligned} \frac{\partial v_{\parallel e}}{\partial t} = & -\frac{1}{B}[\phi, v_{\parallel e}] - v_{\parallel e} \nabla_{\parallel} v_{\parallel e} + \frac{e}{\sigma_{\parallel} m_e} j_{\parallel} \\ & + \frac{e}{m_e} \nabla_{\parallel} \phi - \frac{T_e}{m_e n} \nabla_{\parallel} n - \frac{1.71}{m_e} \nabla_{\parallel} T_e + \mathcal{D}_{v_{\parallel e}} \end{aligned} \quad (2.22)$$

$$\frac{\partial v_{\parallel i}}{\partial t} = -\frac{1}{B}[\phi, v_{\parallel i}] - v_{\parallel i} \nabla_{\parallel} v_{\parallel i} - \frac{1}{m_i n} \nabla_{\parallel} p + \mathcal{D}_{v_{\parallel i}} \quad (2.23)$$

$$\begin{aligned} \frac{\partial T_e}{\partial t} = & -\frac{1}{B}[\phi, T_e] - v_{\parallel e} \nabla_{\parallel} T_e + \frac{4T_e}{3eB} \left[\frac{T_e}{n} C(n) + \frac{7}{2} C(T_e) - eC(\phi) \right] \\ & + \frac{2T_e}{3n} \left[\frac{0.71}{e} \nabla_{\parallel} j_{\parallel} - n \nabla_{\parallel} v_{\parallel e} \right] + \mathcal{D}_{T_e} + \kappa_{\parallel e} \nabla_{\parallel} (T_e^{5/2} \nabla_{\parallel} T_e) + S_{T_e} \end{aligned} \quad (2.24)$$

$$\begin{aligned} \frac{\partial T_i}{\partial t} = & -\frac{1}{B}[\phi, T_i] - v_{\parallel i} \nabla_{\parallel} T_i + \frac{4T_i}{3eB} \left[C(T_e) + \frac{T_e}{n} C(n) - \frac{5}{2} C(T_i) - eC(\phi) \right] \\ & + \frac{2T_i}{3n} \left[\frac{1}{e} \nabla_{\parallel} j_{\parallel} - n \nabla_{\parallel} v_{\parallel i} \right] + \mathcal{D}_{T_i} + \kappa_{\parallel i} \nabla_{\parallel} (T_i^{5/2} \nabla_{\parallel} T_i) + S_{T_i} \end{aligned} \quad (2.25)$$

with $p = n(T_e + T_i)$, the total pressure, $j_{\parallel} = en(v_{\parallel i} - v_{\parallel e})$, $\kappa_{\parallel e}$ and $\kappa_{\parallel i}$ the Spitzer heat conduction coefficients, and $\sigma_{\parallel} = 1.96e^2 n \tau_e / m_e$, the parallel conductivity, where τ_e is the electron collision time. The generalized vorticity, $\tilde{\omega} = \omega + 1/e \nabla_{\perp}^2 T_i$, is related to the electrostatic potential by $\nabla_{\perp}^2 \phi = \tilde{\omega}$. The following operators are used $\nabla_{\parallel} f = \hat{b} \cdot \nabla f$, $[f, g] = \hat{b} \cdot (\nabla f \times \nabla g)$, and $C(f) = B/2[\nabla \times (\hat{b}/B)] \cdot \nabla f$. The perpendicular diffusive terms \mathcal{D}_f are included mostly for numerical reasons.

The source terms (S_n , S_{T_e} , S_{T_i}) mimic the outflow of hot plasma from the confined region to the SOL, and build up the profiles over time, which then drive the turbulence. This is the so-called “flux-driven” approach. The turbulence study presented in this thesis focuses on the steady state regime where the plasma injection, turbulent transport, and losses to the limiter balance each other.

2.7.3 The boundary conditions

The GBS equations (2.20 - 2.25) are solved in the 3D domain (x, y, z) , where x is the radial coordinate, y is the poloidal coordinate and z is the toroidal one. Since the domain covers all the toroidal angles, a periodic boundary condition is applied in the z direction. Along the radial coordinate x , Dirichlet or Neumann boundary condition are usually applied. In particular, for a generic quantity f on the radial boundary $x = x_b$, the Dirichlet boundary condition consists in prescribing the value of the quantity at the boundary $f(x = x_b) = C$, while the Neumann condition consists in prescribing the value of the gradient in the x direction $\partial_x f = D$, where C and D are numerical constants.

The boundaries of the simulation domain in the y direction correspond to the upper and lower

limiter plates. A set of more physically meaningful boundary conditions are hence required at this location to correctly describe the interaction of the plasma with the wall.

When a plasma touches a solid surface, a plasma sheath forms. In the sheath, both ions and electrons are accelerated by large electric fields, the drift approximation breaks down and the plasma eventually becomes non-neutral. When the magnetic field lines are incident to the wall at an oblique angle, three regions form. Moving from the bulk plasma towards the wall, the three regions, sketched in Fig. 2.29, are:

1. The collisional presheath, where the ions are magnetized and the plasma is accelerated in the parallel direction. Ambipolarity $n_e = n_i = n$ holds in this region.
2. The magnetic presheath (MP), where the plasma is quasi-neutral but the drift approximation breaks down due to large electric fields on the ρ_s scale in the direction normal to the wall surface.
3. The Debye sheath, where an even larger electric field is established on the Debye length scale λ_D and quasi-neutrality is no longer satisfied.

A set of generalized Bohm-Chodura boundary conditions is applied at the entrance of the MP, where the drift approximation used to derive Eqs. (2.20 - 2.25) breaks:

$$v_{\parallel i} = c_s \left[\pm 1 + \theta_n \mp \frac{1}{2} \theta_{T_e} - 2 \frac{e\phi}{T_e} \theta_\phi \right] \quad (2.26)$$

$$v_{\parallel e} = c_s \left[\pm \exp \left(\Lambda - \frac{e\phi}{T_e} \right) - 2 \frac{e\phi}{T_e} \theta_\phi + 2(\theta_n + \theta_{T_e}) \right] \quad (2.27)$$

$$\frac{\partial \phi}{\partial y} = \frac{m_i c_s}{e} \left[\pm 1 + \theta_n \pm \frac{1}{2} \theta_{T_e} \right] \frac{\partial v_{\parallel i}}{\partial y} \quad (2.28)$$

$$\frac{\partial n}{\partial y} = - \frac{n}{c_s} \left[\pm 1 + \theta_n \pm \frac{1}{2} \theta_{T_e} \right] \frac{\partial v_{\parallel i}}{\partial y} \quad (2.29)$$

$$\frac{\partial T_e}{\partial y} \approx 0 \quad (2.30)$$

$$\frac{\partial T_i}{\partial y} \approx 0 \quad (2.31)$$

$$\nabla_\perp^2 \phi = \frac{m_i}{e} \left[(1 + \theta_{T_e}) \left(\frac{\partial v_{\parallel i}}{\partial y} \right)^2 + c_s (\pm 1 + \theta_n \pm \theta_{T_e}/2) \frac{\partial^2 v_{\parallel i}}{\partial y^2} \right], \quad (2.32)$$

where the upper signs apply if the magnetic field is directed towards the wall, the lower sign applies in the opposite case, and in GBS geometry

$$\theta_f = - \frac{\rho_s}{2 \tan \alpha} \frac{1}{f} \frac{\partial f}{\partial x} \quad (2.33)$$

for the scalar f , with α being the angle between the magnetic field line and the wall. The derivation of such boundary conditions is explained in details in Ref. [46].

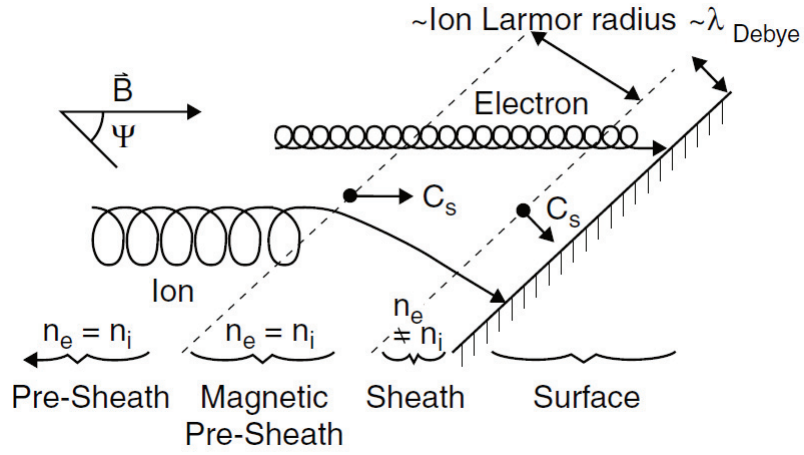


Figure 2.29: Schematics of the different regions forming the sheath of a magnetized plasma, taken from Ref. [10].

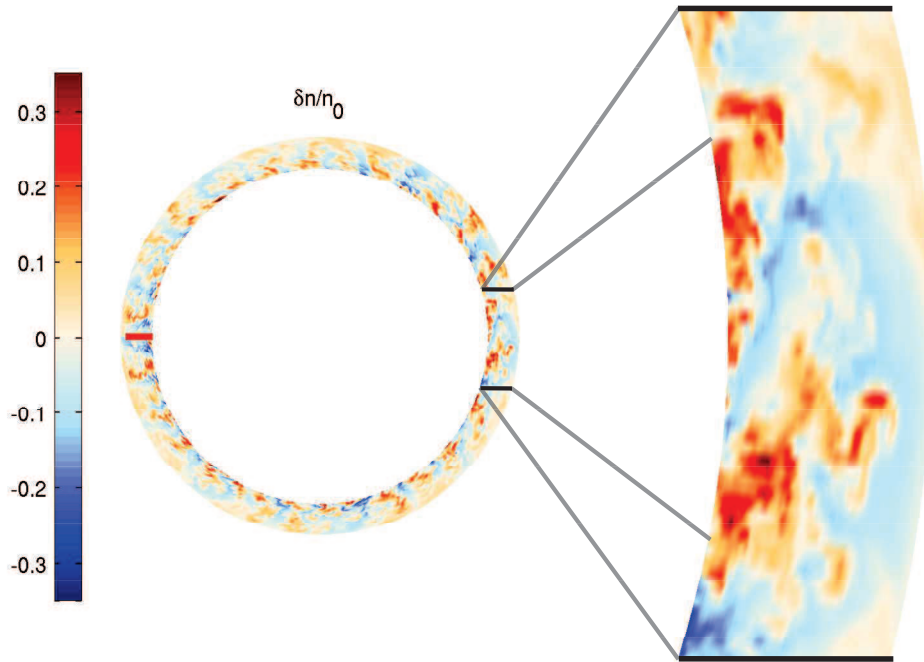


Figure 2.30: Fluctuation of (normalized) plasma density $\delta n/n_0$ on an entire poloidal plane, together with a close-up at the outer midplane, highlighting the presence of turbulent coherent structures (blobs).

2.7.4 The blob detection and tracking technique

A pattern recognition technique, similar to the one used in [53] on experimental data, is used for the first time on full-turbulence simulations to track the motion of the filaments and to study their dynamics. An example of blobs in the GBS simulations is given in Fig. 2.30, where a snapshot of the fluctuation of (normalized) plasma density is shown on an entire poloidal plane, together with a close-up at the outer midplane.

The condition for the blob detection is $n(x, y, z = z_0, t) > \bar{n}(x, y) + 2.5 \sigma(x, y)$ where \bar{n} and σ are the local toroidally- and time-averaged density and its standard deviation, respectively. The different blobs are identified in a given (2D) poloidal plane $z = z_0$ for every frame (simulation output for a given time $t = t_k$) through pattern recognition. They are then tracked to determine their radial and poloidal velocity v_x, v_y : two structures on consecutive frames $b_i(t_{k-1})$ and $b_j(t_k)$ are considered to be the same blob if the area A of their intersection is larger than 10% of the area of the structure in the earlier frame: $A(b_i(t_{k-1}) \cap b_j(t_k)) > A(b_i(t_{k-1}))/10$. Blobs living less than 6 frames are discarded from the analysis.

The merging of two or more different blobs into a new one or the splitting of one blob into two or more parts are considered as the birth of a new blob.

The blob velocity is computed for each frame of its trajectory (except from the first one and the last one for each blob, where it is not defined), as the velocity of the center of mass of the blob. An example of blob detection and tracking is shown in Fig. 2.31, where the contour of a chosen blob (solid black line) is superimposed to the normalized density fluctuation $\delta n/n_0$ for four subsequent simulation frames (equally spaced by 4 frames, corresponding to $1.3 \mu\text{s}$).

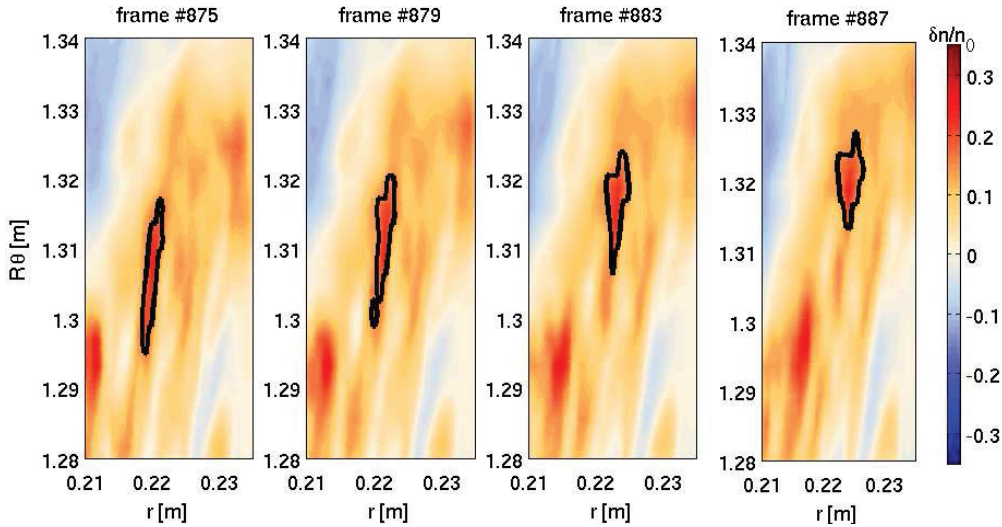


Figure 2.31: Contour of a chosen blob resulting from the blob detection algorithm (solid black line), superimposed to the normalized density fluctuation $\delta n/n_0$ for four subsequent simulation frames (equally spaced by 4 frames, corresponding to $1.3 \mu\text{s}$).

3 SOL physics in inboard limited L-mode plasmas in TCV

In this chapter, the physics of the near and far SOL is investigated in TCV, combining experiments and numerical simulations. The chapter is structured as follows:

In section 3.1, two different sets of experiments performed on TCV are introduced.

In section 3.2, the method used to extract the perpendicular and parallel heat flux radial profiles in the SOL from IR data is detailed. The presence of a near SOL is reported, and its variation with the main plasma parameters is discussed, for both Deuterium and Helium plasmas. The disappearance of the near SOL steep gradients for high resistivity is described. In section 3.3, non-ambipolar currents flowing to the limiter are measured using embedded Langmuir probes (LP). The non-ambipolar currents are shown to correlate with the strength of the heat fluxes in the near SOL, and an interpretation is attempted.

In section 3.4, the measurements performed at the outer midplane (OMP) using the reciprocating Langmuir probe (RP) are discussed. A near SOL feature is present in the radial profiles of the parallel heat flux. This feature is observed at the HFS and LFS, with this latter exhibiting a larger width. The near SOL is observed to disappear at the HFS and LFS simultaneously. Non-ambipolar currents are measured at the LFS as well. In section 3.6, numerical simulations of the TCV SOL using the GBS code are introduced, and their results are compared with the experiments.

Finally, the main results exposed in this chapter are summarized in section 3.7.

3.1 Near SOL experiments in TCV: motivation and overview

In the standard model of the SOL [10], all quantities (density, temperature, heat fluxes) decrease exponentially with the distance from the LCFS. As an example, the plasma density in the SOL is described by $n(r_u) = n_0 \exp(-r_u/L_n)$, where r_u is the upstream radial coordinate, $r_u = 0$ at the LCFS, n_0 is the plasma density at the LCFS, and L_n is the density decay length in the SOL. Similar relations hold for the plasma temperature and parallel heat flux.

Inboard limited L-mode plasmas are foreseen for the ITER start-up and ramp-down phases. The plasma will be limited on the central column, that will be covered by beryllium (Be) tiles. The tiles, or First Wall (FW) panels, are shaped to minimize the heat loads deposited by the



Figure 3.1: ITER FW Be panels. The approximate dimensions are $1.4 \times 1 \times 0.5$ m in the toroidal, vertical and radial direction, respectively. The panels are shaped in the toroidal direction to minimize the deposited heat loads. Picture taken from Ref. [26].

plasma. A rendering of ITER FW panel is shown in Fig. 3.1. The original design of the FW panels [54, 25] assumed an exponential profile of the parallel heat flux in the SOL:

$$q_{||}(r_u) = q_{||0} \exp(-r_u/\lambda_q), \quad (3.1)$$

where the values of the heat flux decay length $\lambda_q = 5$ cm and of the parallel heat flux at the LCFS $q_{||0} = 25$ MW/m² have been extrapolated from a multi-machine database [55]. The parallel heat flux is deposited on the tiles according to

$$q_{dep}(r_u, \alpha) = q_{||}(r_u) \sin \alpha, \quad (3.2)$$

where α is the angle between the magnetic field and the direction tangent to the tile surface, $\alpha = 0$ for tangential incidence. The engineering constraint for the Be FW panels $q_{dep} \leq 5$ MW/m² determines the toroidal shape of the tiles.

Experiments in JET [23], where the heat loads on the limiter have been measured by means of infrared thermography, have shown larger than expected heat fluxes close to the plasma contact point. Heat loads up to a factor of 3 larger with respect to what is foreseen from the standard SOL model have been measured. Furthermore, the radial profile of the parallel heat flux in the SOL is no longer well described by a single exponential and it is better fitted by a sum of two exponentials

$$q_{||}(r_u) = q_n \exp(-r_u/\lambda_n) + q_f \exp(-r_u/\lambda_f), \quad (3.3)$$

where λ_n, λ_f are the parallel heat flux decay length in the near and far SOL, respectively, and q_n and q_f are the associated parallel heat flux magnitudes. The SOL can hence be divided

in two regions: a “near” SOL, extending typically a few mm from the LCFS, characterized by a steep gradient of the parallel heat flux, and a “far” SOL, typically a few cm wide, featuring flatter heat flux profiles. The near SOL is responsible for the peak heat loads on the limiter. If a near SOL is present in the ITER limited start-up plasma, the heat loads on the tiles as originally designed could easily exceed their thermal capabilities, damaging them. A series of experiments has been carried out in different tokamaks [56, 57], including TCV [58], to determine if the presence of the near SOL is an ubiquitous feature of any inboard limited plasma, i.e. it has to be taken into account for the design of ITER FW panels.

3.1.1 First observations of the near SOL in TCV limited plasmas (2013)

A first set of dedicated experiments were performed in TCV in 2013. The main diagnostics used in these experiments were the Thermosensorik HIR system (described in Sec. 2.3.1) and the array of LP embedded on the central column (CC), operated in swept mode. A series of inboard limited L-mode deuterium plasmas has been investigated.

The resulting dataset consists of 35 steady-state phases among which the following plasma parameters have been varied: the plasma current $140 \leq I_p [\text{kA}] \leq 225$, the plasma density $1.7 \leq n_{e,av} [10^{19} \text{m}^{-3}] \leq 6$, the plasma elongation $\kappa = 1, 1.2, 1.4$ and triangularity $\delta = 0, \pm 0.2, \pm 0.4$. The results from the infrared thermography have been presented in Ref.[58]. The main outcome of the experiments can be summarized by two findings:

- A double scale length was observed in all the parallel heat flux profiles measured on the CC.
- The importance of the near SOL can be parametrized by the power entering it, $\Delta P_{\text{SOL}} \sim q_n \lambda_n$, which scales mainly with the normalized plasma resistivity ν , i.e. $\Delta P_{\text{SOL}} \propto n_e^{-1} T_e^{1.5} \propto \nu^{-1}$.

The evidence of the ubiquitous presence of a near SOL and its associated high heat flux in all the dedicated experiments on various tokamaks [23, 56, 57, 58] drove the decision to change the design of ITER FW panels [26]. The change in the shape of ITER FW panels is shown in Fig. 3.2.

However, the physics behind the formation of the near SOL is not completely understood. Moreover, a number of issues affected the set of experiments on TCV:

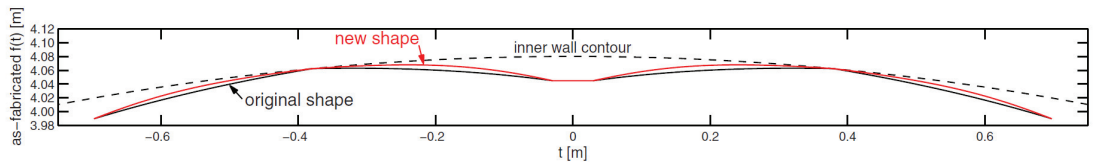


Figure 3.2: ITER FW panel new toroidal shape (red) able to handle the heat flux from the near SOL. The original design shape is shown in black for comparison. Picture taken from Ref. [26].

- The Thermosensorik HIR system was affected by vibrations that could not always be corrected. Part of the data was acquired using a 4 μm filter, lowering the signal-to-noise ratio. The FOV was not optimized for the IR analysis, resulting in a too narrow range of the upstream coordinate r_u for the most shaped plasmas, rendering the determination of the long scale length λ_f unreliable.
- The LP were operated in swept mode, to measure the plasma density, temperature and floating potential at the limiter. The small incidence angle at the contact point $\alpha \simeq 1^\circ$ leads to unreliable fits of the I-V characteristics, overestimating T_e and n_e . The plasma position was kept constant during the discharges, resulting in a poor spatial resolution of the LP data.
- No diagnostic monitoring the LFS was available.
- The scan in the plasma parameters was not performed systematically and the explored range could be increased. An extended scan in resistivity was desirable to search for plasma regimes where the near SOL is not present (if any).

For these reasons, a new set of experiments was performed starting at the end of 2015, taking advantage of an improved and extended set of diagnostics, and leveraging the experience acquired in the previous experiments.

3.1.2 Improved near SOL experiments in Deuterium and Helium plasmas (2015-2016)

The main diagnostics employed in the experiments are the new IRCam HIR system (described in section 2.3.2), the new RP (section 2.5), and the array of LP embedded on the CC. The LP were mainly operated in I_{sat} and V_{fl} mode (every other probe). A few discharges are repeated with the LP operated in grounded and swept mode.

The time traces of plasma current, radiated power, plasma density, elongation and triangularity, are plotted in Fig. 3.3 for one of the discharges, together with the magnetic equilibrium at a given time. A typical discharge is designed with three phases, where all the plasma parameters are kept constant, except the plasma vertical position Z_{ax} , which is varied in time, as shown in Fig. 3.4, to ensure the following:

1. For $0.5 \text{ s} < t < 1 \text{ s}$, $Z_{ax} = -7 \text{ cm}$. This position optimizes the IR FOV, since the plasma contact point is not near the tile edges or other regions that need to be excluded from the analysis (see Sec. 3.2.1). Also the range of the radial upstream coordinate r_u available is increased with respect to the case $Z_{ax} = 0$.
2. For $1 \text{ s} < t < 1.2 \text{ s}$ the vertical position is swept to increase the LP spatial resolution.
3. For $1.2 \text{ s} < t < 2 \text{ s}$, $Z_{ax} = 0$. This position is optimized for the RP plunging, ensuring that the reciprocation of the probe takes place at the OMP, where the flux surfaces fit better

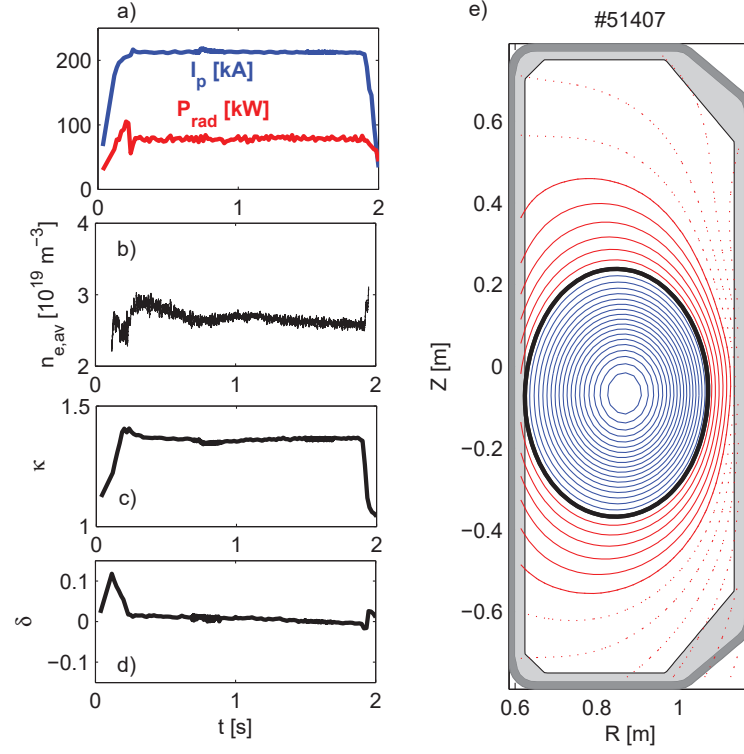


Figure 3.3: Example of plasma discharge of the experiments performed in 2015-2016. Time traces of: a) plasma current I_p (blue) and total radiated power P_{rad} (red), b) average plasma density $n_{e,av}$, c) elongation κ , d) triangularity. e) Magnetic equilibrium from LIUQE reconstruction.

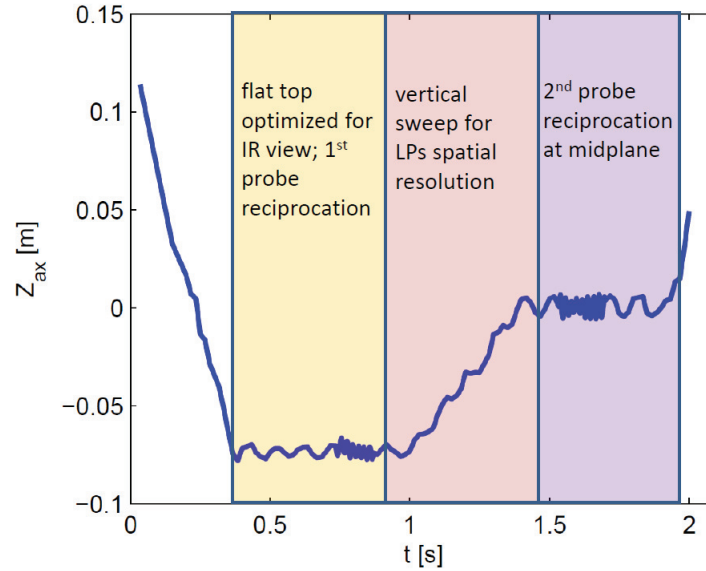


Figure 3.4: Vertical position of the plasma for the typical discharge of the experiments performed in 2015-2016.

the flat profile of the probe head, ensuring that poloidally separated pins lie on the same flux surface.

Two series of inboard limited L-mode deuterium (D) and helium (He) plasmas have been investigated. Systematic scans of plasma current $85 \leq I_p [\text{kA}] \leq 210$, density $1 \leq n_{e,av} [10^{19} \text{m}^{-3}] \leq 5$, and elongation $1 \leq \kappa \leq 1.5$ have been performed. First results of these experiments have been presented at the 21st Joint EU-US Transport Task Force Meeting [59] and at 26th IAEA Fusion energy Conference [60].

The results of the TCV near SOL experiments are exposed in detail in the following and are summarized in section 3.7.

3.2 Heat loads on the limiter

One of the main objectives of the near SOL experiments in TCV is to study the heat loads on the limiter by means of infrared thermography. In particular we aim at computing the radial profiles of the parallel heat flux in the SOL $q_{||}(r_u)$. This is remapped upstream to the OMP to better compare different magnetic configurations. The procedure used to compute such profiles is exposed in details in section 3.2.1, while the results are exposed in section 3.2.3.

3.2.1 IR data analysis method

The steps leading to the evaluation of the temporal evolution of a 2D map of the deposited heat flux $q_{dep}(R\phi, Z, t)$ from the raw IR images is detailed in section 2.3.4. In the following, q_{dep} is time-averaged over time intervals (~ 0.5 s) for which all the plasma parameters are constant.

Mapping onto magnetic coordinates: r_u, α

To compare discharges with different plasma shapes and parameters, we remap each point of the tiles onto magnetic coordinates, namely the upstream radial coordinate r_u and the angle between the magnetic field and the direction tangent to the tile surface α . A schematics of the magnetic coordinates is shown in Fig. 3.5. The mapping is based on the magnetic equilibrium reconstructed by the LIUQE code [33], and the result is shown in Fig. 3.6. The TCV tiles are shaped in the toroidal direction to spread more uniformly the heat loads and to avoid exposed edges. This results in a variation of the angle α both along $R\phi$ and Z . In particular, for limited plasmas, there is a line on the tiles for which $\alpha = 0$. This is shown by the black dots in Fig 3.6b,c.

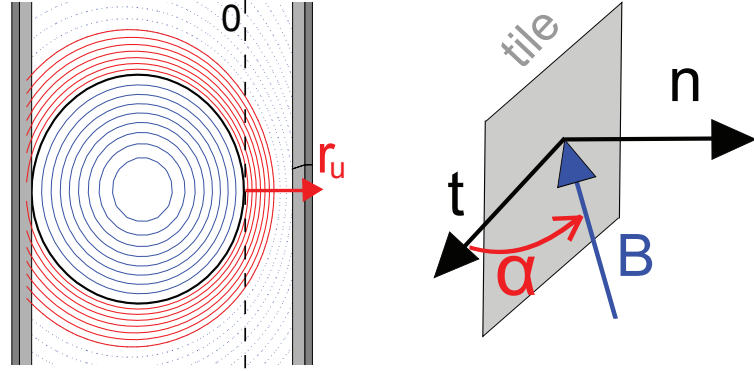


Figure 3.5: Schematics of the upstream radial coordinate r_u and of the angle between the magnetic field and direction tangential to the tile surface α .

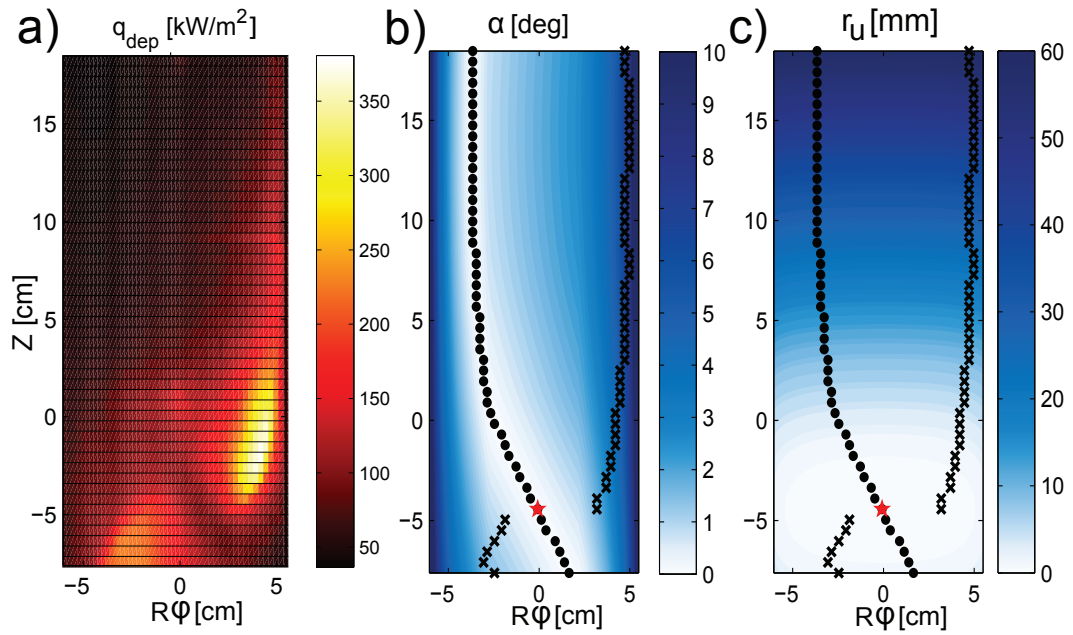


Figure 3.6: a) 2D map of q_{dep} formed by 50 horizontal slices. b) 2d map of the incidence angle α . c) 2D map of the upstream coordinate r_u . The line of tangency $\alpha = 0$ is plotted with black dots. The maxima of q_{dep} on each horizontal slice are marked with a black X. The plasma contact point is shown with a red star. Picture taken from Ref. [58].

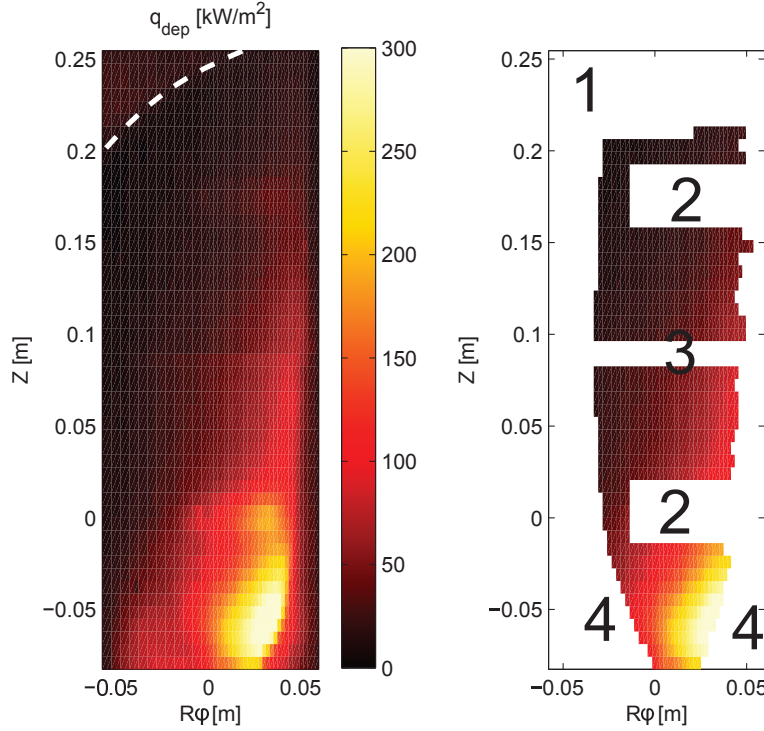


Figure 3.7: Left: deposited heat flux on the CC tiles, q_{dep} , and border of the TCV port (dashed white line). Right: result of the data selection procedure. The zones corresponding to the TCV port (1), the ones close to the tile screws (2), the tile horizontal edge (3), and the region shadowed by the nearby tiles (4) have been excluded.

Data selection

Several zones of the 2D map of the deposited heat flux have to be excluded from the following analysis. The result of the data selection procedure is shown in Fig. 3.7. The zones we exclude are (numbers corresponding to the numbered regions in Fig. 3.7):

1. Region where the TCV port is imaged. This region corresponds to the top-left corner of Fig. 3.7, above the white dashed line.
2. Regions in the vicinity of tile screws. As pointed out in section 2.6, the THEODOR code used to compute q_{dep} allows only for a constant tile thickness. The region of the tile close to the screw used to mount the tile on the CC is much thinner (6 mm) than the average tile thickness (16 mm). The computation of the deposited heat flux with a constant thickness for all the tile results hence in an overestimation of q_{dep} in this region that has to be discarded.
3. Tile edges. The horizontal gap between two tiles can be exposed to penetration of the field lines, leading to heat deposition on the upper (or lower) side of the tile, resulting in a higher temperature. The so-deposited heat is not taken into account in the THEODOR

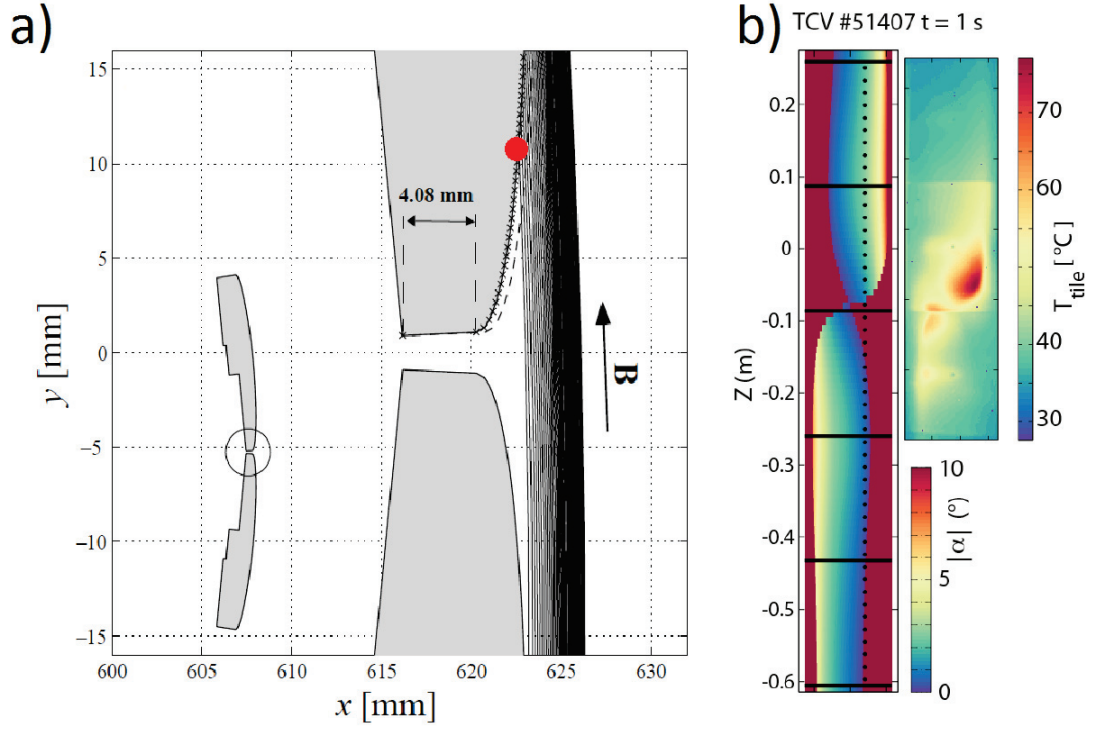


Figure 3.8: a) Shadowing of TCV CC neighboring tiles, edited after Ref. [30]. A close-up of the top view of two tiles on the CC is shown, together with a magnetic field line in the SOL (black line) and its first intersection with the tile (red dot). b) Comparison of the wetted area predicted from the field line tracing based on the LIUQE magnetic equilibrium (left), color coded with the angle of incidence, with the temperature measured by the IR camera (right) for a limited discharge. In the left panel, the shadowed region is displayed in red and the position of the LP is shown with black dots. Picture presented in Ref. [60].

model, and results in an overestimate of the deposited heat on the tile surface. For this reason, a region of 4 mm in the vertical direction, centered around the gap between the two tiles, is excluded from the analysis.

4. Region shadowed by the nearby tiles. The toroidal shape of the tile features recessed wing, to avoid exposed edges. The outermost regions of the tiles are hence shadowed, as it is illustrated in Fig. 3.8a. A comparison between the deposited heat flux and the output of a field line tracing algorithm, based on the LIUQE equilibrium reconstruction, is shown in Fig. 3.8b. For a limited plasma, the wetted (non-shadowed) region is approximately the region in between the $\alpha = 0$ line (black dots in Fig. 3.6) and the line given by the maxima of q_{dep} for a given vertical position Z (black Xs in Fig. 3.6). The region outside these lines is excluded from the following analysis.

Evaluation of perpendicular (q_{\perp}) and parallel (q_{\parallel}) heat fluxes

For the discharges described in section 3.1.2, where the vertical position of the plasma is swept during the discharge, the final 2D map of $q_{dep}(r_u, \alpha)$ is given by the superposition of q_{dep} obtained at three different plasma vertical positions ($Z_{ax} = -7, -3, 0$ cm), to increase the spatial resolution. The deposited heat flux is modeled as the sum of components parallel and perpendicular to the magnetic field and a background component:

$$q_{dep}(r_u, \alpha) = q_{\parallel}(r_u) \sin \alpha + q_{\perp}(r_u) \cos \alpha + q_{BG}. \quad (3.4)$$

The background heat flux q_{BG} results from a combination of different processes like IR reflections, heating of the tiles by the radiation coming from the plasma, and IR radiation from runaway electrons. The peculiar shape of the TCV tiles, featuring a line of tangential incidence for limited plasmas, allows estimating the cross-field heat flux q_{perp} . For $\alpha = 0$ the projection of the parallel heat flux vanishes so that

$$q_{dep}(r_u, \alpha = 0) = q_{\perp}(r_u) + q_{BG}. \quad (3.5)$$

We model $q_{\perp}(r_u)$ as a sum of two exponentials:

$$q_{\perp}(r_u) = q_{\perp n} \exp(-r_u / \lambda_{\perp n}) + q_{\perp f} \exp(-r_u / \lambda_{\perp f}), \quad (3.6)$$

where $\lambda_{\perp n}, \lambda_{\perp f}$ are the perpendicular heat flux decay length in the near and far SOL, respectively, and $q_{\perp n}, q_{\perp f}$ are the associated perpendicular heat flux magnitudes. The background heat flux q_{BG} and the perpendicular heat flux parameters $\lambda_{\perp n}, \lambda_{\perp f}, q_{\perp n}$, and $q_{\perp f}$, are evaluated by fitting the deposited heat flux for tangential incidence (q_{dep} on the $\alpha = 0$ line, black dots in Fig. 3.6) with Eqs. (3.5,3.6). An example of the fitting procedure is shown in the top panel of Fig. 3.9.

A fit with the sum of a single exponential and a background component is also performed for all the discharges. The description of q_{\perp} by a sum of two exponentials or a single one is chosen based on the goodness of fit, R^2 . In the case a single exponential fit produces R^2 equal or bigger than that resulting from the double exponential fit, $q_{\perp}(r_u)$ is still modeled by Eq. 3.6, where $q_{\perp n} = 0$. The perpendicular heat flux at the contact point $q_{\perp 0} = q_{\perp}(r_u = 0) = q_{\perp n} + q_{\perp f}$ can be as high as the 20% of the peak heat load on the limiter [58], and it cannot therefore be neglected.

The parallel heat flux radial profile at the outer midplane is computed inverting Eq. (3.4) and accounting for the flux expansion:

$$q_{\parallel}(r_u) = \frac{q_{dep}(r_u, \alpha) - q_{\perp}(r_u) \cos \alpha - q_{BG}}{\sin \alpha} \frac{B_{us}}{B_{lim}}, \quad (3.7)$$

where $q_{\perp}(r_u)$ is given by Eq. (3.6), B_{us} and B_{lim} are the total magnetic field intensities at the outer midplane (upstream) and at the limiter, respectively. The resulting parallel heat flux

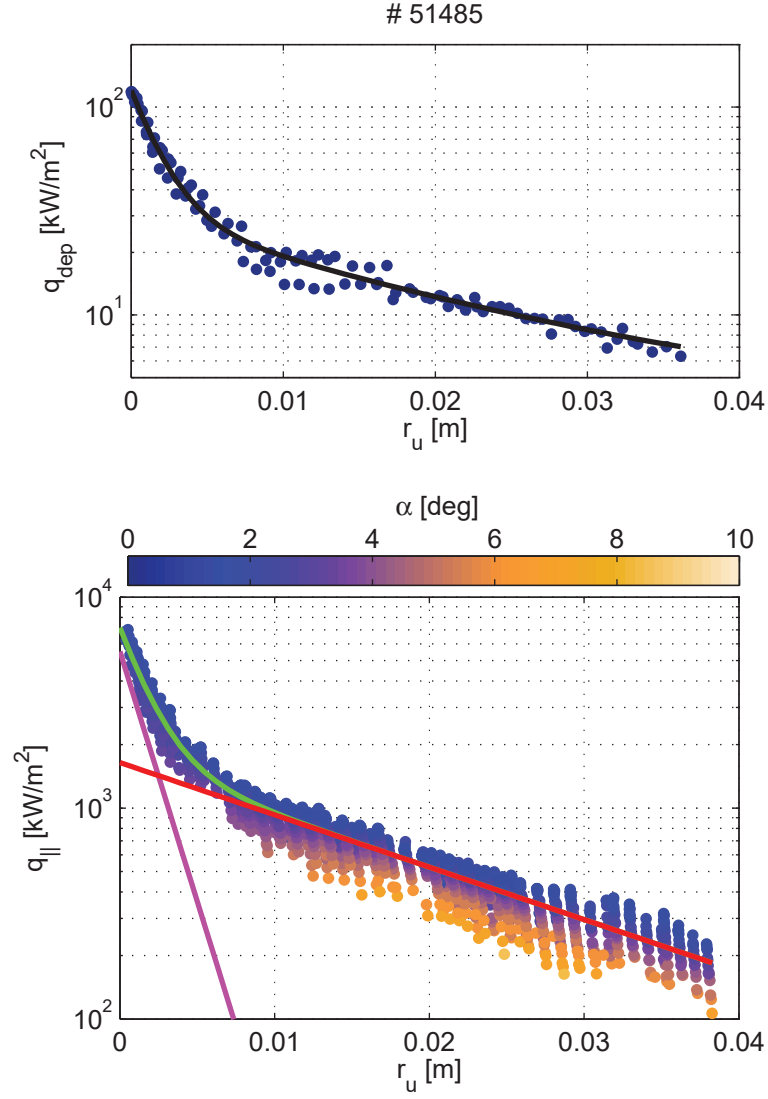


Figure 3.9: Top: deposited heat flux for tangential incidence, $q_{dep}(r_u, \alpha = 0)$, fitted with Eqs. (3.5,3.6) (black line). Bottom: parallel heat flux profile $q_{||}(r_u)$, color coded with the incidence angle α , fitted with Eq. (3.8) (green line). The heat flux associated with the near and far SOL, $q_n \exp(-r_u/\lambda_n)$ and $q_f \exp(-r_u/\lambda_f)$, are plotted in magenta and red, respectively.

radial profile is in general well described by a sum of two exponentials:

$$q_{||}(r_u) = q_n \exp(-r_u/\lambda_n) + q_f \exp(-r_u/\lambda_f), \quad (3.8)$$

where λ_n, λ_f are the parallel heat flux decay length in the near and far SOL, respectively, and q_n, q_f are the associated perpendicular heat flux magnitudes. The parameters $\lambda_n, \lambda_f, q_n$ and q_f are determined fitting the $q_{||}(r_u)$ profile with Eq. 3.8, for all the points for which $\alpha > 1^\circ$. The same procedure as for fitting $q_{\perp}(r_u)$ is applied: a fit with a single exponential is performed, and the model providing the largest R^2 is chosen. In the case when a double exponential does not provide a better fit of the data, $q_{||}(r_u)$ is still modeled by Eq. 3.8, where $q_n = 0$.

In the experiments presented in section 3.1.1, whose results have been first exposed in Ref. [58], all the $q_{\perp}(r_u)$ profiles have been fitted with a single exponential.

As already mentioned in section 3.1.1, the limited FOV of the Thermosensorik HIR system (1.5 useful tiles in the Z direction instead of 2 for the IRCam HIR), and the unoptimized vertical position of the plasma led to a restricted r_u range, for most of the discharges. This was not sufficient to determine accurately the far SOL width λ_f by fitting the $q_{||}(r_u)$ profiles with Eq. (3.8). When a sum of two exponentials is used to fit the data, the determination of the parameters of the far SOL λ_f, q_f can also affect strongly the determination of the parameters for the near SOL λ_n, q_n . When the fit results produce unreliable results for the far SOL, also those for the near SOL are most likely unreliable. For this reason a fit function decoupling the far and the near SOL has been preferred. Following Ref. [23], the $q_{||}(r_u)$ profiles have been fit with

$$q_{||}(r_u) = q_n \exp(-r_u/\lambda_n) \Theta(r_0 - r_u) + q_f \exp(-r_u/\lambda_f) \Theta(r_u - r_0), \quad (3.9)$$

where $\Theta(x)$ is the Heaviside step function and r_0 is the radial position where the profile slope changes, also referred to as “break point”.

3.2.2 Perpendicular heat flux at the contact point

For the 2013 experiments (section 3.1.1), the perpendicular heat flux is fitted to a single exponential, $q_{\perp}(r_u) \exp(-r_u/\lambda_{q\perp})$, where $q_{\perp 0}$ is the perpendicular heat flux at the contact point. For the 2015-2016 experiments (section 3.1.2), the perpendicular heat flux is fitted using Eq. (3.6). In this case, the perpendicular heat flux at the contact point is given by $q_{\perp 0} = q_{\perp n} + q_{\perp f}$. It is observed that $q_{\perp 0}$ can account up to the 20% of the peak heat flux deposited on the tile.

The perpendicular heat flux decay lengths $\lambda_{q\perp}$ and $\lambda_{\perp n}$ are typically a few millimeters, while $\lambda_{\perp f}$ measures a few centimeters. No satisfactory scaling with the plasma parameters could be found for the perpendicular heat flux decay lengths.

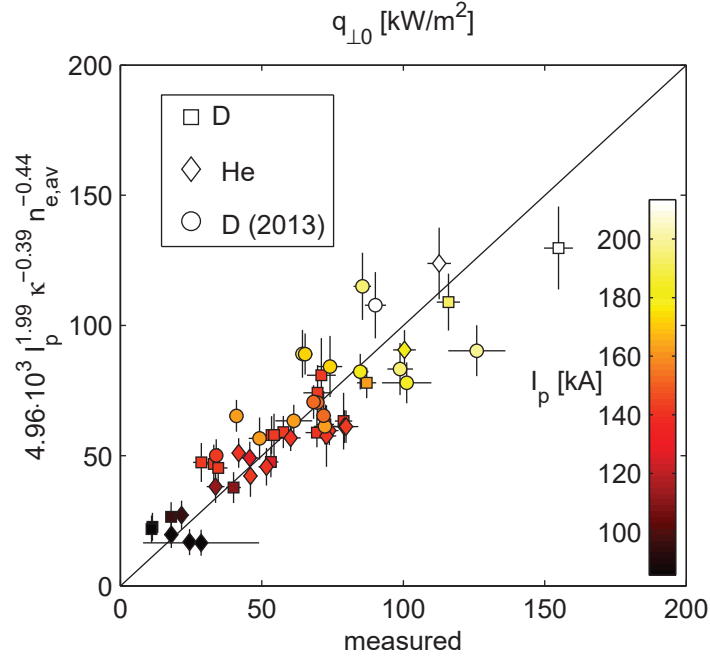


Figure 3.10: Empirical scaling of the perpendicular heat flux at the contact point $q_{\perp 0}$ with the plasma parameters, including D plasmas (squares), He plasmas (diamonds) and D plasmas from the 2013 experiments (circles), for which $q_{\perp 0}$ was evaluated with a different method. The points are color-coded with the plasma current.

Conversely, a nonlinear regression provides an empirical scaling for $q_{\perp 0}$ that reads

$$q_{\perp 0} [\text{kW/m}^2] = 4.96 \cdot 10^3 I_p^{1.99} \kappa^{-0.39} n_{e,av}^{-0.44} \quad (3.10)$$

The empirical scaling, including all the discharges presented in this thesis (D, He), is shown in Fig. 3.10. The main trend is the increase of $q_{\perp 0}$ with the the square of the plasma current, consistent with an increase of the ohmic power. The decrease of $q_{\perp 0}$ with the elongation κ is consistent with an increase of confinement with elongation [61] for constant heating power, resulting in a lower power into the SOL, P_{SOL} . The decrease of $q_{\perp 0}$ with plasma density is consistent with a cooling of the plasma at fixed heating power (I_p).

This trend is consistent with Ref. [58], where a similar scaling was determined using the 2013 discharges only, finding similar results ($q_{\perp 0} \propto I_p^{2.5} \kappa^{-0.9} n_e^{-0.4}$).

3.2.3 Parallel heat fluxes in Deuterium plasmas

The parallel heat flux radial profiles $q_{\parallel}(r_u)$ are well described by a sum of two exponentials (Eq. (3.8)), while their description with a single exponential as in the standard SOL model (Eq. (3.1)) is not equally satisfactory. The SOL can hence be divided into two regions, the “far” and “near” SOL respectively.

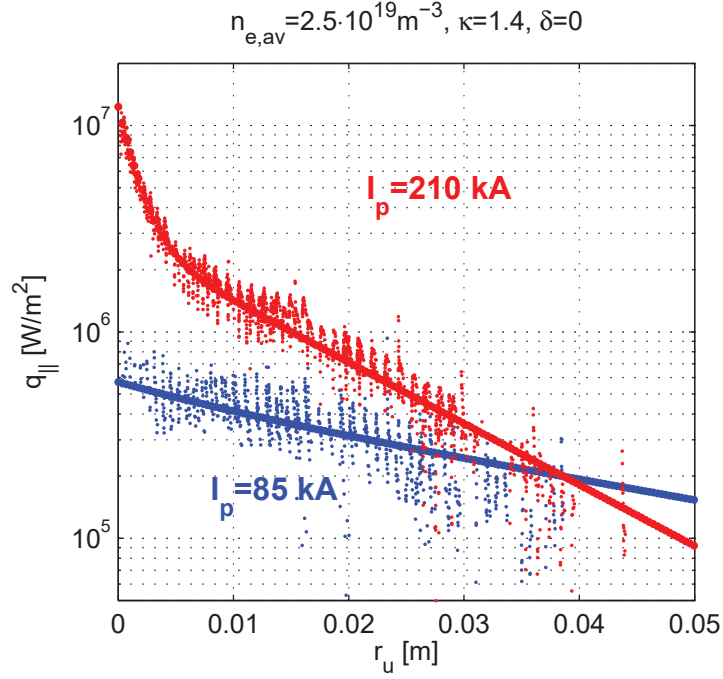


Figure 3.11: Parallel heat flux radial profiles $q_{||}(r_u)$ for $I_p = 210$ kA (red dots) and $I_p = 85$ kA (blue dots). The fit with Eq. (3.8) is shown with solid lines.

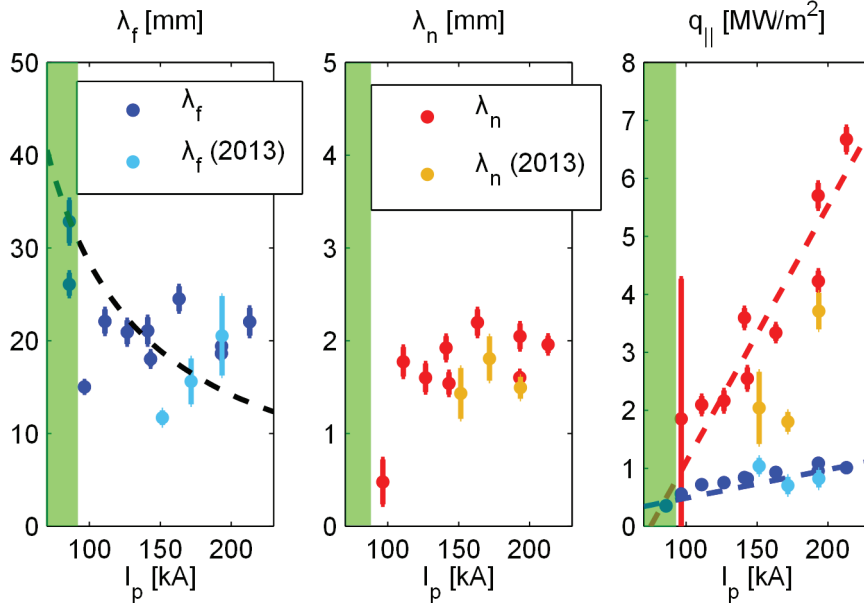


Figure 3.12: Dependence of the fit parameters λ_n , q_n (red), λ_f , q_f (blue) on the plasma current I_p . The line $\lambda_f \propto 1/I_p$ is shown (dashed black). The linear fits of $q_n(I_p)$ (dashed red) and $q_f(I_p)$ (dashed blue) are displayed. In the green shadowed region, no near SOL was measurable. The fit results for discharges of the 2013 experiment with comparable $n_{e,av}$, κ are shown in orange (near SOL) and light blue (far SOL) for comparison.

In the following, the quantities used to parametrize the parallel heat fluxes (λ_n , λ_f , q_n and q_f) are discussed with respect to their dependence on the main plasma parameters. We focus on the results from the experiments presented in section 3.1.2. Some results from the former experiments (section 3.1.1), obtained by re-fitting the $q_{||}(r_u)$ profiles with Eq. (3.8), are shown for comparison.

Plasma current scan in Deuterium

The plasma current has been varied between 85 kA (the lowest value achievable on TCV for vertical stability) and 210 kA. The plasma line averaged density $n_{e,av} = 2.5 \cdot 10^{19} \text{ m}^{-3}$ and the plasma shape $\kappa = 1.4$, $\delta = 0$ are kept constant for all the discharges in the scan. The presence of the near SOL has been observed for all the discharges, except for those corresponding to the lowest plasma current value $I_p = 85 \text{ kA}$. The $q_{||}(r_u)$ profiles corresponding to the lowest and higher plasma currents investigated are compared in Fig. 3.11. The parallel heat flux radial profile at $I_p = 85 \text{ kA}$ is well described by a single exponential.

It is the first time that no presence of the near SOL has been detected at the contact point of a limited plasma, ever since the investigations of the near SOL have began [23, 56, 58, 57].

The variation of the fit parameters λ_n , λ_f , q_n and q_f with the plasma current I_p are shown in Fig. 3.12, and the main results can be summarized as follows:

- The far SOL width λ_f scaling is consistent with the $\lambda_q \propto q_{edge} \propto 1/I_p$ existing scaling of the far SOL width [62] (dashed black line in Fig. 3.12). Indeed in this scan, where the elongation is kept constant, the safety factor at the edge of the plasma varies as $q_{edge} \propto 1/I_p$.
- The near SOL width λ_n is approximately constant over the explored range of plasma current, except for one point ($I_p = 95 \text{ kA}$), for which the fitted λ_n is close to the experimental spatial resolution. The near SOL vanishes for the lowest current value investigated $I_p = 85 \text{ kA}$.
- The near and far SOL parallel heat flux magnitudes q_n and q_f linearly increase with the plasma current, consistently with the increase of the ohmic power, and q_n vanishes for low currents ($I_p = 85 \text{ kA}$). The linear fits of $q_n(I_p)$ and $q_f(I_p)$ are shown in Fig. 3.12 with a red and a blue dashed line, respectively.

Plasma density scan in Deuterium

The plasma density has been varied between $1.2 \cdot 10^{19} \text{ m}^{-3}$ (line averaged value) and $4.7 \cdot 10^{19} \text{ m}^{-3}$. The plasma current $I_p = 140 \text{ kA}$ and the plasma shape $\kappa = 1.4$, $\delta = 0$ are kept constant for all the discharges in the scan. The presence of the near SOL has been observed for all the discharges, except for the ones corresponding to the highest density value $n_{e,av} = 4.7 \cdot 10^{19} \text{ m}^{-3}$. The $q_{||}(r_u)$ profiles corresponding to the lowest and higher density investigated are compared in Fig. 3.13. The parallel heat flux radial profile at $n_{e,av} = 4.7 \cdot 10^{19} \text{ m}^{-3}$ is well described by a

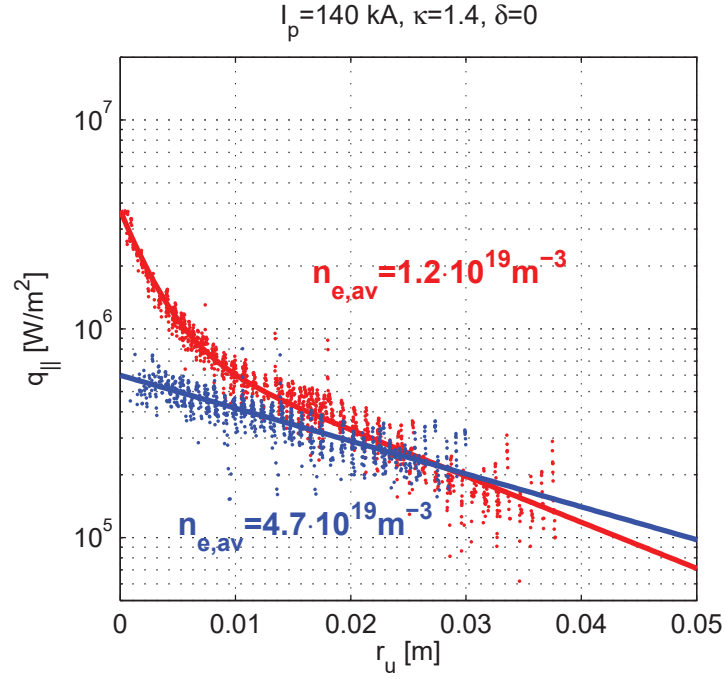


Figure 3.13: Parallel heat flux radial profiles $q_{||}(r_u)$ for $n_{e,av} = 1.2 \cdot 10^{19} \text{ m}^{-3}$ (red dots) and $n_{e,av} = 4.7 \cdot 10^{19} \text{ m}^{-3}$ (blue dots). The fit with Eq. (3.8) is shown with solid lines.

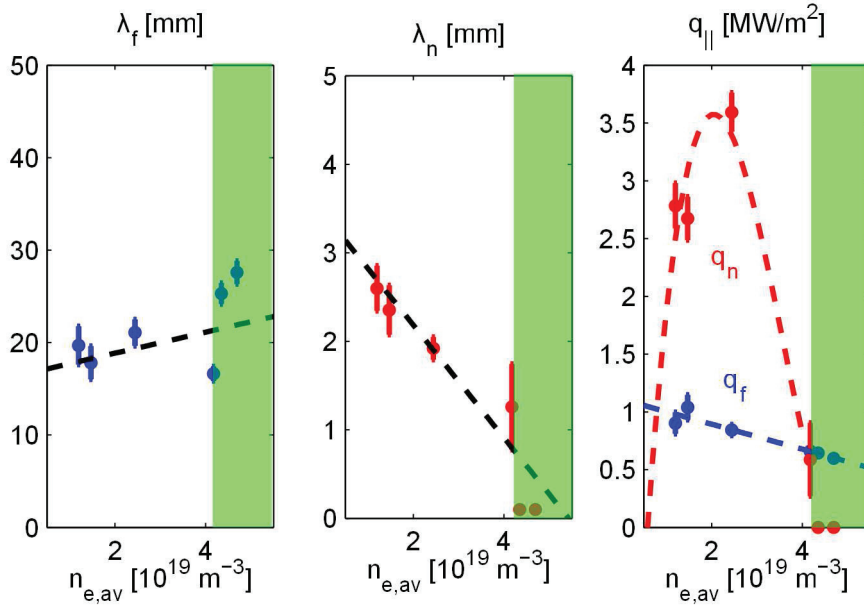


Figure 3.14: Dependence of the fit parameters λ_n , q_n (red), λ_f , q_f (blue) on the plasma line averaged density $n_{e,av}$. Linear fits of $\lambda_f(n_{e,av})$, $\lambda_n(n_{e,av})$ and $q_f(n_{e,av})$ are plotted with black and blue dashed lines, respectively. A cubic interpolation of $q_f(n_{e,av})$ is plotted with a red dashed line. In the green shadowed region, no near SOL was measurable.

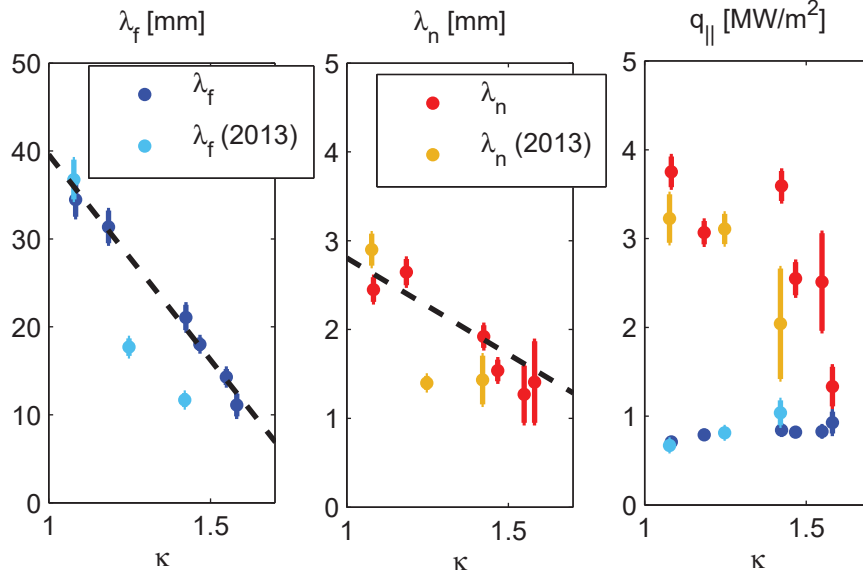


Figure 3.15: Dependence of the fit parameters λ_n , q_n (red), λ_f , q_f (blue) on the elongation κ . Linear fits of $\lambda_f(\kappa)$ and $\lambda_n(\kappa)$ are plotted with black dashed lines. The fit results for discharges of the 2013 experiment with comparable $n_{e,av}$, I_p are shown in orange (near SOL) and light blue (far SOL) for comparison.

single exponential.

The variation of the fit parameters λ_n , λ_f , q_n and q_f with the plasma density $n_{e,av}$ are shown in Fig. 3.14, and the main findings are summarized as follows:

- The far SOL width λ_f increases linearly with $n_{e,av}$, consistently with previous observations in diverted plasmas [63].
- The near SOL width λ_n decreases linearly with $n_{e,av}$ and eventually vanishes.
- The near and far SOL parallel heat flux magnitude q_n and q_f both decrease for increasing density, after an initial increase. q_n vanishes for high densities ($n_{e,av} \gtrsim 4.5 \cdot 10^{19} \text{ m}^{-3}$).

Elongation scan in Deuterium

The plasma elongation has been varied between 1.1 and 1.6. The plasma current $I_p = 140 \text{ kA}$, line averaged density $n_{e,av} = 2.5 \cdot 10^{19} \text{ m}^{-3}$ and triangularity $\delta = 0$ are kept constant for all the discharges in the scan. The variation of the fit parameters λ_n , λ_f , q_n and q_f with the elongation κ are shown in Fig. 3.15, and are summarized in the following:

- The near and far SOL width λ_n , λ_f decrease linearly with κ . This trend is unexpected since in the existing scalings of the SOL width (e.g. [62]) usually $\lambda_q \propto q_{edge}$, where q_{edge}

is the safety factor at the LCFS. Since, for fixed plasma current and toroidal field, $q_{edge} \propto \kappa$, we would expect $\lambda_q \propto \kappa$, contrarily to our observations. Further investigations are required.

- The far SOL parallel heat flux magnitude q_f is constant with κ . The decrease of q_n for increasing elongation can be explained with the increase of confinement with elongation [61] for constant heating power, resulting in a lower power into the SOL, P_{SOL} .

Comparison between electron and ion drift side

The charge dependent drift given by ∇B results in the ions and electrons to flow along the flux surfaces in poloidally opposite directions. The two limiter or divertor plates at the two terminations of a field line can therefore be identified as ion and electron drift side [64]. Heat deposition asymmetries between the ion and electron drift sides are routinely reported in diverted configurations. In the following, we estimate the differences in the heat deposition in between the electron and ion drift side.

The upper part of the limiter, usually analyzed for these experiments, corresponds to the electron-drift side, and the bottom part corresponds to the ion drift side. The same analysis has been carried out also for the lower part of the limiter for discharge #51392 ($I_p = 140$ kA, $n_{e,av} = 2.5 \cdot 10^{19} \text{ m}^{-3}$, $\kappa = 1.4$), representing the central point of the density and current scan. The comparison between the ion and electron drift side is detailed in Fig. 3.16, where the

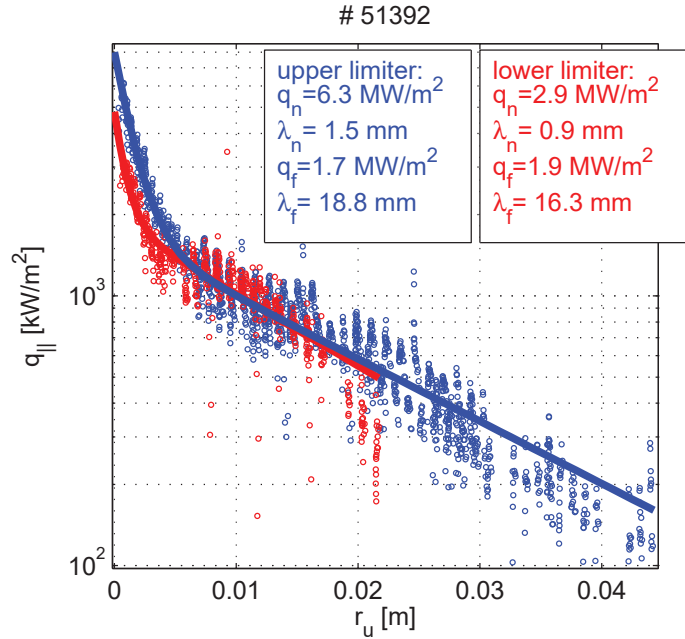


Figure 3.16: Parallel heat flux profile on the electron drift side (blue dots) and ion drift side (red dots). The fits with Eq. (3.8) are shown by continuous lines. The values of the fitting parameters are also displayed.

parallel heat flux radial profiles are shown by red and blue points for the ion and electron drift side, respectively. The fits with Eq. (3.8) are shown by solid lines, and the values of the fitting parameters are also displayed.

The $q_{||}(r_u)$ profiles are matching in the far SOL. The near SOL width is slightly reduced on the ion drift side, while its heat flux magnitude is reduced by a factor 2.

3.2.4 Parallel heat fluxes in Helium plasmas

The scans presented beforehand for D plasmas (I_p , $n_{e,av}$, κ) have been repeated for He plasmas. The presence of the near SOL has been observed in all parallel heat flux radial profiles, being $q_{||}(r_u)$ well described by a sum of two exponentials, except for one case. The observed trends with the plasma parameters are discussed in the following.

Plasma current scan in Helium

The plasma current has been varied between 85 kA (the lowest value achievable on TCV for vertical stability) and 210 kA. The plasma line averaged density $n_{e,av} = 2.5 \cdot 10^{19} \text{ m}^{-3}$ and the plasma shape $\kappa = 1.4$, $\delta = 0$ are kept constant for all the discharges in the scan. Contrarily to the D case, the near SOL does not vanish for the lowest I_p value (85 kA), even though its strength is decreased, as it is shown in Fig. 3.17. The near SOL does vanish for $I_p = 85$ kA and an increased density $n_{e,av} = 3.5 \cdot 10^{19} \text{ m}^{-3}$ (purple profile in Fig. 3.17). The parallel heat flux profile for this discharge is well described by a single exponential.

The variation of the fit parameters λ_n , λ_f , q_n and q_f with the plasma current I_p are shown in Fig. 3.18, where the corresponding results for D plasmas are shown for comparison. The main trends are summarized in the following:

- The far SOL width λ_f values are consistent with the D case, but the scaling $\lambda_f \propto 1/I_p$ [62] is not fulfilled. λ_f is approximately constant over the explored values of plasma current I_p .
- The near SOL width λ_n values are consistent with the D case. λ_n slightly decreases for $I_p < 100$ kA. The near SOL does not vanish for the lowest investigated current $I_p = 85$ kA.
- The near and far SOL parallel heat flux magnitude q_n and q_f increase linearly with the plasma current, as it is observed for D plasmas. The linear fits of $q_n(I_p)$ and $q_f(I_p)$ are shown in Fig. 3.18 with a red and a blue dashed line, respectively.

Plasma density scan in Helium

The plasma density has been varied between $2.2 \cdot 10^{19} \text{ m}^{-3}$ (line averaged value) and $5.3 \cdot 10^{19} \text{ m}^{-3}$. Plasma density is more difficult to control in He, and it has not been possible to achieve densities as low as in D plasmas ($1.2 \cdot 10^{19} \text{ m}^{-3}$). The plasma current $I_p = 140$ kA

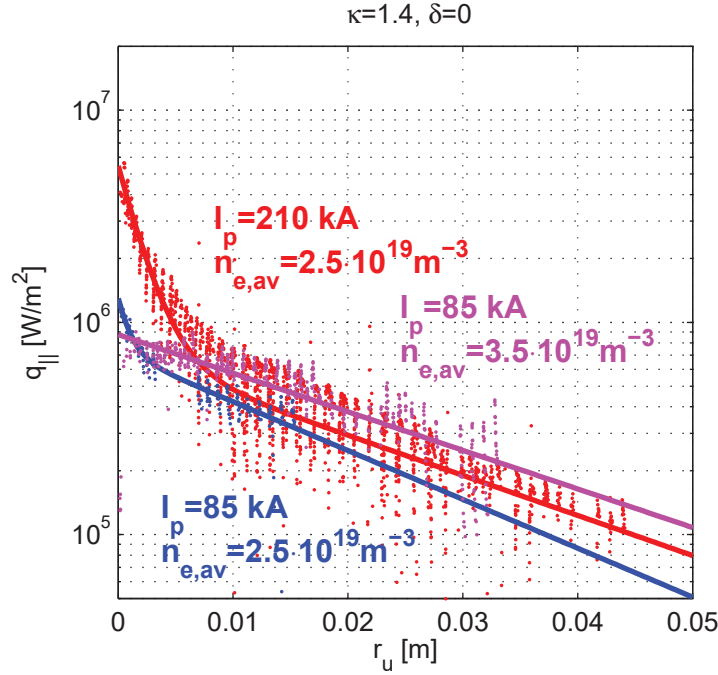


Figure 3.17: Parallel heat flux radial profiles $q_{||}(r_u)$ in He for $I_p = 210$ kA, $n_{e,av} = 2.5 \cdot 10^{19} \text{ m}^{-3}$ (red dots), $I_p = 85$ kA, $n_{e,av} = 2.5 \cdot 10^{19} \text{ m}^{-3}$ (blue dots) and $I_p = 85$ kA, $n_{e,av} = 3.5 \cdot 10^{19} \text{ m}^{-3}$ (magenta dots). The fit with Eq. (3.8) is shown with solid lines.

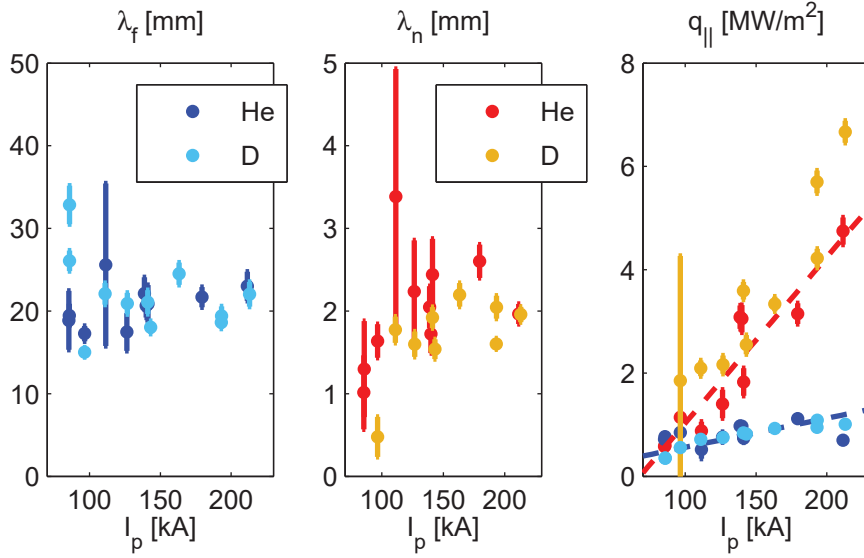


Figure 3.18: Dependence of the fit parameters λ_n , q_n (red), λ_f , q_f (blue) upon plasma current I_p in He plasmas. The linear fits of $q_n(I_p)$ (dashed red) and $q_f(I_p)$ (dashed blue) are displayed. The fit results for the corresponding D discharges are shown in orange (near SOL) and light blue (far SOL) for comparison.

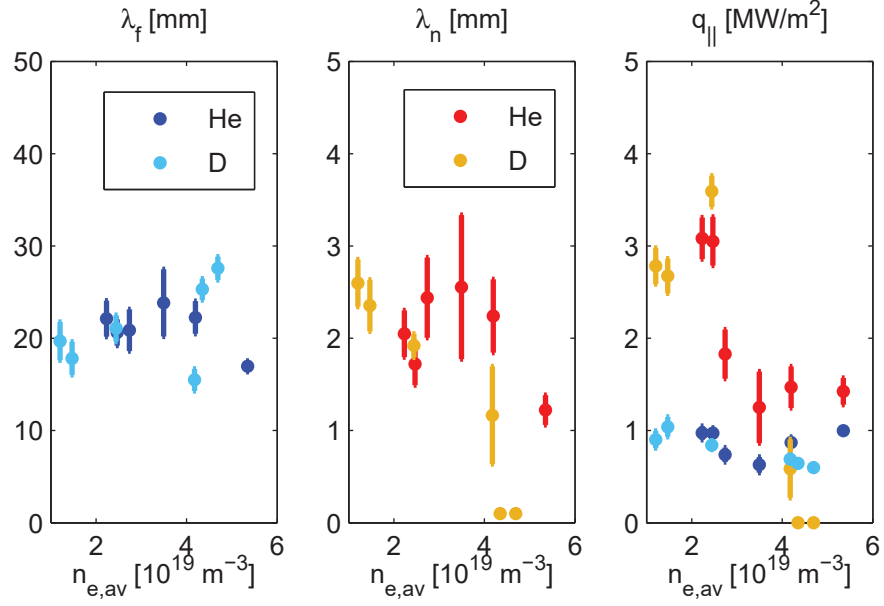


Figure 3.19: Dependence of the fit parameters λ_n , q_n (red), λ_f , q_f (blue) upon plasma density $n_{e,av}$ in He plasmas. The linear fits of $q_n(I_p)$ (dashed red) and $q_f(I_p)$ (dashed blue) are displayed. The fit results for the corresponding D discharges are shown in orange (near SOL) and light blue (far SOL) for comparison.

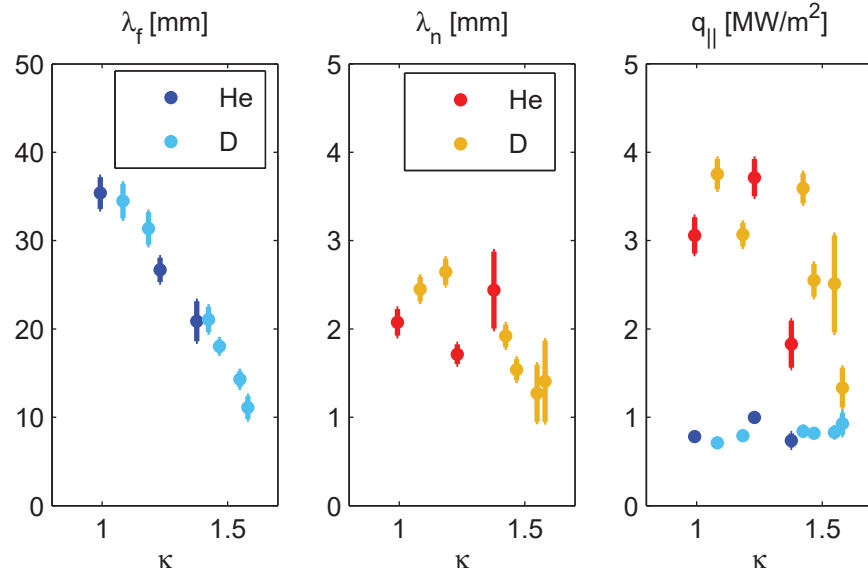


Figure 3.20: Dependence of the fit parameters λ_n , q_n (red), λ_f , q_f (blue) upon elongation κ in He plasmas. Linear fits of $\lambda_f(\kappa)$ and $\lambda_n(\kappa)$ are plotted as black dashed lines. The fit results for the corresponding D discharges are shown in orange (near SOL) and light blue (far SOL) for comparison.

and the plasma shape $\kappa = 1.4$, $\delta = 0$ are kept constant for all the discharges in the scan. The variation of the fit parameters λ_n , λ_f , q_n and q_f with the plasma current I_p are shown in Fig. 3.19, including the corresponding results for D plasmas for comparison. The main trends are summarized in the following:

- The far SOL width λ_f values are similar to the D case. However, λ_f is constant rather than increasing with $n_{e,av}$.
- The near SOL width λ_n values are consistent with the D case. λ_n is constant with $n_{e,av}$ decreasing only for high density ($n_{e,av} = 5.3 \cdot 10^{19} \text{ m}^{-3}$). Contrarily to the D case, the near SOL is not observed to vanish for high densities.
- The far SOL heat flux magnitude q_n is consistent with the D case. The near SOL heat flux magnitude q_n is consistent with the D case for intermediate densities ($n_{e,av} \sim 2.5 \cdot 10^{19} \text{ m}^{-3}$) and it rolls over for increasing densities. Contrarily to the D case, q_n does not vanish for high densities (within the explored range).

Elongation scan in Helium

The plasma elongation has been varied between 1 and 1.4. Elongations as high as in D plasmas ($\kappa = 1.6$) could not be achieved due to plasma vertical instability. The plasma current $I_p = 140 \text{ kA}$, line averaged density $n_{e,av} = 2.5 \cdot 10^{19} \text{ m}^{-3}$ and triangularity $\delta = 0$ are kept constant for all the discharges in the scan. The variation of the fit parameters λ_n , λ_f , q_n and q_f with the elongation κ are shown in Fig. 3.20, where the corresponding results for D plasmas are also shown for comparison. The trends are summarized in the following:

- The far SOL width λ_f decreases linearly with κ , consistently with observations in D plasmas. No clear trend is found for λ_n .
- The far SOL parallel heat flux magnitude q_f is constant with κ , consistently with observations in D plasmas. The decrease of q_n with increasing elongation, which can be explained with the increase of confinement with elongation [61] for constant heating power, starts at lower κ in He than in D plasmas.

3.2.5 Comparison of the near and far SOL widths with existing theoretical scalings

In Figure 3.21, we compare the SOL widths (near and far) resulting from the analysis of the parallel heat flux profiles with existing scalings, for both D and He discharges. In particular, in the left panel, the far SOL width λ_f is compared with the scaling proposed in Ref. [62], obtained from a quasi-linear (QL) model based on the gradient removal theory [65]. The scaling reads:

$$\lambda_{QL}[\text{m}] = 4.96 \cdot 10^{-4} \times n_{e0}^{0.07} T_{e0}^{0.06} R_0^{0.68} q_{95}^{0.84} B_\phi^{-0.38}, \quad (3.11)$$

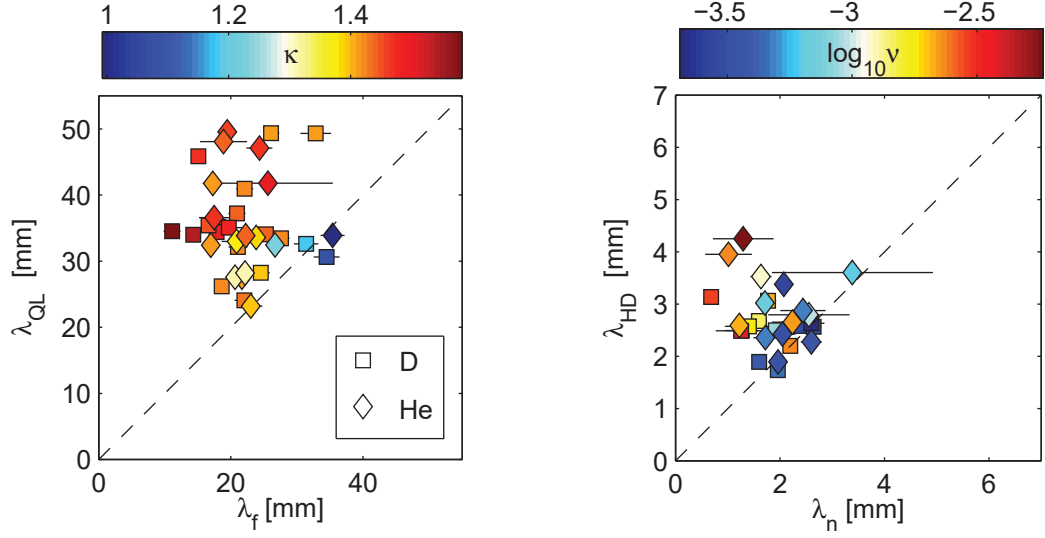


Figure 3.21: Left: comparison of the far SOL width λ_f with the scaling given in Eq. (3.11), for both D (squares) and He (diamonds) plasmas, color coded with the elongation κ . Right: comparison of the near SOL width λ_n with the scaling given in Eq. (3.12), for both D (squares) and He (diamonds) plasmas, color coded with the normalized resistivity ν .

where n_{e0} , T_{e0} are the plasma density and electron temperature at the LCFS, R_0 is the plasma major radius, q_{95} is the edge safety factor, and λ_{QL} is the predicted SOL width. All quantities are expressed in SI units, and the temperature is in eV units. The model that determines the scaling law is developed for circular plasmas. We use therefore for the comparison, instead of q_{95} , the cylindrical safety factor $q_{cyl} = q_{95}/\kappa$, i.e. the safety for a circular plasma, given only by its current and not by the shaping. Furthermore, the model is developed to describe a “classical” SOL, for which only one scale length is present.

As shown in the left panel of Fig. 3.21, there is an overall good agreement between the experimental data and the scaling predictions. The scaling predicts successfully the far SOL width for circular plasmas $\kappa \sim 1$, but it overestimates the far SOL width for shaped plasmas $\kappa \gtrsim 1.4$. This has to be considered as the main cause of the discrepancies between the experimental and the predicted values. In a second instance, as reported in section 3.2.3, an increase in elongation could lead to an improved confinement of the core plasma, leading to less power crossing the LCFS and an overall narrower SOL.

Another possible cause for the observed discrepancies is the fact that the experimental data are measured at the HFS, while the scaling is developed for a poloidally averaged SOL width. The predicted values being larger than the experimental ones could therefore be interpreted as an HFS/LFS asymmetry. This is consistent with a more ballooned type of transport at the OMP and with recent numerical simulations of the SOL [51].

In the right panel of Fig. 3.21, we compare the near SOL width λ_n with the so-called Heuristic-

Drift (HD) model [66]. This model has been originally developed for diverted H-mode plasmas. The main assumption is that, in this low-turbulence regime, the SOL width is determined by the competition of Bohm plasma flows towards the limiter plates ($v_{||} \sim c_s$) with cross field transport determined by the Pfirsch-Schluter currents, generated by the ∇B and curvature drifts. The resulting SOL width is predicted to be:

$$\lambda_{HD}[\text{m}] = 5671 \cdot P_{SOL}^{1/8} \frac{(1 + \kappa)^{5/8} a^{17/8} B^{1/4}}{I_p^{9/8} R_0} \left(\frac{2A}{Z^2(1 + Z)} \right)^{7/16} \left(\frac{Z_{eff} + 4}{5} \right)^{1/8}, \quad (3.12)$$

where P_{SOL} is the power entering the SOL, a is the plasma minor radius, A and Z are respectively the mass and atomic number for the plasma ions, and Z_{eff} is the plasma effective charge, taking into account the presence of impurities. All quantities are expressed in SI units. This scaling, despite having been derived for a different scenario (diverted H-mode), has been shown to describe satisfactorily the near SOL width for inboard-limited L-mode plasmas [67]. As shown in the right panel of Fig. 3.21, there is indeed an overall good agreement between the experimental data and the scaling predictions. The main discrepancies could be attributed to the combined effect of the plasma density and temperature, not included in Eq. (3.12). In the Figure, the points are color coded with the plasma normalized Spitzer resistivity ν , combining both the variation of density and temperature. This is defined as:

$$\nu = \frac{en_{e0}R_0\eta_{||}}{m_i c_{s0}} \propto n_{e0} T_{e0}^{-3/2}, \quad (3.13)$$

where e is the electron charge, n_{e0} , T_{e0} and c_{s0} the plasma electron density, temperature, and the ion sound speed respectively, all evaluated at the LCFS, m_i is the ion mass, R_0 is the plasma major radius (magnetic axis), and $\eta_{||}$ is the Spitzer resistivity [68].

Summarizing the results of this section, the far SOL width λ_f scales consistently with a QL model based on the gradient removal theory. The agreement is satisfactory for circular plasmas, while the theoretical scaling law tends to overestimate the SOL width for elongated plasmas, as the elongation is not included in the theoretical derivation.

The near SOL width λ_n is in agreement with the predictions of the HD model, which assumes a low turbulence level and cross-field transport determined by the Pfirsch-Schluter currents. The model does not describe satisfactorily the experimental measurements at high resistivities, since neither the plasma temperature nor the plasma density are taken into account in the scaling law.

Corrections to the scalings

In the following, we correct the QL and the HD scaling including the effects of elongation κ and resistivity ν , respectively. The evaluation of such corrections is performed through non-linear regressions over the database exposed beforehand (2016 experiments). The refined scalings

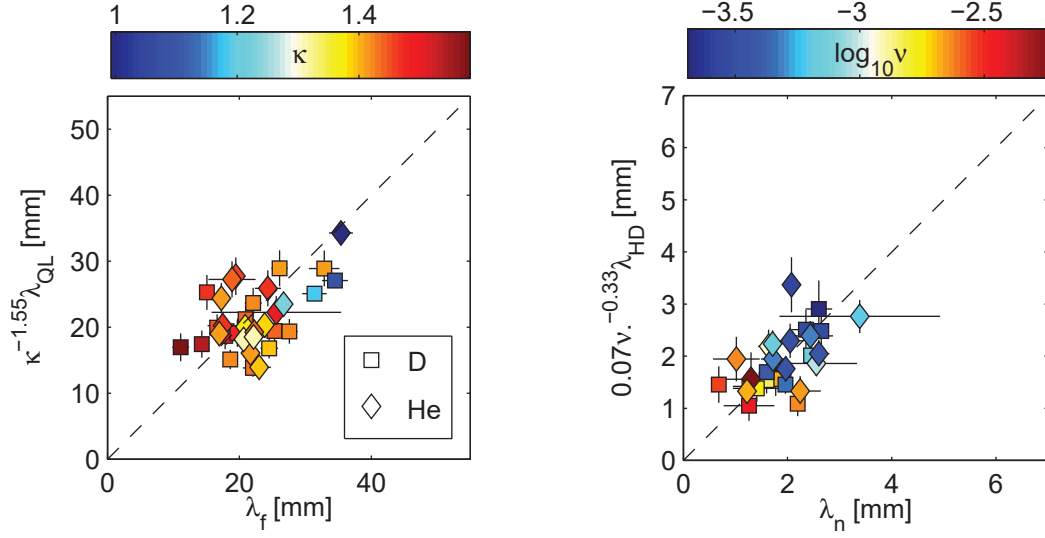


Figure 3.22: Left: comparison of the far SOL width λ_f with the scaling given in Eq. (3.14), for both D (squares) and He (diamonds) plasmas, color coded with the elongation κ . Right: comparison of the near SOL width λ_n with the scaling given in Eq. (3.15), for both D (squares) and He (diamonds) plasmas, color coded with the normalized resistivity ν .

for the near and far SOL widths, respectively, read:

$$\lambda_f = \kappa^{-1.55} \lambda_{QL}, \quad (3.14)$$

$$\lambda_n = 0.07 \nu^{-0.33} \lambda_{HD}, \quad (3.15)$$

where λ_{QL} and λ_{HD} are given in Eq. (3.11) and Eq. (3.12), respectively. The experimental data are compared with the refined scalings in Eqs. (3.14,3.15) in Fig. 3.22, showing a better agreement.

3.2.6 Power in the near SOL and correlation with resistivity and collisionality

Following Ref. [23], the power entering the SOL can be computed as

$$P_{SOL} = 2\pi R_{LCFS} \frac{B_{\theta,u}}{B_{\phi,u}} \int_0^\infty 2q_{||}(r_u) dr_u, \quad (3.16)$$

where R_{LCFS} is the major radius of the LCFS at the outer midplane, $B_{\theta,u}$ and $B_{\phi,u}$ are the poloidal and toroidal components, respectively, of the magnetic field at the outer midplane. $q_{||}(r_u)$ is the parallel heat flux radial profile measured on one side of the limiter and remapped upstream. The factor two inside the integral accounts for the heat deposition on the two sides of the limiter (upper and lower), assumed to be equal.

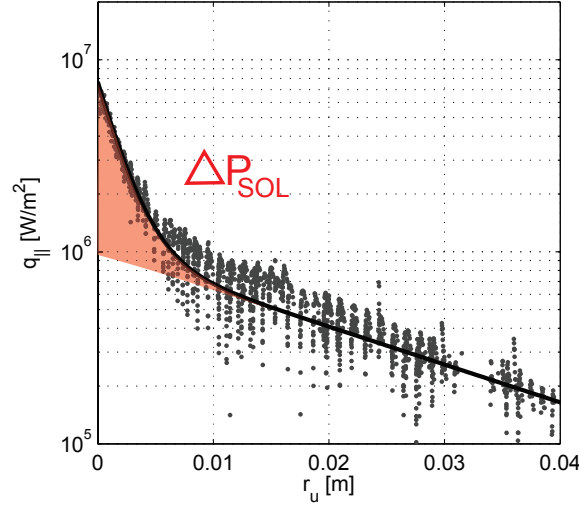


Figure 3.23: Schematics of the power entering the near SOL, ΔP_{SOL} . A parallel heat flux radial profile $q_{||}(r_u)$ is shown (grey dots), together with the fit with Eq. (3.8). ΔP_{SOL} corresponds to the integral of the red-shaded area.

Similarly, we define the power entering the near SOL as:

$$\Delta P_{SOL} = 4\pi R_{LCFS} \frac{B_{\theta,u}}{B_{\phi,u}} \int_0^\infty [q_{||}(r_u) - q_{||,f}(r_u)] dr_u. \quad (3.17)$$

In Eq. 3.17, $q_{||,f}(r_u)$ is obtained by extrapolating the parallel heat flux profile in the far SOL up to the LCFS. In the formalism used in this thesis, $q_{||,f}(r_u) = q_f \exp(-r_u/\lambda_f)$. The power entering the near SOL is represented in Fig. 3.23 by the shaded area. In the experiments presented in section 3.1.1, the parallel heat flux profiles have been fitted with Eq. (3.9). In this case the power entering the SOL is given by:

$$\begin{aligned} \Delta P_{SOL} &= 4\pi R_{LCFS} \frac{B_{\theta,u}}{B_{\phi,u}} \int_0^{r_0} (q_n e^{-r_u/\lambda_n} - q_f e^{-r_u/\lambda_f}) dr_u \\ &= 4\pi R_{LCFS} \frac{B_{\theta,u}}{B_{\phi,u}} \left[q_n \lambda_n (1 - e^{-r_0/\lambda_n}) - q_f \lambda_f (1 - e^{-r_0/\lambda_f}) \right], \end{aligned} \quad (3.18)$$

where r_0 is the radial position of the break point. If the parallel heat flux radial profile $q_{||}(r_u)$ is described by a sum of two exponentials (Eq. (3.8)), as it is the case for the experiments introduced in section 3.1.2, the power entering the near SOL is given by

$$\Delta P_{SOL} = 4\pi R_{LCFS} \frac{B_{\theta,u}}{B_{\phi,u}} \int_0^\infty q_n e^{-r_u/\lambda_n} dr_u = 4\pi R_{LCFS} \frac{B_{\theta,u}}{B_{\phi,u}} q_n \lambda_n. \quad (3.19)$$

In the following, we use ΔP_{SOL} as a measure of the “strength” of the near SOL. In Ref. [58], a nonlinear regression with the plasma parameters of ΔP_{SOL} has been performed for the 2013

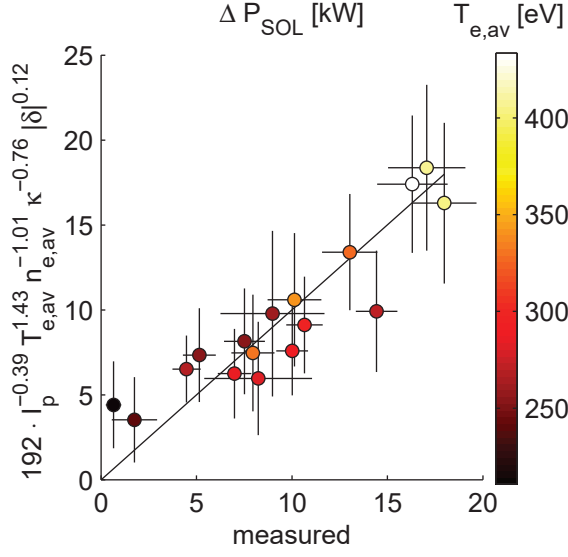


Figure 3.24: Empirical scaling of ΔP_{SOL} with the plasma parameters for the 2013 experiments, first presented in ref. [58]. The power in the near SOL scales mainly as $\Delta P_{SOL} \propto T_e^{3/2} n_e^{-1}$.

experiments (section 3.1.1), showing that ΔP_{SOL} is well described by the empirical scaling

$$\Delta P_{SOL} [kW] = 192 T_{e,av}^{1.43} n_{e,av}^{-1.01} I_p^{-0.39} \kappa^{-0.76} |\delta|^{0.12}. \quad (3.20)$$

The empirical scaling (Eq. (3.20)), shown in Fig. 3.24, has its main dependence on temperature and density, and can be approximated by $\Delta P_{SOL} \propto T_e^{3/2} n_e^{-1} \propto \nu^{-1}$, where ν is the normalized Spitzer resistivity (Eq. (3.13)).

The relationship $\Delta P_{SOL} \propto 1/\nu$ is confirmed for all experiments exposed in this thesis (D, He). In the top panel of Fig. 3.25, ΔP_{SOL} is plotted for all the discharges against the normalized resistivity ν . The curve $\Delta P_{SOL}(\nu) \propto 1/\nu$ is plotted in black. The resistivity is here computed using the plasma electron density and temperature resulting from Thomson scattering measurements, averaged in the edge region $0.9 < \rho < 1$, where ρ is the normalized poloidal flux coordinate ($\rho = 1$ at the LCFS). This method is preferred rather than using n_e and T_e measurements at the LCFS from the RP since this diagnostic was not available for the first set of experiments (2013). The resistivity used here provides an underestimate of the normalized resistivity defined in Eq. (3.13), since the temperature we used is larger than the temperature at the LCFS. As it is visible from the top panel of Fig. 3.25, a smooth transition occurs for high resistivities ($\nu \sim 10^{-2}$) to a regime where no near SOL steep gradients are present.

In the bottom panel of Fig. 3.25, ΔP_{SOL} is plotted for all the discharges against the SOL collisionality [10]

$$\nu^* = L/\lambda_{ee} = 10^{-16} n_{e0} [m^{-3}] \frac{L}{T_{e0} [eV]^2}, \quad (3.21)$$

where $L = 2\pi R_0 q_{edge}$ is the connection length and λ_{ee} is the electron-electron collisional

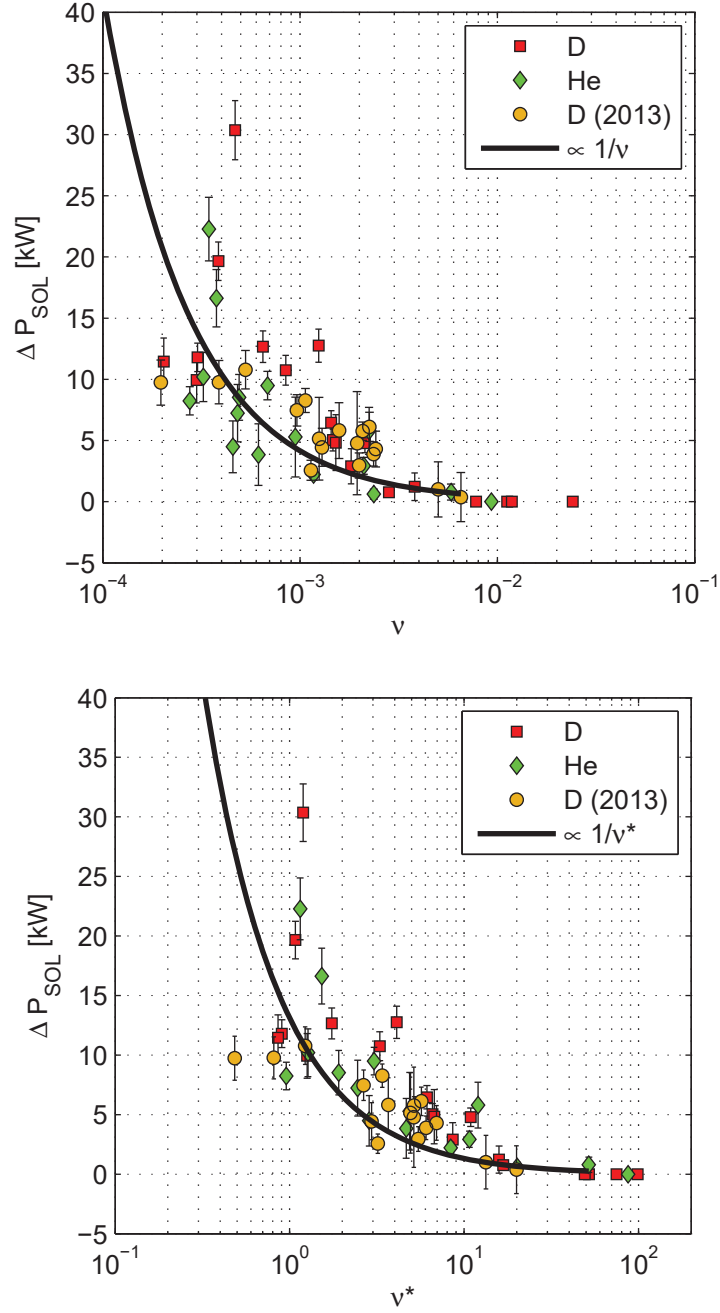


Figure 3.25: The power in the near SOL ΔP_{SOL} as a function of the normalized resistivity ν (top panel), and of the collisionality ν^* (bottom panel). The results from the D (squares) and He (diamonds) experiments are plotted together with results from 2013 D experiments (circles), for which ΔP_{SOL} was evaluated with a different method. The lines $\Delta P_{SOL} \propto 1/\nu$ (top panel) and $\Delta P_{SOL} \propto 1/\nu^*$ (bottom panel) are plotted in black.

mean free path. The collisionality is defined as the ratio of the electron collision frequency to the electron bounce frequency [7]. The bounce frequency is the frequency at which electrons trapped on banana orbits oscillate back and forth between the turning points. When $\nu^* \gg 1$, collisionality is too large to permit the electrons to behave in this ‘neoclassical’ way.

As it has been done for the resistivity ν , the collisionality ν^* plotted in Fig. 3.25 is computed using the average edge ($0.9 < \rho < 1$) electron temperature and density from Thomson scattering. As shown in Fig. 3.26, the normalized Spitzer resistivity ν and the SOL collisionality ν^* are correlated, but ν^* provides some additional physical insight since it determines the transition between different regimes in the SOL, as explained in the following.

The two-point model and the different SOL regimes

The two-point model [10] is a 1D model of the SOL relating the upstream density and temperature, $n_{e,u}$ and $T_{e,u}$, to the density and temperature at the target (limiter, divertor), $n_{e,t}$ and $T_{e,t}$. The main assumptions of the model are that, within a flux tube, the particle flux and the total plasma pressure $P = 2n_e k_b T_e + n_e m_i v_{||}^2$ are conserved, and that the heat is transported by parallel heat conductivity. The last assumption results in the relationship

$$T_{e,u}^{7/2} = T_{e,t}^{7/2} = + \frac{7}{2} q_{||} \frac{L}{\kappa_{0e}}, \quad (3.22)$$

where $q_{||}$ is the parallel heat flux, assumed to enter the SOL entirely upstream, and κ_{0e} is the electron parallel conductivity coefficient. The ratio of the target temperature to the upstream temperature can be expressed as a function of collisionality (Eq. 5.109 of Ref. [10]):

$$\frac{T_{e,u}}{T_{e,t}} \approx 2.3 \cdot 10^{-3} \left(\frac{\nu^*}{1 - f_{power}} \right)^2, \quad (3.23)$$

where f_{power} is the power loss fraction accounting for volumetric losses in the SOL. Following Ref. [10], we assume here $f_{power} = 1/2$. The ratio $T_{e,u}/T_{e,t}$, i.e. ν^* , determines different regimes for the SOL. In limited configuration, these regimes are:

- The “sheath limited” regime ($\nu^* \lesssim 10$). In this regime, the plasma heat conductivity, i.e. the parallel gradients (along the field line) of temperature, $\nabla_{||} T_e$, are negligible, and the temperature upstream $T_{e,u}$ and at the target $T_{e,t}$ are basically equal. Since no ionization is present within the SOL, cross-field transport from the main plasma provides the only particle source in the SOL. No volumetric recombination and neutral friction occur in the SOL, and the plasma sheaths at the target plates are the only particle and heat sinks.
- The “conduction limited” regime ($\nu^* \gtrsim 15$). In this regime, the plasma heat conductivity, i.e. $\nabla_{||} T_e$, is no longer negligible, leading to $T_{e,t} < T_{e,u}$. The total pressure is still conserved along the field lines. As $T_{e,t}$ decreases, the particle flux (and i.e. the plasma density) at the target increases. The plasma ion outflow to the target is balanced by the inflow of neutrals released from the solid surface (steady-state recycling).

In diverted configurations, two more SOL regimes are achievable:

- The “high recycling” regime ($\nu^* \gtrsim 15$). Similarly to the conduction-limited regime, strong parallel gradients of temperature develop. The main difference with the conduction limited regime is the high value of ν^* being determined by a large density, rather than by a low temperature.
- The “detached” regime ($\nu^* \gtrsim 85$). In this regime, ∇T_e is so large that the temperature at the target can drop down to a few eV. Here, neutral physics become important, and processes such as recombination and frictional drag by neutrals play a major role. A neutral cushion forms in front of the target, resulting in strongly decreased particle/heat fluxes to the solid surfaces.

The actual values of ν^* determining the transitions between the different regimes depend on the the ratio $T_{e,u}/T_{e,t}$ regarded as the threshold for the transition, and on the power loss fraction f_{power} .

The near SOL disappears in conduction limited regime

As shown in the bottom panel of Fig. 3.25, a substantial decrease in ΔP_{SOL} is observed for $\nu^* \gtrsim 15$, corresponding to the transition to the conduction limited regime. The transition to the near SOL-free regime happens for $\nu^* \sim 40$.

Using the Greenwald fraction to parametrize the near SOL

The power in the near SOL has been shown to depend strongly on the plasma current I_p and the plasma density $n_{e,av}$. A useful parameter combining these two quantities, widely used in tokamak physics, is the Greenwald fraction:

$$f_G = n_{e,av}/n_G = n_{e,av} \left(\frac{I_p}{\pi a^2} \right)^{-1}, \quad (3.24)$$

where $n_G = I_p/\pi a^2$ is the Greenwald density and a is the plasma minor radius. In ohmically heated plasmas, such as those exposed in this thesis, the temperature is determined mainly by the plasma current. In this case, ν , ν^* and f_G are strongly correlated, as it is shown in Fig. 3.26. Even though from the physical point of view the normalized resistivity and the collisionality are more meaningful quantities, one could correlate the SOL strength ΔP_{SOL} to the more practical engineering parameter f_G . It could hence be stated that ΔP_{SOL} decreases with f_G and vanishes at sufficiently high Greenwald fractions $f_G \gtrsim 0.5$.

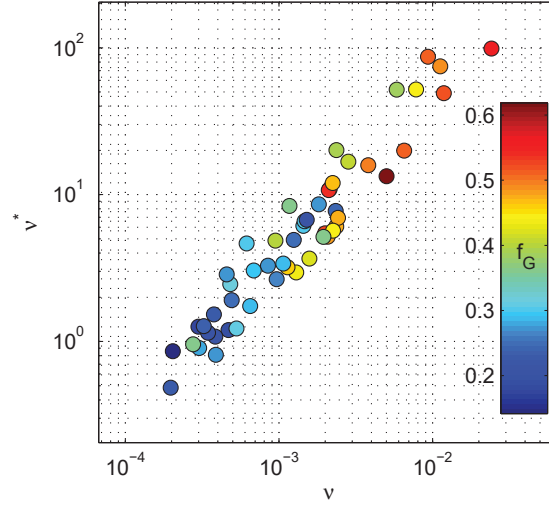


Figure 3.26: Correlation between the normalized resistivity ν , the SOL collisionality ν^* and the Greenwald fraction f_G , plotted for all the discharges discussed in this thesis. .

3.3 Non-ambipolar currents flowing to the limiter

The presence of non-ambipolar currents in the near SOL of inboard limited plasmas has been first reported in COMPASS [69]. The contribution of the non-ambipolar currents, measured both in the ion and electron-drift sides of the limiter, to the deposited heat fluxes has been evaluated in Ref. [69]. As a conclusion, such currents were judged not to be the cause of the enhanced heat flux in the near SOL. To have a better understanding of the role of non-ambipolar currents in the formation of the near SOL, we perform measurements of such currents in TCV limited plasmas. The measurements are performed at the limiter using flush mounted Langmuir probes (LP).

In TCV, the plasma parameters are monitored at the HFS by the flush mounted LP embedded in the limiter. The probes were operated in swept mode in the experiments introduced in section 3.1.1, while in the experiments introduced in section 3.1.2, they were operated in I_{sat} and V_{fl} mode (every other probe). A sweep in the plasma vertical position was introduced to increase the spatial resolution. The ion saturation current and electron temperature tend to be overestimated by the fitting of the I-V curve at grazing incidence [39] (which is the case close to the contact point of a limited plasma), but the estimate of the floating potential is still reliable, since it is a direct measurement (the probe potential for which the measured current is zero). A comparison between the V_{fl} measurements obtained with the two different methods is shown in Fig. 3.27. A typical high spatial resolution V_{fl} profile obtained with the probe in floating mode (blue dots) is compared with the profile obtained from the I-V fit (light blue diamonds) for plasmas with comparable parameters ($I_p = 190$ kA, $\kappa = 1.4$, $\delta = 0$, $n_{e,av} = 2.5 \cdot 10^{19} \text{ m}^{-3}$). The two profiles are in good agreement.

In the outer part of the far SOL, the floating potential is equal to the limiter potential ($V = 0$). Approaching the LCFS, V_{fl} increases up to $V_{fl,max} \sim 10$ V. Entering the near SOL, the floating

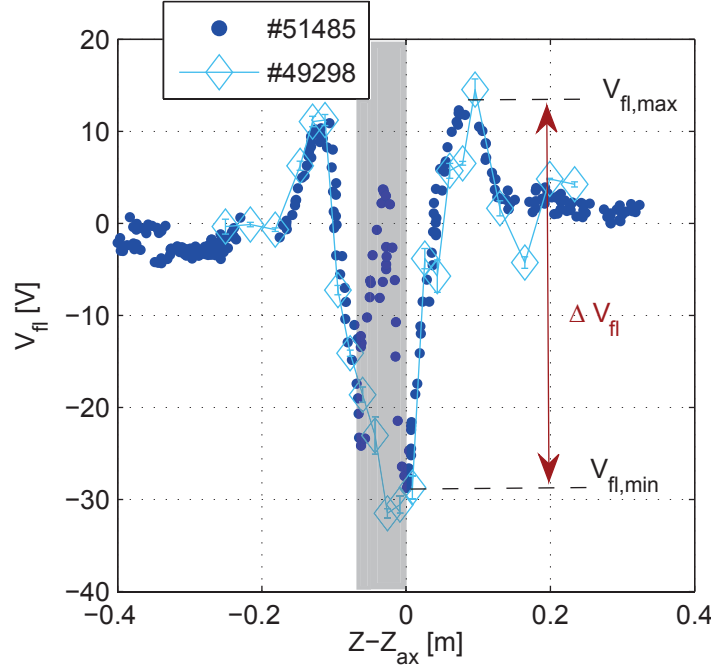


Figure 3.27: Floating potential profile along the vertical direction of the limiter for a discharge with probes operated in floating mode (blue dots) and in swept mode (light blue diamonds). The grey shaded area identifies the region shadowed by the neighboring tile. The maximum and the minimum of the floating potential on the upper side of the limiter $V_{fl,max}$, $V_{fl,min}$ and the potential drop in the SOL $\Delta V_{fl,max}$ are indicated. .

potential starts to decrease and changes sign, reaching high negative values at the contact point, $V_{fl,min} \sim -20$ V. A non-zero floating potential is the result of non-ambipolar currents flowing to the limiter, and the sign of the floating potential is given by the sign of the non-ambipolar currents, as explained in section 2.4.

In the following, we use the floating potential as a proxy for non-ambipolar currents. We parametrize the non-ambipolar currents with the floating potential drop in the SOL, that we define as

$$\Delta V_{fl} = V_{fl,max} - V_{fl,min} , \quad (3.25)$$

where $V_{fl,max}$ and $V_{fl,min}$ are respectively the maximum and minimum value of V_{fl} in the SOL, measured in the upper part of the limiter (electron drift side). This is schematically illustrated in Fig. 3.27.

In all the discharges discussed beforehand exhibiting a near SOL in the $q_{||}(r_u)$ profiles, a floating potential drop in the near SOL has been measured, indicating the presence of non-ambipolar currents flowing to the limiter. The variation of the floating potential radial profiles with the plasma current and density is shown in Fig. 3.28, where $V_{fl}(r_u)$ is plotted for different values of I_p and $n_{e,av}$. The intensity of the floating potential drop, related to non-ambipolar currents, increases with I_p and decreases with $n_{e,av}$, as can be seen in the figure.

3.3. Non-ambipolar currents flowing to the limiter

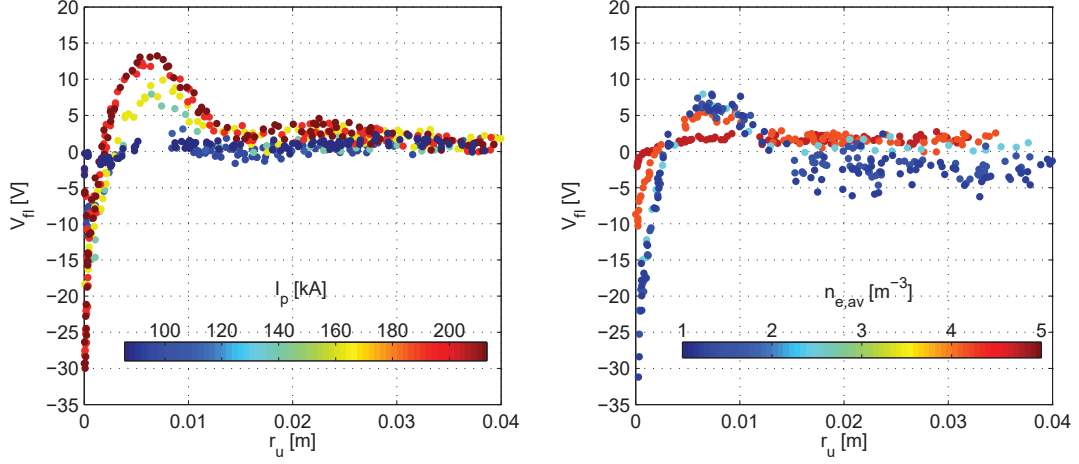


Figure 3.28: Floating potential profile remapped upstream $V_{fl}(r_u)$ for the I_p scan (left), $\kappa = 1.4$, $\delta = 0$, $n_{e,av} = 2.5 \cdot 10^{19} \text{ m}^{-3}$, and for the $n_{e,av}$ scan (right), $I_p = 140 \text{ kA}$, $\kappa = 1.4$, $\delta = 0$ (D plasmas).

The non-ambipolar currents (ΔV_{fl}) are observed to vanish in the case where no near SOL is measured in the parallel heat flux profiles, i.e. for the lowest current in the I_p scan, $I_p = 85 \text{ kA}$, and for the highest density in the density scan $n_{e,av} = 4.7 \cdot 10^{19} \text{ m}^{-3}$.

ΔV_{fl} is found to be correlated with the strength of the near SOL, ΔP_{SOL} , as shown in Fig. 3.29, where ΔP_{SOL} is plotted against ΔV_{fl} , color coded with the normalized resistivity ν , for both D and He plasmas. For He plasmas, a larger ΔV_{fl} , associated with increased non-ambipolar currents, is measured for the same power in the near SOL, ΔP_{SOL} .

We remark that, similarly to what observed for the power in the near SOL ΔP_{SOL} , the drop

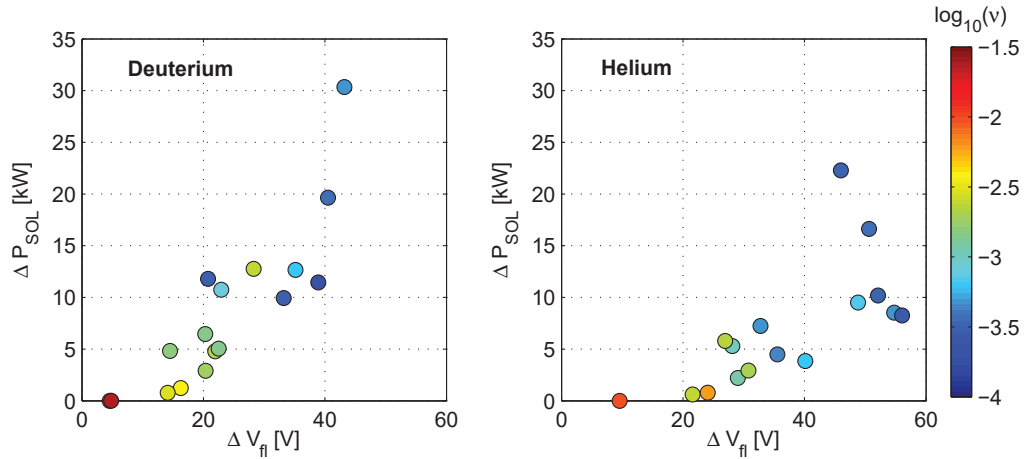


Figure 3.29: Power in the near SOL ΔP_{SOL} as a function of the floating potential drop ΔV_{fl} , color-coded with the normalized resistivity $\log_{10}(\nu)$, for D plasmas (left) and He plasmas (right).

in the floating potential ΔV_{fl} decreases with the normalized resistivity $\nu \propto n_e T_e^{-3/2}$. In the plasma current scan (left panel of Fig. 3.28), the ν variation is mostly attributed to the increase of the electron temperature T_e with I_p , since the density is approximately constant for all the (ohmically heated) discharges in the scan. We recall that the normalized resistivity ν is here computed using the edge-averaged ($\rho > 0.9$) electron temperature T_e from Thomson scattering measurements. Consistently, a similar trend of increasing T_e at the LCFS with the plasma current I_p is observed in reciprocating probe data.

3.3.1 Role of the velocity shear layer

The $\mathbf{E} \times \mathbf{B}$ drift velocity $\mathbf{v}_{E \times B} = \frac{\mathbf{E} \times \mathbf{B}}{B^2}$ in the SOL is mainly in the poloidal direction, since the electric field is mostly in the radial direction $\mathbf{E} \approx E_r \hat{r}$ and the magnetic field can be approximated by its toroidal component $\mathbf{B} \approx B_\phi \hat{\phi}$, where \hat{r} and $\hat{\phi}$ are the unit vectors of the radial and toroidal coordinate, respectively. We can hence approximate $\mathbf{v}_{E \times B}$ with its poloidal component:

$$\mathbf{v}_{E \times B} = \frac{\mathbf{E} \times \mathbf{B}}{B^2} \approx \frac{E_r \hat{r} \times B_\phi \hat{\phi}}{B^2} \approx -\frac{E_r}{B} \hat{\theta} = v_\theta \hat{\theta}, \quad (3.26)$$

where we approximated $B_\phi \approx B$, $\hat{\theta}$ is the unit vector of the poloidal coordinate, and $v_\theta = -E_r/B$ is the poloidal $\mathbf{E} \times \mathbf{B}$ velocity. The radial shear of the poloidal velocity is given by:

$$v'_\theta \equiv \frac{\partial v_\theta}{\partial r} \approx -\frac{1}{B} \frac{\partial E_r}{\partial r} = \frac{1}{B} \frac{\partial^2 V_{pl}}{\partial r^2}, \quad (3.27)$$

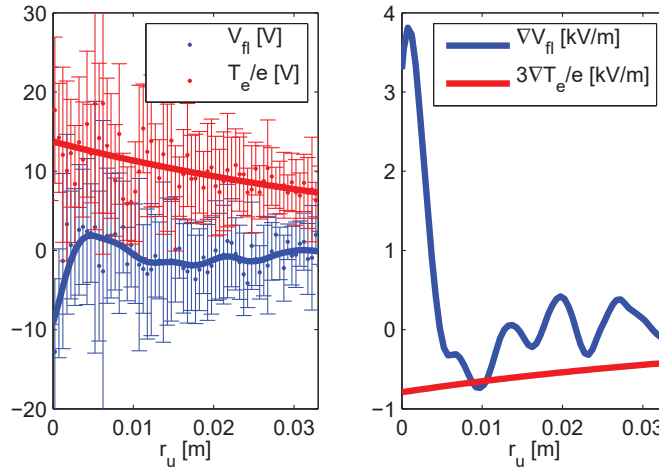


Figure 3.30: Left: radial profiles of floating potential $V_{fl}(r_u)$ (blue) and electron temperature $T_e(r_u)/e$ (red) from LP measurements. The smoothed $V_{fl}(r_u)$ profile (thick blue) and the fit of the $T_e(r_u)/e$ profile with an exponential (thick red) are also shown. Right: radial gradients of $V_{fl}(r_u)$ (blue) and $3T_e(r_u)/e$ (red).

where we neglected the dependence of B upon the radial coordinate r , and we used the relationship $E_r = -\partial V_{pl}/\partial r$, with V_{pl} being the plasma potential. The plasma potential is related to the floating potential by Eq. (2.12), namely $V_{pl} = V_{fl} + \Lambda T_e$. In the near SOL, we observe a strong variation of the floating potential, happening on a scale length comparable with the near SOL parallel heat flux decay length λ_n . We assume that the radial gradient of the electron temperature is small with respect to the radial gradient of V_{fl} . To support this assumption, in Fig. 3.30 we compare the two contributions to the radial gradient of the plasma potential ∇V_{pl} , i.e. the contribution of the floating potential ∇V_{fl} and of the temperature $\Lambda \nabla T_e$ ($\Lambda = 3$ for Deuterium plasmas). On the left of the figure, the radial profile of floating potential $V_{fl}(r_u)$ (blue) and electron temperature $T_e(r_u)$ (red) are shown. The profiles are obtained using LP operated in swept mode. The smoothed $V_{fl}(r_u)$ profile (thick blue) and the fit of the $T_e(r_u)$ profile with an exponential (thick red) are also shown. In the right panel of Fig. 3.30, the radial gradients of the smoothed V_{fl} profile is finally compared with three times the radial gradient of the (fitted) T_e profile (we recall that $V_{pl} = V_{fl} + \Lambda T_e$, where $\Lambda \cong 3$). We can conclude that in the near SOL the approximation $\nabla V_{fl} \gg 3 \nabla T_e$ is appropriate. Equation (3.27) can then be rewritten as:

$$v'_\theta \approx \frac{1}{B} \frac{\partial^2 V_{fl}}{\partial r^2} \approx \frac{\Delta V_{fl}}{B \lambda_n^2}. \quad (3.28)$$

The potential drop in the SOL ΔV_{fl} can hence be considered, in a first approximation, as a proxy for the velocity shear.

The results presented in section 3.3 can then be interpreted in the following way: the presence of the near SOL ΔP_{SOL} is correlated with the presence of a radial shear in the $\mathbf{E} \times \mathbf{B}$ velocity. This interpretation is consistent with a recent theoretical model of the near SOL, presented in Ref. [70], and summarized in the following.

Turbulence suppression by velocity shear

Sheared flows can substantially affect turbulence in magnetically confined plasmas, the most relevant case being the spontaneous formation of the high-confinement barrier at the edge of tokamak plasmas (H-mode). The turbulence is suppressed when the shearing rate of the $\mathbf{E} \times \mathbf{B}$ velocity v'_θ (defined in Eq. (3.27)) is of the order of (or larger than) the linear growth rate of the turbulent modes. The same mechanism can be invoked to explain the formation of the near SOL in limited plasmas. Indeed in the edge region (inside the LCFS), the radial electric field E_r is always negative. Conversely, in the SOL the relationship $V_{pl} \sim 3T_e$ holds, so the temperature profile of the typical form $T_e = T_{e0} \exp(-r_u/\lambda_T)$ results in a positive E_r . The radial electric field has then to change sign across the LCFS, resulting in a shear of the poloidal $\mathbf{E} \times \mathbf{B}$ velocity. In the near SOL, the shearing rate v'_θ is larger than the ballooning growth rate $\gamma_b \sim c_s/R_0 \sqrt{2R_0/L_p}$ ($\gamma_b \sim 3.6 \cdot 10^5 \text{ s}^{-1}$ for a typical TCV discharge), resulting in the suppression of the turbulence. In this case, the width of the near SOL λ_n can be derived starting from the vorticity balance equation Eq. (2.21), corresponding to a balance between the parallel and perpendicular components of the plasma current, $j_{||}$ and j_\perp . The

parallel (non-ambipolar) currents $j_{||} = enc_s \exp(eV_{fI}/T_e)$ are compensated by a polarization contribution, namely $\{\phi, \omega\}/B$. In the cold ion approximation ($\tau = 0$), the perturbed vorticity $\tilde{\Omega}$ can be estimated in terms of the perturbed plasma potential \tilde{V}_{fI} as $\tilde{\Omega} = -k_{\perp}^2 \tilde{V}_{fI}$, where $k_{\perp} \sim k_r \sim k_{\theta}$ is the perpendicular wave number (close to the LCFS the turbulent eddies are assumed to have comparable sizes in the radial and poloidal directions). The balance between the perpendicular and parallel particle flows results finally in an estimate of λ_n :

$$\lambda_n \sim \frac{1}{2k_{\perp}} \left(\frac{q}{\rho^*} \right)^{1/4}, \quad (3.29)$$

where $\rho^* = \rho_s/R_0$. As a secondary result of this model, the strength of the currents flowing to the limiter can directly be related to k_{\perp} (by balancing the perpendicular and parallel flows). We point out that the suppression of turbulence by the velocity shear, steepening the gradients in the near SOL, is compatible with the hypothesis underlying the heuristic drift model, discussed in section 3.2.5.

3.4 Steady state profiles at the outer midplane

In the following, we discuss the radial profiles of $q_{||}$ and V_{fI} at the outer midplane (OMP) and we compare them with those at the HFS that have been discussed earlier in this chapter. The profiles at the OMP are obtained from RP measurements. The floating potential V_{fI} is measured by several pins on the probe head. We focus on the floating potential measured by the “middle” pin #2 (see Fig. 2.26). An example of V_{fI} measurement from the RP is shown in Fig. 3.31, where the floating potential is plotted as a function of the distance from the LCFS r_u (continuous line). The bin-averaged data are shown with blue diamonds, and the V_{fI} measured at the HFS by the LP (remapped upstream) is shown with red diamonds.

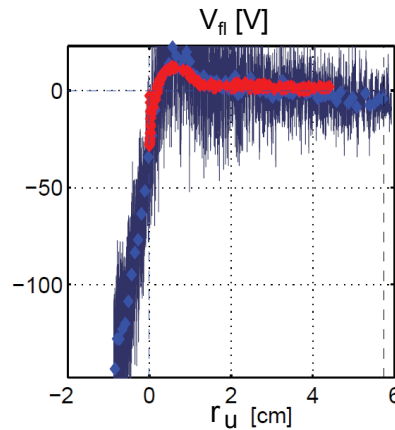


Figure 3.31: Radial profile of $V_{fI}(r_u)$ measured by the RP (continuous line) for discharge #51485 ($I_p = 190$ kA, $n_{e,av} = 2.5 \cdot 10^{19} \text{ m}^{-3}$, $\kappa = 1.4$, $\delta = 0$). Bin-averaged data are shown with blue diamonds. $V_{fI}(r_u)$ measured by LP at the HFS is shown with red diamonds.

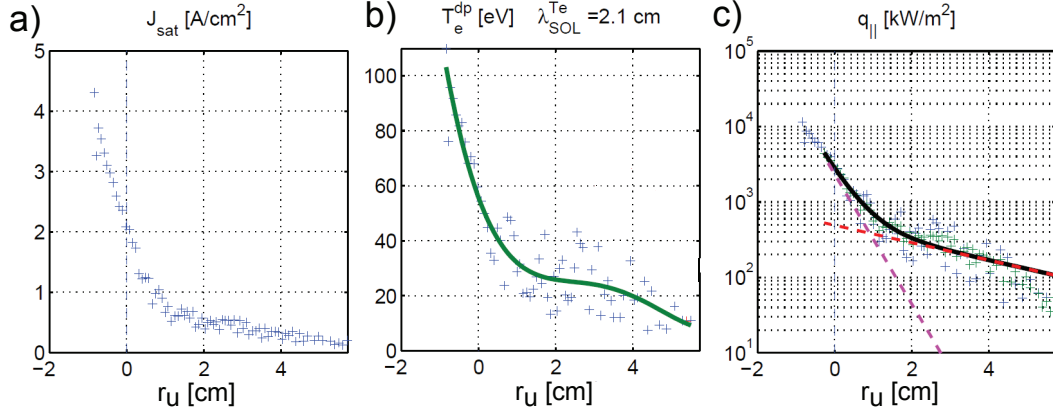


Figure 3.32: Radial profiles of ion saturation current density J_{sat} (a), electron temperature T_e (b) and parallel heat flux $q_{||}$ (c) computed from RP data, all shown by blue crosses. The smoothed temperature profile is shown with a green continuous line. In c), $q_{||}$ computed using the smoothed temperature is shown with green crosses. The fit of $q_{||}(r_u)$ with Eq. (3.8) is shown with a black line. The heat fluxes associated with the near and far SOL are plotted with a magenta and red dashed line, respectively.

The determination of the LCFS radial position at the OMP is quite delicate and several methods could be applied. Indeed, the magnetic reconstruction given by LIUQE can be subject to errors of the order of several mm, i.e. larger than the size of the near SOL λ_n . Other methods that do not rely on the magnetic reconstruction consist, e.g., in locating the LCFS at the position where the plasma potential V_{pl} is maximum, or where the poloidal velocity of the fluctuation, computed via cross-correlation of poloidally separated pins signals, changes its sign. In the following, the choice has been made to shift the LCFS so that the remapped $V_{f1}(r_u)$ profiles measured at the HFS and LFS superimpose. For the database used in this thesis, the applied radial shift is $-17 \leq \Delta r_u [mm] \leq 2.5$, the average value being $\langle \Delta r_u \rangle = 2.3$ mm.

The electron temperature T_e and the ion saturation current I_{sat} are determined by fitting the I-V curves from the double probe with Eq. (2.14). The ion saturation current density is given by $J_{sat} = I_{sat} / A_p$, where A_p is the pin projected collecting area. An example of the J_{sat} and T_e profiles resulting from the fit procedure is shown in Fig. 3.32 (a,b) respectively. Since, as seen in Fig. 3.32b, the temperature measurements are, in general, quite noisy (blue crosses), a smoothing procedure is applied to the profile $T_e(r_u)$. The smoothed profile is shown in Fig. 3.32b with a green line. The parallel heat flux is finally computed with Eq. (2.13), using the smoothed T_e profile. The resulting $q_{||}(r_u)$ profile is shown in Fig. 3.32c with green crosses. The $q_{||}(r_u)$ profile computed using the raw T_e measurements is shown with blue crosses for comparison.

Similarly to the procedure adopted to fit the profiles obtained by IR thermography, $q_{||}(r_u)$ is fitted with a sum of two exponentials (Eq. 3.8). The result of the fit is plotted with a black line in Fig. 3.32c, while the heat fluxes associated with the near and far SOL, $q_n \exp(-r_u / \lambda_n)$ and $q_f \exp(-r_u / \lambda_f)$, are plotted with magenta and red dashed lines, respectively.

The fit parameters for the discharge shown in Fig. 3.32c are $q_{n,RP} = 2817$ kW/m², $\lambda_{n,RP} = 5.1$

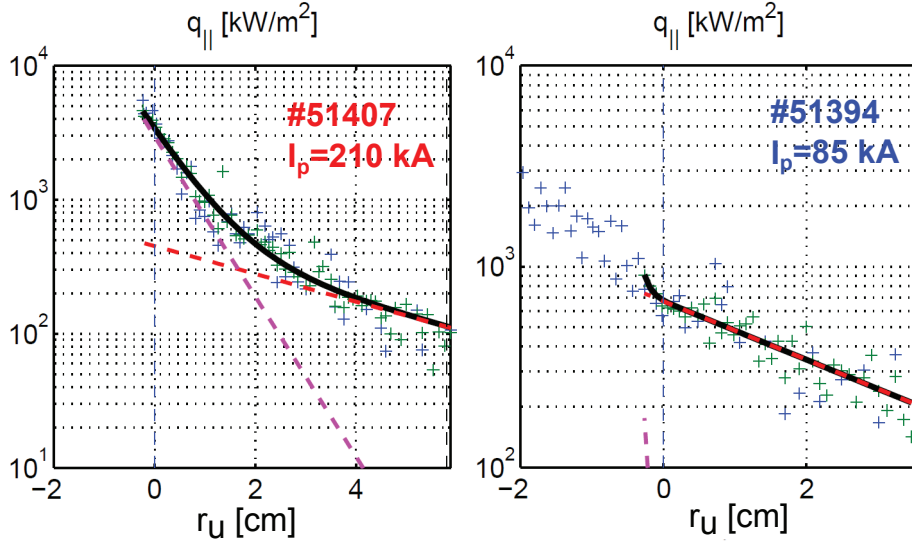


Figure 3.33: Radial profiles of parallel heat flux $q_{||}$ computed from RP data for $I_p = 210$ kA (left) and for $I_p = 85$ kA (right). For both discharges $n_{e,av} = 2.5 \cdot 10^{19} \text{ m}^{-3}$, $\kappa = 1.4$, $\delta = 0$. The fits of $q_{||}(r_u)$ with Eq. (3.8) are shown by black lines. The heat fluxes associated with the near and far SOL are plotted with magenta and red dashed lines, respectively.

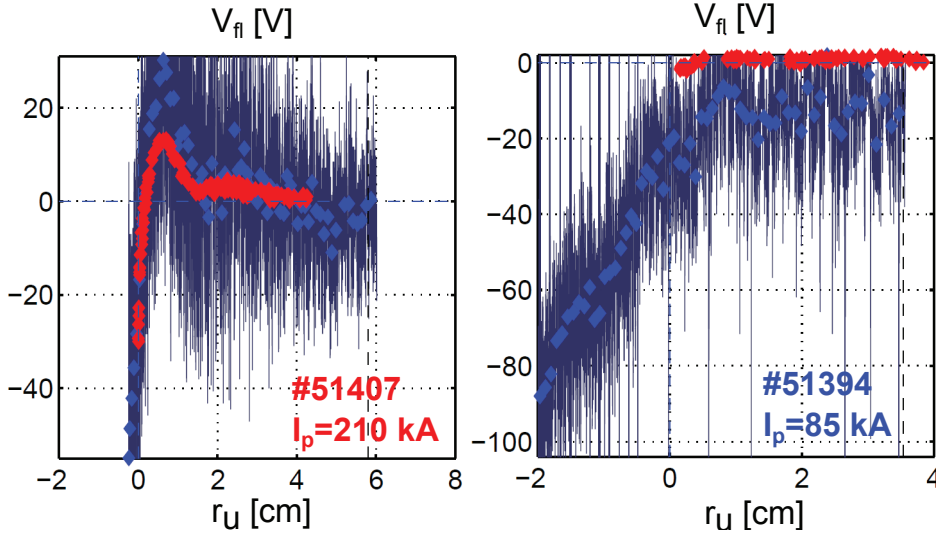


Figure 3.34: Radial profiles of floating potential V_{fl} computed from RP data (continuous lines) for $I_p = 210$ kA (left) and for $I_p = 85$ kA (right). For both discharges $n_{e,av} = 2.5 \cdot 10^{19} \text{ m}^{-3}$, $\kappa = 1.4$, $\delta = 0$. Bin-averaged data are shown by blue diamonds. $V_{fl}(r_u)$ measured by LP at the HFS is shown by red diamonds.

3.5. Mitigation and suppression of the near SOL by impurity seeding

mm, $q_{f,RP} = 1140 \text{ kW/m}^2$, $\lambda_{f,RP} = 38 \text{ mm}$. The fit results from the HFS $q_{||}(r_u)$ profile for the same discharge (#51485) are $q_{n,IR} = 5701 \text{ kW/m}^2$, $\lambda_{n,RP} = 1.6 \text{ mm}$, $q_{f,RP} = 951 \text{ kW/m}^2$, $\lambda_{f,RP} = 19 \text{ mm}$. It is observed that the SOL is broader at the LFS than at the HFS, with $\lambda_{n,RP}/\lambda_{n,IR} \approx 3$ and $\lambda_{f,RP}/\lambda_{f,IR} \approx 2$. A broader SOL at the LFS is consistent with a more ballooned type of transport at this location, and with the poloidal asymmetries observed in numerical simulations of the SOL [51]. Also, the near SOL parallel heat flux is smaller at the LFS with respect to the HFS, being $q_{n,RP}/q_{n,IR} \approx 0.5$.

Similar considerations hold for all the discharges for which RP data are available. In particular, in all cases where a near SOL is present in the HFS $q_{||}(r_u)$ profile, it is also visible in the LFS $q_{||}(r_u)$ profile. Also, the floating potential V_{fl} becomes negative in the near SOL, as observed at the HFS from LP measurements. An example is shown in Fig. 3.31. Non-ambipolar currents/velocity shear layer are then also present at the LFS midplane.

Furthermore, in the cases where the near SOL vanishes at the HFS, it also vanishes at the LFS. As an example, the $q_{||}(r_u)$ profiles from the RP for the two discharges with the highest and lowest value of I_p (210 and 85 kA, respectively) are compared in Fig. 3.33. The $q_{||}(r_u)$ profiles measured at the limiter for the same two discharges have been compared previously in Fig. 3.11, where the near SOL is shown to vanish at the HFS for $I_p = 85 \text{ kA}$. As shown in Fig. 3.33, the near SOL vanishes at the LFS as well for the same discharge.

The floating potential profiles at the HFS and LFS are shown in Fig. 3.34, for the same two discharges as in Fig. 3.33. The vanishing of the near SOL in the $q_{||}(r_u)$ profile is associated with a flattening of the $V_{fl}(r_u)$ profile at the HFS (red diamonds in Fig. 3.34). On the LFS instead, the floating potential becomes negative through the entire SOL (blue diamonds in Fig. 3.34). This effect can be interpreted as a change in the poloidal distribution of the non-ambipolar currents, that are no longer flowing to the limiter plates and might be dissipated in the SOL.

3.5 Mitigation and suppression of the near SOL by impurity seeding

Taking advantage of the dependence of the power entering the near SOL upon resistivity $\Delta P_{SOL} \propto 1/\nu$ and its vanishing for high resistivity/collisionality, several methods to suppress the near SOL, or at least mitigate it, could be devised. These might be useful in a future fusion reactor (ITER, DEMO...) to mitigate excessive heat loads on the limiter during the start-up/ramp-down phase, which would otherwise damage the first wall and/or limiting the plasma operational space.

The mitigation of the near SOL heat flux by reducing the plasma current is not possible for a start-up scenario. Indeed, a minimum I_p is required to create a diverted configuration, which might not be low enough to prevent the formation of the near SOL. Increasing the density might not be a viable solution because wall pumping is usually strong during the start-up phase in metal wall (e.g. Be), resulting in a rather low collisionality. Also, as shown before, the heat flux associated with the near SOL q_n first increases with n_e at low densities, it rolls over at intermediate densities (corresponding to the conduction limited regime) and eventually decreases to negligible values for high densities. Increasing the density could then actually

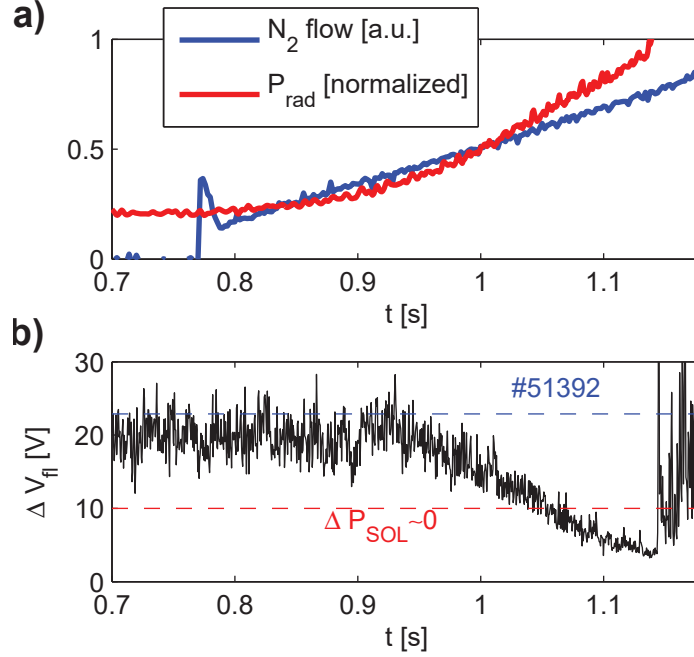


Figure 3.35: a) N_2 gas flow measured by the piezoelectric valve (blue) and total radiated power P_{rad} from bolometric measurements (red), normalized to its maximum value. b) Time evolution of the drop of the floating potential in the near SOL ΔV_{fl} (black), the value of ΔV_{fl} from the reference discharge (dashed blue), and the lowest value of ΔV_{fl} for which the near SOL is observed in the $q_{||}(r_u)$ profile (dashed red).

increase the heat fluxes, reaching high heat loads that could damage the FW panels.

Another possibility would be to increase the resistivity by decreasing the temperature, since $\nu \propto T_e^{-3/2}$. Cooling the SOL plasma can be done, for example, by increasing the radiated power P_{rad} via impurity seeding.

To test this method, a plasma discharge has been performed in TCV with N_2 impurity seeding (#53958). The plasma parameters are the same as in discharge #51392: $I_p = 140$ kA, $n_{e,av} = 2.5 \cdot 10^{19} \text{ m}^{-3}$, $\kappa = 1.4$, $\delta = 0$. Nitrogen (N_2) gas is injected using a piezoelectric valve located on the TCV floor. The flow is increased from zero up to levels such that the discharge is terminated by a disruption at $t \sim 1.26$ s.

The time trace of the gas flow is shown in Fig. 3.35a in blue. The total radiated power P_{rad} computed from bolometric measurements is shown in red. The time trace of the floating potential drop in the near SOL ΔV_{fl} is plotted in black in Fig. 3.35b. As P_{rad} increases, ΔV_{fl} decreases to $\Delta V_{fl} \sim 5$ V. The line $\Delta V_{fl} = 10$ V is plotted with a dashed red line, corresponding to the lowest value of ΔV_{fl} for which a near SOL was observed in the $q_{||}$ profiles (see Fig. 3.29). Unfortunately, no sweep of the vertical position is possible during plasma transitory phases, as it is the case for the injection ramp discussed here. The spatial resolution of the $V_{fl}(r_u)$ profile is lower with respect to the ones discussed in section 3.3. Since every other probe is operated in I_{sat} mode, the spacing on the central column of the probes measuring V_{fl} is 3.5

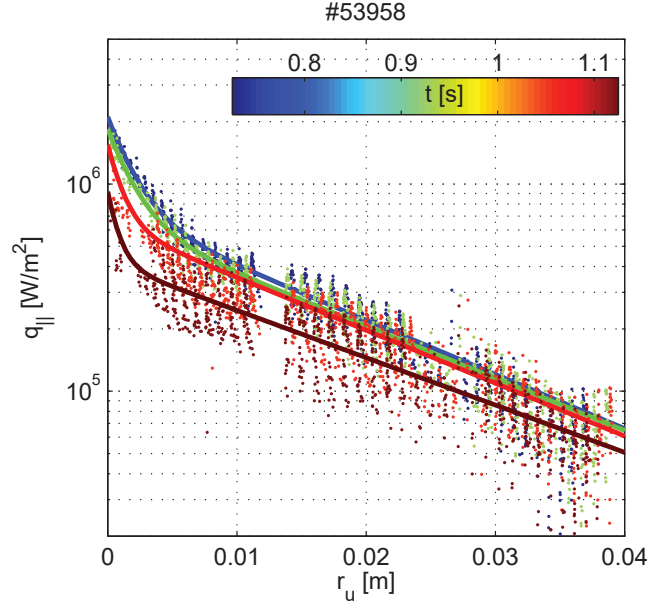


Figure 3.36: Parallel heat flux profiles $q_{\parallel}(r_u)$ for different times of discharge #53958, color coded with time. The fit of the profiles with Eq. (3.8) are shown by solid lines.

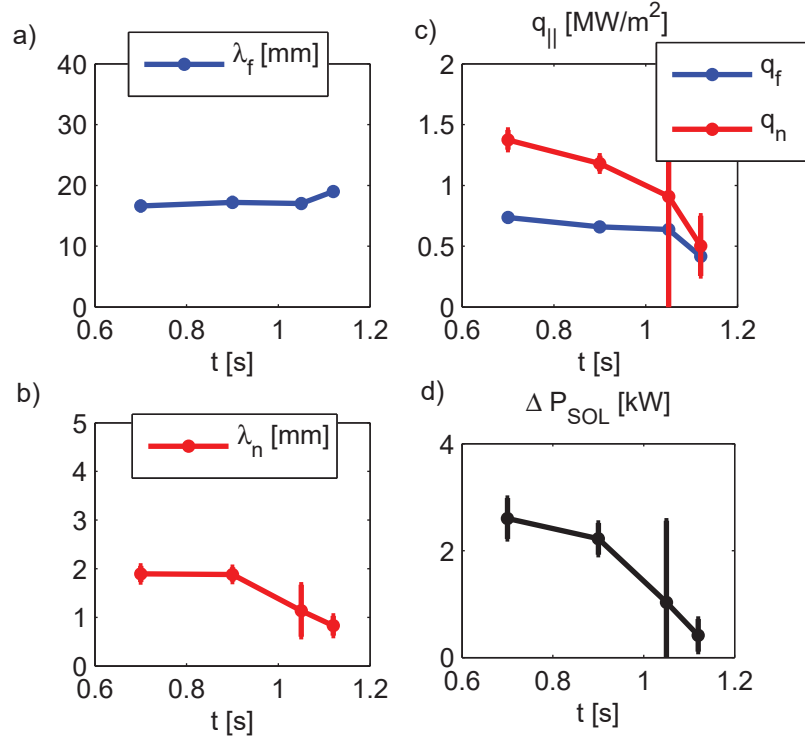


Figure 3.37: Evolution in time during discharge #53958 of: a) the far SOL width λ_f , b) the near SOL width λ_n , c) the near and far SOL heat fluxes q_f (blue) and q_n (red), d) the power in the near SOL ΔP_{SOL} .

cm, leading to a spatial resolution of the $V_{fl}(r_u)$ profile of approximately 2 mm close to the contact point. Thus ΔV_{fl} plotted in Fig. 3.35b provides an underestimate of the real one. The floating potential drop in the near SOL for the reference discharge (#51392), $\Delta V_{fl} = 23$ V, is plotted as a blue dashed line in Fig. 3.35b. Since the average ΔV_{fl} for $t < 0.75$ s (before the start of N_2 injection) is $\langle \Delta V_{fl} \rangle = 21$ V, we conclude that the underestimate of ΔV_{fl} due to poor spatial resolution is $\leq 10\%$.

This suggests that the near SOL is mitigated by the injection of N_2 and the consequent increase of radiation, cooling the plasma, and eventually vanishes for $t \geq 1.1$ s.

In Fig. 3.36, the parallel heat flux radial profiles from IR thermography are plotted at four different times during the discharges. The heat flux in the near SOL strongly decreases in time (i.e. with N_2 concentration), while the heat flux in the far SOL is less affected. This is clearly shown in Fig. 3.37, where the time evolution of the fit parameters λ_f , λ_n , q_f and q_n is displayed, together with the evolution of the power in the near SOL, ΔP_{SOL} . As the N_2 concentration increases, both q_n and λ_n are strongly reduced (~ 2.5 times with respect to values before N_2 injection), while q_l and λ_f are approximately constant. The decrease in λ_n and q_n leads to a reduction of a factor ~ 6.5 for ΔP_{SOL} , resulting in its almost complete disappearance.

The results from the IR together with LP measurements show that the near SOL heat flux is successfully mitigated by the gas injection. Also, we demonstrated how LP embedded in the limiter are a reliable diagnostic to monitor the presence of a near SOL through V_{fl} measurements. This measurements does not require an elaborated analysis, like for the IR camera, and it can produce reliable results immediately after each discharge, or even in real time, and could therefore be used as an actuator during the start-up phase.

Further investigations, featuring discharges with flat tops at different N_2 concentrations, allowing for steady state IR and RP measurements and vertical position sweep to increase the LP spatial resolution, are foreseen.

3.6 Comparison with nonlinear simulations

To investigate the mechanisms leading to the heat deposition onto the first wall in the SOL, we perform dedicated numerical non-linear simulations of the SOL plasma dynamics of a TCV discharge using the GBS code. In particular, we aim at reproducing the separation between the near and far SOL and at giving some insight on the physical mechanisms behind this phenomena. This section is organized as follows:

In section 3.6.1 we introduce a simulation modeling a TCV discharge (# 49170). In section 3.6.2 we compare the numerical simulation results with the experimental data. In particular, we compare the heat flux and the parallel current density at the magnetic pre-sheath (MP) entrance with the IR and LP results, finding qualitative agreement. In section 3.6.3 we compare the results of the former simulation with a second one, differing only for a 40 times higher resistivity. We discuss how resistivity affects the near SOL, the poloidal plasma flow, and the skewness of the density fluctuations. The results exposed in this section have been also

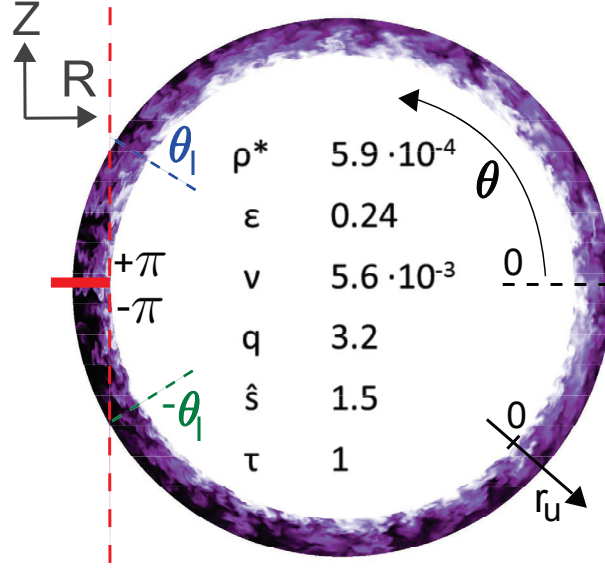


Figure 3.38: Snapshot of plasma density from the simulation of #49170. The coordinate system is displayed together with limiter geometry for the simulation (thick red) and TCV (dashed red). The simulation parameters are displayed: $\rho^* = \rho_s/R$, the inverse aspect ratio ϵ , the normalized Spitzer resistivity ν , the safety factor q , the magnetic shear \hat{s} and $\tau = T_{i,0}/T_{e,0}$.

published in Ref. [71].

3.6.1 Numerical modeling of TCV discharge #49170

Using the GBS code, we model TCV discharge #49170. This is a circular inboard-limited ohmic L-mode deuterium plasma, with plasma current and toroidal magnetic field on axis being $I_p = 145$ kA and $B_\phi = 1.45$ T, respectively. The values of the plasma density and temperature at the LCFS, $n_{e,0} = 5 \times 10^{18} \text{ m}^{-3}$ and $T_{e,0} = 25$ eV, are deduced from Langmuir probes embedded in the limiter. These parameters set the normalized Spitzer resistivity $\nu = q_e n_{e,0} R_0 / (m_i c_{s,0} \sigma_{\parallel}) \propto n_{e,0} R_0 \Lambda m_e / (m_i c_{s,0} T_{e,0}^{3/2})$, $\nu = 5.9 \times 10^{-4}$, and the dimensionless size of the system through the ion sound Larmor radius $\rho_s = m_i c_{s,0} / (q_e B) = 0.5$ mm. Here Λ is the Coulomb logarithm, R_0 is the major radius of the plasma, $c_{s,0} = \sqrt{k_b T_e / m_i}$ is the ion sound speed at the LCFS, and k_b is the Boltzmann constant. The resulting simulation domain consists of $128 \times 820 \times 128$ points in the radial (x), poloidal (y) and toroidal (z) direction, respectively. The sources of plasma temperature and density are located at $x = 20$. The shape of the sources is gaussian in the radial direction with a width corresponding to 3 grid points. The sources are poloidally and toroidally uniform. The safety factor $q = 3.2$, the magnetic shear $\hat{s} = 1.5$ and the inverse aspect ratio $\epsilon = 0.24$ are obtained from the magnetic reconstruction of the discharge, provided by the LIUQE code [33]. The ion temperature at the LCFS is assumed

to be $T_{i,0} = T_{e,0}$.

The equations governing the plasma dynamics have been described in section 2.7.2. Effects due to finite aspect ratio, ion temperature and magnetic shear are included in the simulations. The boundary conditions at the limiters are detailed in section 2.7.2. Neumann boundary conditions are used for all quantities at the inner and outer radial boundaries of the simulations, with the exception of the plasma potential (at the outer boundary) and the vorticity (at both boundaries), for which Dirichlet conditions are imposed. This simulation features only open field lines and the LCFS is set by the radial position of the plasma density and temperature source that mimics the injection of plasma from the core. The position and amplitude of the sources could hence affect quantitatively the results. To better address the physics at the LCFS and in the near SOL, simulations including both open and closed field line regions are ongoing, whose first results are presented in Ref. [48].

In this simulation, the toroidal magnetic field and the plasma current are antiparallel, while in the experiment they are parallel. Indeed, the possibility to change the sign of the magnetic field is not yet implemented in the code and is foreseen in future works. This difference could lead to some discrepancies when comparing numerical and experimental results, since the direction of the drift velocities is reversed.

In Fig. 3.38, a snapshot of the plasma density from the simulation is shown, together with the limiter geometry for the simulation (thick red) and TCV (dashed red), respectively.

3.6.2 Comparison with the experimental data

The GBS numerical simulations provide the three-dimensional temporal evolution of the plasma density n (quasi-neutrality is assumed), the electron and ion temperature T_e and T_i , the electron and ion parallel velocities $v_{||,e}$, and $v_{||,i}$ and the plasma potential ϕ . The equilibrium 2D profiles are obtained averaging over time and over the toroidal direction. The plasma pressure and parallel current are computed as $p = n(T_e + T_i)$ and $j_{||} = en(v_{||,i} - v_{||,e})$ respectively. The parallel heat flux on the limiters is given by

$$q_{||} = q_{||,e} + q_{||,i}, \quad (3.30)$$

$$q_{||,e} = \frac{5}{2} n T_e v_{||,e} - 0.71 \frac{j_{||}}{e} T_e \quad (3.31)$$

$$q_{||,i} = \frac{5}{2} n T_i v_{||,i} + \frac{1}{2} n v_{||,i}^3. \quad (3.32)$$

The term including the kinetic energy of the net ion flow is often referred to as macroscopic heat flux. The term including the parallel current comes from the Braginskii closure of the energy equation and is referred to as microscopic heat flux. Finally, the terms proportional to ion and electron temperature are called mesoscopic heat fluxes, accounting for the thermal energy advected by the mean flow.

Figure 3.39 shows the resulting heat flux profile for one of the two limiter plates and the comparison with the experimental profile. The simulated parallel heat flux radial profiles on the limiter are well described by a sum of two exponentials, as given in Eq. (3.8). The

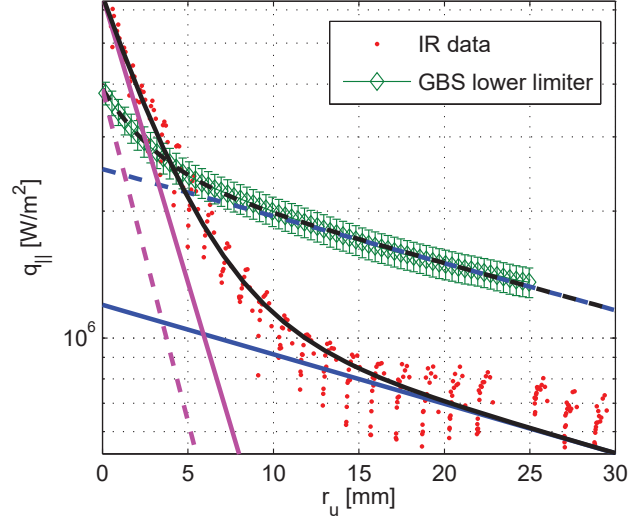


Figure 3.39: Heat flux onto the lower limiter (green diamonds) is compared with experimental data from IR thermography (red dots). The fit with the sum of two exponentials is shown (black lines), the short exponential in magenta and the long one in blue, solid lines for experimental data and dashed lines for one of the two limiters in the simulation. The fitted lengths of far and near SOL are in good agreement between simulation and experiment, but not the magnitude of the associated heat fluxes.

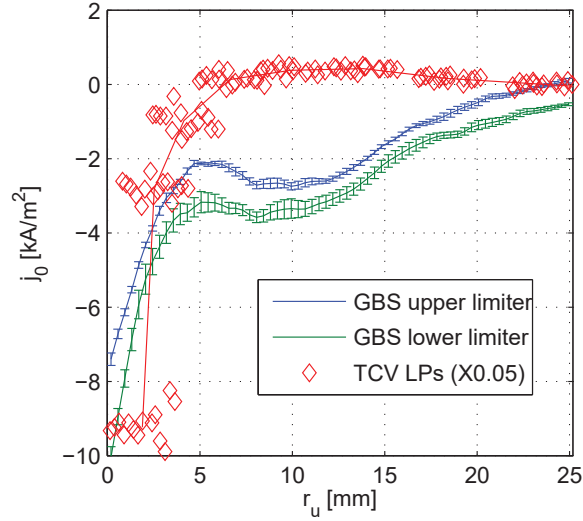


Figure 3.40: Parallel currents to the limiters in the GBS simulation (blue and green). They qualitatively agree with the current density to the grounded wall measured in TCV with flush mounted Langmuir probes (red diamonds, rescaled for plotting).

fitted values for the simulation result, $\lambda_n = 2.3$ mm (2.5 mm) and $\lambda_f = 35$ mm (35 mm) for the upper (lower) limiter, respectively, are in quantitative agreement with the experimental ones obtained by means of infrared thermography $\lambda_{n,IR} = 3.2$ mm, $\lambda_{f,IR} = 37$ mm (the infrared analysis was possible only for the upper part of the limiter). Nevertheless, the strength of the near SOL in the simulation $\Delta P_{SOL}^{sim} \approx 1$ kW, is much smaller than in the experiment, $\Delta P_{SOL}^{exp} \approx 15$ kW.

If one neglects the near SOL and fits the whole profiles from the simulation with a single exponential, the resulting fall off lengths are $L_q = 57\rho_s$ ($50\rho_s$) for the upper (lower) limiter respectively. We compare these values with two adimensional scalings presented in Ref. [62]:

$$L_{q,QL}[\rho_s] = 0.22 \cdot \nu^{0.07} \rho_*^{-0.62} q_{95}^{0.84}, \quad (3.33)$$

$$L_{q,fit}[\rho_s] = 0.094 \cdot \nu^{0.02} \rho_*^{-0.71} q_{95}^{0.76}, \quad (3.34)$$

where Eq. (3.33) is obtained from quasi-linear theory, and Eq. (3.34) is obtained from the fit on the ITPA database published in Ref. [12], and q_{95} is the edge safety factor. Both scalings are in good agreement with the simulated fall off lengths, being $L_{q,QL} = 43\rho_s$ and $L_{q,fit} = 49\rho_s$.

Net electron currents flow to the limiter in the near SOL, as observed experimentally with Langmuir probes, suggesting their contribution to the formation of the narrow feature. Though, the simulated currents are one order of magnitude smaller than the measured ones, as it is shown in Fig. 3.40, where the simulation current, poloidally averaged over 3 simulation points at the sheath entrance, are compared with the experimental TCV data from the upper part of the limiter. The parallel current computed from the experimental data as $j_{||} = I_0 / (A_p \sin \alpha)$, where I_0 is the current measured at ground potential and A_p is the geometric surface of the probe, is likely to be overestimated due to the vanishing angle α between the magnetic field and the probe surface, as one approaches the contact point ($r_u = 0$). The difference in behavior of such currents in the far SOL between the simulation (always negative) and the experiment (positive in the far SOL) is under investigation and it is probably due to the Boussinesq approximation. Indeed, to address this problem, we performed smaller simulations (TCV-size simulations require a huge amount of computational resources), where the Boussinesq approximation, used to evaluate the divergence of the polarization drift, is relaxed. The possibility of removing such approximation has been recently implemented in GBS [72]. In the non-Boussinesq (NB) simulation, the charge is conserved and the integral of the currents is close to zero. Still, the parallel currents flowing to the limiter are negative and the shape of the current profiles is similar to the ones of the corresponding simulation where the Boussinesq approximation was applied (BA). We therefore attribute the non-perfect closure of the total current in the TCV simulations (currents flowing to the limiter always negatives) to the Boussinesq approximation. From the comparison of the small BA and NB simulations we conclude that relaxing the approximation will not produce a qualitative change in the current profile in the TCV simulations, so that the qualitative results presented herein will still hold for a TCV-size NB simulation.

In Fig. 3.41, the microscopic heat flux associated with the non-ambipolar current is compared with the mesoscopic and microscopic ones. As a result, its contribution to the total heat flux is

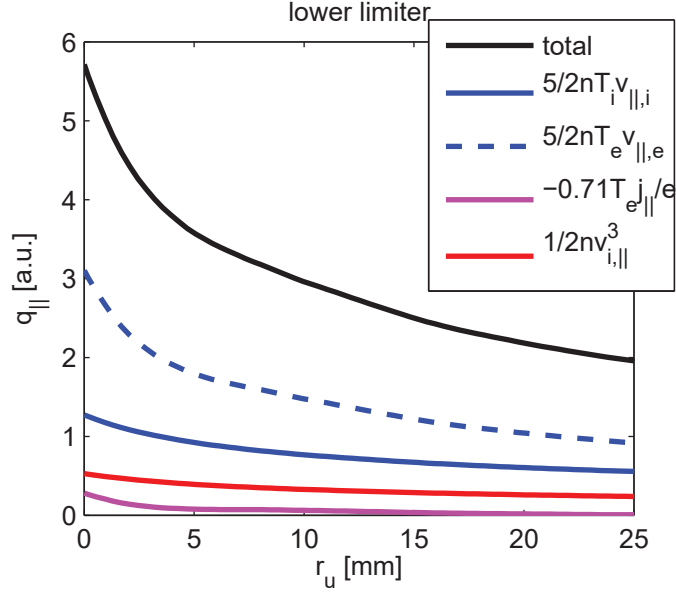


Figure 3.41: Different components contributing to the heat flux arriving onto the lower limiter in the GBS simulation. The microscopic heat flux associated with the non-ambipolar currents (magenta line) contributes only marginally to the total heat flux. Similar results for the upper limiter.

negligible. As suggested in Ref. [69], this confirms that although non-ambipolar currents are correlated to the presence of a near SOL steep-gradient, they are not directly responsible for the excess heat flux to the limiter.

3.6.3 Effect of resistivity on simulation results

From now on, we will refer to the simulation described in section 3.6.1 as simulation A. We introduce here a second simulation (B), identical to the first one, except for the normalized resistivity which is 40 times larger. This choice is driven by the trend discussed in Ref. [58], i.e. that the heat flux associated with the near SOL increases with electron temperature and decreases with plasma density $\Delta P_{SOL} \propto T_e^{3/2} n_e^{-1} \propto \nu^{-1}$.

In simulation B, the heat flux profiles at the limiters are still well fitted by a sum of two exponentials. The increase of the resistivity causes the SOL profiles to flatten and the poloidal asymmetry to increase. We find $\lambda_n = 8.3$ mm (5.0 mm), $\lambda_f = 164$ mm (62 mm) for the upper (lower) limiter, respectively. As the resistivity is increased, the current flowing to the upper limiter is reduced by a factor 2, while the one flowing to the lower limiter does not vary substantially.

A double scale length is observed, for simulation A, not only in the heat flux radial profiles, but in the pressure radial profiles as well. The pressure radial profiles fit well to a sum of two exponentials $p = p_n \exp(-r_u/\lambda_n) + p_f \exp(-r_u/\lambda_f)$. The poloidal variation of the two scale lengths is shown in Fig. 3.42, color coded with the relative strength of the near SOL p_n/p_f . In

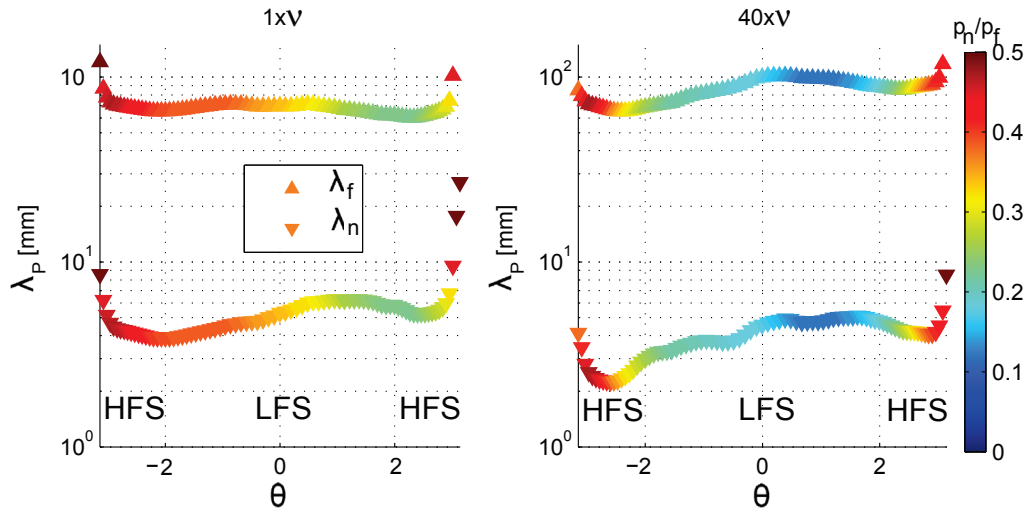


Figure 3.42: Poloidal variation of the two decay lengths resulting from the fit of the pressure profiles with the sum of two exponentials, color coded with the relative strength of the short component. Simulation A on the left, simulation B on the right. The increase of resistivity causes the near SOL to become relatively less important on the low field side.

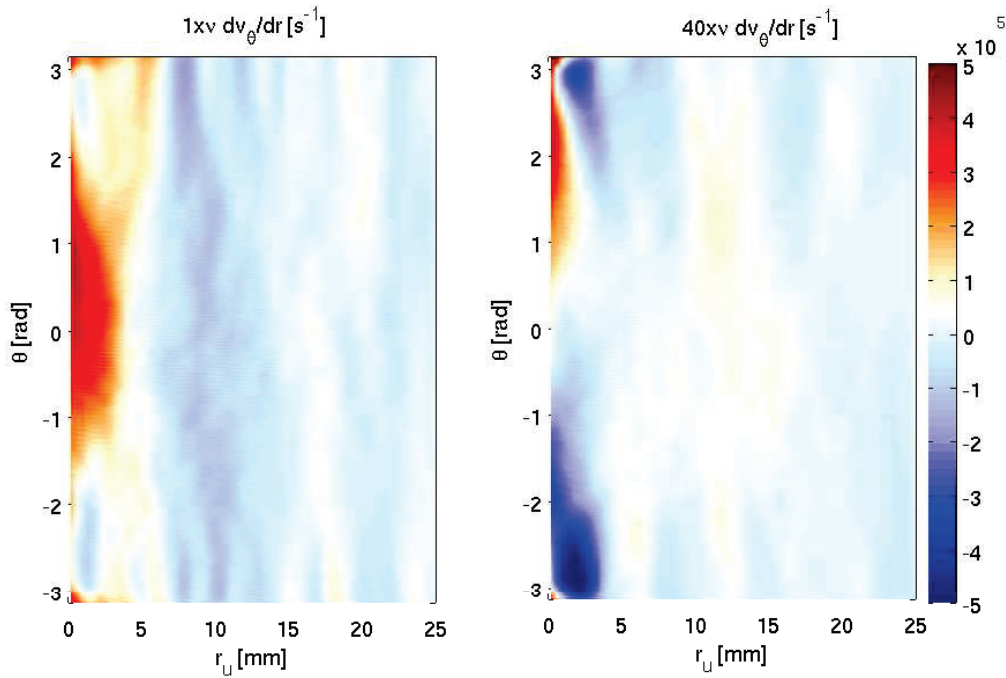


Figure 3.43: Radial shear of the poloidal velocity $dv_{E \times B, \theta}/dr$ for simulation A (left) and B (right).

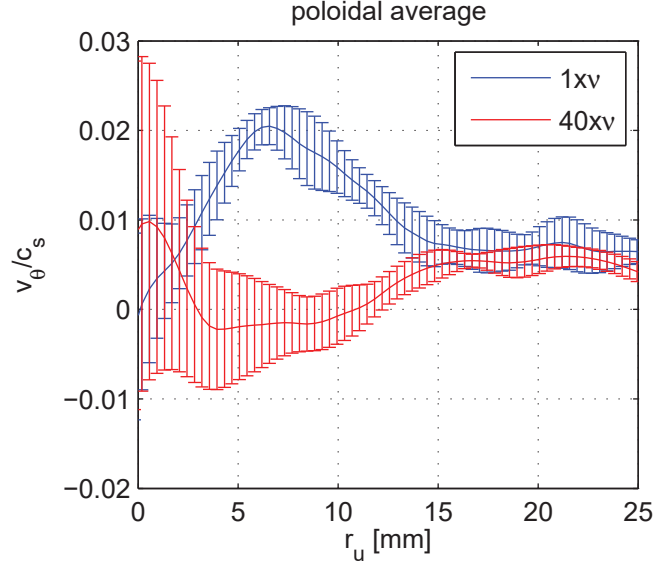


Figure 3.44: Poloidal average of the poloidal component of the $\mathbf{E} \times \mathbf{B}$ flow for simulation A (blue) and B (red). The error bars are given by the standard deviation over the poloidal profile. As the resistivity is increased, the poloidal flow is suppressed.

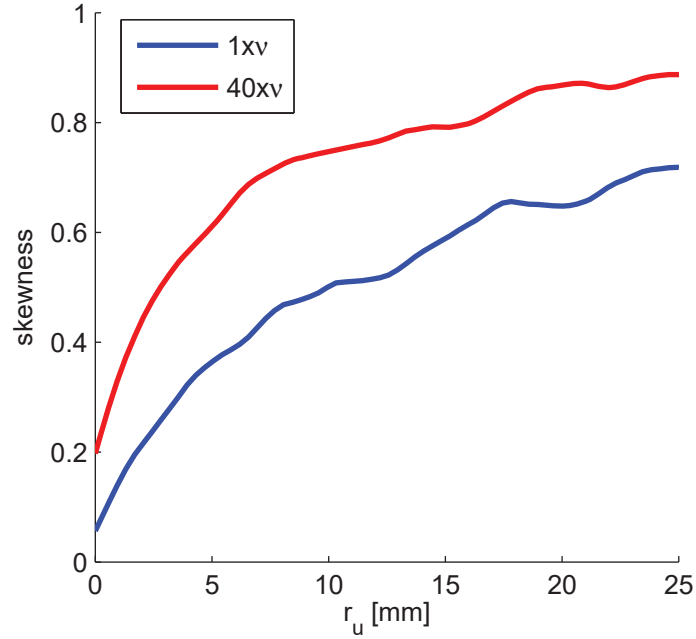


Figure 3.45: Poloidal average of the skewness of the density fluctuations for simulation A (blue) and B (red). The skewness increases moving away from the LCFS. The skewness for simulation B is approximately 30% higher than in simulation A.

simulation A, two scale lengths are visible at all poloidal locations. The separation in scales is more pronounced in the bottom half of the poloidal section.

In simulation B, the widening of the far SOL and the increase of the poloidal asymmetry is observed in the pressure profiles as well, as shown in Fig.3.42. The separation between the two scale lengths is sensible close to the limiters ($p_n/p_f \sim 0.5$), while it vanishes at the low field side ($p_n/p_f \sim 0.1$). The persistence of the near SOL at the limiter for simulation B might be caused by the velocity shear $d v_{E \times B, \theta} / dr$, which exhibits high values close to the limiters, as shown in Fig. 3.43, where the velocity shear is plotted on the poloidal plane (r_u, θ) for simulation A (left) and B (right).

The increase of resistivity also results in an overall reduction of the $\mathbf{E} \times \mathbf{B}$ velocity flow, as shown in Fig. 3.44, where the poloidal average of $v_{E \times B, \theta}$ is displayed for the two cases. In both simulations, the $\mathbf{E} \times \mathbf{B}$ flow is mainly poloidal towards the upper limiter, its radial component being negligible.

The poloidally averaged skewness profiles for density fluctuations are shown in Fig. 3.45 for both simulations. The positive skewness, as shown in the picture, is an indication of the presence of blobs, which can play an important role in the transport in the far SOL. The skewness increases moving radially outward from the LCFS, being > 0.5 in the far SOL. Also, as the resistivity is increased, the skewness increases by more than 30%.

The dynamics of the blobs and their impact on heat transport in the SOL will be discussed in section 4.2.

3.7 Summary

In this chapter, the near SOL experiments in TCV, featuring D and He plasmas, have been described. A method to compute the perpendicular heat flux q_{\perp} and the parallel heat flux radial profiles remapped at the outer midplane $q_{\parallel}(r_u)$ from the IR data has been detailed. An empirical scaling for the perpendicular heat flux at the contact point $q_{\perp 0}$ has been presented: the scaling can be approximated by $q_{\perp 0} \propto I_p^2 n_e^{-0.45} \kappa^{-0.4}$.

We discussed the dependence of parallel heat flux profiles upon the plasma parameters I_p , $n_{e,av}$ and κ , for both D and He plasmas. First observations of the near SOL in TCV for both D and He plasmas have been reported. The vanishing of the near SOL in both D and He plasmas is shown for the first time.

The power in the near SOL ΔP_{SOL} is found to scale with the normalized Spitzer resistivity ν as $\Delta P_{SOL} \propto 1/\nu$, and to vanish for high values of collisionality $\nu^* \geq 40$. This corresponds to a conduction limited regime of the SOL.

The presence of non ambipolar currents in the HFS near SOL has been reported. The floating potential drop in the near SOL ΔV_{fl} is used as a proxy for the presence of non-ambipolar currents. ΔV_{fl} and ΔP_{SOL} have been shown to be strongly correlated. A simple model involving the shear of $\mathbf{E} \times \mathbf{B}$ velocity has been discussed.

The profiles of q_{\parallel} and V_{fl} at the LFS have been presented and compared with those at the HFS. In all cases where a near SOL is present at the HFS, it is also visible in the LFS. The SOL

is typically wider at the LFS than at the HFS. Furthermore, in the cases where the near SOL vanishes at the HFS, it also vanishes at the LFS.

Based on the experimental findings, in particular the ν dependence of the power in the near SOL, we have proposed a method to mitigate and suppress the near SOL via impurity seeding. First successful experimental evidences have been shown.

Numerical simulations of the TCV SOL using the GBS code have been introduced and discussed. The $q_{||}$ profile at the simulation limiter feature a double scale length and non-ambipolar currents are observed to flow to the limiter, qualitatively agreeing with the experimental data. Still, both the near SOL heat flux strength and the intensity of the non-ambipolar currents are an order of magnitude lower than in the experiments. The heat flux directly associated to the non-ambipolar currents has been computed, and found to be negligible. The effect of a 40 times increase in the resistivity on the simulation results has been discussed. The near SOL is observed to almost disappear at the LFS, but not at the HFS.

4 Blob Physics in inboard limited L-mode plasmas in TCV

As it has been introduced in section 1.3, plasma filaments (blobs) are an ubiquitous feature of plasmas in open magnetic field line configurations and are routinely detected in the tokamak SOL, using Langmuir probes or fast imaging techniques. Due to their radially outwards motion, they are believed to enhance the cross field transport in the SOL [13], substantially contributing to the heat deposition on the first wall and divertor plates, both on the HFS and LFS. Therefore, the comprehension of their dynamics is of crucial importance for a better prediction of the heat loads onto the first wall.

In this chapter, we focus on the study of blob dynamics. Our investigation is carried out combining experimental data from TCV experiments and results from non-linear simulations. In particular, in section 4.1, we characterize blob dynamics at the outer midplane (OMP) using reciprocating Langmuir probe (RP) data. The blob sizes and velocities are computed using a conditional average sampling technique for two TCV discharges with different resistivities. The radial velocity of the blobs is compared with an existing scaling. In section 4.2, a blob detection and tracking technique is applied to GBS simulation results, giving better insight on blob dynamics. The blob shape and size is characterized. The results of a cross-correlation analysis are discussed. Blob velocities are determined and compared with an existing scaling. The blob contribution to cross field particle and heat fluxes is evaluated. Finally, the results of this analysis are compared with the experimental ones.

4.1 Blob detection with the reciprocating Langmuir probe (RP) in TCV

Blobs are detected in TCV limited L-mode plasmas using the conditional average sampling technique [73] on the RP data. We describe here the blob detection technique, and the method used to evaluate the blob velocity and size. Finally, we expose the results of the analysis for two discharges as an example.

The RP can perform up to two reciprocations for each plasma discharge. For each reciprocation, the probe head is propelled by $\Delta R = 20$ cm and retracted using a pneumatic piston. The

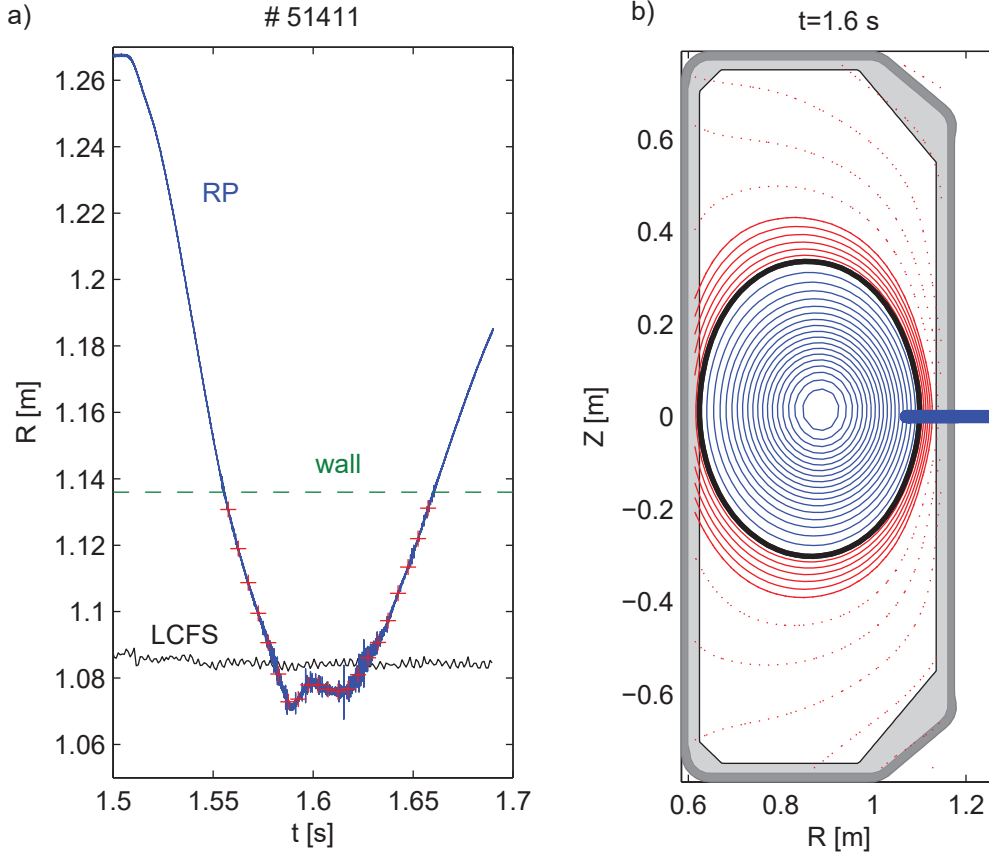


Figure 4.1: a) Probe radial trajectory for discharge #51411 (blue), position of the outer wall (dashed green), and radial position of the LCFS (black). The probe radial position averaged over time windows of $\Delta t = 5$ ms is shown by red crosses. b) Magnetic equilibrium of discharge #51411 during the probe reciprocation, reconstructed by LIUQE. The LCFS is shown in black. The projection on the poloidal cross section of the probe trajectory is plotted with a thick blue line.

reciprocation lasts in total ~ 200 ms. Initially, the probe head sits in a position R_{out} recessed with respect to the outer wall tiles. Such initial position is chosen so that the innermost point of the reciprocation $R_{out} - \Delta R$, is approximately 1 cm inside the LCFS.

In Fig. 4.1a, the probe radial trajectory for TCV discharge #51411 is shown in blue, together with the position of the outer wall (dashed green) and the position of the LCFS (black).

4.1.1 Conditional Average Sampling (CAS) of blobs

We divide the probe reciprocation into time windows of $\Delta t = 5$ ms. These time intervals correspond to radial displacements of the probe head of $\Delta R \lesssim 1$ cm. The probe position in each time window is shown in Fig. 4.1a by red crosses. Such time window is chosen as a trade

4.1. Blob detection with the reciprocating Langmuir probe (RP) in TCV

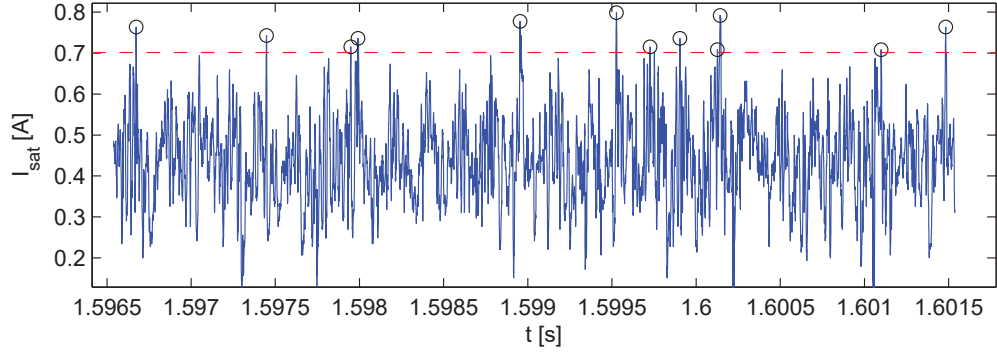


Figure 4.2: Example of $I_{sat}(t)$ trace from pin #4 on the RP head, in a $\Delta t = 5$ ms time window (blue), together with the detection level $\langle I_{sat} \rangle + 2.5\sigma$ (dashed red). The detected blobs are shown by black circles.

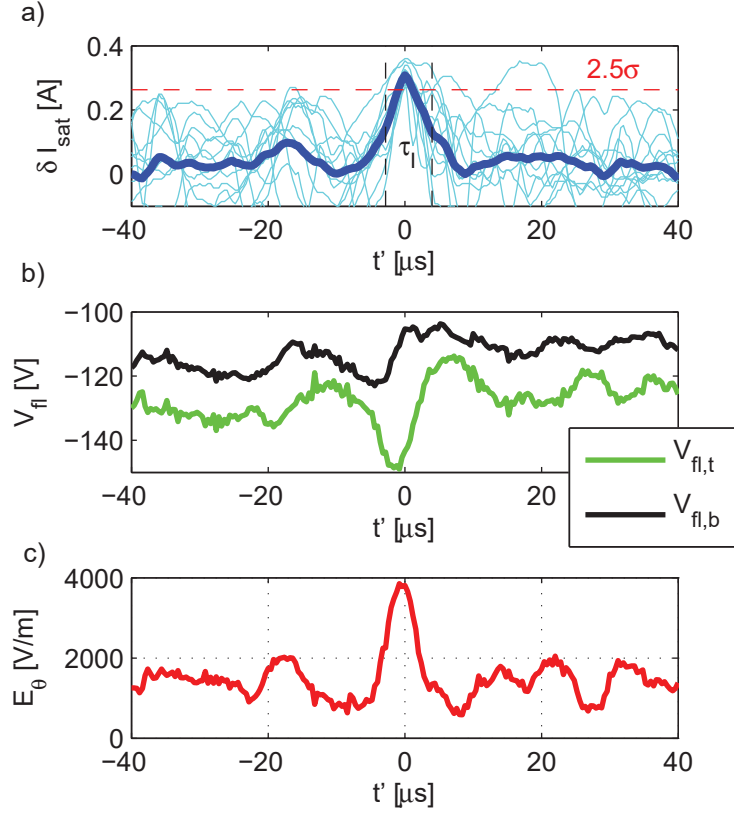


Figure 4.3: Example of a result from the CAS technique. a) All $\delta I_{sat}(t)$ signals for the detected blobs shifted by t_j (cyan), the conditionally averaged $\delta I_{sat, blob}(t')$ (blue), the detection threshold 2.5σ (dashed red). The FWHM of the $\delta I_{sat}(t')$ trace, τ_I , is delimited by vertical dashed lines. b) The CAS profiles of V_{fl} for the top (green) and bottom (black) pins, respectively. c) The CAS poloidal electric field E_θ .

off between the need for a sufficient number of detected blobs to perform the CAS, and the ideal condition for approximating the probe position as fixed during the blob detection. The probe radial velocity is $\Delta R/\Delta t \sim 2$ m/s, which is negligible with respect to the radial velocity of the blobs, typically of the order of 1 km/s. We can hence state that the probe position is fixed during blob detection.

The ion saturation signal, $I_{sat}(t)$, measured from pin #4 in Fig. 2.26, is used to detect blobs. The condition for blob detection is $\delta I_{sat}(t) = I_{sat}(t) - \langle I_{sat} \rangle > 2.5\sigma$, where the brackets denote the average over Δt , and σ is the signal standard deviation over the same time interval. An example of blob detection is shown in Fig. 4.2, where the $I_{sat}(t)$ trace in the Δt time window is shown (blue), together with the detection level $\langle I_{sat} \rangle + 2.5\sigma$ (dashed red). The detected blobs are shown by black circles. Typically, ~ 15 blobs are detected in each time window. For each detected blob j in the considered time window, the time corresponding to the maximum of $\delta I_{sat}(t)$, t_j , is determined. The shifted δI_{sat} time traces, $\delta I_{sat}(t - t_j)$, plotted in cyan in Fig. 4.3a, are ensemble averaged. The result of this procedure, plotted in blue in Fig. 4.3a, is the δI_{sat} time trace of the ensemble averaged blob

$$\delta I_{sat,blob}(t') = \frac{1}{N} \sum_{j=1}^N \delta I_{sat}(t' + t_j), \quad (4.1)$$

where $N \sim 15$ is the total number of blobs in the considered time window, $t' = t - t_j$ is a new time coordinate, with $t' = 0$ at the blob j detection, and the $\delta I_{sat}(t - t_j)$ are considered in a reduced time window $|t - t_j| < 40 \mu\text{s}$. This choice, driven by the attempt to maximize the number of detected events, is justified a posteriori by the fact that the typical autocorrelation time of the blobs is $\tau_c < 10 \mu\text{s}$.

The same averaging is applied to other signals from different pins on the RP head, by keeping the t_j determined from the I_{sat} measurements as a reference (trigger). In particular, we average the V_{fl} signals from the pins #1, #2 and #3 in Fig. 2.26, operated in floating mode. In the following, we will refer to these pins as the “top”, “middle” and “bottom” pin, respectively. By using the CAS technique, we compute the average time traces $V_{fl,t}(t')$, $V_{fl,m}(t')$ and $V_{fl,b}(t')$ for the top, middle and bottom pin, respectively. $V_{fl,t}(t')$ and $V_{fl,b}(t')$ are plotted in green and black, respectively, in Fig. 4.3b.

The CAS $V_{fl}(t')$ traces of the two poloidally separated pins are used to compute the poloidal electric field inside the blob

$$E_\theta(t') = - \frac{V_{fl,t}(t') - V_{fl,b}(t')}{d_{t-b}}, \quad (4.2)$$

where $d_{t-b} = 1.06$ cm is the poloidal distance between the top and bottom pins. An example of CAS electric poloidal field E_θ is shown in Fig. 4.3c. We point out that, in the sign conventions used here, $E_\theta > 0$ when it is directed towards positive values of the poloidal coordinate θ , i.e. when E_θ is directed vertically upwards (since the RP is located at the OMP).

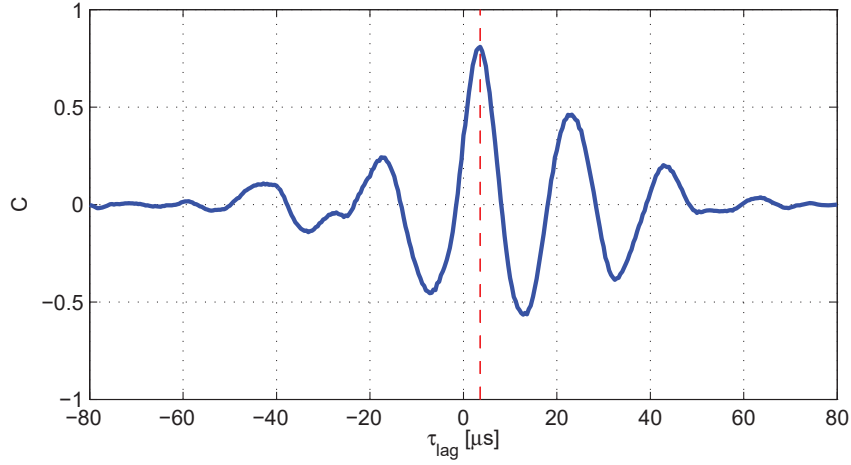


Figure 4.4: Cross-correlation function C of the potential traces in Fig. 4.3b (blue). The cross-correlation time τ_θ is indicated by a red dashed line.

4.1.2 Determination of blob velocity and size

The blob poloidal velocity v_θ is evaluated by computing the cross correlation of the CAS floating potential traces [15], as

$$v_\theta = d/\tau_\theta, \quad (4.3)$$

where d is the (poloidal) distance between two poloidally separated pins, and τ_θ is the cross-correlation time between two floating potential CAS time traces. In Fig. 4.4, the cross-correlation function C of the potential traces in Fig. 4.3b is plotted in blue, and the cross-correlation time τ_θ (the time for which C is maximum) is indicated by a red dashed line. This technique relies on the assumption that the blobs have a non-zero poloidal velocity, which is usually the case. We remark that in the case the blob has a purely radial velocity, the resulting correlation time between the two considered V_{fl} signals is zero, and the estimate of v_θ with Eq. (4.3) fails. In the attempt to avoid this possibility and improve our analysis, v_θ is computed for each combination of the poloidally separated pins (top/bottom, top/middle, middle/bottom), and then averaged.

It is not possible to compute the blob radial velocity v_r with the same technique used for v_θ . Indeed, the distance between radially separated pins on the RP head (e.g. pin #2 and pin #9 in Fig. 2.26), $\Delta r = 1.5$ mm, is too small. The blobs can have radial velocities of the order of 1 km/s. The blob would cover the distance in between the two pins in $\sim 1 \mu\text{s}$. This time is comparable with the sampling time $1/f = 0.4 \mu\text{s}$, where $f = 2.5$ MHz is the acquisition frequency. The correlation time between the two radially separated pins would then always be below the time resolution of this technique.

The blob radial velocity is then evaluated as the radial component of the $\mathbf{E} \times \mathbf{B}$ drift velocity,

$$v_r = \frac{E_\theta B_\phi}{B^2}, \quad (4.4)$$

where E_θ is the CAS poloidal component of the electric field, given by Eq. (4.2). Unless the distance of the pins coincides with the distance between the maximum and the minimum of the dipolar potential structure, Eq. (4.2) underestimates the poloidal electric field inside the blob. For this reason, the electric field is evaluated also using the top/middle and middle/bottom pins. The highest values of the three ones is chosen to better describe the blob internal E_θ . Finally, the blob size is evaluated as follows. The FWHM of the average blob $\delta I_{sat,blob}(t')$ trace, τ_I , is computed (black dashed lines in Fig. 4.3a). The blob effective diameter is evaluated to be

$$2a_b = \tau_I v = \tau_I \sqrt{v_\theta^2 + v_r^2}, \quad (4.5)$$

where a_b is the blob radius, and v_θ and v_r are obtained from Eqs. (4.3,4.4).

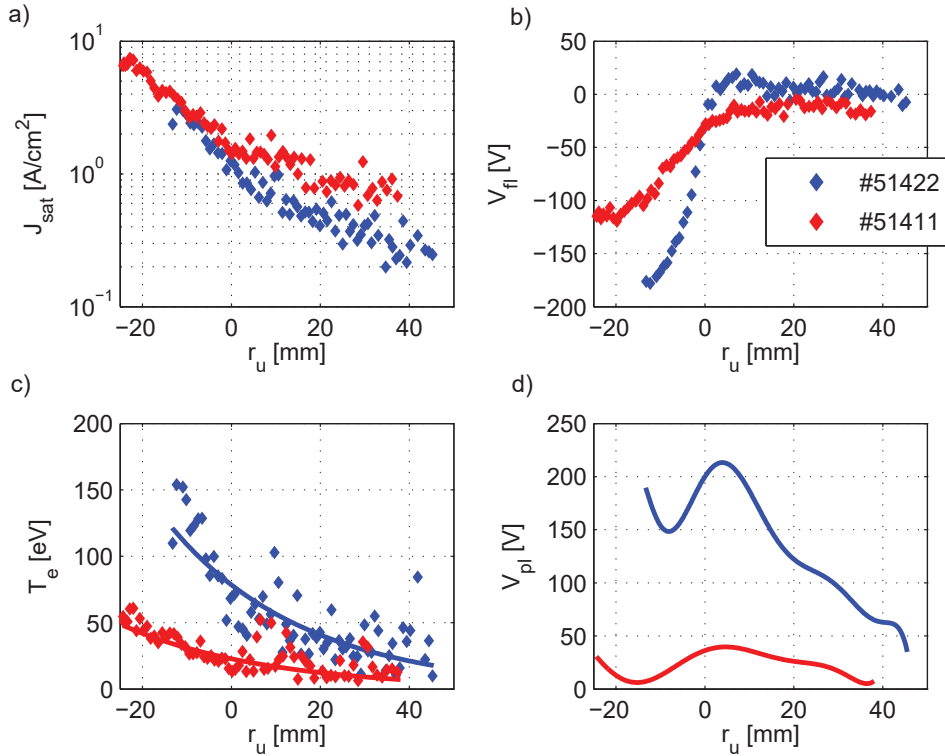


Figure 4.5: Radial profiles for discharges #51422 (blue) and #51411 (red) of: a) ion saturation current density J_{sat} , b) floating potential V_{fl} , and c) electron temperature T_e , obtained from the double probe. The fit of the noisy $T_e(r_u)$ profiles with exponentials are also shown by solid lines. d) Radial profiles of the smoothed plasma potential $V_{pl} = V_{fl} + 3T_e$.

4.1.3 Blob detection results

In this section, we present the results of the blob detection through CAS for two TCV discharges, #51422 and #51411. For both discharges, $I_p = 140$ kA, $\kappa = 1.4$, $\delta = 0$, while $n_{e,av} = 1.2 \cdot 10^{19} \text{ m}^{-3}$ in discharge #51422, and $n_{e,av} = 4.3 \cdot 10^{19} \text{ m}^{-3}$ in discharge #51411. The higher density in the former discharge, for which $\Delta P_{SOL} \sim 0$, leads to a colder SOL and results in a normalized resistivity $\nu \sim 50$ times larger than the one of #51422. This variation in resistivity is comparable to the one between the two GBS simulations introduced in section 3.6. The magnetic equilibrium of discharge #51411 is shown in Fig. 4.1b; the equilibrium for discharge #51422 is identical.

In Figure 4.5, the radial profiles of ion saturation current density J_{sat} , floating potential V_{fl} , and electron temperature T_e , obtained from the double probe, are shown. The fit of the noisy $T_e(r_u)$ profiles with exponentials are also shown in Fig. 4.5c by solid lines. In Fig. 4.5d, the smoothed plasma potential computed as $V_{pl} = V_{fl} + 3T_e$ is shown for the two discharges. The blob radial and poloidal velocities v_r , v_θ , the blob time widths τ_I and the blob diameters $2a_b$ resulting from the CAS analysis for both discharges are shown in Fig. 4.6.

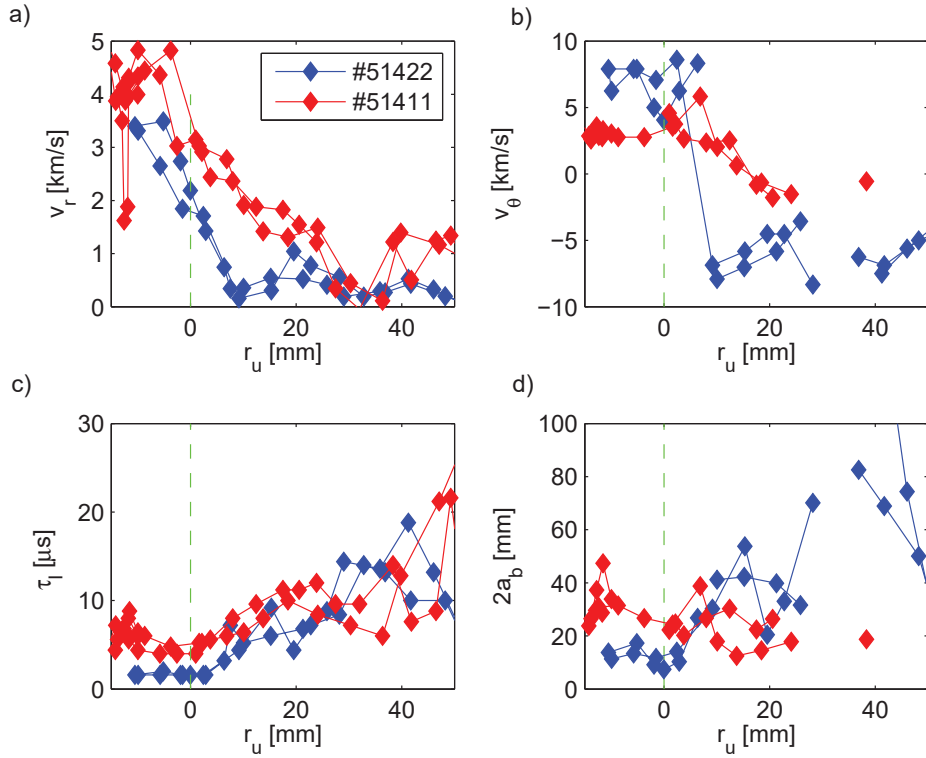


Figure 4.6: Results from CAS analysis on RP data, for TCV discharge #51422 (blue) and discharge #51411 (red), with ~ 50 times higher ν . a) Blob radial velocity v_r , b) blob poloidal velocity v_θ , c) blob time width τ_I , d) blob diameter $2a_b$. The position of the LCFS is shown with a green dashed line.

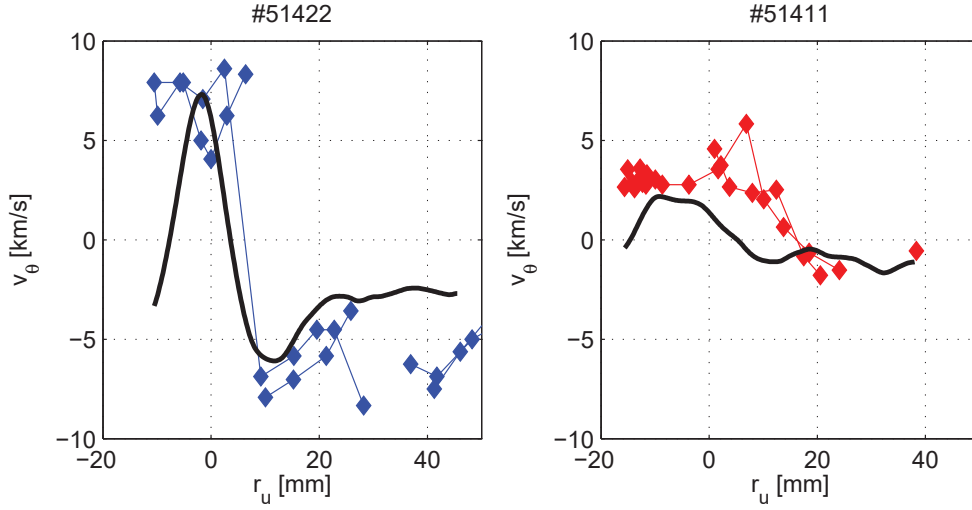


Figure 4.7: Comparison between the blob poloidal velocity (diamonds) and the background poloidal $\mathbf{E} \times \mathbf{B}$ flow (solid black lines) for discharge #51422 (left) and discharge #51411 (right).

As shown in Fig. 4.6a, the radial velocity of the blob is positive (i.e. outwards) in the SOL, being consistent with the standard blob model [13]. In this model, charge separation due to charge dependent drifts results in a mainly vertical electric field inside the blob, that in turn leads to an outwards radial $\mathbf{E} \times \mathbf{B}$ velocity that propels the blob. The blob radial velocity increases substantially with v , being 4 times larger for discharge #51411 with respect to #51422. This could be an indication that blobs are disconnected from the limiter plates for high resistivity, being in the so-called inertial regime [14].

As displayed in Fig. 4.6b, the poloidal velocity of the blobs is negative in the far SOL. This is consistent with a blob poloidal velocity mainly determined by the background $\mathbf{E} \times \mathbf{B}$ drift velocity. The comparison between the blob poloidal velocities shown in Fig. 4.6b and the poloidal component of the $\mathbf{E} \times \mathbf{B}$ drift, is shown in Fig. 4.7. Here, the background poloidal velocity \bar{v}_θ is computed as $\bar{v}_\theta = -E_r / B_\phi$, where $E_r = -\nabla_r V_{pl}$ is computed using the plasma potential profile $V_{pl}(r_u)$ shown in Fig. 4.5d. An overall good agreement is found.

The poloidal velocity is observed to change sign approaching the LCFS. The increase of resistivity by a factor 50 results in a substantial decrease of the poloidal velocity in the SOL, as it was observed in GBS simulations for comparable resistivities (Fig. 3.44).

The blob time width τ_I , plotted in Fig. 4.6c, is on average around $10 \mu\text{s}$, and it increases with r_u . Close to the LCFS, τ_I for #51411 (high resistivity) is twice as big than for #51422, while in the far SOL the two discharges exhibit a comparable τ_I . The blob diameter, displayed in Fig. 4.6d, is found to be of the order of 30 mm in the SOL. We note that this value is comparable with the far SOL width at the LFS, $\lambda_{f,RP} \sim 40$ mm. In discharge #51422, the blob size is observed to be ~ 3 times smaller in the near SOL than in the far SOL. In discharge #51411, where $\Delta P_{SOL} \sim 0$, the blob size is constant through all the entire SOL.

We point out that in this analysis the blob size and velocity are directly proportional, i.e. the increase of blob size in the far SOL for low resistivity can be partially due to the high poloidal

velocity determined by means of cross correlation measurements.

4.1.4 Scaling of blob radial velocity

In the following, we compare the blob sizes and velocities resulting from the CAS analysis with the scaling presented in Ref. [14]:

$$\tilde{v} = \frac{\sqrt{2\tilde{a}} \delta n/n}{1 + 2\sigma_l \sqrt{2\tilde{a}}^{5/2}}, \quad (4.6)$$

where the term due to ion-neutral collisions is here neglected. The sheath density drop σ_l is assumed to be equal to 0.5, $\tilde{a} = a_{b,\theta}/a^*$ and $\tilde{v} = v_r/v^*$ are the blob normalized poloidal size and velocity. The normalizations are given by:

$$a^* = \left(\frac{4L^2}{\rho_s R} \right)^{1/5} \rho_s, \quad v^* = \left(\frac{2L\rho_s^2}{R^3} \right)^{1/5} c_{s0}, \quad (4.7)$$

where L and R are the connection length and major radius respectively, ρ_s is the ion sound gyroradius, and c_{s0} is the sound speed evaluated at the LCFS. In Eq. (4.6), $\delta n/n$ is the blob relative density fluctuation, here computed using the I_{sat} measurements as $\delta n/n = 2.5\sigma/(\langle I_{sat} \rangle + 2.5\sigma)$ for each $\Delta t = 5$ ms time window, and then averaged over the entire SOL.

The inertial limit of the scaling, $\tilde{v} = \sqrt{2\tilde{a}} \delta n/n$, and the sheath dominated limit, $\tilde{v} = \frac{1}{\tilde{a}^2} \frac{\delta n/n}{2\sigma_l}$,

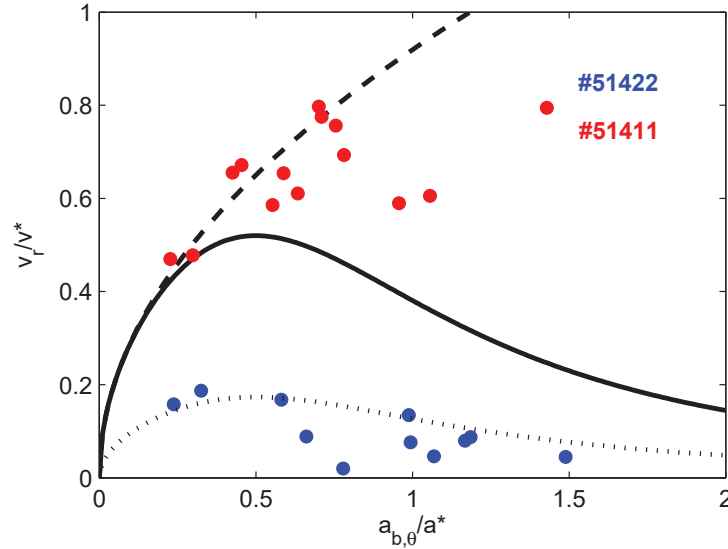


Figure 4.8: Comparison of the blob radial normalized velocity v_r/v^* and normalized poloidal size $a_{b,\theta}/a^*$ with the scaling in Eq. (4.6) (solid black) for discharge #51422 (blue dots) and discharge #51411 (red dots). The inertial limit of the scaling is shown (dashed black). The scaling the scaling in Eq.(4.6) divided by 3 is plotted with a dotted line for comparison.

can be recovered for $\tilde{a} \ll 1$ and $\tilde{a} \gg 1$, respectively. The inertial limit can also be obtained from Eq. (4.6) for blobs disconnected from the solid surfaces, i.e. for $\sigma_I = 0$.

The poloidal size of the blobs resulting from CAS analysis is computed, similarly to Eq. (4.5), as

$$2a_{b,\theta} = \tau_I |\nu_\theta|. \quad (4.8)$$

Figure 4.8 shows ν_r / ν^* plotted against $a_{b,\theta} / a^*$ for both discharge, together with the scaling in Eq. (4.6).

The blobs detected in discharge #51411 (high ν) are in good agreement with the scaling, in particular with its inertial branch, indicating possible disconnection of the blobs from the limiter plate. For the blobs detected in discharge #51422 (low ν), the CAS radial velocity is approximately a factor 3 smaller than the one predicted by the scaling. One possible cause for this could be the underestimation of the poloidal electric field E_θ used to compute ν_r .

We point out that these two discharges represents the two extreme values of plasma density explored in our experiments. We expect the results of the blob analysis from the other discharges to fall between the red and blue points in Fig. 4.8, having a better agreement with the scaling law in Eq. (4.6), than for discharge #51422.

A possible conclusion is also that the scaling in Eq. (4.6) does not applies to the cases in which a strong near SOL is present, which is the case for discharge #51422, where the blob radial velocity scales somehow differently.

4.2 Blob tracking in the GBS simulations

While the blob dynamics has been investigated experimentally in tokamaks [74, 16, 75], basic plasmas experiments [53, 76, 14, 77] and with numerical simulations of single seeded blobs [78, 79, 80], some questions are still open. Indeed, seeded simulations do not give any indication on blob shape and behavior in a SOL plasma, since they lack the interaction with the background plasma. Blob measurements in tokamaks with an exhaustive diagnostic coverage, as done in basic plasmas experiments, is prohibitive. Furthermore, the mechanisms governing blob formation and dynamics could differ in basic plasma experiments and in tokamaks SOL.

To have a better understanding of blobs generation and dynamics, we apply for the first time a blob detection technique, described in section 2.7.4, to the full-turbulence numerical simulation of two plasma discharges (section 3.6). The blobs, generated self-consistently by the turbulence, are detected and tracked in time, from their birth to their death.

Resistivity can substantially affect blobs dynamics, as predicted in Ref. [81] and experimentally measured in Ref. [16]. This has also been observed in the TCV experimental results exposed beforehand. We investigate therefore the influence of the resistivity on blob dynamics by applying our analysis to simulations introduced in section 3.6, A and B (with 40 times higher resistivity), and comparing the results.

The analysis presented in this section is applied to a simulated time interval of $23 R_0 / c_{s0}$

corresponding to 0.55 ms, the results output frequency being 3 MHz. In the following, we will refer to the simulation output result at a given time as “frame”.

In section 4.2.1, we expose the results of the application of the blob detection technique on the simulations. In section 4.2.2, the birth of the blobs is discussed, while in section 4.2.3, the 3D shape of the blobs is analyzed. In section 4.2.4, the results of the cross-correlation analysis are exposed, confirming the results from the previous subsection and giving some more insight on blob generation. In section 4.2.5, the velocities resulting from blob tracking are analyzed and compared with an existing scaling law. Finally, in section 4.2.6, we quantify the contribution of the blobs to the radial particle and heat fluxes.

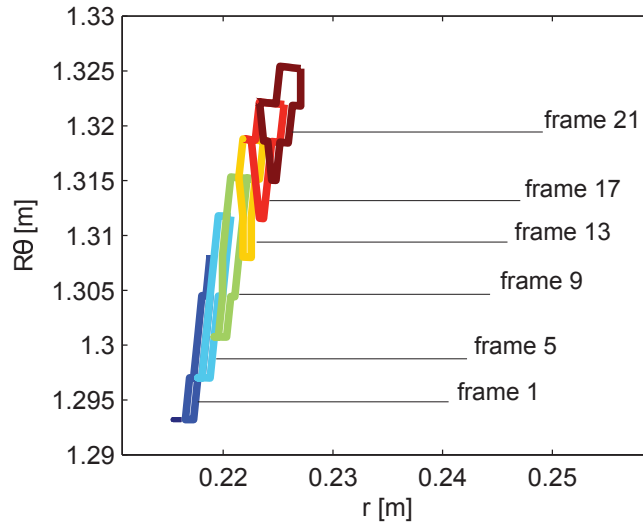


Figure 4.9: The contour of a blob as detected by the pattern recognition algorithm is plotted in the poloidal plane for subsequent simulation frames (equally spaced by 4 frames, corresponding to $1.3 \mu\text{s}$). Even though several blobs are present in the same simulation frame (~ 40), only one is plotted here for clarity.

4.2.1 Blob detection

The blob detection technique, described in section 2.7.4, is applied to the simulation output, resulting in the detection and tracking of over 5900 blobs for simulation A. A typical result of the blob tracking is shown in Fig. 4.9, in which the contour of a detected blob is displayed for subsequent frames. The results of the blob detection algorithm are summarized in Table 4.1. The higher resistivity in simulation B results in the detection of $\sim 30\%$ more filaments. This is consistent with the increase of the skewness reported in section 3.6.3. Blobs originating from merging events account for approximately 23% (22%) of the total, while 24% (30%) of the blobs results from splitting events, for simulations A (B), respectively. The average blob life time is $\langle t_l \rangle = 0.14R_0/c_{s0}$ for simulation A and $\langle t_l \rangle = 0.16R_0/c_{s0}$ for simulation B.

Simulation	# blobs	merging	splitting	$\langle a_\theta \rangle$	$\langle a_r \rangle$	$\langle a_{ } \rangle$
A ($1 \times v$)	5902	23%	24%	$7.4 \rho_s$	$4.5 \rho_s$	$6026 \rho_s$
B ($40 \times v$)	7611	22%	30%	$6.3 \rho_s$	$4.3 \rho_s$	$4460 \rho_s$
Simulation	$\langle \delta n_{max}/n_{max} \rangle$	$\langle t_l \rangle$	$\langle \sigma_{l,bottom} \rangle$	$\langle \sigma_{l,top} \rangle$	$\langle v_\theta \rangle$	$\langle v_r \rangle$
A ($1 \times v$)	0.33	$0.14 R_0/c_{s0}$	0.35	0.30	$0.011 c_{s0}$	$0.015 c_{s0}$
B ($40 \times v$)	0.30	$0.16 R_0/c_{s0}$	0.16	0.28	$0.004 c_{s0}$	$0.020 c_{s0}$

Table 4.1: Summary of the results from the blob detection method for both simulations. The quantities are defined in the text.

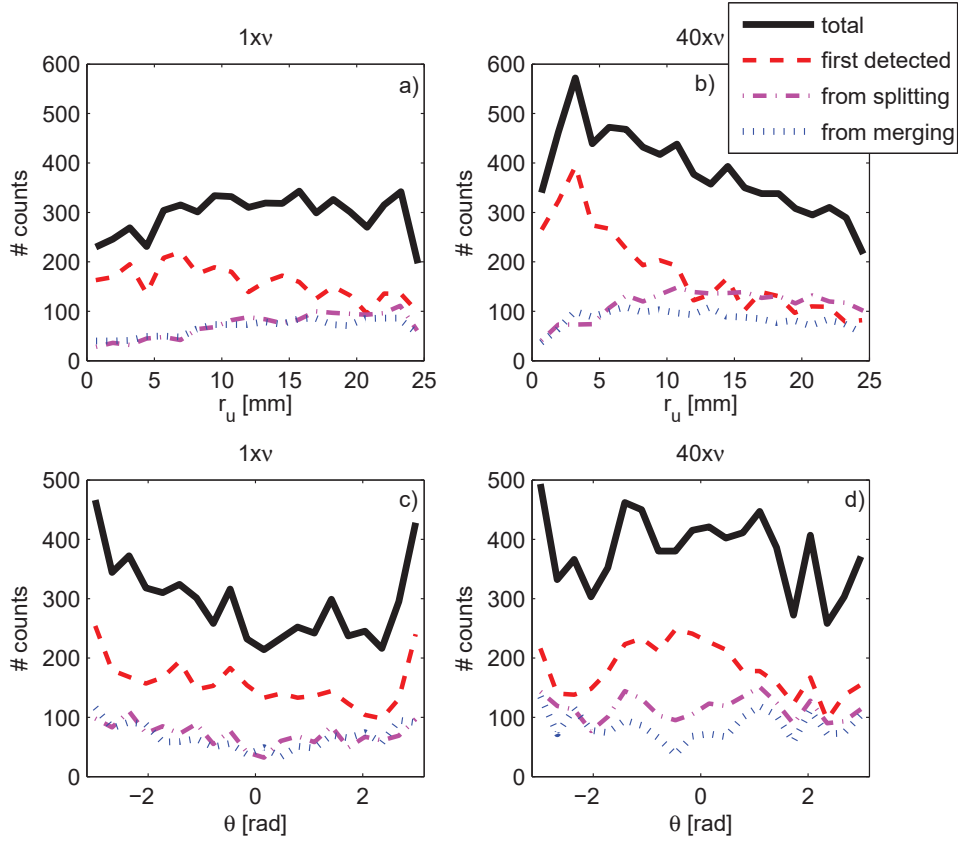


Figure 4.10: Histograms of the birth events along the radial coordinate r_u (a,b) and along the poloidal coordinate θ (c,d), for simulation A (a,c) and B (b,d). The contribution to the total birth rate (thick black lines) of blobs originating from splitting (dash-dotted magenta) or merging events (dotted blue) is distinguished from the blobs that are detected for the first time (dashed red).

4.2.2 Blob generation

In the following, we discuss the spatial distribution of the blob birth position. In Fig. 4.10(a,b), the histograms of birth events against the radial coordinate are shown for both simulations. From the detection algorithm, the birth of a blob can be due to three different mechanisms: 1) a blob is detected for the first time, i.e. it does not superimpose to any blob present in the previous simulation frame; 2) a blob is born from the splitting of a blob in the previous frame into two or more distinct parts; 3) a blob is born from the merging of two or more blobs in the previous frame. The histogram of the blob birth position is dominated by blobs which are detected for the first time (case 1), accounting for $\sim 50\%$ of the total detected blobs for both simulations. The profiles of the birth rate are hence dominated by the “first detected” blobs (red solid lines in Fig. 4.10). The radial profile of the blob first detections is quite broad and peaks around $r_u = 6$ mm for simulation A. Increasing the resistivity, the point of maximum birth rate moves radially inwards to $r_u = 3$ mm and the profile is more pronounced. Also, as shown in Fig. 4.10(c,d), where the histograms of birth events against the poloidal coordinate are shown for both simulations, the blobs are more likely to be first detected at the HFS SOL for simulation A and at the LFS SOL for simulation B. This is consistent with the transport being more ballooned due to at higher resistivity [82].

4.2.3 Characterization of the blob size and shape

The linear size of each blob in the radial and poloidal direction, a_r and a_θ , are computed as the HWHM of the density fluctuation $\delta n(r_u, \theta, t) = n(r_u, \theta, t) - \bar{n}(r_u, \theta)$, where \bar{n} is the local time-averaged density. The procedure to compute the radial HWHM is described in the following, and it is illustrated schematically in Fig. 4.11. In the poloidal and parallel directions, a similar method is applied.

Given a blob b , its density fluctuation at time t is maximum at the point (r_b, θ_b) , with $\delta n_{b,max} = \delta n(r_b, \theta_b)$. The radial profile of density fluctuations at the blob poloidal location $\delta n(r_u, \theta_b)$, in blue in Fig. 4.11, is checked for intersections with the detected areas of all the other blobs in the same simulation frame. The intersection with a second blob is shown, in Fig. 4.11, by orange vertical lines. The part of the profile not superimposed to any other blob $\delta n'(r_u, \theta_b)$ is extracted. The radial HWHM is then half of the extent of the region for which $\delta n'(r_u, \theta_b) > \delta n_{b,max}/2$ (red line in the plot).

The average poloidal size of the filaments is $\langle a_\theta \rangle = 7.4\rho_s$ and $6.3\rho_s$ for simulations A and B, respectively. This is comparable to the poloidal HWHM of the positive part of the mode shown in Fig. 4.12, where a snapshot of the normalized density fluctuation $\delta n/n_0$ is displayed. A mode with poloidal number $m = 30$ is visible close to the LCFS, and the poloidal extent of the

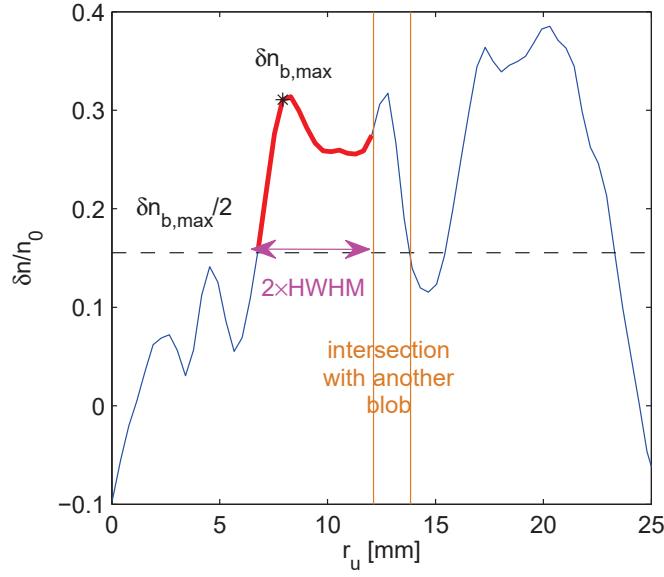


Figure 4.11: The (normalized) plasma density fluctuation radial profile $\delta n(r_u, \theta_b, t_b)$ (blue), where r_b, θ_b are the coordinate of the detected blob, at time t_b . r_b . The maximum of the density fluctuation inside the blob $\delta n_{b,max}$ are plotted with a black star. The level $\delta n = \delta n_{b,max}/2$ is indicated by a black dashed line. The region between orange lines corresponds to the intersection of the considered blob with a second one. The resulting reduced profile used for the evaluation of the blob size is shown in red. The blob size, 2HWHM, is shown in magenta.

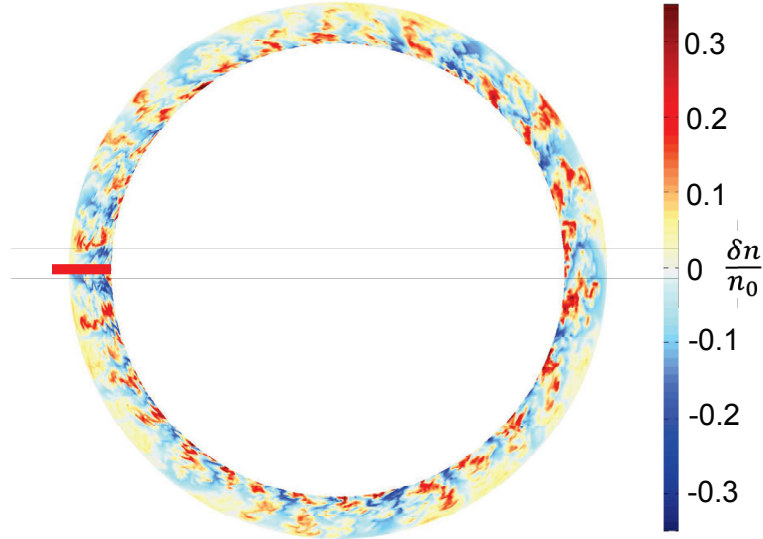


Figure 4.12: Snapshot of normalized plasma density fluctuation for simulation A, where a mode with poloidal number $m = 30$ is clearly visible.

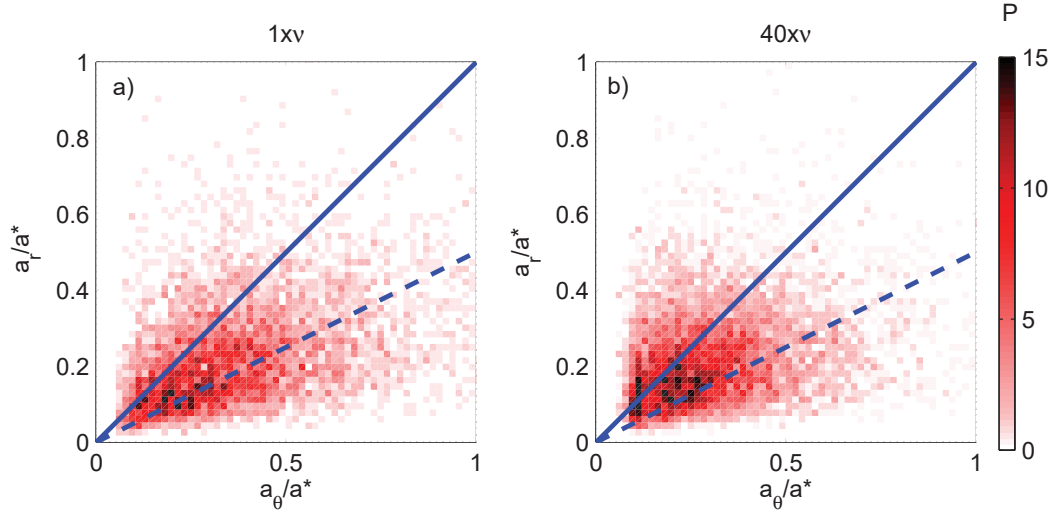


Figure 4.13: Joint probability distribution P of the poloidal and radial normalized blob size a_θ/a^* , a_r/a^* for simulations A (a) and B (b). The lines $a_r = a_\theta$ (solid) and $a_r = a_\theta/2$ (dashed) are plotted to guide the eye.

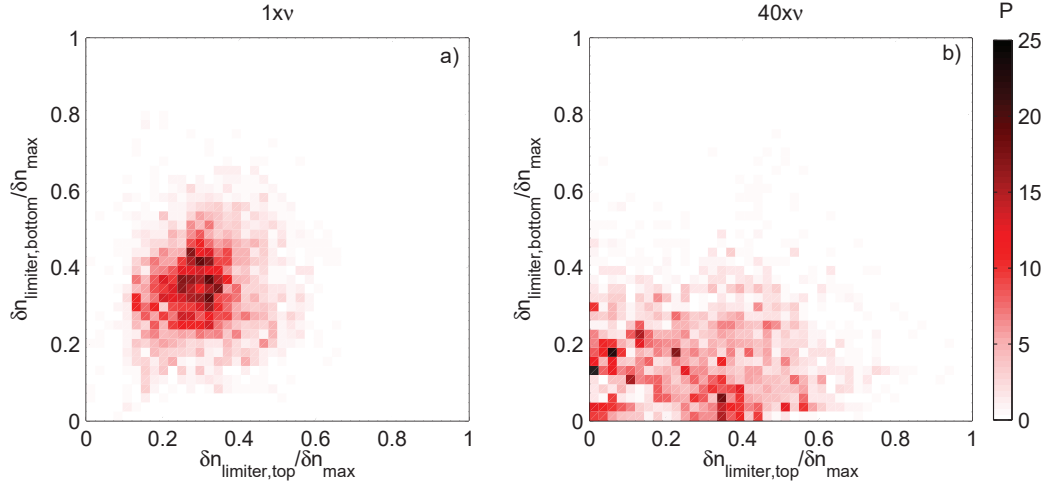


Figure 4.14: Joint probability distribution P of sheath density drop along the field line $\sigma_l = \delta n_{\text{limiter}}/\delta n_{\text{max}}$ on the two sides of the limiter. The values of σ_l are displayed for simulations A (a) and B (b) respectively.

positive density fluctuation is $L_{\theta, HWHM} \sim L_{\theta}/6 = (2\pi a_{min}/m)/6 = 14\rho_s$. The blobs are found to be elongated in the poloidal direction being $a_r/a_{\theta} \sim 1/2$, as displayed in Fig. 4.13, where the joint probability distribution of the poloidal and radial blob size (normalized to a^*) is shown for both simulations.

Taking advantage of the 3D geometry of the simulations, the density profile along the field line is extracted for blobs detected in a given 2D poloidal plane. We compute the maximum blob (normalized) density fluctuation along the field line $\delta n_{max}/n_{max}$, the blob size in the parallel direction $a_{||}$ and the sheath density drop along the field line $\sigma_l = \delta n_{limiter}/\delta n_{max}$.

Similarly to a_{θ} and a_r , $a_{||}$ is computed as the HWHM of the fluctuation profile along the field line, $\delta n(r_u, s, t) = n(r_u, s, t) - \bar{n}(r_u, s)$, where s is the coordinate along the field line.

The maximum of the density fluctuation along the field line is on average located on the low field side, just above the midplane. The average value of the fluctuation is $\langle \delta n_{max}/n_{max} \rangle = 0.33$ and 0.3 for simulations A and B, respectively. The parallel size $a_{||}$ is ~ 800 (700) times larger than the poloidal size, which corresponds to 35% (26%) of the connection length, for simulation A (B). The average values of the sheath density drop are $\langle \sigma_l \rangle = 0.32$ and 0.22 for simulations A and B, respectively, while the theoretical prediction for the sheath limited case is 0.6 [83].

As shown in Fig. 4.14, where the joint probability of the sheath density drop at the two limiter plates is displayed, the blobs disconnect from the bottom limiter plate for high resistivity (simulation B) while remaining partly attached to the top one. Indeed, assuming a blob to be detached when $\sigma_l < 0.2$, for simulation B the 66% of the blobs are detached from the bottom plate and only 36% of them are detached from the top one. The average values of the sheath density drop at the two limiter plates are $\langle \sigma_{l, bottom} \rangle = 0.16$ and $\langle \sigma_{l, top} \rangle = 0.28$.

4.2.4 Cross correlation analysis

In the GBS simulations, all physical quantities are accessible for the desired time at any point of the 3D domain. On the other hand, in the tokamak SOL, only a limited number of measurements at fixed locations is available, often from different diagnostics. Typically, fluctuations measurements are carried out at the target (limiter or divertor) using embedded Langmuir probes, while at the LFS one has to rely on gas puff imaging diagnostics [74], reciprocating Langmuir probes [16], or fast framing visible cameras [75]. Cross correlation analysis might be then one of the most powerful and reliable methods to relate target and upstream blob measurements. To give some insight on whether this technique provides valuable results, we perform a cross correlation analysis on the GBS simulation outputs and we compare the results with those obtained with the blob detection technique.

We compute the cross correlation between the density time trace at a fixed point at the outer midplane ($r_{u,0}, \theta_0 = 0, \phi_0 = 0$) and the density time traces at all the other points in the 3D domain (r_u, θ, ϕ), where ϕ is the toroidal angle. This is performed for six different values of $r_{u,0}$ and a typical result is shown in Fig. 4.15, where the amplitude of the correlation function at zero time lag C_0 is plotted for each point in the poloidal plane and on a flux surface respectively. The correlation clearly peaks along the field line passing through the reference point ($r_{u,0}, 0, 0$).

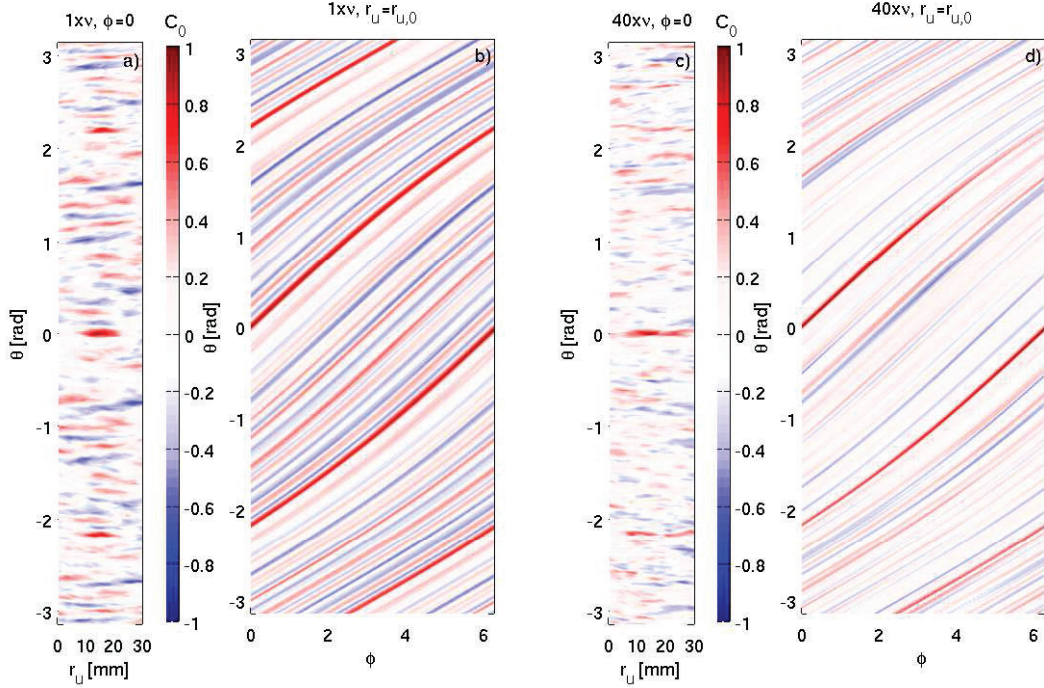


Figure 4.15: Correlation amplitude at zero time lag C_0 between a point at the outer midplane ($r_{u,0} = 14$ mm, $\theta = 0$, $\phi = 0$) and all the other points in the poloidal section defined by $\phi = 0$ (a,c) and on the flux surface $r_u = r_{u,0}$ (b,d), for simulation A (a,b) and B (c,d).

The profiles of C_0 along the field line are shown in Fig. 4.16 for simulations A and B, where C_0 is plotted along the field lines for the six reference points at the outer midplane. The time lag of maximum of correlation τ_{lag}^{max} is always shorter than $7\mu s \sim 0.04L/c_{s0}$ along the field line, where L is the connection length. This evidence supports the picture of a blob being born all along the whole field line from the beginning, rather than being generated mostly on the low field side and progressively elongating towards the limiter.

For simulation A, $C_0 > 0.5$ all along the field line from limiter to limiter, and the correlation increases moving away from the LCFS, as shown in Fig. 4.16. For simulation B, C_0 drops below 0.5 moving towards the limiters for all the considered $r_{u,0}$ values. The limiter plates and the LFS SOL are therefore decorrelated in simulation B. This picture is consistent with the result of the analysis of the sheath density drop from the 3D structure of the blobs exposed beforehand, showing that blobs disconnect from the limiter as the resistivity increases (Fig. 4.14). From an experimental point of view, this means that cross correlating measurements performed at the limiter and at the LFS would be possible in the low resistivity case (simulation A), while in the high resistivity one (simulation B), a negligible level of correlation would be found. Practically, LP usually embedded in the limiter/divertor could be used to detect the same blobs as at the OMP in the low resistivity case. Though, for high resistivity, such two measurements would be decorrelated, and a blob detection at the OMP would not correspond to a blob detection at the target.

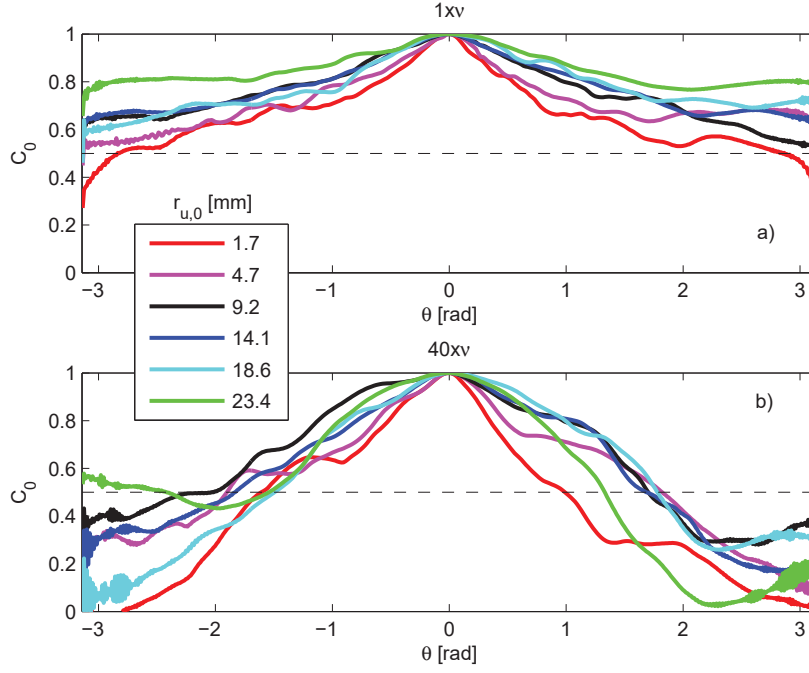


Figure 4.16: Correlation amplitude at zero time lag C_0 between a point at the outer midplane ($r_{u,0}, \theta = 0, \phi = 0$) and all the other points along the field line for simulation A (a) and B (b), plotted against the poloidal coordinate θ .

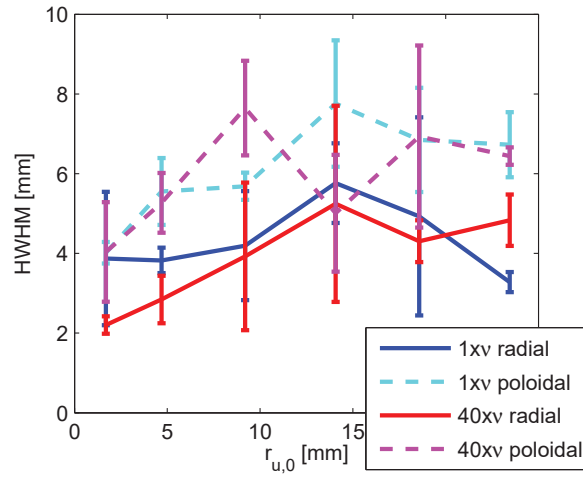


Figure 4.17: Radial (solid lines) and poloidal (dashed lines) HWHM of the correlation amplitude at zero time lag C_0 between a point at the outer midplane ($r_{u,0}, \theta = 0, \phi = 0$) and all the other points on the same poloidal plane for simulation A (blue, cyan) and B (red, magenta). The errorbars are given by the difference between the two HWHMs (“left” and “right”).

In the poloidal cross section (Fig. 4.15 a,c), the extent of the region for which $C_0 > 0.5$ gives an estimate of the size of the blobs. The variation of the poloidal and radial HWHM of such a region with the radial coordinate $r_{u,0}$ of the reference point used to compute the correlation are displayed in Fig. 4.17. The blob size estimated in this way varies between 4 and 16 ρ_s , and increases slightly moving radially outwards. These values are compatible with the results from the blob detection algorithm and with experimental findings [74]. Also, the poloidal HWHM is approximately twice the radial HWHM, consistently with the results of the blob detection analysis (Fig. 4.13).

4.2.5 Blob velocity

The detected blob velocities are found to be consistent with the local $\mathbf{E} \times \mathbf{B}$ drift, as shown in Fig. 4.18, where the blob radial and poloidal velocities resulting from the tracking algorithm v_r , v_θ are plotted against the local components of the $\mathbf{E} \times \mathbf{B}$ drift $v_{E \times B, r}$, $v_{E \times B, \theta}$. The poloidal component of the blob velocity is to be attributed to the background $\mathbf{E} \times \mathbf{B}$ flow, which is mainly poloidal towards the upper limiter. Since the background radial flow is negligible, the blob radial velocity is then consistent with the model [13] of an electrical dipole inside the blob due to vertical charge separation caused by ∇B and magnetic field curvature, resulting in a radial $\mathbf{E} \times \mathbf{B}$ drift. The average blob velocities are $\langle v_r \rangle \cong 0.016 c_{s0} = 0.15 v^*$ and $\langle v_\theta \rangle \cong 0.011 c_{s0} = 0.1 v^*$ for simulation A. In simulation B the higher resistivity causes the blobs to increase their radial velocity of about 10%, while decreasing their poloidal velocity by approximately a factor 2, being $\langle v_r \rangle \cong 0.02 c_{s0} = 0.18 v^*$ and $\langle v_\theta \rangle \cong 0.004 c_{s0} = 0.036 v^*$. This is consistent with the substantial decrease in the background $\mathbf{E} \times \mathbf{B}$ flow from simulation A to simulation B, as shown in Sec. 3.6, and with the disconnection of the blobs from the limiter discussed beforehand. Following Ref. [14], the blob radial velocity and poloidal size are normalized $\tilde{v} = v_r / v^*$ and $\tilde{a} = a_\theta / a^*$, where v^* and a^* are defined in Eq. (4.7). We compare the results of the blob detection analysis with the scaling, taken from Ref. [14], and given in Eq. (4.6), where the term due to ion-neutral collisions is here neglected, since neutrals dynamics is not included in these simulations. The comparison is carried out in Fig. 4.19, where the joint probability distribution of the blob poloidal size versus their radial velocity is plotted for both simulations. The scaling in Eq. (4.6) is displayed as a continuous blue line, and its inertial and sheath dominated limits are plotted as a dashed and dot-dashed line, respectively. An overall good agreement between the detected velocities and the scaling predictions is found. Furthermore, the agreement is particularly good with the inertial branch of the scaling. This is consistent with the observation of the blobs being partially disconnected at the limiter ($\sigma_l = 0.32$ for simulation A). The agreement with the inertial branch of the scaling is even better for simulation B, where the blobs detach from the bottom plate of the limiter.

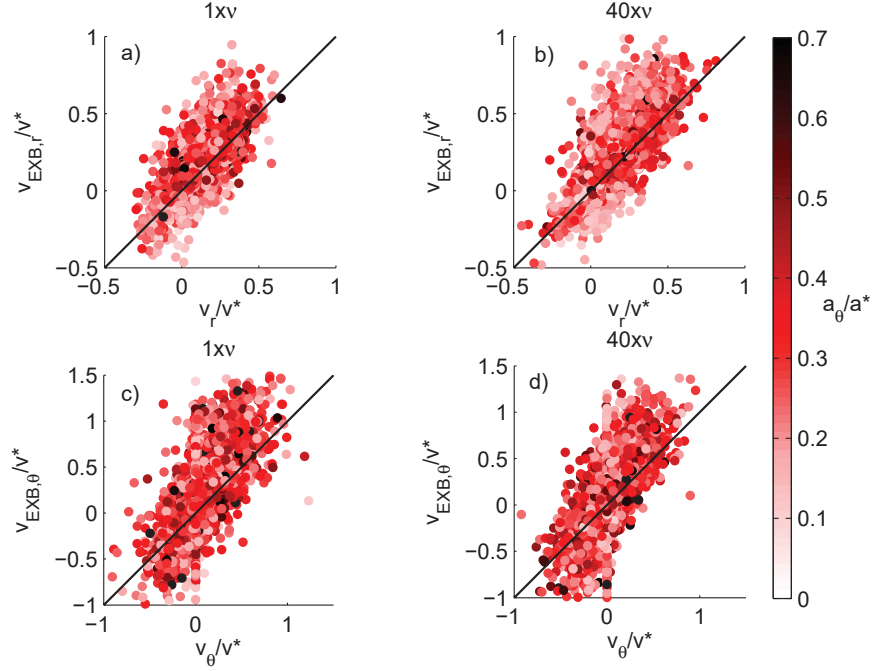


Figure 4.18: The blob radial and poloidal velocities resulting from the tracking algorithm v_r , v_θ are compared with the local components of the $\mathbf{E} \times \mathbf{B}$ drift $v_{E \times B, r}$, $v_{E \times B, \theta}$, color coded with the blob poloidal size $a_{b, \theta}$. All quantities are normalized according to Eq. (4.7).

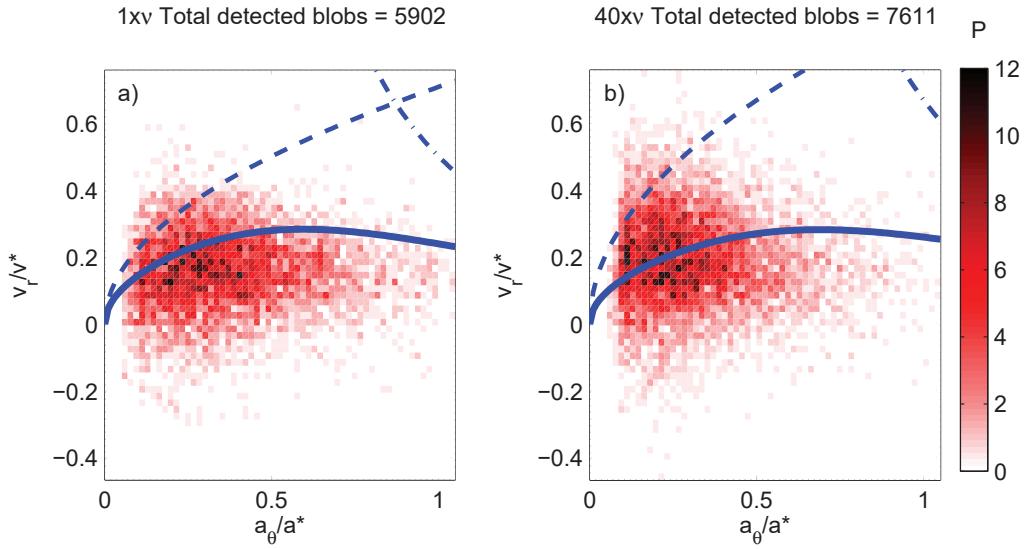


Figure 4.19: Joint probability distribution P of the normalized blob size in the poloidal plane $a_\theta/a^* \equiv \tilde{a}$ versus their normalized radial velocity $v_r/v^* \equiv \tilde{v}$ for simulations A (a) and B (b). The scaling in Eq. (4.6) (solid blue lines), its inertial limit $\tilde{v} = \sqrt{2\tilde{a}}\delta n/n$ (dashed blue lines), and the sheath dominated limit $\tilde{v} = \frac{1}{\tilde{a}^2} \frac{\delta n/n}{2\sigma_l}$ (dot-dashed blue lines), are also displayed.

4.2.6 Blob contribution to particle and heat radial fluxes

Once the blobs are generated, their radial motion is in most cases outwards. We quantify the blob contribution to the radial particle and heat fluxes. In the following, blobs are assumed to have a gaussian profile in the radial and poloidal directions with HWHM a_r , a_θ respectively:

$$\delta n_b(r_u, \theta) = \delta n_{b,max} \exp\left(-\frac{(r_u - r_{u,b})^2}{2\sigma_r}\right) \exp\left(-\frac{[(a_{min} + r_{u,b})(\theta - \theta_b)]^2}{2\sigma_\theta}\right), \quad (4.9)$$

where $\sigma_r = a_r/\sqrt{\ln 2}$ and $\sigma_\theta = a_\theta/\sqrt{\ln 2}$ are the gaussian widths in the radial and poloidal direction, respectively, $\delta n_{b,max}$ is the maximum of the density fluctuation inside the blob, located at coordinates $(r_{u,b}, \theta_b)$, and $a_{min} = 0.2$ m is the plasma minor radius. The number of particles advected by each blob is computed as

$$\delta N_b = \iint \delta n_b(r_u, \theta) dr_u d\theta = \delta n_{b,max} 2\pi \sigma_r \sigma_\theta = \delta n_{b,max} \frac{2\pi}{\ln 2} a_r a_\theta. \quad (4.10)$$

The poloidally and time averaged radial particle flux due to blobs is then computed as

$$\Gamma_b(r_u) = \frac{\sum_b \delta n_{b,max} \frac{2\pi}{\ln 2} a_r a_\theta}{2\pi(a_{min} + r_u)\Delta t}, \quad (4.11)$$

where the sum is performed over all the blobs crossing a $r_u = \text{const}$ line, and $\Delta t = 0.55$ ms is the simulated time interval used for all the analysis in this thesis. This quantity is compared with the turbulent particle flux $\Gamma_t = \langle \delta n \delta v_{E \times B, r} \rangle$ where the brackets mean average over time and poloidal direction. We remark that the turbulent flux is given by blobs ($\delta n > 0$) and holes ($\delta n < 0$). We consider here only the contribution due to positive density fluctuations $\Gamma_{t,+} = \langle \delta n \delta v_{E \times B, r} | \delta n > 0 \rangle$, resulting in $\Gamma_{t,+} \sim \Gamma_t/2$. We compare Γ_b to $\Gamma_{t,+}$ in Fig. 4.20a), where the fluxes Γ_t , $\Gamma_{t,+}$ and Γ_b are plotted, for both simulations. The error bars are given by the amount of blobs for which the computation of the HWHMs was not possible. As it emerges from Fig. 4.20b), where the ratios Γ_b/Γ_t and $\Gamma_b/\Gamma_{t,+}$ are displayed, the flux due to blobs contributes only marginally to the turbulent outward flux in the near SOL, while it accounts for up to 100% of $\Gamma_{t,+}$ in the far SOL for simulation A and 90% for simulation B.

We assume that the ion and electron temperatures inside a blob are spatially uniform. The poloidally and time averaged radial heat flux due to blobs is then given by

$$q_b(r_u) = \frac{\sum_b \delta n_{b,max} \frac{2\pi}{\ln 2} a_r a_\theta (T_{e,b} + T_{i,b})}{2\pi(a_{min} + r_u)\Delta t}, \quad (4.12)$$

where $T_{i,b}$ and $T_{e,b}$ are computed as the average ion and electron temperature inside the blob, respectively. The shape of the radial profile of the heat flux associated with the blobs $q_b(r_u)$ is qualitatively the same as for the particle flux $\Gamma_b(r_u)$. In Fig. 4.21, we compare this flux with the turbulent radial heat flux $q_t = \langle \delta p \delta v_{E \times B, r} \rangle$ and with the part of the latter due only to positive pressure fluctuations $q_{t,+} = \langle \delta p \delta v_{E \times B, r} | \delta p > 0 \rangle$. Similarly to the radial particle flux, we find

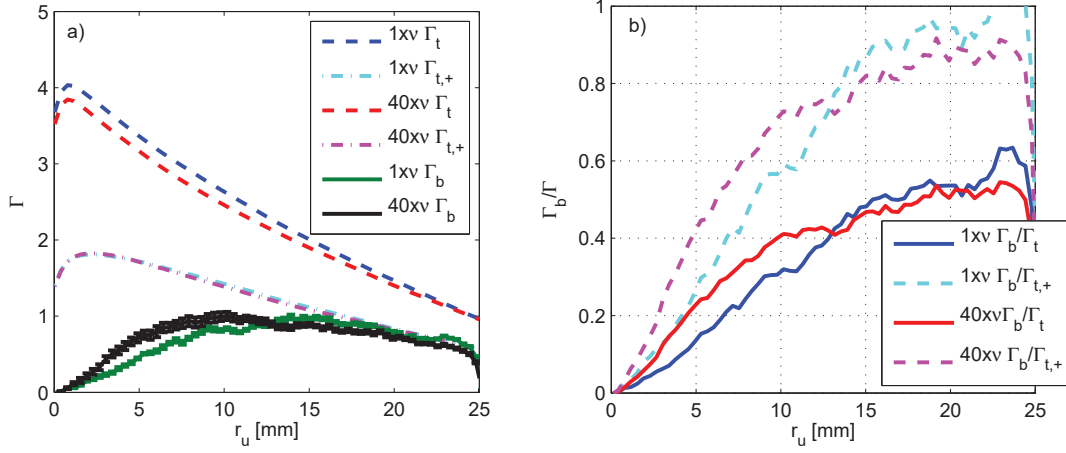


Figure 4.20: a) Particle radial fluxes Γ_b [Eq. (4.11)], Γ_t and $\Gamma_{t,+}$, for both simulations. Error bars are given by the amount of blobs for which the computation of the HWHMs was not possible. b) Ratio of blob particle flux over turbulent particle fluxes.

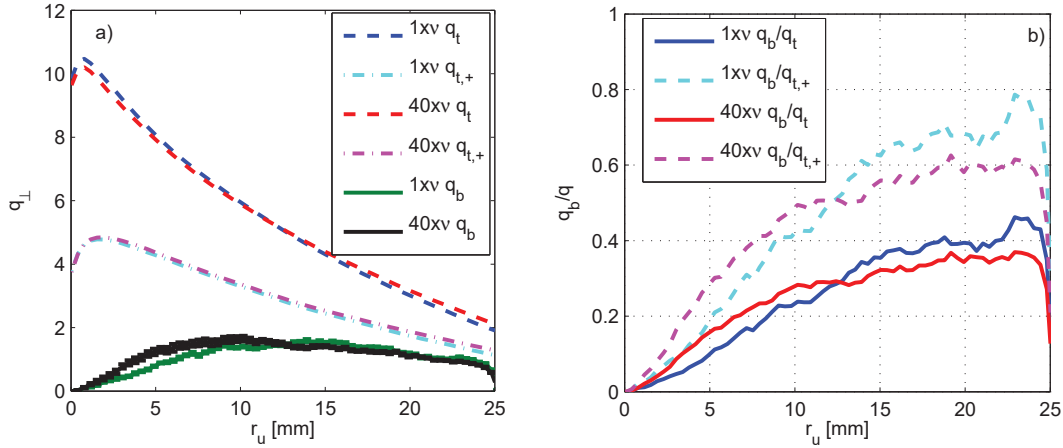


Figure 4.21: a) Heat radial fluxes q_b [Eq. (4.12)], q_t and $q_{t,+}$, for both simulations. Error bars are given by the amount of blobs for which the computation of the HWHMs was not possible. b) Ratio of blob heat flux over turbulent heat fluxes.

that the blobs do not contribute substantially to the radial heat flux in the near SOL, while they can contribute up to 70% (60%) of the turbulent flux in the far SOL for simulation A (B), respectively.

4.2.7 Experiments/simulations comparison

In the following, we compare the results from the blob detection and tracking in the simulation results with the experimental ones.

The experimental blob sizes, presented in Fig. 4.6d, correspond to blob HWHM $5\rho_s \leq a_b \leq$

$40\rho_s$, the average being $a_b \sim 20\rho_s$. The blob HWHM from the correlation analysis of the simulation outputs, shown in Fig. 4.17, corresponds to $4\rho_s \leq a_b \leq 16\rho_s$, the average being $a_b \sim 10\rho_s$. The simulated and measured blob sizes are in good quantitative agreement.

The experimentally measured blob radial velocities are of the order of $v_r \sim 0.01c_s$ for #51422 and $v_r \sim 0.05c_s$ for #51411 (high ν). These values are compatible with the average blob radial velocities from the blob tracking analysis on the simulations, exposed in Table 4.1, being $\langle v_\theta \rangle = 0.015c_s$ for simulation A and $\langle v_\theta \rangle = 0.020c_s$ for simulation B. The increase of blob radial velocity with ν , observed experimentally, is qualitatively recovered in the simulations.

The blob poloidal velocity is consistent with the poloidal component of the background $\mathbf{E} \times \mathbf{B}$ drift velocity, for both experiments and simulations. Though, the experimentally measured poloidal velocities are approximately one order of magnitude larger than the simulated ones, being $v_\theta \sim 0.1c_s$ for the experiments and $v_\theta \sim 0.01c_s$ for the simulations. Still, the decrease in blob poloidal velocity with resistivity, observed in the experiments, is recovered in the simulations.

Also, the comparison of the experimentally determined blob velocities with the scaling from Ref. [14], indicates that the blobs are probably disconnected from the limiter plates for the high resistivity discharge. This is in qualitative agreement with the 3D analysis of the blobs in the simulations (σ_I), and with the cross correlation analysis, showing that the HFS and LFS SOL are decorrelated for high resistivity ν .

4.3 Summary

In this chapter, a method based on conditional average sampling to detect and characterize blobs in TCV using the reciprocating Langmuir probe (RP) has been described.

The results of blob detection for two discharges with different resistivities have been presented. The diameter of an average blob is estimated to be of the order of 30 mm in both cases. The radial velocity of the blobs is found to increase substantially with resistivity. This is consistent with blobs being disconnected from the limiter for high resistivity, which is also suggested from the comparison of the blob size and velocities with the scaling from Ref. [14]. Indeed, for the high resistivity case, the normalized blob radial velocity \tilde{v} agrees with the inertial limit of the scaling, $\tilde{v} \propto \sqrt{\tilde{a}}$, where \tilde{a} is the normalized blob poloidal size.

The results of the application of a blob detection and tracking algorithm to GBS simulation outputs have been described. Blob generation has been investigated, discriminating the contributions from splitting and merging events. The radial and poloidal distributions of blob birth position are fairly flat for the low resistivity case. For the high resistivity case, the blob birth position radial and poloidal distributions are more peaked, respectively, close to the LCFS and at the outer midplane (OMP).

The blob size and shape have been characterized. The poloidal dimension (HWHM) of the blobs is $a_\theta \sim 7\rho_s$. The blob cross section has been found to be more elongated poloidally than radially, being $a_r/a_\theta \sim 2/3$. The blobs are found to be field aligned and elongated in the parallel direction, being $a_{||}/a_\theta \sim 850$. The blobs are partially detached from the limiters for

simulation A, being $\sigma_l \sim 0.33$, and they detach from one side of the limiter at high ν .

The results of the cross correlation analysis on the GBS simulations have been presented, confirming the results from the blob detection algorithm and showing how the blobs are generated all along the whole field line, and not being generated at the LFS and propagating towards the limiter. Also, the cross-correlation analysis shows that, in a tokamak SOL, the cross-correlation of two measurements at different locations along the same field line, at the OMP and at the target (limiter, divertor) respectively, would be possible in the low resistivity case. Practically, Langmuir probes usually embedded in the limiter/divertor could be used to detect the same blobs as at the OMP. Though, for high resistivity, such two measurements would be decorrelated, and an eventual blob detections at the target would not be relatable to blob detection at the OMP.

Blob velocities resulting from the tracking have been discussed. They suggest that blob poloidal velocity is mainly determined by the background $\mathbf{E} \times \mathbf{B}$ flow, while their radial velocity is set by the internal electric dipole, resulting in an outwards $\mathbf{E} \times \mathbf{B}$ drift. The blob velocities have been compared with the scaling developed in Ref. [14], finding good agreement.

The blob contribution to radial particle and heat fluxes has been evaluated. According to the GBS model, blobs can contribute up to 100% of the turbulent particle flux and 70% of the turbulent heat flux in the far SOL.

The experimental and numerical results have been compared, finding in general good qualitative agreement: in both cases the blob poloidal velocity is reduced for high resistivity, while the blob radial velocity is increased, indicating a transition to the inertial regime for high resistivity.

5 Conclusions and outlook

In this thesis, the physics of the Scrape-Off Layer (SOL) has been investigated in limited plasmas. Limited configurations will be used in the start-up and ramp-down phases of fusion reactors, such as ITER. The plasma-surface interaction through the SOL, possibly damaging the tokamak first wall, is the main issue for this phase and needs to be fully understood.

In particular, in this thesis we focused on two aspects of the SOL physics: the separation between a near and a far SOL, and the relationship with blob dynamics. Our investigation combines experiments on the TCV tokamak and numerical simulations of the SOL using the GBS code. We obtain the following picture of the SOL in limited plasmas, in which two main scenarios are possible, depending on the SOL normalized resistivity $\nu = \frac{en_{e0}R_0\eta_{||}}{m_i c_{s0}} \propto n_{e0} T_{e0}^{-3/2}$.

For low resistivity, $\nu \ll 10^{-2}$, the SOL is in the sheath-limited regime. In the immediate vicinity of the LCFS, non-ambipolar currents are observed to flow to the limiters. Such currents are associated with the presence of a shear layer in the poloidal $\mathbf{E} \times \mathbf{B}$ flow. This sheared flow suppresses the turbulence, otherwise typically dominated by ballooning modes, locally steepening the pressure profile. As a result, two distinct regions form in the SOL: the “near” and “far” SOL. The near SOL, typically a few mm wide, is characterized by steep radial gradients of plasma density and parallel heat flux, and is responsible for peak of the heat load deposited on the limiter, while the far SOL, typically a few cm wide, exhibits flatter profiles and accounts for the majority of the deposited heat. Furthermore, in this low resistivity scenario, blobs are electrically connected to the limiter, exhibiting modest radial velocities.

For high resistivity, $\nu \gtrsim 10^{-2}$, the SOL is in the conduction-limited regime. None (or weak) currents are observed to flow to the limiters. The corresponding sheared flow is not strong enough to suppress the turbulence, which is dominated by ballooning modes through the entire SOL. As a result, only one scale length is present, and it can be identified with the so-called far SOL in the previous scenario. In the high resistivity case, blobs are electrically disconnected from the limiters. This results in an increase of radial velocity with respect to the low resistivity case, which in turn widens the SOL.

Nevertheless, some issues remain open. Indeed, the ultimate physics mechanism, providing the connection (if any) between the disappearance of the near SOL and the blobs transitioning to the inertial regime, relating the resistivity to the intensity of the $\mathbf{E} \times \mathbf{B}$ shear and of the

Chapter 5. Conclusions and outlook

associated currents, is still missing. Additional experimental and modeling work are required. In the following, the main results presented in this thesis are summarized in more details, and possible future studies are proposed.

Two sets of experiments have been performed on the TCV tokamak during this thesis, featuring inboard-limited, ohmic L-mode deuterium (D) and helium (He) plasmas. The plasma current, density and elongation have been varied. Using infrared (IR) thermography of the central column tiles, we have measured in detail the heat flux deposited on the limiter, and we have been able to compute its perpendicular and parallel components.

The perpendicular heat flux at the contact point, $q_{\perp 0}$, accounting for up to 20% of the peak deposited heat flux, has been found to be satisfactorily described by the empirical scaling law $q_{\perp 0} \propto I_p^2 \kappa^{-0.4} n_e^{-0.45}$, for both D and He plasmas.

The SOL parallel heat flux radial profiles $q_{\parallel}(r_u)$ exhibit two different regions: a near SOL, characterized by a steep gradient of q_{\parallel} , typically a few mm wide and responsible for the peak heat loads on the limiter, and a far SOL, featuring flatter profiles of q_{\parallel} , typically a few cm wide, accounting for the majority of the heat deposited on the limiter.

For the first time, the presence of a near SOL in TCV limited plasmas has been reported in both D and He plasmas. The variation of the near and far SOL widths and of the associated heat fluxes with the main plasma parameters has been investigated. In particular, the near SOL has been observed to disappear for low plasma current or high plasma density. The power entering the near SOL, ΔP_{SOL} , has been shown to scale with the normalized resistivity ν as $\Delta P_{SOL} \propto \nu^{-1}$ and $\Delta P_{SOL} = 0$ for $\nu \gtrsim 10^{-2}$. This corresponds to a collisionality $\nu^* \gtrsim 40$, indicating that the near SOL disappears when the SOL is in conduction-limited regime, where the plasma temperature at the limiter can be much lower than at outer midplane. As a consequence, the conduction-limited regime has to be further investigated, since it can be of primary importance in a fusion reactor, not only in the diverted configuration, but also during the start-up and ramp-down phases in limited configuration.

Using flush mounted Langmuir probes (LP), non-ambipolar currents have been inferred to flow to the limiter in the near SOL, based on a nonzero floating potential V_{fl} . The presence of the non-ambipolar currents, parametrized with the floating potential drop in the near SOL, ΔV_{fl} , has been shown to correlate with the power in the near SOL, ΔP_{SOL} . A simple model relating non-ambipolar currents to the presence of a velocity shear layer has been discussed, based on the approximation $\frac{d}{dr_u} V_{pl} \sim \frac{d}{dr_u} V_{fl} \sim \Delta V_{fl} / \lambda_n$ in the near SOL, where V_{pl} is the plasma potential and λ_n is the near SOL width. The correlation between ΔV_{fl} and ΔP_{SOL} is therefore consistent with turbulence suppression due to velocity shear being the cause for the steepening of the gradient in the near SOL, as proposed in a recent theoretical model [70].

The $q_{\parallel}(r_u)$ and $V_{fl}(r_u)$ profiles measured at the outer midplane (OMP) using a reciprocating Langmuir probe (RP) are shown to be consistent with the measurements at the limiter, performed using IR thermography and flush-mounted LP, respectively. The near SOL is present simultaneously in the LFS and HFS SOL, even though it is wider at the OMP than at the limiter,

and it disappears on both sides for normalized resistivity $\nu \gtrsim 10^{-2}$. Non-ambipolar currents are measured at the OMP as well, and the floating potential radial profiles are observed to change substantially in the high ν case, being $V_{fl} < 0$ through the entire SOL at the OMP.

A mechanism to mitigate/suppress the power entering the near SOL, ΔP_{SOL} , through impurity seeding has been proposed, and first experimental evidences from a TCV discharge, where N_2 has been progressively injected, have been presented. Further investigations of impurity seeded limited plasmas are needed, featuring flat-tops at constant N_2 . This would allow for 1) steady state IR thermographic measurements 2) increasing the LP profiles spatial resolution by sweeping the plasma vertical position 3) RP reciprocation.

In the experiments discussed in this thesis, all plasmas are Ohmically heated. For future studies, we suggest the investigation of limited plasmas heated with additional external sources (ECRH, NBH), to disentangle the contributions due to the plasma temperature and the safety factor, respectively, in the observed trends with the plasma current. The plasma temperature is expected to play a major role in determining the near SOL width and the associated heat flux.

The power in the near SOL, ΔP_{SOL} , could be related to the L-H transition for limited plasmas. Limited H-mode ohmic discharges have been performed in the past in TCV [84], and the access to this regime could be facilitated with NBH. For future works, we suggest to extend the analysis performed in this thesis to limited H-mode plasmas. Another open issue is the role played by the first wall material. Indeed, the wall material (and wall conditioning in general) can change drastically the recycling, modifying the threshold for the transition to the no-near SOL regime. The repetition of similar experiments in full-tungsten tokamak (ASDEX) or with beryllium ITER-like wall (ITLW, in JET) are advisable.

The results of the numerical modeling of a TCV discharge SOL using the GBS code have been presented and compared with the experimental data, finding qualitative agreement. In particular, the simulated $q_{||}(r_u)$ profiles at the limiter exhibit a near and a far SOL, featuring widths in agreement with the experimentally measured ones. Non-ambipolar currents have been observed to flow to the limiter in the simulations, similarly to experimental measurements. Nevertheless, the magnitude of the near SOL heat flux and the non-ambipolar currents is ~ 10 times smaller in the simulation than in the experiments. The effects of resistivity on the simulation results have been discussed, comparing the first simulation with a second one with a 40 times larger normalized resistivity ν . In the latter simulation, the poloidal velocity is strongly decreased and the poloidal asymmetry is increased. The strength of the near SOL is substantially reduced at the LFS, but not at the limiter, conversely to the experimental observations.

The simulations presented in this thesis feature only open field lines, and the LCFS is set by the position of the plasma sources. The repetition of TCV-sized simulations, featuring a recently developed coupling with a closed field line region [43], are expected to show a stronger near SOL at the limiter, potentially addressing the discrepancies with the experimental data, and to provide a better insight on the physical processes at the LCFS. Recently the GBS code has been implemented with the possibility of removing the Boussinesq approximation [72], used

in the simulations performed during this thesis. Non-Boussinesq simulations are expected to resolve the discrepancies between the simulated and experimentally observed non-ambipolar currents. Furthermore, the simulations discussed here do not include neutral dynamics. A module including a kinetic description of the neutrals has been recently developed for GBS [49]. Neutrals and atomic physics, in particular recombination at low plasma temperature, are expected to play a major role in the disappearance of the near SOL for high resistivities, corresponding to conduction-limited SOL regimes in the limited configuration. Here, processes such as wall neutral recycling, recombination and neutral drag friction, play an increased role in the plasma dynamics. The inclusion of neutral dynamics in similar simulations is foreseen to be able to describe the regime where no-near SOL is observed in TCV.

Blobs are filamentary plasma structures, ubiquitous in open magnetic field line plasmas. In the tokamak SOL, blobs are believed to enhance the cross-field transport due to their radially outwards motion, accelerating the first wall erosion.

Blob dynamics is investigated in TCV using the reciprocating Langmuir probe (RP) to measure blob statistical properties such as blob speed and size. The blob size resulting from a conditional average sampling analysis is on average 30 mm. The blob radial velocity has been measured to increase substantially with the normalized resistivity ν , while the poloidal velocity is reduced, consistently with the simulation results. The comparison of the blob poloidal size and radial velocity with an existing scaling law [14] suggests that the blobs are disconnected from the limiter for high resistivity.

The computation of blob size and velocity using RP data depends on numerous assumptions. A more rigorous characterization of blob dynamics in TCV would be possible, e.g., by implementing a gas puff imaging (GPI) diagnostic.

A blob detection and tracking algorithm is applied to the simulation results. The spatial distribution of blob generation events is investigated. The blob size and shape are characterized, finding an average poloidal HWHM of $a_b \sim 7\rho_s$. The blob poloidal cross section is more elongated in the poloidal direction, being $a_r/a_\theta \lesssim 2/3$. Blobs are found to be field aligned and elongated in the parallel direction, being $a_{||}/a_\theta \sim 850$. Blobs are also partially disconnected from the limiter, and they completely detach from the limiter plate below the midplane in the simulation with high resistivity.

These results are supported by a cross-correlation analysis, which also shows that blobs are born all along the field lines, and not generated at the LFS and progressively extending towards the limiter plates.

The blob velocity obtained from the application of the blob tracking technique to the GBS simulations is discussed. The blob radial velocity is consistent with the $\mathbf{E} \times \mathbf{B}$ drift due to charge separation inside the blob, while the blob poloidal velocity is to be attributed to the background $\mathbf{E} \times \mathbf{B}$ flow. The blob size and radial velocity resulting from the detection and tracking algorithm have been shown to be in agreement with an existing scaling law [14].

The blob contribution to the perpendicular particle and heat fluxes has been evaluated. In the far SOL, blobs are found to contribute up to 100% of the turbulent particle flux and up to 70%

of the turbulent heat flux. Blob-driven cross field heat fluxes on the first wall can therefore not be neglected, and have to be taken into account, e.g., when computing the power balance of a discharge.

For future work, we suggest the application of the blob analysis presented in this thesis to TCV-sized simulations including a closed field line region. The coupling of the SOL with the closed field line region is foreseen to provide a better insight into the dynamics of the blobs in the near SOL and on their generation location and mechanism. The investigation of the effect of neutrals on the blob dynamics is also an open issue, which can be investigated in future studies.

Bibliography

- [1] Washington DC: Central Intelligence Agency. **The World Factbook 2013-2014.** <https://www.cia.gov/library/publications/the-world-factbook/geos/xx.html>, 2013.
- [2] A. Einstein. **Ist die Trägheit eines Körpers von seinem Energieinhalt abhängig?** *Annalen der Physik*, **18**:doi:10.1002/andp.19053231314, 1905.
- [3] J.D. Lawson. **Some criteria for a power producing thermonuclear reactor.** *Proceedings of the physical society of London section B*, **70**:6–10, 1957.
- [4] J.H. Nuckolls. **Early steps toward inertial fusion energy (IFE) (1952 to 1962).** DOI: 10.2172/658936, 1998.
- [5] G. Federici et al. **Overview of EU DEMO design and R&D activities.** *Fusion Engineering and Design*, **89**:1464–1474, 2014.
- [6] J.P. Freidberg. **Plasma Physics and Fusion Energy** . Cambridge University Press, 2008.
- [7] J. Wesson. **Tokamaks 2nd edn** . Oxford: Oxford University Press, page 670, 1997.
- [8] M. Keilhacker and the JET team. **Fusion physics progress on the Joint European Torus (JET).** *Plasma Physics Controlled Fusion*, **41**:B1–B23, 1999.
- [9] K. Tomabechi for the ITER team. **ITER: design overview.** *Journal of Nuclear Materials*, **171-181**, 1991.
- [10] P.C. Stangeby. **The Plasma Boundary of Magnetic Fusion Devices** . Institute of Physics Publishing Bristol and Philadelphia, 2000.
- [11] T. Eich et al. **Inter-ELM power decay length for JET and ASDEX Upgrade: measurement and comparison with the heuristic drift-based model.** *Physical Review Letters*, **107**:215001, 2011.
- [12] J. Horacek et al. **Multi-machine scaling of the main SOL parallel heat flux in tokamak limiter plasmas.** *Plasma Physics and Controlled Fusion*, **58**:074005, 2016.
- [13] S.I. Krasheninnikov et al. **Recent theoretical progress in understanding coherent structures in edge and SOL turbulence.** *Journal of Plasma Physics*, **74**:679–717, 2008.

Bibliography

- [14] C. Theiler et al. **Cross-field motion of plasma blobs in an open magnetic field line configuration.** *Physical Review Letters*, **103**:065001, 2009.
- [15] N. Vianello et al. **On filamentary transport in the TCV tokamak: addressing the role of the parallel connection length.** *26th IAEA Fusion Energy Conference, Kyoto, Japan*, 2016.
- [16] D. Carallero et al. **Experimental validation of a filament transport model in turbulent magnetized plasmas.** *Physical Review Letters*, **115**:215002, 2015.
- [17] B. Lipschultz et al. **Plasma-surface interaction, scrape-off layer and divertor physics: implications for ITER.** *Nuclear Fusion*, **47**:1189–1205, 2007.
- [18] D.D. Ryutov et al. **A snowflake divertor: a possible solution to the power exhaust problem for tokamaks.** *Plasma Physics and Controlled Fusion*, **54**:124050, 2012.
- [19] M. Kotschenreuther et al. **On heat loading, novel divertors, and fusion reactors.** *Physics of Plasmas*, **14**:072502, 2007.
- [20] P. M. Valanju et al. **Super-X divertors and high power density fusion devices.** *Physics of Plasmas*, **16**:056110, 2009.
- [21] B. LaBombard et al. **ADX: a high field, high power density, advanced divertor and RF tokamak.** *Nuclear Fusion*, **55**:053020, 2015.
- [22] H. Reimerdes et al. **Experimental investigation of neon seeding in the snowflake configuration in TCV.** *Journal of Nuclear Materials*, **463**:1196–1199, 2015.
- [23] G. Arnoux et al. **Scrape-off layer properties of ITER-like limiter start-up plasmas in JET.** *Nuclear Fusion*, **53**:073016, 2013.
- [24] R.A. Pitts et al. **Physics basis and design of the ITER plasma-facing components.** *Journal of Nuclear Materials*, **415**:S957–S964, 2011.
- [25] A.R. Raffray et al. **The ITER blanket system design challenge.** *Nuclear Fusion*, **54**:033004, 2014.
- [26] M. Kocan et al. **Impact of a narrow limiter SOL heat flux channel on the ITER first wall panel shaping.** *Nuclear Fusion*, **55**:033019, 2015.
- [27] F. Hofmann et al. **Creation and control of variably shaped plasmas in TCV.** *Plasma Physics and Controlled Fusion*, **36**:B277–B287, 1994.
- [28] F. Hofmann et al. **Extension of the TCV operating space towards higher elongation and higher normalized current.** *Nuclear Fusion*, **42**:743–749, 2002.
- [29] R.A. Pitts. https://crppwww.epfl.ch/~pitts/pages/rap_firstwall.html.
- [30] R.A. Pitts et al. **The design of central column protection tiles for the TCV tokamak.** *Nuclear Fusion*, **39**:1433–1449, 1999.

-
- [31] K.F. Mast et al. **A low noise highly integrated bolometer array for absolute measurement of VUV and soft x radiation.** *Review of Scientific Instruments*, **62**:744–750, 1991.
- [32] J. Kamleitner. **Suprathermal electron studies in Tokamak plasmas by means of diagnostic measurements and modeling.** *EPFL thesis 6523*, 2015.
- [33] F. Hofmann and G. Tonetti. **Tokamak equilibrium reconstruction using Faraday rotation measurements.** *Nuclear Fusion*, **28**:1871–1878, 1988.
- [34] D. Halliday R. Resnick and J. Walker. **Fundamentals of Physics .** *John Wiley & Sons, Inc*, 2005.
- [35] A. Herrmann. **Limitations for divertor heat flux calculations of fast events in tokamaks.** *ECA*, **25A**:2109–2112, 2001.
- [36] H.M Mott and I. Langmuir. **The theory of collectors in gaseous discharges.** *Physical Review*, **28**:727–763, 1926.
- [37] C.D. Child. **Discharge from a hot CaO.** *Physical Review (Series I)*, **32**:492–511, 1911.
- [38] H. Reimerdes et al. **Power distribution in the snowflake divertor in TCV.** *Plasma Physics and Controlled Fusion*, **55**:124027, 2013.
- [39] G. F. Matthews et al. **Investigation of the fluxes to a surface at grazing angles of incidence in the tokamak boundary.** *Plasma Physics and Controlled Fusion*, **32**:1301–1320, 1990.
- [40] J.A. Boedo et al. **Fast scanning probe for the NSTX spherical tokamak.** *The Review of Scientific Instruments*, **80**:123506, 2009,.
- [41] B.A. Sieglin. **Experimental Investigation of Heat Transport and Divertor Loads of Fusion Plasma in All Metal ASDEX Upgrade and JET.** *Technische Universitat Munchen thesis*, 2014.
- [42] P. Ricci et al. **Simulation of plasma turbulence in scrape-off layer conditions: the GBS code, simulation results and code validation.** *Plasma Physics and Controlled Fusion*, **54**:124047, 2012.
- [43] F.D. Halpern et al. **The GBS code for tokamak scrape-off layer simulations.** *Journal of Computational Physics*, **315**:388–408, 2016.
- [44] B.N. Rogers and P. Ricci. **Low-frequency turbulence in a linear magnetized plasma.** *Physical Review Letters*, **104**:225002, 2010.
- [45] P. Ricci and B.N. Rogers. **Turbulence Phase Space in Simple Magnetized Toroidal Plasmas.** *Physical Review Letters*, **104**:145001, 2010.
- [46] J. Loizu et al. **Boundary conditions for plasma fluid models at the magnetic presheath entrance.** *Physics of Plasmas*, **19**:122307, 2012.

Bibliography

- [47] A. Masetto et al. **Turbulent regimes in the tokamak scrape-off layer.** *Physics of Plasmas*, **20**:092308, 2013.
- [48] F.D. Halpern et al. **Comparison of 3D flux-driven scrape-off layer turbulence simulations with gas-puff imaging of Alcator C-Mod inner-wall limited discharges.** *Plasma Physics and Controlled Fusion*, **57**:054005, 2015.
- [49] C. Wersal and P. Ricci. **A first-principles self-consistent model of plasma turbulence and kinetic neutral dynamics in the tokamak scrape-off layer.** *Nuclear Fusion*, **55**:123014, 2015.
- [50] P. Paruta et al. **A flexible numerical scheme for simulating plasma turbulence in the tokamak scrape off layer.** *Joint Varenna-Lausanne International workshop, Villa Monastero, Varenna, Italy*, 2016.
- [51] J. Loizu. **The role of the sheath in magnetized plasma turbulence and flows .** *EPFL thesis* 5985, 2013.
- [52] S.I. Braginskii. **Transport Processes in a Plasma.** *Reviews of Plasma Physics*, **1**:205, 1965.
- [53] S.H. Mueller et al. **Probabilistic analysis of turbulent structures from two-dimensional plasma imaging.** *Physics of Plasmas*, **13**:100701, 2006.
- [54] M. Merola et al. **ITER plasma-facing components.** *Fusion Engineering and Design*, **85**:2312–2322, 2010.
- [55] ITER Physics Basis. **Chapter 4.** *Nuclear Fusion*, **39**:2391, 1999.
- [56] J. Horacek et al. **Narrow heat flux channels in the COMPASS limiter scrape-off layer.** *Journal of Nuclear Materials*, **463**:385–388, 2015.
- [57] P.C. Stangeby et al. **Power deposition on the DIII-D inner wall limiter.** *Journal of Nuclear Materials*, **463**:389–392, 2015.
- [58] F. Nespoli et al. **Heat loads in inboard-limited L-mode plasmas in TCV.** *Journal of Nuclear Materials*, **463**:393–396, 2015.
- [59] F. Nespoli et al. **Near and far SOL physics in inboard-limited plasmas in TCV.** *21st Joint EU-US Transport Task Force Meeting, Leysin, Switzerland*, 2016.
- [60] B. Labit et al. **The physics of the heat flux narrow decay length in the TCV scrape-off layer: experiments and simulations.** *26th IAEA Fusion Energy Conference, Kyoto, Japan*, 2016.
- [61] H. Weisen et al. **Effect of plasma shape on confinement and MHD behaviour in the TCV tokamak.** *Nuclear Fusion*, **37**:1741–1758, 1997.

-
- [62] F. D. Halpern et al. **A theoretical interpretation of the main scrape-off layer heat-flux width scaling for tokamak inner-wall limited plasmas.** *Plasma Physics and Controlled Fusion*, **58**:084003, 2016.
- [63] D. Carallero et al. **An experimental investigation of the high-density transition of the scrape-off layer transport in ASDEX Upgrade.** *Nuclear Fusion*, **54**:123005, 2014.
- [64] W.M. Stacey. **Fusion Plasma Physics**. John Wiley & Sons, 2012.
- [65] P. Ricci and B.N. Rogers. **Plasma turbulence in the scrape-off layer of tokamak devices.** *Physics of Plasmas*, **20**:010702, 2013.
- [66] R.J. Goldston. **Heuristic drift-based model of the power scrape-off width in low-gas-puff H-mode tokamaks.** *Nuclear Fusion*, **52**:013009, 2012.
- [67] R.J. Goldston. **Theoretical aspects and practical implications of the heuristic drift SOL model.** *Journal of Nuclear Materials*, **463**:397–400, 2015.
- [68] R.J. Goldston and P.H. Rutherford. **Introduction to Plasma Physics**. Bristol: Institute of Physics Publishing, 1997.
- [69] R. Dejarnac et al. **Understanding narrow SOL power flux component in COMPASS limiter plasmas by use of Langmuir probes.** *Journal of Nuclear Materials*, **463**:381–384, 2015.
- [70] F. D. Halpern and P. Ricci. **Velocity shear, turbulent saturation, and steep plasma gradients in the scrape-off layer of inner-wall limited tokamaks.** *Nuclear Fusion*, **57**:034001, 2016.
- [71] F. Nespoli et al. **Non-linear simulations of the TCV Scrape-Off Layer.** *Nuclear Materials and Energy*, <http://dx.doi.org/10.1016/j.nme.2016.10.019>, 2016.
- [72] J. Morales et al. **The impact of the Boussinesq approximation on plasma turbulence in the scrape-off layer.** *43rd European Physical Society Conference on Plasma Physics, Leuven, Belgium*, 2016.
- [73] I. Furno et al. **Mechanism for blob generation in the TORPEX toroidal plasma.** *Physics of Plasmas*, **15**:055903, 2008.
- [74] S.J. Zweben et al. **Edge and SOL turbulence and blob variations over a large database in NSTX.** *Nuclear Fusion*, **55**:093035, 2015.
- [75] A. Kirk et al. **L-mode filament characteristics on MAST as a function of plasma current measured using visible imaging.** *Plasma Physics and Controlled Fusion*, **58**:085008, 2016.
- [76] S.H. Mueller et al. **Studies of blob formation, propagation and transport mechanisms in basic experimental plasmas (TORPEX and CSDX).** *Plasma Physics and Controlled Fusion*, **51**:055020, 2009.

Bibliography

- [77] P. Manz et al. **Plasma blob generation due to cooperative elliptic stability.** *Physical Review Letters*, **107**:195004, 2011.
- [78] D.A. D'Ippolito et al. **Blob stability and transport in the scrape-off layer.** *Physics of Plasmas*, **10**:4029, 2003.
- [79] F. Riva et al. **Blob dynamics in the TORPEX experiment: a multi-code validation .** *Plasma Physics and Controlled Fusion*, **58**:044005, 2016.
- [80] N. Walkden et al. **Dynamics of 3D isolated thermal filaments .** *Plasma Physics and Controlled Fusion*, **58**:115010, 2016.
- [81] J. R. Myra et al. **Collisionality and magnetic geometry effects on tokamak turbulent transport. I. A two-region model with application to blobs.** *Physics of Plasmas*, **13**:112502, 2006.
- [82] A. Masetto et al. **Finite ion temperature effects on scrape-off layer turbulence.** *Physics of Plasmas*, **22**:012308, 2015.
- [83] F.F. Chen and J.P. Chang. **Lecture Notes on Principles of Plasma Processing.** *Kluwer Academic/Plenium Publishers*, 2003.
- [84] J.-M. Moret et al. **Ohmic H-mode and confinement in TCV.** *Plasma Physics and Controlled Fusion*, **37**:A215–A226, 1995.

Acknowledgements

First of all,

I would like to thank my thesis directors, Ivo and Benoit, without whom this work would have not been possible. Thank you for your guidance, for your patience, and your careful revision of all of my manuscripts.

I would also like to thank Holger and Paolo, who have been like additional supervisors to me, guiding my first steps in the wonderful worlds of infrared thermography and GBS simulations, respectively. For similar reasons, I would like to thank Gustavo and Josef, and the GBS team, in particular Federico, Fabio and Christoph. Many thanks also to Cedric, for the massive work done on the reciprocating probe, whose data constitute a good part of this thesis, and for his availability.

A huge thanks is due to the TCV team, without whom the experimental part of this thesis would have just not been possible. A special thanks goes to my colleagues, Fabio, Gabriele, Claudio, Alex and Oulfa, for their availability in discussing everyday issues.

Thanks also to Alan, for revising the English of this work.

I would like to thank the entirety of the people working at CRPP (SPC) for making it such an enjoyable and friendly place in which to work. In particular, I am happy to have been part of the lively big group of the PhD students; not everybody gets so lucky!

So, thanks to the "veteran" PhDs for including me from the first moment I put my foot on campus: thanks Fabio for all the help he would give me in any situation, Alex for hosting me when I had nowhere to go, Josef for always having an answer to my numerous questions in the early days, Daniele for the horrible movies, Lucia and Silvano for the banana split... and Julien, for the first challenging nights in Sat, and for being an astronaut, together with Joaquim and Alex. Thanks to Falk, Annamaria and David, for sharing with me many experiences in the mountains that I will not forget.

Thanks to the people that had the disgrace to be stuck in the same office with me: Joyeeta, Francesco, Mengdi, Fabian. A big thanks to Pedro, Hamish and Alberto for sharing with me the glory of playing on Sat's stage as "Nick and the Tamers". Thanks to Fabio for the carnival, Christoph for the metro dancing, Himank for the gym workout attempts, Matteo and Rogerio for the karaoke, and Paola for introducing me to all her attractive friends. Male friends. Also,

Acknowledgements

thanks to Antoine for not writing my thesis.

Many thanks to Claudio and Gabriele for sharing with me a huge number of different experiences, featuring the ingestion of several mildly alcoholic and/or caffeinated beverages. Thanks Oulfa for the many dinners and house parties, always very sober and aristocratic. Thanks Jonny for doing his PhD in parallel with me, sharing beers and experiences in different parts of the world. That was lovely. Thanks to Umar for dragging me into a lot of fun situations, last but not least the Aussie road trip, during which I am writing these lines on the backseat of the car.

On a different note, I would also like to thank Daniele for being my "mountain buddy", together with Damiano, and Piero and Edo for making my Lausanne experience surely more enjoyable.

Many thanks to my friends in the Brianza Velenosa, Dario, Ste, Cespu, Grigghi, Fio, Andre, Paglia, Franzo, and all the group, for making me feel at home every time I came back, like I never left. A special thanks goes to Erica, who I stressed the most with all my complaints through the years. Also thanks to the Panda Fight Club, for all the wonderful music we made together (that, by the way, is available online...just saying).

Infine, vorrei ringraziare la mia famiglia: mamma e babbo e il mio piccolo fratellino, e la zia Miriam, per tutto il supporto e per esserci sempre...grazie.

Oh, I almost forgot, so I'll leave this here. As promised, I would like to thank Marie for "fruitful conversations"....but that's another story.

Federico Nespoli

Email: nespolifederico@gmail.com

Tel: +41 788 744 253

Date of birth: 5/11/1987, Giussano (MB), Italy



Education

- 2012-2016: **PhD candidate, Ecole Polytechnique de Lausanne (EPFL), Switzerland**
 - PhD in Physics at the Swiss Plasma Center (SPC)
 - Title : Scrape-Off Layer physics in limited plasmas in TCV
 - Supervisors: Dr. Ivo Furno, Dr. Benoit Labit
 - Work description: Investigation of the Scrape-Off Layer combining experiments (Infrared thermography, Langmuir probes, bolometry) on the TCV tokamak and numerical simulations of plasma turbulence. Study of the separation of the near and far SOL and of blob dynamics.
- 2009-2012: **Msc. in Physics, Università degli Studi, Milano, Italy**
 - Master thesis at IFP-CNR, Milano, Italy
 - Title: "Acceleration mechanisms of ferromagnetic dust in tokamaks"
 - Supervisors: Dr. Enzo Lazzaro, Dr. Massimiliano Romé
 - Work description: Investigation of ferromagnetic dust particles dynamics in the FTU tokamak through dedicated numerical simulations.
- 2006-2009: **Bachelor in Physics, Università degli Studi, Milano, Italy**
 - Thesis title: "Caratterizzazione sperimentale della dinamica di un bunch di elettroni nella trappola di Malmberg-Penning, ELTRAP"; (in Italian language).
 - Supervisor: Dr. Massimiliano Romé
- 2006: **Highschool diploma, Liceo Scientifico Marie Curie, Meda (MB), Italy**

Teaching Experience and Refereeing Activity

- Teaching assistant for different Bachelor and Master courses: Physique Generale I with Prof. Schneider, Physique Generale II with Prof. Tran, Physique Generale II with Prof. Ricci, Nuclear Fusion and Plasma Physics with Prof. Fasoli and Tran.
- Refereeing papers for Journal of Nuclear Materials.

Professional Experience

- Operation, maintenance and implementation of TCV diagnostics: Infrared camera, bolometers, reciprocating Langmuir probe.
- Development of analysis tools (Matlab) for both experimental and numerical data.
- Basic knowledge of COMSOL Multiphysics, IDL.
- Experience in the design and coordination of experiments in international collaboration: Scientific Coordinator of the EUROFUSION MST1 experiments TCV15-2.2.-4 and TCV15-He-13.

Language knowledge

- Italian (mother tongue)
- English (fluent)
- French (fluent)

First author publications:

F. Nespoli et al., **Blob properties in full-turbulence simulations of the TCV Scrape-Off Layer**, Plasma Physics and Controlled Fusion (2016), submitted for publication

F. Nespoli et al., **Non-linear simulations of the TCV Scrape-Off Layer**, Nuclear Materials and Energy, (2016) <http://dx.doi.org/10.1016/j.nme.2016.10.019>

F. Nespoli et al. **Heat loads in inboard-limited L-mode plasmas in TCV**, Journal of Nuclear Materials, 463 (2015) <http://dx.doi.org/10.1016/j.jnucmat.2014.11.137>

Conference contributions and invited talks (1st author)

Near and far SOL physics in inboard-limited plasmas in TCV, 21st Joint EU-US Transport Task Force Meeting, Leysin, Switzerland, 2016 (invited talk).

Blob properties in nonlinear simulations of the TCV Scrape-Off Layer, 22nd International Conference on Plasma Surface Interaction, May 30-June 3, 2016, Rome, Italy (poster).

Investigating the double scale length of limited plasmas with nonlinear simulations of the TCV Scrape-Off Layer, 42nd European Physical Society Conference on Plasma Physics, Lisbon, Portugal 22nd—26th June 2015 (poster).

Heat loads in inboard limited L-mode plasma as in TCV, Annual Meeting of the Swiss Physical Society, July 2, 2014, Fribourg, Switzerland (talk).

Heat loads in inboard limited L-mode plasmas in TCV, 21st PSI - International Conference on Plasma Surface Interactions in Controlled Fusion Devices, Kanazawa City, Japan, 26-30 May 2014 (poster).

Modelling and diagnostics of hypervelocity dust particles in a tokamak, 39th European Physical Society Conference on Plasma Physics, Stockholm, Sweden, 2-6 July 2012 (poster).

Co-authored publications

H. Meyer et al., **Overview of progress in European medium sized tokamaks towards an integrated plasma-edge/wall solution**, Nuclear Fusion (2016), submitted for publication

S. Coda et al., **Overview of the TCV tokamak program: scientific progress and facility upgrades**, Nuclear Fusion (2016), submitted for publication

C. Theiler et al., **Results from recent detachment experiments in alternative divertor configurations on TCV**, Nuclear Fusion (2016), submitted for publication

Gallo et al., **Effect of plasma geometry on divertor heat flux spreading: MONALISA simulations and experimental results from TCV**, Nuclear Materials and Energy, (2016) accepted for publication

Labit et al, **Experimental studies of the snowflake divertor in TCV**, Nuclear Materials and Energy (2016), submitted for publication

K.A. Verhaegh et al., **Spectroscopic investigations of divertor detachment in TCV**, Nuclear Materials and Energy (2016), accepted for publication

U. Sheikh et al., **A novel carbon coating technique for foil bolometers**, Review of Scientific Instruments 87 (2016)

M. Kocan et al. **Impact of a narrow limiter SOL heat flux channel on the ITER first wall panel shaping**, Nuclear Fusion 55 (2015)

H. Reimerdes et al. **Experimental investigation of neon seeding in the snowflake configuration in TCV**, Journal Of Nuclear Materials 463 p. 1196-1199 (2015).

H. Reimerdes et al., **Power distribution in the snowflake divertor in TCV**, Plasma Physics and Controlled Fusion 55 p. 124027 (2013)

E. Lazzaro et al., **Transport and effects of ferromagnetic dust in a tokamak with a metallic vessel**, Plasma Physics and Controlled Fusion 54 (2012).